EFFECT OF FUTURE EXTREME PRECIPITATION EVENTS ON THE STABILITY OF SOIL EMBANKMENTS ACROSS ONTARIO

Leila Baninajarian

A THESIS SUBMITTED TO THE FACULTY OF GRADUATE STUDIES IN PARTIAL FULFILLMENT OF THE REQUIREMENTS FOR THE DEGREE OF MASTER OF APPLIED SCIENCE

GRADUATE PROGRAM IN CIVIL ENGINEERING

YORK UNIVERSITY

TORONTO, ONTARIO

SEPTEMBER 2020

Abstract

Changes in climatic conditions have been observed since about 1950. Climate change is expected to increase the magnitude and frequency of extreme events as well as long-term changes in average climatic conditions. The stability of earth embankments plays a critical role in transportation infrastructure sustainability. The stability of embankments is susceptible to water infiltration as a result of intense rainfall events. The primary objective of this research is to quantify the impacts of future climate change on the stability of typical highway soil embankments across Ontario. These quantifications have been done by making use of numerical modelling techniques. Furthermore, a probabilistic approach has been considered to evaluate the probability of slope failures.

The results indicate that a higher probability of slope failure is expected under extreme precipitation events with longer return periods. Moreover, in silt embankments, the annual probability of failure in the future is greater than the historical ones. However, in the sand embankment, only Toronto and Kenora would experience higher values of the annual probability of failure in the future compared to the historical period. In addition, embankments constructed with fine-grained materials have the potential of triggering slope failure in comparison to those constructed with coarse-grained materials. The maximum expected value of the annual probability of failure is 1.2% for the sand embankment. However, the maximum estimated value is 8% for the silt embankment. The comparison between general and shallow failure shows that shallower failures are more susceptible to climatic events with considerable increase in the annual probability of shallow failure in many locations in the future.

Dedication

I am dedicating this thesis to my late uncle Ali, gone forever away from our loving eyes and who left a void never to be filled in our lives. Though his life was short, I will make sure his memory lives on as long as I live.

And for bringing me into this world and making me the person I am today, I owe the greatest debt, a debt I can never repay, to my parents. This work is also dedicated to my resilient parents who always put their lives on hold for the sake of others. I feel so grateful for their love and blessings.

Acknowledgments

For nurturing my work these past years and steering me down the road that led me to this thesis, I owe many thanks to my supervisor, Professor Bashir. I am grateful for all the guidance and scientific support that he has provided me with. Professor Bashir has been supportive through all the obstacles that I have faced during the making of this thesis, especially during the life-changing pandemic.

I am appreciative of my committee, Dr. Matthew Perras, for his support during this research. I would also like to thank Dr. Ghassemi and Mr. Moustafa for all the valuable help and assistance with the completion of this document.

I would like to express my sincere appreciation to Ms. Sindy Mahal for her precious help and support. She is always there for us, graduate students.

My special thanks to the Ministry of Transportation, Ontario (MTO). This project would not have been possible without them and their support.

Finally, I would like to acknowledge with gratitude, the support of my husband Mehdi and my daughter Sogol.

Table of Contents

List of Tables

List of Figures

Chapter 1: Introduction

The Intergovernmental Panel on Climate Change (IPCC) has reported that the climate change process would continue over the next century (IPCC 2013). Climate change is associated with considerable alteration of important climate variables such as precipitation, potential evaporation, and intensity and frequency of extreme weather events. These changes can affect the geotechnical infrastructure in many different ways. For example, an increase in the intensity of extreme precipitation may intensify soil erosion, increase the mobility of contaminants, or trigger hydro-mechanical failures in slopes.

Ministry of Transportation Ontario (MTO) manages approximately 17,000 km of highways in the province of Ontario, Canada. Embankment fills comprised of different soils, and rock types make up a significant portion of the highway infrastructure. Infrastructure sustainability is a provincial highway management priority in the province of Ontario. Due to the continuous exposure to the environment, the stability of embankments can be affected by many different climate variables. The most critical climate parameter that affects the stability of soil embankments is the precipitation. Meteoric water can seep through the embankment soil mass. As a result, the effective stress and shear strength of the soil, which are dependent on the quantity of water in the soil pores, are affected. This can adversely affect the stability of the embankment slopes. Therefore, any changes in the intensity, duration, and frequency of the precipitation events due to climate change have the potential to affect the stability of the embankments.

1.1. Thesis objective

The primary objective of this research is to quantify the impacts of future climate change on the stability of typical highway soil embankments across Ontario. These quantifications have been

done by making use of numerical modelling techniques. Furthermore, risk assessment of possible instabilities using a probabilistic approach has also been considered in this research.

Numerical simulation of climate change impact on the stability of embankments requires a multidisciplinary approach. The innovative multidisciplinary approach that has been employed in this research pursuits four different but related sub-objectives for this research:

- Construction of an appropriate long-term design climate for slope stability assessments;
- Estimation of long-term variation of slope moisture conditions;
- Assessment of long-term performance of embankments under changing climate;
- Evaluation of effects of uncertainties in soil properties and extreme rainfalls on the slope stability.

Figure 1.1 shows a summary of the applied procedure and the objective of this research. As can be seen from this flowchart, in this study, a 30-year historical climate dataset (i.e., 1981-2010) and sixteen 90-year (i.e., 2011-2100) future climate datasets were compiled. Long-term variation of soil moisture conditions under different future climate scenarios was investigated using 1D transient variably saturated seepage finite-element (FE) simulations, considering two different soil types, with distinctively different hydraulic properties. Long-term variations of the spatial and temporal distribution of pore water pressure (PWP) within the embankments were obtained using 2D transient variably saturated seepage finite-element (FE) models, with consideration for both precipitation and actual evaporation using the soil–atmosphere boundary. Assessment of slope stability overtime during extreme precipitation events was carried out by exporting PWP spatial distributions from the hydrological model into the limit equilibrium slope stability models. The models were able to take into account the contribution of matric suction on the soil strength.

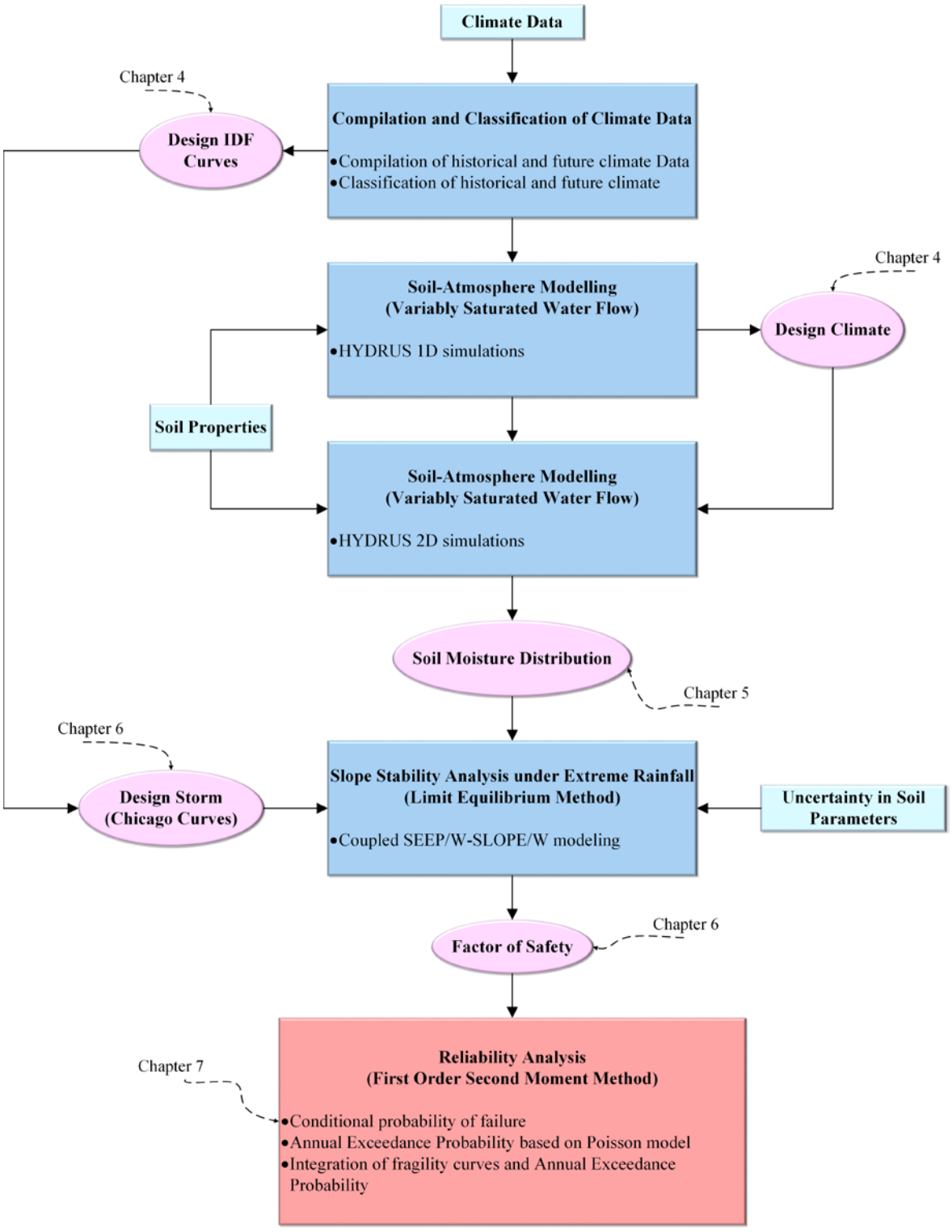

Figure 1.1 A flowchart summary of the strategy of this research

The soil-atmosphere boundary for the hydrological model was prepared using Chicago storm hyetographs based on historical and future Intensity-Duration-Frequency (IDF) curves. Based on the obtained results, the impact of future climate change was quantified by comparing the future stability condition of embankments with their historical performance for ten different locations across the province of Ontario. Then, the uncertainties in soil properties and extreme rainfall characteristics were taken into consideration using reliability analyses. In the reliability analyses, the annual probability of slope failure was evaluated as the principal representative index showing the estimated probability that the slope failure would occur during a year.

1.2. Thesis outline

This thesis has been organized into eight chapters:

- Chapter 1 presents the objective and summary of the procedures adopted in accomplishing the desired objectives;
- Chapter 2 provides a review of the previous related studies and their limitations;
- The selection of the embankment materials and the estimation of soil geotechnical and hydraulic parameters are discussed in Chapter 3;
- In chapter 4, climate data investigation is presented. This includes an overview of historical and future climate data compilation and analyses. The overview is then followed by the construction of an appropriate long-term design climate for slope stability assessments. This chapter concludes with the evaluation of rainfall IDF curves and selection of design IDF curves for slope stability assessments under extreme rainfall events for various locations across Ontario;
- In Chapter 5, the estimation of long-term variation of slope moisture conditions based on the time history of soil-atmosphere interactions is presented. First, an innovative approach

is employed to generate sub-daily data for the soil-atmosphere boundary for the HYDRUS 2D models. Then, the evaluation of spatial and temporal variation of moisture distribution within the embankment using statistical analyses is presented. This chapter concludes with the identification of average and extreme slope moisture conditions for historical and future climatic conditions;

- Chapter 6 presents the methodology and results of slope stability assessments under historical and future extreme rainfalls. The temporal variation of the factor of safety with two different initial conditions and under different extreme rainfalls is presented in this chapter. The comparison of the critical factor of safety of all locations under consideration for three different durations of extreme rainfall concludes this chapter.
- The probabilistic analyses are discussed and presented in Chapter 7. The results of the analyses are presented in the form of fragility curves and the annual probability of failure for the embankments. This chapter concludes by presenting the annual probabilities of failure for all locations.
- In Chapter 8, the summary and conclusions of this research are presented. It also includes the discussion on the contribution of this research and recommendations for future work.

Chapter 2: Literature review

2.1. Climate change

According to the Intergovernmental Panel on Climate Change (IPCC), changes in climatic conditions have been observed since about 1950. Changes in many extreme kinds of weather and climatic events, including an increase in warm temperature extremes, a decrease in cold temperature extremes, an increase in sea levels, and an increase in the number of extreme precipitation events in several regions have been observed since the mid-twentieth century (IPCC 2015). It is now recognized that global warming may change the hydrological cycle, with increasing either the frequency, or magnitude, or both of these characteristics of the extreme rainfall events (Fowler and Hennessy 1995).

Fowler and Hennessy (1995) investigated the potential effect of global warming on the frequency and magnitude of extreme rainfalls in Australia, Europe, India, China, and the USA. They reviewed physical and empirical evidence and results derived from enhanced-greenhouse experiments using global climate models (GCMs). They observed the consistency between them and concluded that global warming might result in a more intense hydrological cycle. These results were derived from enhanced-greenhouse experiments using global climate models and the physical and empirical arguments. They also observed substantial increases in the frequency and magnitude of extreme precipitation based on the analysis of output from three different GCMs.

In another study, Whetton et al. (1993) also investigated the potential impacts of climate change on extreme rainfall events in Australia. They reanalyzed 28-30 years of historical data under doubled CO_2 conditions. The modelling results indicated an increase in the frequency of extreme rainfall events and associated flooding. Goswami et al. (2006) have reported a rising trend in the frequency and magnitude of the extreme rainfall events in India. They noticed that despite the

considerable year-to-year variability, there were significant increases in the frequency and intensity of extreme rainfall events in central India over the past half-century.

Muzik (2002) examined the change in the frequency and magnitude of peak flood flows in a midsize subalpine watershed on the eastern slopes of the Rocky Mountains in Alberta, Canada, under the doubling of CO_2. He considered two scenarios of likely most severe changes. The first scenario is based on a 25% increase in the mean and standard deviation of Gumbel distribution of rainfall depth for storm durations of 6- to 48-hour. The second scenario only considers a 50% increase in the standard deviation. He generated synthetic flood frequency curves for the watershed by employing hydrologic rainfall-runoff watershed models in Monte Carlo simulations. Then, he compared the derived flood frequency curves to the derived synthetic flood frequency curve for the present climate. He noticed that both flood flow would increase under both scenarios. It was also reported that although scenario 1 is more critical than scenario 2, however, even small to moderate increases in rainfall intensity has the potential to impact flood flows.

In another study, Peck et al. (2012) assessed the Intensity-Duration-Frequency curve changes under changing climatic conditions for the City of London, Ontario, Canada. They collected nine daily maximum rainfall datasets (5, 10, 15, 30 minutes, 1, 2, 6, 12, and 24 hours) from the London Airport station between 1961 to 2002. These datasets were used as input for a weather generator (WG) algorithm to create a long-time series of weather data. By comparing the estimated future IDF curves with historical IDF curves reported by Environment Canada, they reported an increase in intensity and frequency of future extreme rainfalls.

Pk (2017) reviewed and quantified the temporal changes in the climate variables over the next 90 years for Toronto, Ontario, Canada. He reported a rising trend for annual precipitation and extreme

rainfall events in the future. He also indicated that not only would be intensity increases, but the number of extreme events could potentially double from the historical period.

2.2. Slope stability

Changes in extreme rainfall patterns due to climate change have the potential to affect the stability of both natural and constructed slopes. Highway embankments, as an example, are likely to experience rainfall-induced slope failures because of their continuous exposure to changing atmospheric conditions. A considerable amount of water exchanges takes place at the soil-atmosphere boundary. Prevailing atmospheric conditions at the ground surface can change the water storage in the slope. Increased water storage can cause an increase in the pore water pressure and a decrease in the suction component of the shear strength. These changes in pore pressure and shear strength can lead to slope instabilities (Fredlund et al. 2012). However, it is difficult to predict the changes in climate and determine their related impact on the geohydrological hazards, including landslides (Gariano and Guzzetti 2016). Following is the review of the literature on reported relationships between climate change and slope instabilities.

In 1999, a European project titled "The temporal stability and activity of landslides in Europe concerning the climatic change (TESLEC)," was carried to study the interrelationship between landslides and climate over time. The study areas of this project included eight different sites located in five different European countries. These countries are England, France, Italy, Portugal, and Spain. The main criteria for the selection of these test sites were related to (1) the existence of ongoing research with landslide monitoring and historical data, (2) site-specific hazard potential, (3) high recent landslide activity, and (4) different landslide types. The TESLEC project pursued three main objectives: (a) development of criteria for the recognition of landslides, (b) reconstruction of past distributions of landslide incidence related to the change of various climate

parameters, and (c) development of a hydrological and slope stability modelling framework for the prediction of landslide activity in a changing climate. This project concluded that the establishment of a single "universal law" all of Europe is impossible because the relationships between climate and landslides are quite complex. However, a cumulative rainfall-duration threshold for the reactivation of landslides was developed based on some areas as part of this project. Furthermore, the analysis of hydrological and slope stability models indicated that physically based models are not always the best solution because of the model complexity and data requirements. They recommended that future model development should consider sudden changes in permeability, larger landslide volumes, and complex landslide topography (Dikau and Schrott 1999).

Collison et al. (2000) assessed the potential impact of predicted climate change on landslides in southeast England. They used downscaled GCM (the second generation of the UK Hadley Centre GCM) output and modelled a 4 km section of a slope using a hydro-geotechnical simulation. The model was based on a geographical information system (GIS). Their results demonstrated that climate change would not cause frequent massive landslides; however, water storage in shallow depths could potentially increase, which may change the frequency and periods of instability.

In a later study in 2004, Schmidt and Dikau studied the effect of historical climate variability on slope stability. They assessed the stability of hillslopes under changing climate by coupling proxy-derived climate series with a groundwater/slope stability model. The model was applied to three hillslopes near Bonn (Germany). Their results showed that the stability of landslides is sensitive to climatic changes. The found out that sensitivity to climate change is dependent on the internal configuration of the landscape, such as topographical and structural convergences, and the location

of sensitive soil layers. They also found that the modelled climate scenario with a higher frequency of intense rainfall events was generally more effective in increasing slope instability.

The International Conference on Landslides and Climate Change was held in Ventor, UK, in 2007. The purpose of the Conference was to understand the relationship between climate change and increased landslide hazards, landslide management, and risk mitigation. Three steps were identified to be fundamental to studying the possible effects of climate change on the landslides. These steps are: knowing the causes of critical behaviour, the potential impact of climate change on the landscape and vegetation cover, and determining the real behaviour of landslide movements, particularly during the pre-failure phases (McInnes et al. 2007).

Dixon and Brook (2007) assessed the potential effect of global climate change on the active Mam Tor landslide in the UK. They used historical climate data obtained from a weather station that lies approximately 10 km southwest of Mam Tor and obtained monthly precipitation predicted from the UKCIP 2002 report based on HadCM3 model, downscaled to a 50-km resolution. They indicated that Mam Tor could be more vulnerable to the predicted winter rainfall and could experience a shorter return period for slope movements due to the wetter conditions. This was due to changing rainfall frequency from 4 to 3.5 years in winter. However, they observed a decreasing trend for annual rainfall over 1961-2080 and noted this might have a positive effect on landslide stability.

In 2010, Rahardjo et al. investigated the effects of the position of the groundwater table, rainfall intensity, and soil properties on the stability of different natural slopes in Singapore. They considered three different groundwater table positions, corresponding to the typical, driest, and wettest periods. They also considered four different rainfall intensities of 9, 22, 36, and 80 mm/h. The soil properties were selected based on two main residual soils found in the area, the Bukit

Timah Granite and the Sedimentary Jurong Formation. They reported that the position of the groundwater table in reference to the ground surface during rainfall did not significantly affect the factor of safety. This was attributed to the relatively small changes in the matric suction. They also reported that soil properties had a large effect on the factor of safety. A higher percentage of fine particles in the soil would lead to a higher air-entry value, a lower soil permeability, and a rapid decrease in the factor of safety. They also noted that the minimum factor of safety might not occur at the end of the rainfall event, but several hours after the rain would stop because the rainwater has not percolated to the critical slip surface depth by the end of the rainfall. They also mentioned that different slope geometries and soil properties would have different values for the minimum factor of safety.

Coe and Godt (2012) identified fourteen technical approaches for assessing the impact of climate change on landslide activity. They classified them into three groups, including 1) long-term monitoring of climate change and landslide activities, 2) retrospective approaches that establish a connection between climate data and landslide activity based on historical records, and 3) prospective approaches that develop patterns between historical landslide activity and climate records and then use these patterns with downscaled climate projections to predict future landslide activity. They concluded that predicting the frequency and magnitude of extreme short-term storms is difficult; therefore, the prediction of shallow landslides under these storms have the most significant uncertainty. However, the results of predicting the landslide considering air temperature, sea-level rise, or seasonal/annual rainfall show a lower uncertainty, as there is less difficulty in their prediction.

Comegna et al. (2013) evaluated the potential changes in climate variables and predicted the future behaviour of an active, slow-moving earthflow in the Basento River valley in southern Italy. Their

methodology was based on the coupling the climatic scenarios and geotechnical analyses. It embodied three steps: 1) calibration of a model linking weather parameters to the pore water pressure regime, (2) establishing a relationship between pore water pressure and landslide movement, and (3) assessment of the long-time behaviour of the landslide based on available climate scenarios. They obtained climate variables by solving the differential equations implemented in the COSMO-CLM regional model and validated the simulated data by comparing it with monitoring data over the time interval of 2005–2007. Their analyses show a reduction of 6–8 mm per decade in the groundwater level due to the expected increase in temperature and decrease in precipitation. They estimated the displacement rate of the earthflow and implied that the expected change in climate is not an influential factor in the dynamic behaviour of the slow landslide in clay. They reasoned that the moderate decrease in annual precipitation and the increase in temperature do not alter the evaporation and groundwater levels enough to be of any significance.

In 2014, Rianna et al. investigated the long-term behaviour of Orvieto clayey landslide behaviour in Italy. They used a 30-year-long monitoring record of the landslide and established a relationship between rainfall and rate of landslide movement. They took advantage of historical climate data with high-resolution (up to 8 km) and climate data provided by COSMO-CLM based on two different emission scenarios, RCP4.5 and RCP8.5. They predicted the slope displacement until the end of 2100 and concluded that the predicted climate changes could cause a significant landslide movement.

Ciabatta et al. (2016) assessed the impact of climate-change scenarios on landslide occurrence in the Umbria Region, Italy. They downscaled the outputs of five different GCMs and applied weather generators to convert daily rainfall and temperature data to hourly data. Then, they

estimated the number of landslide occurrence for three distinct periods, 1990–2013 (as the baseline), 2040–2069 and 2070–2099. They concluded that the number of landslides could increase by up to 45% in the future. They also observed that there is not a simple relation between climate parameters and the number of landslides, and suggested soil moisture conditions should also be taken into consideration as well. They found that during the warm-dry season, decreasing soil moisture leads to an unchanged number of landslide occurrences. Contrarily, during the cold-wet season, the number of landslide events increased considerably because of the significant increase in soil moisture. They also pointed out that the type of GCM, downscaling method, and climate data resolution could influence the results.

Batali and Andreea (2016) investigated the slope stability considering the unsaturated soil condition above the water table. They investigated the slope stability of a landslide located in Cluj-Napoca city, in the center of Romania using SVSlope software (SVOffice 2009), considering various unsaturated shear strength values predicted by different models. They also evaluated the effect of a drainage system on the slope stabilization for the case study. They noted that the models based on Fredlund and Xing (1994) show acceptable performance for the estimation of the unsaturated condition. This conclusion was based on the comparison of the results with measured values of suction obtained from the site. They also concluded that more realistic results could be obtained if unsaturated properties are considered for the soil above the groundwater table. They also reported an increase in values of factor of safety for consideration of unsaturated soil properties. Improvement in slope stability due to the drainage system was also reported.

Robinson et al. (2017) assessed the effect of extreme rainfall events on a homogeneous silty soil slope under current and future climate scenarios. They selected Seattle, Washington, as the study area for analyzing the historical and future IDF curves. Future precipitation data were obtained

from the coupled model intercomparison project phase 5 (CMIP5) simulations. They used a fully coupled two-dimensional stress-strain and unsaturated flow finite element model. The model considered a 7-day duration of baseline and future rainfall data as the boundary condition. Their results indicate that the increase in rainfall intensity could result in increasing the pore water pressure that would adversely affect the stability of the embankment slope.

Pk et al. (2018) studied the effect of climate change on the stability of embankments. They quantified the effects of future long term and extreme precipitation events on the probable instability of a typical highway embankment in Southern Ontario, Canada. They considered two different embankment fills, sand and silt, and compared the stability results of historical climate with future climate data sets. For their analysis, they used a two-dimensional (2D) transient variably saturated seepage finite-element model to analyze pore-water pressures and a 2D limit equilibrium slope stability model for stability assessments. Their results indicated that the cumulative annual net infiltration in the future could increase by 41%, which would result in a 30% reduction in the embankments' factor of safety. They also reported that the hydraulic properties of the fill materials play a critical role in the embankment's stability under changing climatic conditions. The highly permeable sand embankment was found to drain water quickly without any significant effect on stability. On the other hand, embankments constructed with low permeability finer materials such as silt showed a lower factor of safety (FOS) owing to their ability to retain water and conduct it slowly.

2.3. Probabilistic stability analysis and fragility curves for geotechnical structures

Reliability analyses offer an option for evaluating the uncertainties and estimating their effects on the performance of slopes using probabilistic concepts. Through such analyses, assigning a probability distribution function to input parameters allows engineers to evaluate the probability

of the desired level of performance. Fragility curves are an appropriate tool for reliability-based analysis of slope stability. They are an attractive tool for carrying out risk assessments of large systems, such as major transport networks (Martinović et al. 2018). To date, most research on vulnerability assessment of slopes has focused on slope performance under earthquake loading, and only a few researchers have presented fragility curves for slope stability under extreme rainfall events. A brief review of these studies is presented as follows.

Otálvaro and Cordao-Neto (2013) performed probabilistic analyses of slope stability under infiltration conditions. They used the Finite Element Method (FEM) to analyze the seepage problem and the Limit Equilibrium Method (LEM) to determine the factor of safety. They applied the First Order Second Moment (FOSM) method to quantify the influence of mechanical and hydraulic parameters on the factor of safety of slope. They concluded that in the initial time step, the effective angle of internal friction and effective cohesion influence the factor of safety, so hydraulic parameters should not be considered as the variables with the most significant impact on the mean value of the factor of safety. However, after the start of the infiltration, hydraulic parameters have the most influence on the factor of safety.

Park et al. (2013) evaluated the probability of failure using an infinite slope model linked to GIS. A coupled hydrogeological model with an infinite slope model was their tool to evaluate changes in pore water pressure caused by rainfall. They took advantage of a GIS-based environment since it provided spatial data-processing capacity over a vast area. The probabilistic analyses were carried out using the Monte Carlo simulation method. They compared the results of the probabilistic analyses with the landslide inventory available in the GIS environment. This comparison indicated the acceptable performance of the probabilistic method. Their results

showed that proper consideration and understanding of uncertainties are necessary for an accurate prediction of susceptibility to shallow landslides.

Calamak and Yanmaz (2014) analyzed the slope stability of earth-fill dams using a probabilistic approach. They considered hydraulic conductivity, unit weight, cohesion, and internal friction angle of the soil as the random variables. They used two different software, using the finite element method and limit equilibrium methods for seepage and stability analyses, respectively. Their results show that the factor of safety could vary between 19 to 25%. This range is considerable and might lead to lower values of factor of safety and a higher probability of failure. They also investigated the effect of material variability through the slip surface. They highlighted the importance of spatial variation of hydraulic conductivity in probabilistic stability analyses.

Martinović et al. (2016) assessed the susceptibility of Irish rail network earthworks to climate change. They obtained geometric information from the existing Irish Rail LiDAR scans of the entire network and compared them to walkover assessment data. They also performed a statistical analysis on the LiDAR geometry data (slope heights and slope angles) to understand the differences between the aged railway infrastructure and modern earthworks designs on this network. They noticed that the visual assessment is not reliable because it overestimated both the slope height and the angle. Moreover, they developed fragility curves for rainfall-triggered shallow landslides for transport networks to see the effect of slope angles on the vulnerability of slope. Their results show that the probability of failure would increase by increasing the slope angle and rainfall durations.

According to Zhang and Huang (2016), a slope may have many potential slip surfaces, and the consequence of slope failure along different slip surfaces could be quite different. The uncertainty in soil parameters causes uncertainty in the location of the critical slip surface. They proposed a

method for quantitative risk assessment of slopes considering a large number of potential slip surfaces since the traditional equation is only suitable for slope failure along a given slip surface. This method considers multiple slip surfaces in the risk assessment analysis since the most probable failure is not necessarily the surface with the largest larger risk. They also suggested that the risk associated with a slope as a system is different from the risk associated with a single slip surface.

Tsubaki et al. (2016) investigated two well-documented events of railway embankment failures during floods in Japan and generated fragility curves for risk assessment purposes. They developed normal and log-normal fragility curves based on damage probability derived from the field records and the estimated overtopping water depth. They evaluated their work by comparing calculated probabilities with the actual damage records. At one location with recorded continuous washout, the damage probability based on fragility curves agreed with the observed damage. However, the model did not show an agreement with the available records in flat locations with level railway crests. In such locations, variations in the simulated overtopping water depth were affected by the small errors in the topographic data.

In 2017, Liu et al. evaluated the uncertainty in the soil-water Characteristic Curve on stability assessment of an unsaturated slope under rainfall events. They took advantage of the Bayesian approach and the Markov chain Monte Carlo (MCMC) method. They concluded that the uncertainty in SWCC has notable effects on slope seepage and associated stability. They highlighted the importance of uncertainties in SWCC parameters, which could lead to unreliable predictions of pore-water pressure profiles leading to inaccurate values of factor of safety for the slope under rainfall conditions.

In 2017, Jasim et al. developed fragility curves for earthen levees subjected to extreme precipitations. They numerically simulated the levee behaviour using a fully coupled 2D stress-strain and a variably saturated flow finite element model. They developed the fragility curves for the historical and future periods to compare the probability of levee's failure under both past and future climate conditions. They concluded that a rainstorm for more than three consecutive days, especially if its intensity is more than 27 mm/day would be determinal for the levee . They demonstrated that climate change increases the probability of failure in levee systems for extreme events. Their results also showed that the levee's probability of failure in the future would increase by 12% compared to the baseline scenario.

Martinović et al. (2018) developed fragility curves for shallow landslides induced by rainfall on the Irish Rail network. They concluded that the probability of shallow failure is increasing as a result of more intense and longer duration rainfall events due to climate change. They used Monte Carlo simulations, determined the change in reliability with rainfall duration, and developed the fragility curves. The fragility curves show the changes in slope capacity and its vulnerability to the rainfall. They also verified their result by back-analyzing historical failure at four sites and noted a good agreement with the actual time of failure. Both historical data and fragility curves showed that the failure events happened after a relatively long rainfall duration, not during the early infiltration period. They recommended their methodology for assessing geo infrastructures such as cuttings and embankments on the road, rail, and water transport networks. The also highlighted that soil suction plays an important role in the occurrence of failure.

In another study, Sharma (2016) assessed the effect of the variability of soil properties on the stability of a natural slope in district Bilaspur, Himachal Pradesh, India. Probabilistic and deterministic analyses using Monte Carlo simulation and Geo-Studio respectively were carried

out, and the comparison of the results obtained from the two approaches indicated their efficacy for slope stability assessments. It was implied that the deterministic approach generally results in conservative values of factor of safety since the assigned input parameters are single-valued, and the spatial variation of them is not considered. The results obtained from the probabilistic approach can be used to determine the probability of failure corresponding to a particular factor of safety, and an allowable risk criterion can be used to establish a consistent target for the design process.

2.4. Gaps and limitations of the previous studies

Generally, all previous studies indicate the climate is changing with an increase in temperatures, melting of ice and snow, rising sea levels, changes in precipitation patterns, and increases in the frequency and intensity of extreme events. These climatic changes have the potential to adversely affect the stability of the slopes. However, it should be noted that these findings are dependent on the various simplifications and assumptions that are made in the development of the numerical models. Assumption of simple initial conditions for pore pressure distribution (e.g., Robinson et al. 2017), selecting future climate data based only on hydrological aspects (e.g., Bo et al. 2008), and considering uniform rainfall intensity during extreme events (e.g., Rahardjo et al. 2010) are some the examples of these assumptions in previous studies. Moreover, most of the earlier studies have focused on the effect of climate change on FOS values, and the probability of the predicted stability condition has received less attention.

In studies to date, fragility curves have been established to estimate the probability of failure for all feasible loads (herein rainfall events). However, the probability of load exceedance is not taken into account explicitly. Hence, the probability of failure given by the fragility curves is indeed the conditional probability of failure. This issue is fundamental to be addressed in the development of fragility curves. However, most of the previous studies have focused on rainfall intensity and

duration without taking into consideration the probability of event occurrence. For example, Martinović et al. (2018) only addressed the conditional probability of failure under different rainfall conditions, and the probability of rainfall reoccurrence was ignored in their study.

Moreover, Jasim et al. (2017) developed fragility curves for a case study, considering rainfall durations of 1 to 7 days and recurrence intervals of 25, 50, and 100 years. In the developed fragility curve, the rainfall intensity was set as the primary independent variable for fragility curves. Although such fragility curves have the advantage of inclusion rainfall return periods, the occurrence of rainfalls with more than 1-day duration with uniform intensity is rare.

Chapter 3: Geotechnical and Hydraulic Parameters

To study the impact of climate change on the stability of a soil embankment, soil's geotechnical and hydraulic parameters must be known. In this chapter, the methodology for selecting the soil properties for this study is presented. Material selection is based on the information provided by the Ministry of Transportation, Ontario (MTO). According to MTO, Select Subgrade Material (SSM) is often used in embankment construction across Ontario. Figure 3.1 shows the range of gradation for SSM, based on Ontario Provincial Standard Specification 1010 (OPSS 1010). This figure shows that the SSM is in the range of silty sand to sandy gravel. The parameters of the particle distribution for the average SSM curve are also shown in Figure 3.1.

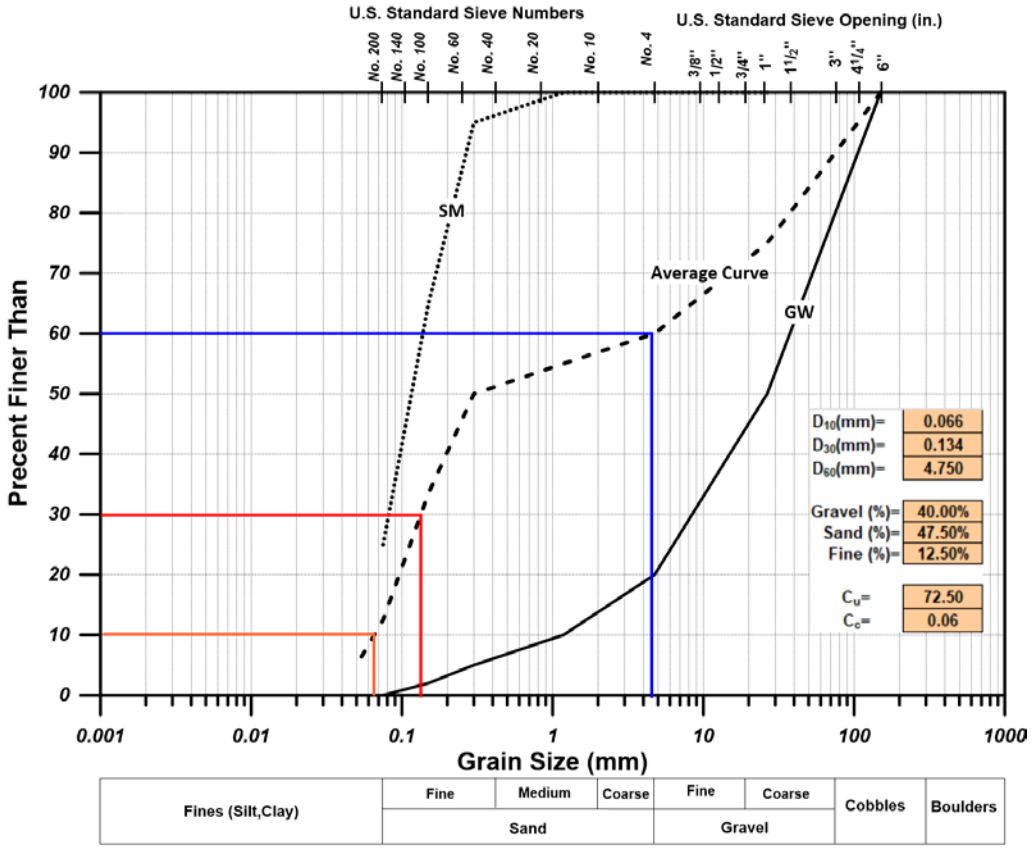

Figure 3.1 The range of gradation for Select Subgrade Material (modified from OPSS 1010)

The high drainage capacity of materials such as gravel or coarse sands makes them the right choice for the embankment fill because the embankments are expected not to be significantly affected by the environmental loads. Therefore, silty sand material was considered as one of the embankment fill types in this study. The hydraulic characteristics of silty sand are highly dependent on fine material content, so the finer limit of allowable SSM range was conservatively assumed as the gradation of the silty sand material. This material can be classified as silty sand (SM), according to the Unified Soil Classification System (USCS) or loamy sand (LS), based on the U.S. Department of Agriculture (USDA) classification. In some instances, due to the unavailability of coarser earth materials for embankment construction, some existing embankments across Ontario have also been constructed using silty materials. Therefore, typical sandy silt (ML, according to USCS, or SL (silty loam), according to USDA), was considered as another type of embankment fill in this study.

3.1. Geotechnical parameters

Unit weight, effective angle of internal friction, and effective cohesion are three primary geotechnical parameters that control the stability of earth embankments. The effective cohesion is assumed to be zero in this study since the materials used in the construction of embankments are non-cementitious. Unit weight and effective angle of internal friction are discussed in the following sections.

3.1.1. Unit weight

All embankment fill materials used in MTO projects are to be placed and compacted following OPSS 206 and OPSS 501, respectively. These specifications require a relatively high degree of compaction for the fill material. For sand material, maximum dry density (corresponding to minimum void ratio) is dependent upon uniformity coefficient (C_u), as well as particle angularity

(FHWA 2002). In this study, the estimation of dry unit weight of silty sand is based on the correlation shown in Figure 3.2.

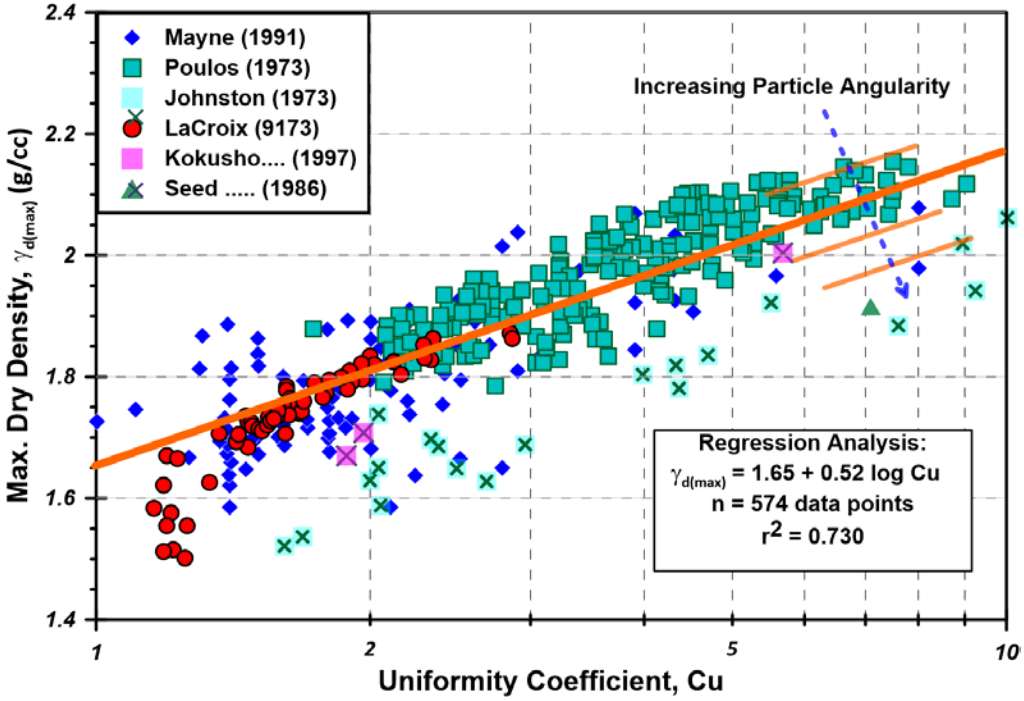

Figure 3.2 Maximum dry density relationship with sand uniformity coefficient (FHWA 2002)

According to OPSS 206 and OPSS 501, the fill material must be compacted to a density of 95% of the maximum dry density. Therefore, the dry unit weight of silty sand is estimated by substituting the value of 2.75 for the uniformity coefficient in Equation 3.1.

$$\gamma_d = 0.95 * \gamma_{d,max} = 0.95 * (1.65 + 0.52 * \log(2.75)) = 1.78\ g/cm^3 \backsimeq 17.5\ kN/m^3 \quad (3.1)$$

This value is in agreement with the values proposed by USDA (2018) for dense loamy sand (LS zone in Figure 3.3) and the range proposed by Naval Facilities Engineering Command (NAVFAC, 1982) for dense SM (Figure 3.4).

For typical sandy silt, a dry density value of 14.7 kN/m^3 (1.5 g/cm^3) was assumed. This value is less than the value for silty sand since the dry density of compacted fine-grained material is

generally less than coarse-grained material. This value is also within the suggested range for silty loam by USDA (2018) and NAVFAC (1982) for ML.

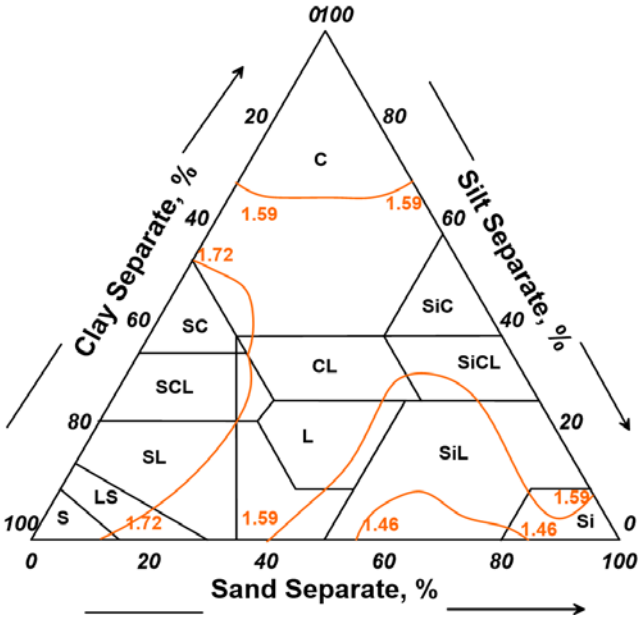

Figure 3.3 Range of bulk density for different dense materials (USDA 2018)

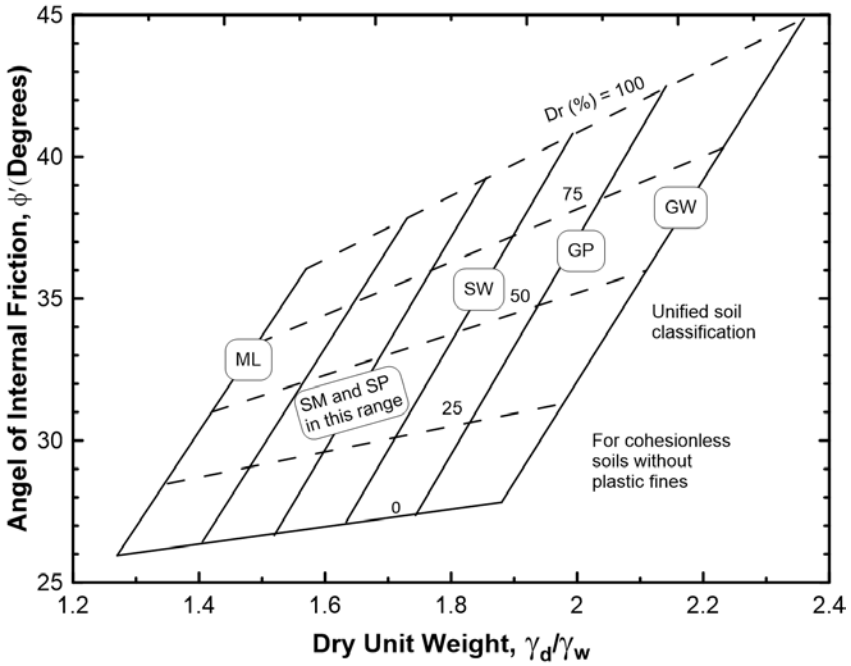

Figure 3.4 Phi and unit weight for cohesionless soils (modified from (NAVFAC 1982)

3.1.2. Effective angle of internal friction

The factor of safety for slope stability assessments is highly dependent on the soil angle of internal friction (φ). The friction angle of cohesionless soils mainly depends on soil gradation, density, and grain angularity, particularly for the coarse-grained soils. Table 3.1 from FHWA (2002) shows friction angles of 34±1° and 32±2° for silty sand (SM) and inorganic silt (ML), respectively. The values of geotechnical parameters considered in this research are shown in Table 3.2.

3.2. Hydraulic parameters

The hydraulic behaviour of unsaturated soils is defined by the soil-water Characteristic Curve (SWCC) and unsaturated hydraulic conductivity function (HCF). The stability performance of variably saturated slopes has been shown to be dependent on the SWCC and HCF parameters (Pk et al. 2018).

3.2.1. Saturated Hydraulic conductivity

Saturated hydraulic conductivity is a primary parameter that controls the water seepage through the soil. It relies on the intrinsic permeability of the material and the density and viscosity of the liquid. The last two factors can be assumed constant under normal operating temperatures.

There are several methods for predicting the saturated hydraulic conductivity of sandy soils in the literature (e.g., Hazen 1911, Powers 1992, Carsel and Parrish 1988, Mbonimpa et al. 2002, USDA 2018). Figure 3.5 shows the range of hydraulic conductivity values corresponding to the soil texture triangle from USDA (2018). This particular figure is for the soils with high bulk density. This figure can be used together with the density diagram of the texture triangle shown in Figure 3.3 to estimate hydraulic conductivity.

Table 3.1 Values for dry density and shear strength parameters of various soils (modified from FHWA, 2002)

Unified Classification	Soil Type	Standard Proctor Compaction (AASHTO T 99)		As Compacted Cohesion, C_0 (kPa)	Saturated Cohesion, C_{sat} (kPa)	Friction Angel, φ (deg)
		Maximum Dry Density (KN/m^3)	Optimum Moisture Content (%)			
GW	well graded clean gravels, gravel-sand mixture	> 18.7	< 13.3	*	*	> 38
GP	poorly graded clean gravels, gravel-sand mixture	> 17.3	< 12.4	*	*	> 37
GM	silty gravels, poorly graded gravel-sand-silt	> 17.9	< 14.5	*	*	> 34
GC	clayey gravels, poorly graded gravel-sand-clay	> 18.1	< 14.7	*	*	> 31
SW	well graded clean sands, gravely sands	18.7 ± 0.8	13.3 ± 2.5	39 ± 4	*	38 ± 1
SP	poorly graded clean sands, sand-gravel mixture	17.3 ± 0.3	12.4 ± 1.0	23 ± 6	*	37 ± 1
SM	silty sands, poorly graded sand-silt mixture	17.9 ± 0.2	14.5 ± 0.4	51 ± 6	20 ± 7	34 ± 1
SM - SC	sand-silt-clay with slightly plastic fines	18.7 ± 0.2	12.8 ± 0.5	50 ± 21	14 ± 6	33 ± 4
SC	clayey sands, poorly graded sand-clay mixture	18.1 ± 0.2	14.7 ± 0.4	75 ± 15	11 ± 6	31 ± 4
ML	inorganic silts and clayey silts	16.2 ± 0.2	19.2 ± 0.7	67 ± 10	9 ± *	32 ± 2
ML - CL	mixture of inorganic silts and clays	17.1 ± 0.3	16.8 ± 0.7	63 ± 17	22 ± *	32 ± 3
CL	inorganic clays of low to medium plasticity	17.1 ± 0.2	17.3 ± 0.3	87 ± 10	13 ± 2	28 ± 2
OL	organic silts and silty clays of low plasticity	*	*	*	*	*
MH	inorganic clayey silts, elastic silts	12.9 ± 0.6	36.3 ± 3.2	72 ± 30	20 ± 9	25 ± 3
CH	inorganic clays of high plasticity	14.8 ± 0.3	25.5 ± 1.2	103 ± 34	11 ± 6	19 ± 5
OH	organic clays and silty clays	*	*	*	*	*

± : 90% confidence limits of the average value, * : insufficient data, > : greater than, < : less than

Table 3.2 Geotechnical parameters considered in this research

Material	Cohesion (kPa)	Dry unit weight (kN/m^3)	Saturated unit weight (kN/m^3)	Angle of internal friction (degree)	Porosity (-)
Silty sand	0	17.5	20.7	34	0.33
Sandy silt	0	14.7	19	32	0.44

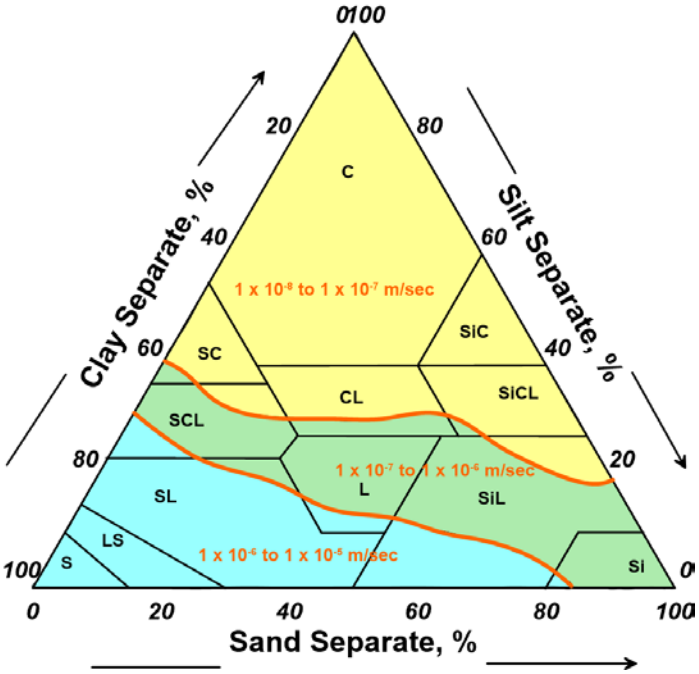

Figure 3.5 Range of saturated hydraulic conductivity for dense soil (USDA 2018)

Carsel and Parrish (1988) have also suggested values of hydraulic conductivity for different soils in the soil texture triangle, as presented in Table 3.3. There are also other correlations in the literature that consider the effect of soil density and gradation on hydraulic conductivity. Figure 3.6 shows other relationships that can be used to estimate the hydraulic conductivity of dense sandy soil based on *Cu* and D_{50} (Powers 1992). The estimation of hydraulic conductivity based on the abovementioned references for silty sand is summarized in Table 3.4.

Table 3.3 Suggested values of hydraulic conductivity for different soils (modified from Carsel and Parrish 1988)

Soil Type	Hydraulic Conductivity Ks (m/s)			
	x	SD	CV	n
Clay*	5.56×10^{-7}	1.2×10^{-6}	210.3	114
Clay loam	7.22×10^{-7}	1.9×10^{-6}	267.2	345
Loam	2.89×10^{-6}	5.1×10^{-6}	174.6	735
Loamy sand	4.05×10^{-5}	3.2×10^{-5}	77.9	315
Silt	6.94×10^{-7}	9.2×10^{-7}	129.9	88
Silt loam	1.25×10^{-6}	3.4×10^{-6}	275.1	1093
Silt clay	5.56×10^{-8}	3.1×10^{-7}	453.3	126
Silty clay loam	1.94×10^{-7}	5.3×10^{-7}	288.7	592
Sand	8.25×10^{-5}	4.3×10^{-5}	52.4	246
Sandy clay	3.33×10^{-7}	7.8×10^{-7}	234.1	466
Sandy clay loam	3.64×10^{-6}	7.6×10^{-6}	208.6	214
Sandy loam	1.23×10^{-5}	1.6×10^{-5}	127	1183

x: Mean value, SD: Standard deviation, CV: Coefficient of variation (%), and n: sample size. *Agricultural soil: less than 60%clay.

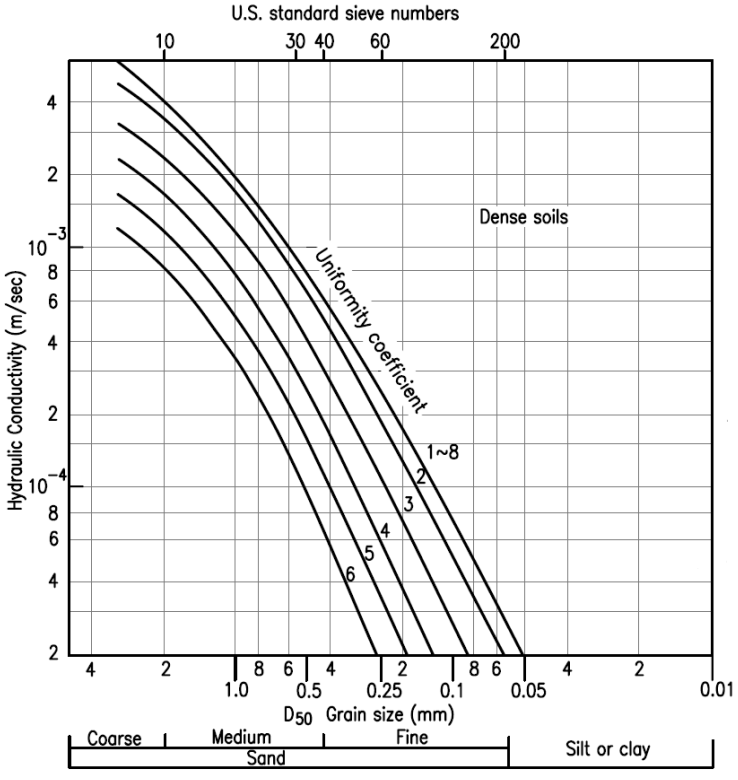

Figure 3.6 Hydraulic conductivity estimates for dense soils (Powers, 1992)

Table 3.4 Estimated values of hydraulic conductivity for silty sand using different methods

Reference	Density	Hydraulic conductivity (m/s)
Hazen (1911)	Loose	2.5×10^{-5}
Powers (1992)	Dense	$2\times10^{-5} \sim 3\times10^{-5}$
USDA (2018)	Dense	$1\times10^{-6} \sim 1\times10^{-5}$
Carsel & Perrish (1988)	Porosity=0.41	4.05×10^{-5}
Mbonimpa et al. (2002)	Porosity=0.33	7×10^{-6}

Compared to sandy soils, the hydraulic conductivity of silty materials is expected to be much lower because of the higher specific surface of the fine-grained soils (the surface area of soil grains in a given volume of soil). The higher specific surface induces more resistance to water flow through the soil. According to USDA (2018), on average, the hydraulic conductivity of silty loam is expected to be in the range of one to two orders of magnitude less than loamy sand. Carsel and Parrish (1988) have proposed an average value of 1.25×10^{-6} m/s for silty loam, with an average porosity of 0.45, as can be seen in Table 3.3. The range of soil hydraulic conductivity may vary over several orders of magnitude. As it is shown in Figure 3.7, for each soil type, hydraulic conductivity is usually reported within a range of three to four orders of magnitude. Even for a given soil, the coefficient of variation (COV) of measured data in the laboratory may exceed 100% (Carsel and Parrish 1988). The values of saturated hydraulic conductivities and their range for silty sand and sandy silt considered in this study are presented in Table 3.5.

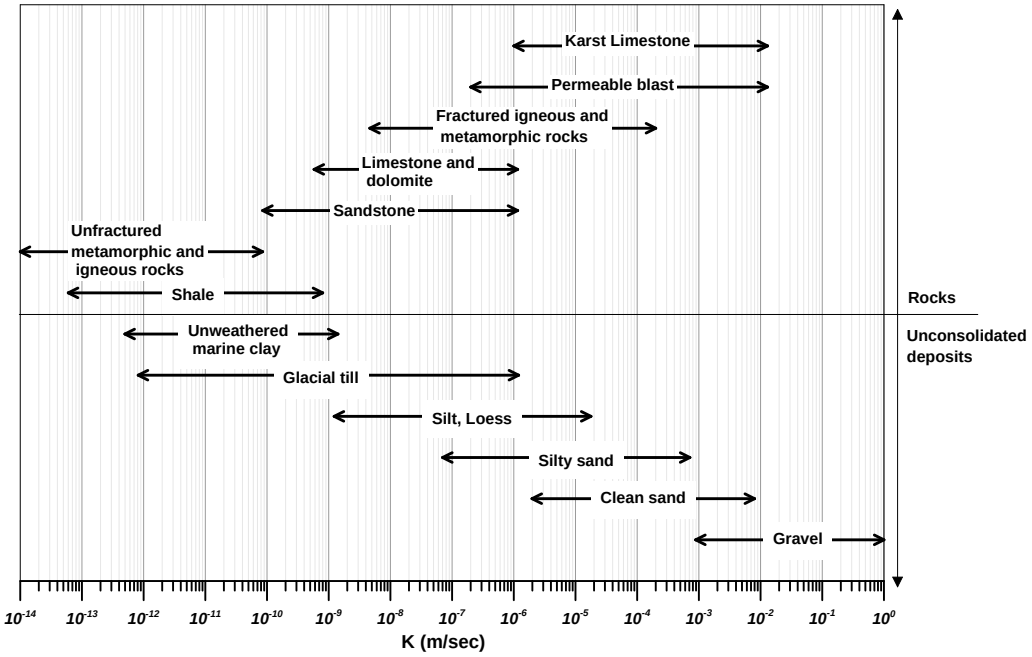

Figure 3.7 Range of hydraulic conductivity for different soils

Table 3.5 Values of hydraulic conductivity used in this study

	Hydraulic conductivity (m/s)	
	Average	Range
Silty sand	1.00×10^{-5}	$2.15\times10^{-6} \sim 46.4\times10^{-6}$
Sandy silt	1.25×10^{-6}	$0.27\times10^{-6} \sim 5.80\times10^{-6}$

3.2.2. Soil-Water Characteristic Curve

In this study, van Genuchten (1980) function (VG) was used to describe the soil-water Characteristic Curves (SWCC), as shown in Equation 3.2.

$$\theta - \theta_r = (\theta_s - \theta_r)\left[\frac{1}{1+(\alpha|\psi|)^n}\right]^{(1-\frac{1}{n})} \quad (3.2)$$

This function describes the relationship between soil volumetric water content and matric suction (ψ) for given saturated water content (θ_s) and residual water content (θ_r). There are also two

empirical coefficients α and n in this function, which are related to the air entry value and pore size distribution of the soil.

Parameters of soil-water Characteristic Curves can be determined through field or laboratory measurements. The measurement of hydraulic parameters is a time-consuming and costly task. Therefore, it is usually limited to a small number of tests. In the absence of measurements, VG parameters can also be estimated from available databases. Carsel and Parrish (1988) used an extensive database to obtain the saturated hydraulic conductivity and SWCC parameters for the van Genuchten (1980) function using multiple regression techniques. Parameters and associated statistics for all soil types in the USDA textural triangle have been presented by Carsel and Parrish (1988) and are reproduced in Appendix A. As previously shown in Table 3.2, the average value of porosity for dense sandy silt material is estimated at around 0.44, which is close to the values of θ_s proposed by Carsel and Parrish (1988). As there is no pre-defined gradation curve for this type of soil considered in this study, therefore values of SWCC parameters proposed by Carsel and Parrish (1988) for sandy silt material were used.

Additionally, the hydraulic parameters of soils can also be estimated from readily available soil information using correlations, commonly known as pedotransfer functions (PTFs). The main advantage of using PTFs is that the hydraulic parameters of soil can be estimated based on readily available information such as soil gradation, porosity, density, organic content, etc. Table 3.6 shows the values of SWCC parameters for silty sand obtained by different pedotransfer functions. Other details and the required inputs for these PTFs are presented in Appendix A. For silty sand material, the mean value was calculated based on averaging the values given by different PTFs presented in Table 3.6.

Table 3.6 Estimated values of SWCC parameters for dense silty sand using different PTFs

Reference	θ_r	θ_s	α (1/cm)	n
Gupta and Larson (1979)	0.097	0.32	0.093	1.56
Rawls et al., 1982	0.042	0.32	0.027	1.54
Rawls et al., 1983	0.041	0.32	0.05	1.54
Schaap et al. (2001)	0.034	0.3	0.056	1.47

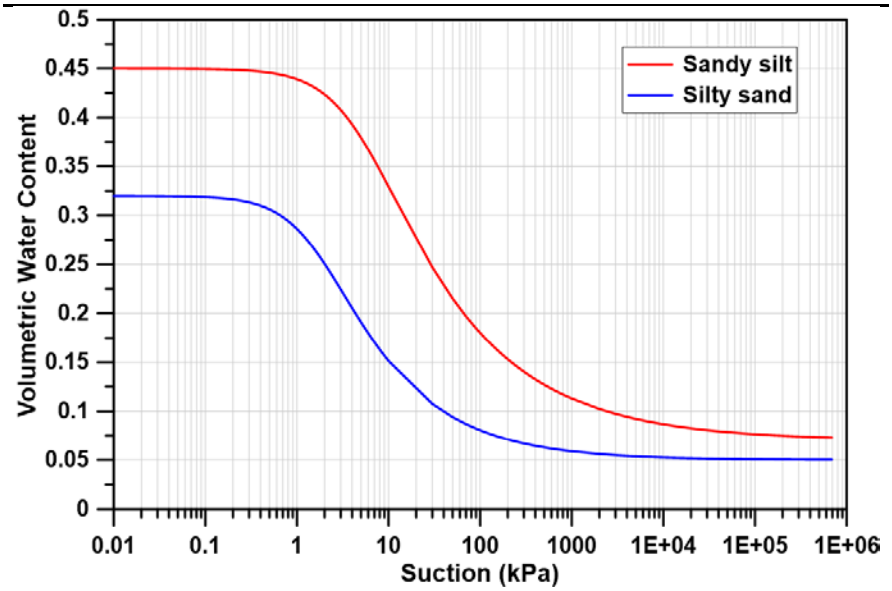

Figure 3.8 Soil water characteristic curves used in this study

In this study, unsaturated hydraulic conductivity functions (HCF) for the materials were determined from SWCC parameters using the van Genuchten-Mualem approach (Mualem, 1976; van Genuchten, 1980). Soil-water Characteristic Curves for both silty sand and sandy silt are shown in Figure 3.8. For the sake of brevity, selected values of SWCC parameters used in this study are summarized in Table 3.7.

Table 3.7 Values of VG parameters used in this study

	θ_s	θ_r	α (1/cm)	n
Silty sand	0.32 (0.25~0.39)	0.05 (0.04~0.06)	0.06 (0.04~0.08)	1.53 (1.35~1.71)
Sandy silt	0.45 (0.37~0.53)	0.07 (0.05~0.08)	0.02 (0.01~0.03)	1.411.29~1.53)

3.3. Soil parameters uncertainty

In this study, the uncertainties in the values of six important soil parameters were considered. These parameters include the angle of internal friction, saturated hydraulic conductivity, and all four parameters of the van Genuchten (1980) function to describe the soil-water Characteristic Curve. These parameters were considered to estimate the overall uncertainty in the slope stability assessments.

For the angle of internal friction, the coefficient of variation (COV) between 2 to 13% has been suggested by several researchers (e.g., Kulhawy 1992 and Harr 1984). In this study, COV of 7%, and consequently, the standard deviation of two degrees was considered for the angle of internal friction.

To establish a rational range of hydraulic conductivity values, a simple method called “three-sigma rule” was used. This method was first suggested by Dai and Wang (1992), and its primary assumption is that 99.73% of all the values of a normally distributed parameter usually fall within plus or minus three standard deviations (three sigmas) from the average. Thus, an extremely low value would be three standard deviations below the average, and an extremely high value would be three standard deviations above the average. They suggested that, by estimating the extreme low and high values, and dividing the difference between them by six, the standard deviation could be estimated using the following equation (Duncan and Sleep 2018):

$$\sigma = \frac{HCV - LCV}{6} \tag{3.3}$$

Where HCV is the highest conceivable value, and LCV is the lowest conceivable value. It should be noted that for a variable such as hydraulic conductivity that is log-normal distributed, the natural logarithm of the parameters is used in the above equation.

In this research, the standard deviation was calculated based on a range of four orders of magnitude for both materials using the three-sigma rule. Then, based on the estimated standard deviation, plus or minus one standard deviation values from the average were considered in sensitivity analyses and probabilistic assessments.

The inherent heterogeneity of soils and errors in SWCC measurements and estimation procedures warrant that uncertainty in parameters used to describe SWCC should also be considered in the probabilistic analyses. The proposed coefficients of variation by Carsel and Parrish (1988) for loamy sand (silty sand) and silt loam (sandy silt) were considered for SWCC's parameters. The mean values of soil parameters considered in probabilistic analyses and their mean ±1 standard deviation values for silty sand and sandy silt material are presented in Table 3.8. Hereinafter, silty sand and sandy silt are named sand and silt, respectively.

Table 3.8 Values of soil parameters considered in this study for probabilistic analyses

Parameters	Mean value		+ SD*		– SD	
	Sand	Silt	Sand	Silt	Sand	Silt
φ	34	32	36	34	32	30
K_{sat} (m/s)*	1×10^{-5}	1.25×10^{-6}	4.6×10^{-5}	5.8×10^{-6}	2.2×10^{-6}	2.8×10^{-7}
θs	0.32	0.45	0.38	0.53	0.25	0.37
θr	0.054	0.067	0.068	0.081	0.040	0.053
α (1/cm)	0.056	0.020	0.076	0.033	0.036	0.007
n	1.53	1.41	1.71	1.53	1.34	1.29

* SD: Standard deviation; The log scale was used for K_{sat}.

Chapter 4: Design Climates

The surface of the embankment is the boundary between the soil and the atmosphere, and it is continuously exposed to changing atmospheric conditions. Figure 4.1 shows a typical embankment surface boundary subjected to various surface-atmosphere processes. A considerable amount of water exchange takes place between the soil-atmosphere boundary. Prevailing atmospheric conditions at the ground surface can change the water storage in the slope. Increased water storage in the soil would increase pore pressures and change the suction component of soil shear strength. Depending on the soil type and current potential conditions, increased pore water pressure can decrease the suction strength and cause slope instabilities (Fredlund et al. 2012).

In this chapter, climate data investigation is presented, including an overview of historical and future climate data compilation and analyses. This is then followed by the construction of an appropriate long-term design climate for slope stability assessments. Finally, this chapter concludes with the evaluation of rainfall Intensity-Duration-Frequency (IDF) curves and the selection of design IDF curves for slope stability assessments under extreme rainfall.

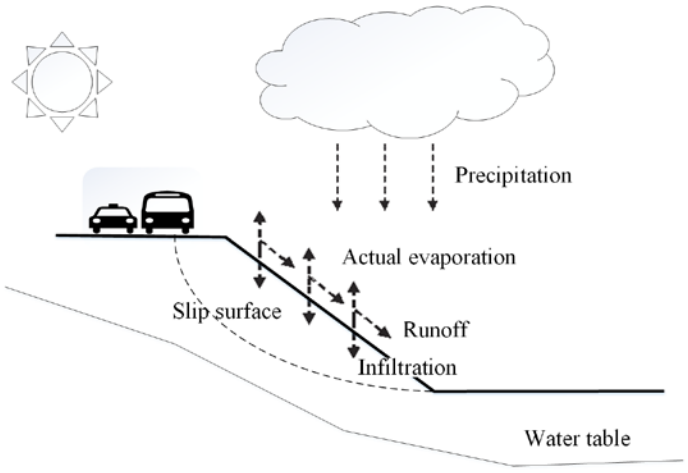

Figure 4.1 Climatic parameters and their interaction with the embankment (modified from Lu and Godt, 2012)

4.1. Compilation and classification of climate data

Quantification of climate change impacts requires a detailed compilation and review of the historical and future climate data. In this research, the climate compilation and review were carried out to come up with design climates that can be used in the soil-atmosphere models. Historical climate data for the period 1981-2010 and future climate data for the period 2011-2100 were collected from different sources for ten different locations across Ontario. These locations are large urban centers in the five administrative regions of the Ministry of Transportation, Ontario (MTO). The five administrative regions of MTO are shown in Figure 4.2. Kenora and Thunder Bay are in the northwestern region, Timmins and North Bay are in the northeastern region, Ottawa and Kingston are in the eastern region, London and Windsor in the western region, and Niagara Falls and Toronto are in the central region.

Figure 4.2 Five administrative regions of the Ministry of Transportation, Ontario (modified from Ontario Regions Map, 2011)

4.1.1. Historical climate data

Historical climate data, namely baseline climate (BC), is used as a datum to assess the possible changes in the future climate. Historical weather records were collected from the Environment and Climate Change Canada portal (Environment and Climate Change Canada 2018). Baseline climate data for each location was compiled from the weather station that had the most complete daily data for the period 1981-2010. In some instances, multiple stations were used. The details of the weather stations are presented in Table 4.1. The compiled climate datasets comprised of the daily values of precipitation, relative humidity, temperature, wind speed, and net radiation. The compiled climate datasets were statistically analyzed to compute historical averages, maximum and minimum values, and other pertinent information for various climate variables over the 30 years. This was accomplished for all the ten locations. Following is a brief presentation of the complied climate data set for the city of Niagara Falls, ON. Details of these datasets for other locations are available in Appendix B.

Table 4.1 Weather stations for different locations

Location	Weather Station (WMO ID or Station ID)
Ottawa	Ottawa MacDonald International A (71628)
Kenora	Kenora Airport (71850)
London	London International Airport (71623), London CS (71622)
Windsor	Windsor A (71538)
North bay	North Bay Airport (71731)
Thunder Bay	Thunder Bay A (4055), Thunder Bay AWOS (71749), Thunder Bay Burwood (N/A), Lakehead University (4018), Thunder Bay CS (71667)
Niagara Falls	Niagara Falls NPCSH (4659), Welland Ontario (4712), Niagara Falls International Airport (N/A), NY US (N/A), St Catharines A (4683)
Kingston	Kingston Pumping (4300), Kingston climate (71820), Hartington IHD (71621)
Toronto	Pearson International airport (71624)
Timmins	Victor Power Airport weather station (N/A)

Figure 4.3 shows the compiled climate data for the city of Niagara Falls for the period 1981 to 2010. A review of the precipitation data presented in this figure reveals that the average annual precipitation over this period is 929 mm. It can also be observed that over the 30-year period, precipitation events of 40 mm/day or more occurred 27 times. However, the number of precipitation events equal to or higher than 30 mm/day is 74 during the same period. The highest daily precipitation of 85 mm was recorded on August 30, 2005.

Temperature data presented in Figure 4.3 indicates that the highest daily mean temperature over the 30-year period was 30.3°C, which was recorded on July 25, 2005. The coldest mean temperature was recorded to be -21.3°C on January 1 of 1994. The temperature records also indicate that the average positive and negative mean temperatures over the 30-year period were 13.2°C and -4.9°C, respectively.

The review of the historical daily relative humidity data shows that the average of daily mean relative humidity is 72% over the historical period. The lowest daily mean relative humidity value of 31.7% was recorded in 1999, while the highest mean relative humidity value of 100% was recorded in the years 1986, 1992, 1994 - 1996, and 2000.

For the wind speed data, the highest wind speed of 35.59 km/hr was recorded on November 11 of 2003. It can also be observed that there was no wind in some days in the historical period. The average daily wind speed for the historical period can be estimated at 10.97 km/hr.

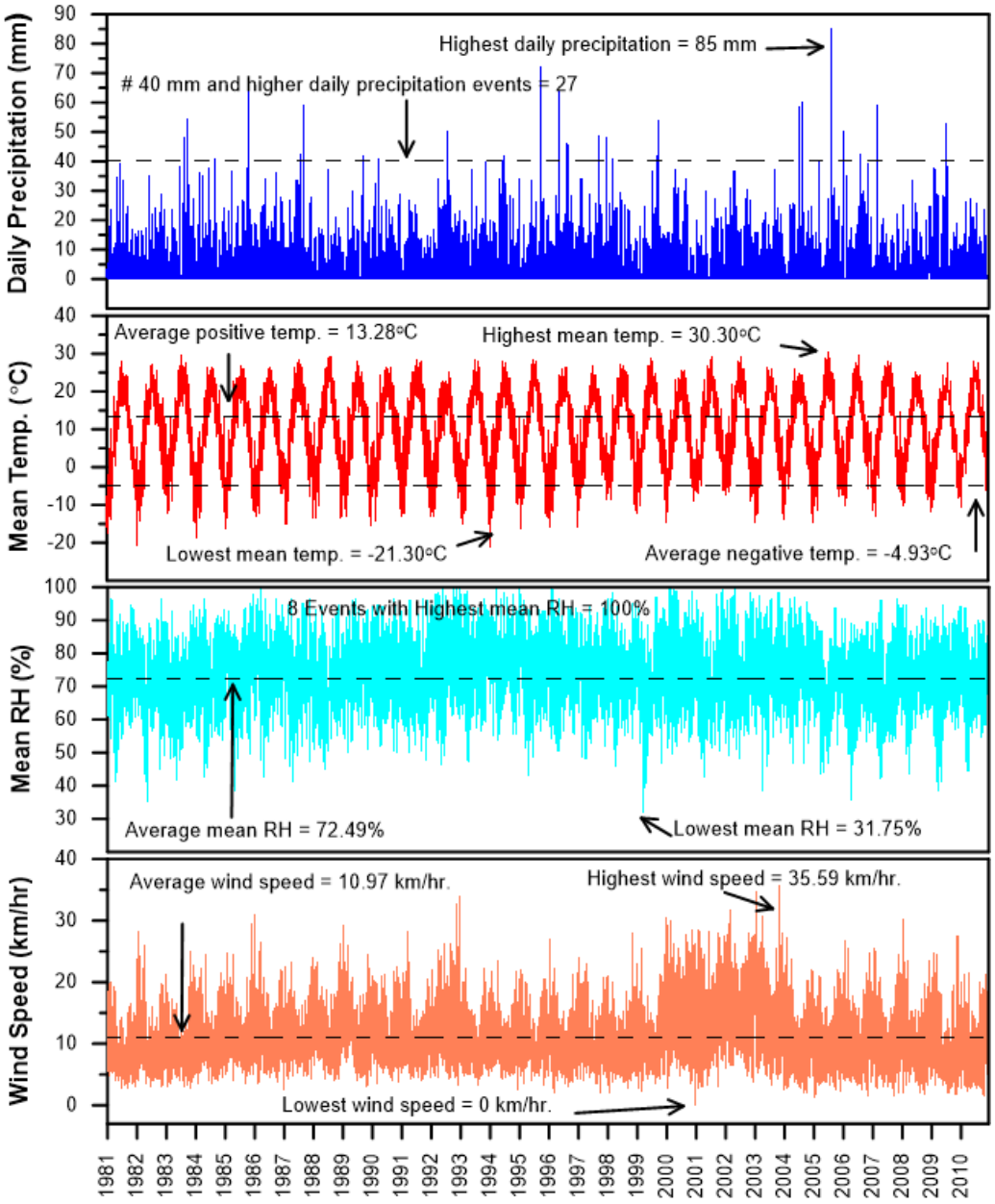

Figure 4.3 Historical climate data for Niagara Falls

4.1.2. Seasonal considerations

Ontario's climate, in general, consists of a warmer summer and a colder winter for several months. During the winter months, the ground could remain frozen for an extended period, and precipitation is mostly in the form of snow. Therefore, partitioning of yearly climate into active and inactive periods can significantly simplify the estimation of water balance at the ground

surface. In the active period, the ground condition remains thawed, and water can enter the ground surface and can move vertically and laterally. During the inactive period, the ground surface remains frozen, and the precipitation comes in the form of snow and accumulates on the ground surface. It is commonly assumed that in the inactive period, little to no water enters the ground, and there is minimal to no flow in the subsurface (Fredlund et al. 2012, Bashir et al. 2016, and Pk 2017). The inactive period starts with the date of freeze and ends with the date of thaw. In order to reduce the computation time and unnecessary complexities related to ground freezing, development, and thawing of the snowpack, the inactive periods could be ignored in soil-atmosphere modelling. This approach has been used by others, e.g., Fredlund et al. (2012), Bashir et al. (2016), and Pk (2017). In these studies, water activity throughout the active period was used to estimate the water balance at the ground surface.

The freezing and thawing dates can be identified by analyzing the air temperature records for the area of interest. The 30 years' maximum, minimum, and mean air temperature data were analyzed to estimate the freezing and thawing dates for all locations. Figure 4.4 (a) and (b) show the result of analysis for the city of Niagara Falls for the period 1980-2010. It can be observed from Figure 4.4 that the freezing dates can start as early as the first week of December. However, December 11 was found to be the average of freezing dates for the historical period. Similar to the freezing graph, the thawing graph shows thawing dates can vary over an 8-week period starting as early as February 25. It can also be observed that the thawing dates for more recent years (after 2000) are within the last week of March, and the average thawing date of March 24 can be selected for the city of Niagara Falls. In short, for the city of Niagara Falls, the active period starts from March 24 and ends on January 2. Accordingly, the inactive period is from January 3 to March 23.

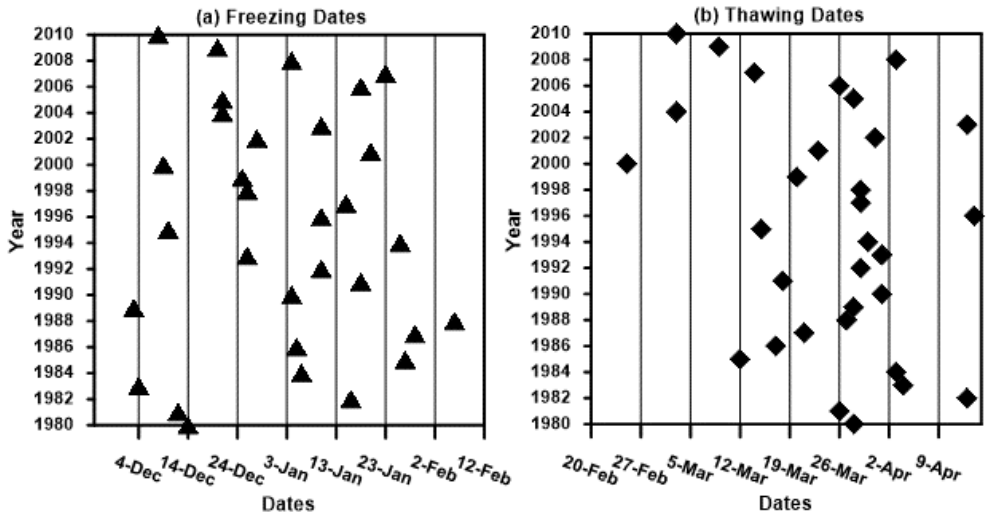

Figure 4.4 (a) Freezing and (b) Thawing dates for the past 30 years of Niagara Falls climate

Figure 4.5 illustrates a comparison between active and inactive periods for all ten locations under consideration. For Niagara Falls, the active period climate comprises of 247 days. Windsor, with 250 days, experienced the longest active period in comparison to the other locations under consideration. In contrast, Timmins had the shortest active period of 185 days.

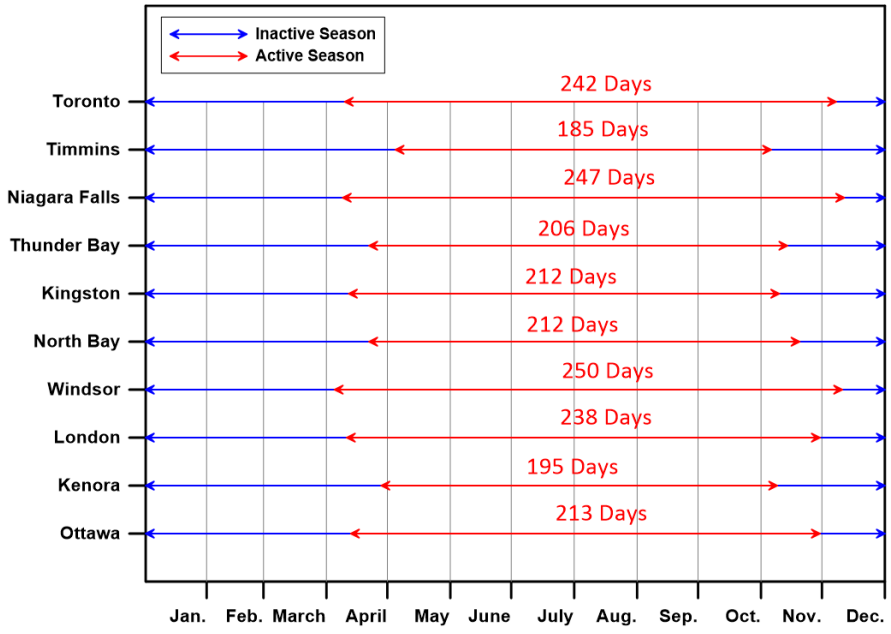

Figure 4.5 Active and inactive periods for all location in the past 30 years

Figure 4.6 presents the distribution of measured precipitation and estimated potential evaporation (PE) over the active and inactive periods for the city of Niagara Falls. It can be inferred from this figure that the average of cumulative precipitation for the 30-year historical period during the active periods is 747.8 mm, while the value during the inactive period is 181.46 mm. It also shows that the precipitation during the active period is around 80% more than precipitation during the inactive period. A similar assessment was carried out for other locations, and corresponding graphs are available in appendix B.

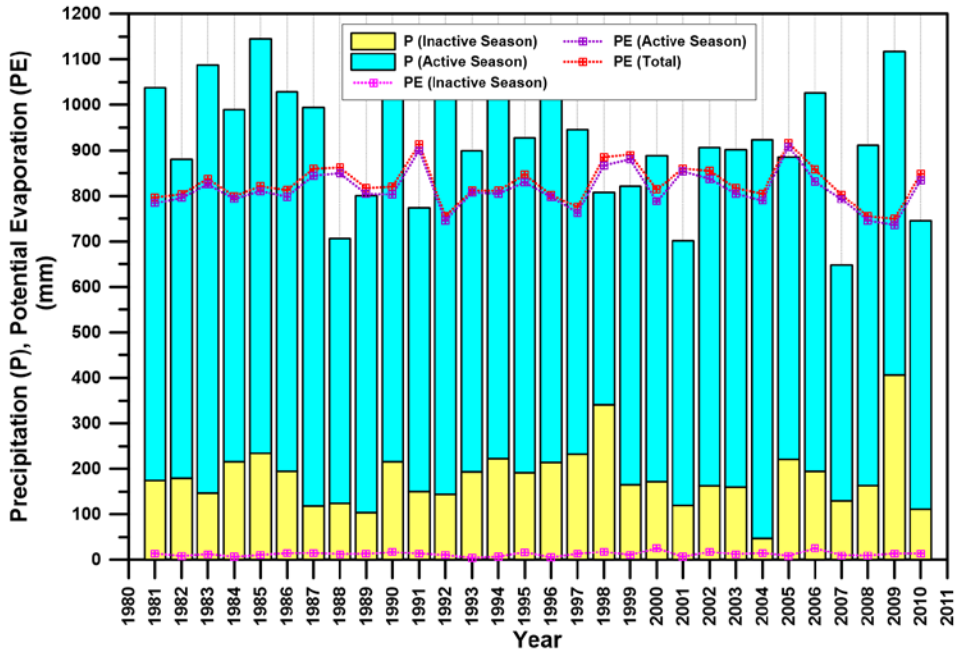

Figure 4.6 Precipitation during active and inactive periods, and PE during the active period for Niagara Falls

4.1.3. Climate classification

Climatic classification provides the geotechnical engineer with general guidance regarding the water availability at a particular site. It is based on the water balance calculation in reference to the ground surface (Fredlund et al. 2012). Climate classification presents a general view of weather

setting for a location under consideration. The Thornthwaite climate classification system (Thornthwaite 1948; Thornthwaite and Hare 1955) can be used for climate evaluation for engineering purposes. This system is empirical and was developed from climatic data collected in the United States (Thornthwaite 1948). It is based on the calculation of the annual moisture index and requires estimates of annual precipitation and potential evaporation. The annual moisture index can be expressed after Thornthwaite and Hare (1955) as:

$$I_m = 100\left(\frac{P}{PE} - 1\right) \quad (4.1)$$

where I_m is the annual moisture index (Thornthwaite and Hare 1955), P is the total annual precipitation, and PE is the total annual potential evaporation.

An I_m value of zero indicates that the annual precipitation and the potential evaporation are equal, and net neutral water balance conditions can be expected at the ground surface. A positive I_m value implies a surplus of the net water, and the climate condition could be from Moist Humid to Perhumid. While a negative I_m value indicates a scarcity of the net water, and the climate could be from Dry Subhumid to Arid.

4.1.4. Estimation of potential evaporation

Thornthwaite and Hare (1955) climate classification requires the estimation of the ratio between annual precipitation and potential evaporation. Precipitation is usually measured at most weather stations. Potential evaporation can be estimated by several different methods, such as Thornthwaite (1948), Penman (1948), Blaney and Criddle (1950), and Priestley-Taylor (1972). The details of these methods can be found in Fredlund et al. 2012. All of these methods require some weather variables such as relative humidity, air temperature, wind speed, and net radiation to estimate potential evaporation. For example, Penman's (1948) method requires all five variables mentioned, while Thornthwaite (1948) method only requires temperature measurements to estimate potential

evaporation (Tegos et al. 2015). Although all of the climate variables are usually available for historical data, only reliable predictions for precipitation and temperature data are available for the future climates. Therefore, for the estimation of potential evaporation for future climates, a method that requires minimal climate data is preferred.

Pk (2017) and Ahmad (2018) used Pereira and Pruitt's (2004) method, which is a modification of the Thornthwaite (1948) method, to estimate *PE* for the cities of Toronto and Timmins, respectively. They found that the estimated values were similar to those estimated from the Penman (1948) method. In this research, Pereira and Pruitt's (2004) method was used to estimate *PE* for all ten locations across Ontario. Figure 4.7 shows the comparison of historical *PE* estimates from these two methods for the city of Niagara Falls. It can be observed that estimates from them are very similar. A similar comparison for all locations was carried out, and results were found to be satisfactory.

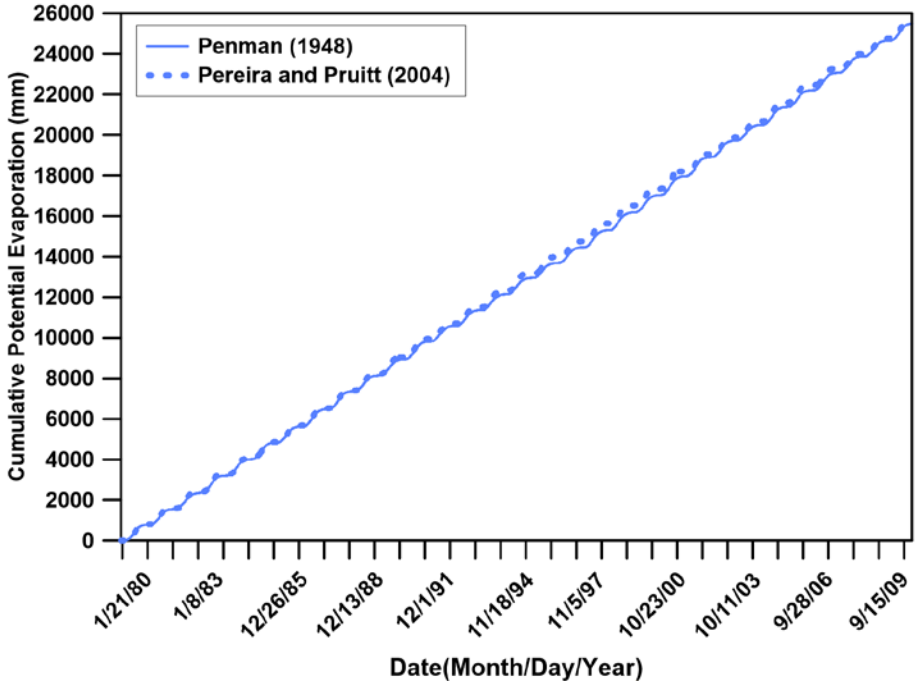

Figure 4.7 Comparison of cumulative PE calculated using Penman (1948) and Pereira and Pruitt (2004) methods

4.1.5. Climate classification results

The climate classification for the 30-year historical period for the city of Niagara Falls is shown in Figure 4.8. As can be seen in this figure, on average, the climate of Niagara Falls is in the moist-humid category with an average I_m value of 13. The standard deviation of the I_m for Niagara Falls was estimated to be 25. The mean plus one standard deviation gives a moisture index of 33 (humid), while the mean minus one standard deviation gives -7.2 (dry subhumid). For the 11 years of the 30 years under consideration, the climate can be classified as humid, and the climate of 9 years is in the moist-humid range. The lowest I_m was estimated for the year 2007, which falls within the dry subhumid range. It can be observed that there are 9 years in the dry sub-humid regions as well. For the majority of the years, the availability of the water is higher than the evaporative demand. The year to year variability in climatic conditions highlights the importance of consideration of multi-year climate datasets so that year to year variation in the climate can be taken into consideration for engineering analyses and designs.

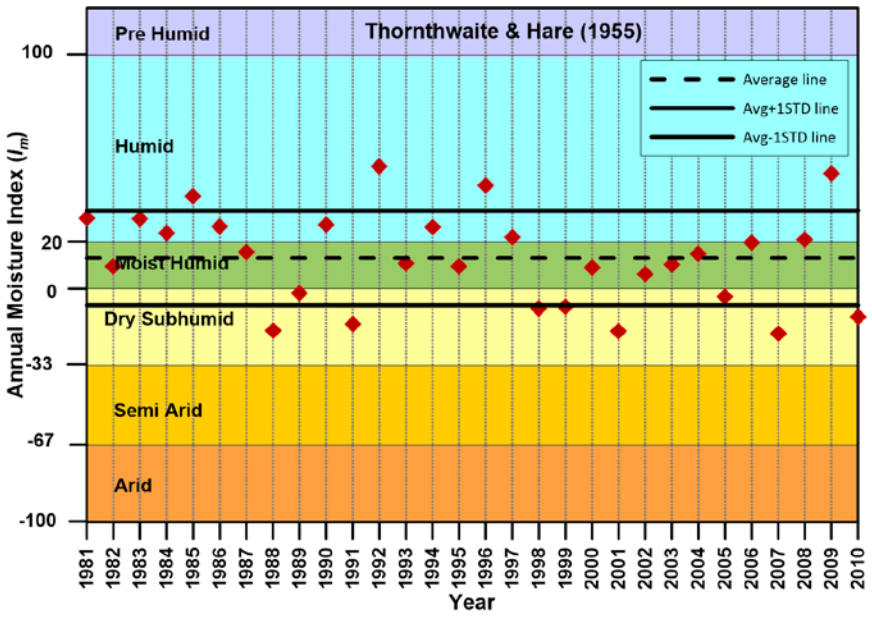

Figure 4.8 The climate classification for the city of Niagara Falls for the period 1981-2010

A similar climate classification was carried out for all the ten different locations under consideration. The results of all these locations are summarized in Figure 4.9 in the form of box and whisker plots. This figure compares the availability of moisture at the ground surface for all of these locations over a 30-year period from 1981-2010. It can be observed that for all the cities under consideration, North Bay has the wettest climate and thus the highest moisture availability. It can also be seen that Toronto has the driest climatic conditions and thus the lowest moisture availability over the 30-year period. Other notable observations are that the city of North Bay experienced the maximum year to year variation, while the city of Ottawa experienced the minimum year to year variation in climate over the historical period.

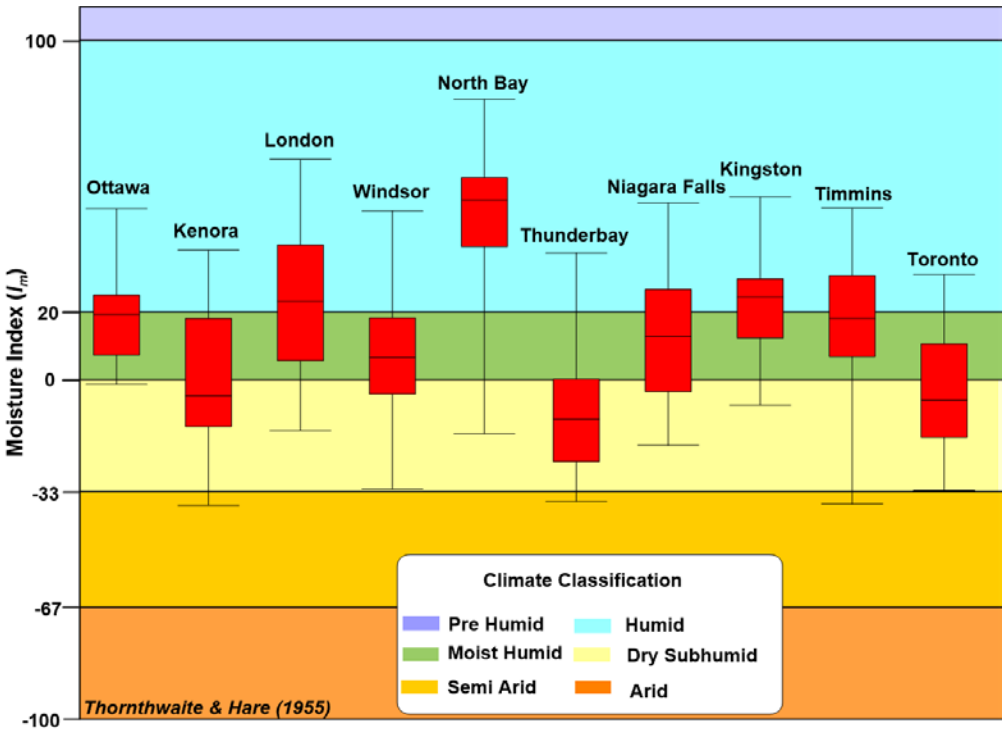

Figure 4.9 Climate classification for all location over the period 1981-2010

4.2. Future climate data

Future climate prediction is an attempt to estimate the actual evolution of the climate. Global Climate Models (GCMs) are the primary tool used for understanding and attribution of past climate variations and future predictions. Simulations by climate models provide the response of the climate system to emission or concentration scenarios of greenhouse gases or radiative forcing scenarios (IPCC 2007, 2013). The pathways of total radiative forcing or cumulative measure of human emissions of greenhouse gases from all sources are termed Representative Concentration Pathways (RCPs) (van Vuuren et al. 2011). Four different RCPs (RCP 2.6, RCP 4.5, RCP 6.0, and RCP 8.5) are suggested in the fifth assessment report of IPCC (2013). Every RCP number expresses a different cumulative radiative forcing by the year 2100. The increasing number in RCP indicates more accumulation of radiative force; the RCP 2.6 represents the best-case scenario with the lowest concentration of radiative forces by the end of 2100, whereas RCP 8.5 shows the worst-case scenario where the concentration of radiative forces would be the highest at the end of 2100.

4.2.1. Data sources and compilation

The future climate (FC) data for all locations was obtained from published sources in the public domain. The available sources are the Ontario Climate Change Data Portal (CCDP) published by the Institute of Energy, Environment and Sustainable Communities (IEESC), University of Regina, and the Ontario Climate Change Projections (OCCP) published by the Laboratory of Mathematical Parallel System (LAMPS), York University.

A previous study (Pk et al. 2018) indicated that the climate data from OCCP is superior in the sense that the climate models used by OCCP do a better job in back predicting the historical climate. Therefore, climate data from OCCP was used in this study. The OCCP datasets cover the period from 1980 to 2100 and contain four climate variables, namely precipitation, maximum,

average, and minimum temperatures over a 10×10 km grid for the whole of Ontario. This data is available for 33 different GCMs and all four RCPs (i.e., 2.6, 4.5, 6.0, and 8.5). Previous studies (e.g., Pk et al. 2018, and Bashir et al. 2020) have indicated that among all the GCMs, CCSM4, GFDL-ESM2M, Had GEM2_ES, and NorESM1-M show better performance in predicting the historical data for the cities of Toronto and Timmins. Therefore, data for these four GCMs for all four RCPs was downloaded from the OCCP website (www.occp.lamps.yorku.ca). To assess the performance of the OCCP predictions, predicted mean temperature and precipitation data for the period 1981-2010 based on various GCMs and RCPs were compared to the climate normals reported by (Environment and Climate Change Canada 2019) for all locations. The results for the city of Niagara Falls for GCM Had GEM2_ES and RCP 8.5, are shown in Figure 4.10 (a) and (b). The review of these figures indicates that both the precipitation and temperature data show a good agreement with the historical climate normals.

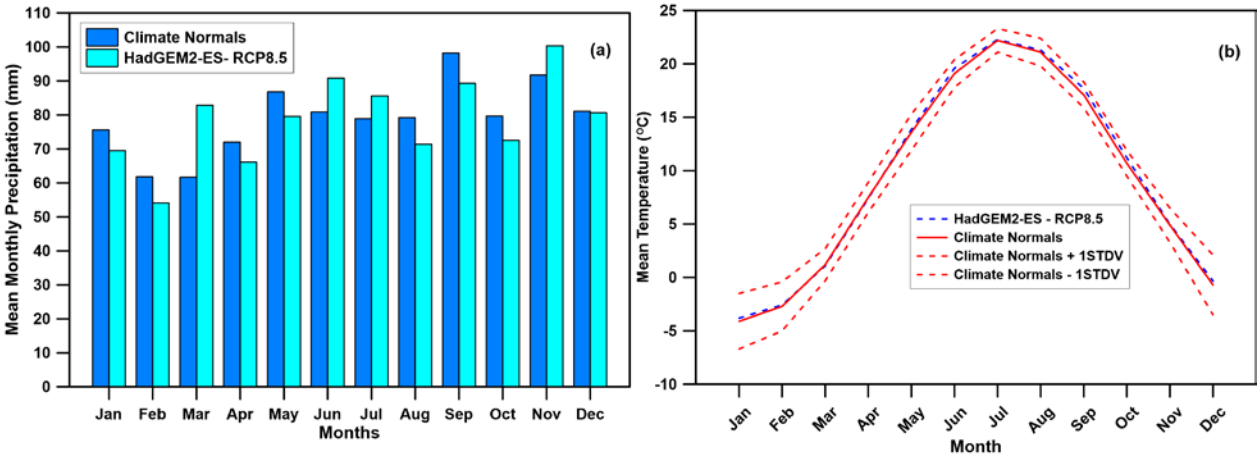

Figure 4.10 Comparison between climate normals and predicted (a) precipitation, (b) temperature for Niagara Falls for GCM HadGEM2-ES and RCP 8.5

The climate data for each GCM and RCP was compiled into thirty-year periods. These periods correspond to the start (2011-240), middle (2041-2070), and end (2071-2100) of the current century. This resulted in 48, thirty-year climate datasets for each of the locations under

consideration. Each thirty-year climate dataset can be referred to as a climate ensemble. Each of these ensembles corresponds to a particular GCM and RCP and is representative of the climatic conditions in one of the 30 year period of the current century. Considering the historical 30 year period (1981-2010) as an additional ensemble, the total number of ensembles for each of the location becomes 49. A schematic of the ensembles is shown in Figure 4.11. It should be noted that compilation of the historical and future climate data resulted in 49 thirty-year climate datasets for each of the 10 locations resulting in 490 thirty-year climate datasets in total.

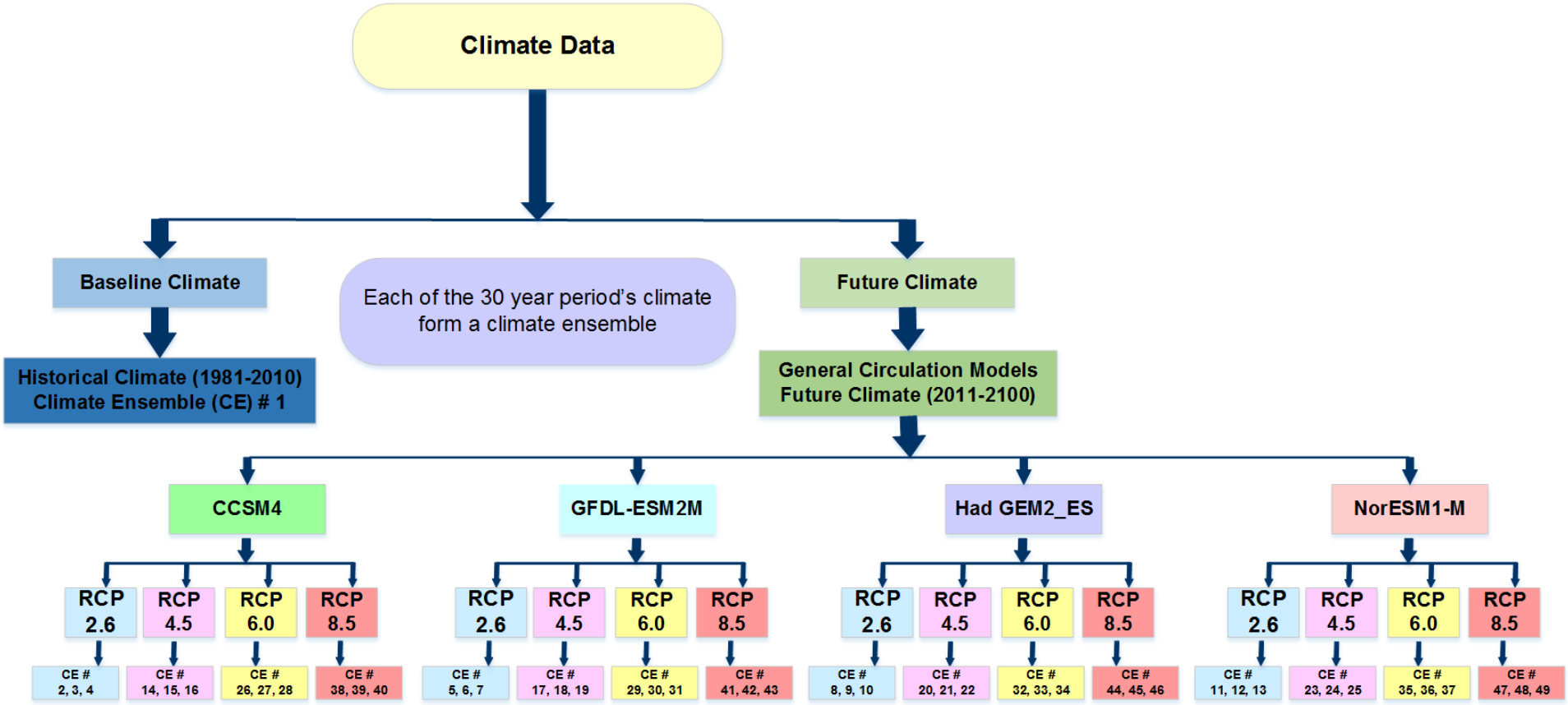

Figure 4.11 Flow chart showing baseline and future climate ensembles

4.2.2. Review and analysis of future climate data

Descriptive statistics of the future climate data was carried out to analyze the trend in precipitation, temperature, potential evaporation, and annual moisture index data for all locations. The results from these analyses are presented in the form of box and whisker plots.

Figure 4.12 presents the graph for total annual precipitation for Niagara Falls for all climate ensembles. This graph shows that for Niagara Falls, there is an increase in maximum annual precipitation for most climate ensembles. Ensemble 8 shows the most significant increase in maximum annual precipitation. This ensemble corresponds to the first 30 years of the future period (2011-2040) under GCM Had GEM2-E5 and RCP 2.6.

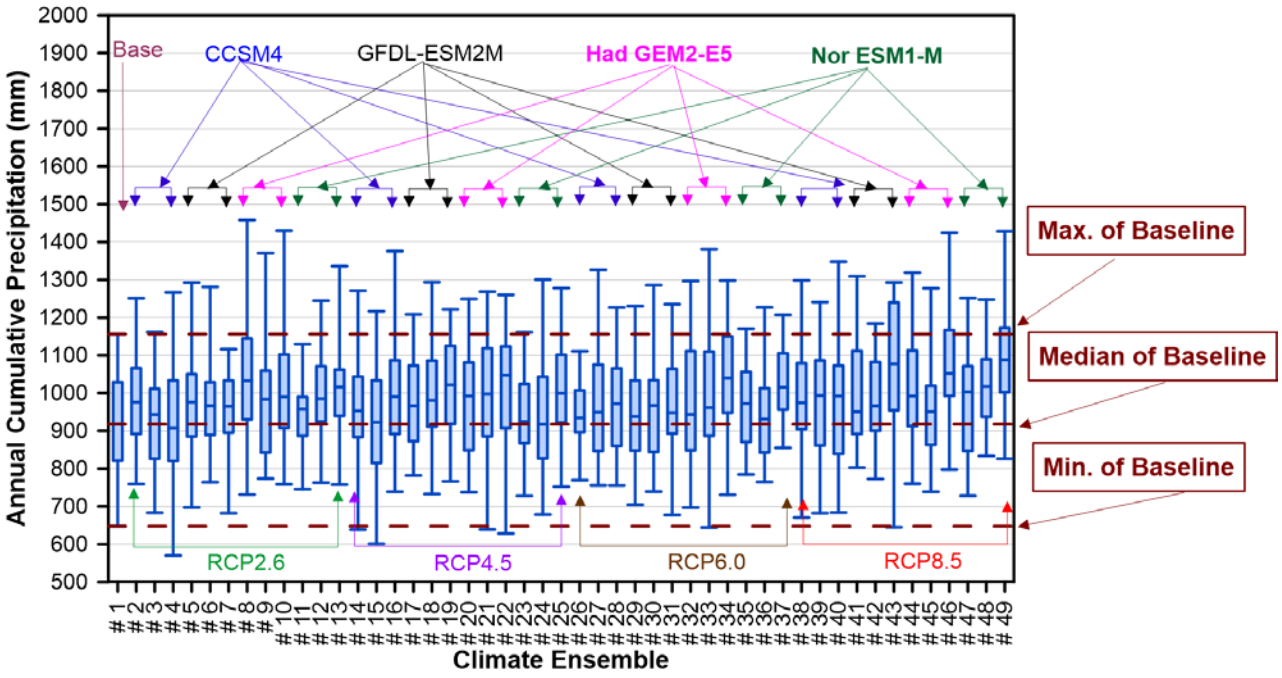

Figure 4.12 Box and whisker plot for annual precipitation of Niagara Falls

According to Figure 4.12, the future median values show an increasing trend for most ensembles. The only exception is the last 30-year of the future period under GCM CCSM4, and RCP 2.6

(ensemble 4). The maximum increase in median precipitation was observed for ensemble 49, which corresponds to GCM Nor ESM1-M, RCP 8.5 for the third part of the current century. Similarly, the minimum annual precipitation for most climate ensembles also shows an increasing trend; the only exceptions are climate ensemble 4 and 15, which show an appreciable decrease in minimum annual precipitation.

From the review of the precipitation data for the city of Niagara Falls, it can be concluded that future precipitation has an increasing trend. It also becomes evident that there would be a considerable increase in maximum yearly precipitation and modest to a considerable reduction in minimum yearly precipitation values. Accordingly, it can be concluded that the availability of meteoritic water would increase in the future.

Selected results from all descriptive statistical analyses for the ten locations across Ontario are summarized in Figure 4.13. This graph presents the box and whisker plots of the baseline ensemble and a selected future climate ensemble. This future ensemble was selected considering the most significant change in the average 30 years precipitation.

From this figure, it can be observed that for all locations, the median value of average yearly precipitation is expected to increase more than the 75^{th} percentile historical value. For the city of Kingston, the median future annual precipitation could be even more than the maximum historical value. The results presented in Fig. 4.13 also show that maximum and minimum yearly values are expected to increase for all locations as well.

It can be also be observed that Windsor has the highest value of maximum future precipitation, and the lowest maximum precipitation would occur in Thunder Bay. For Ottawa and Thunder Bay, there is a slight increase in precipitation in comparison to the baseline values. Thunder Bay also has the lowest value of minimum future precipitation in comparison to all locations under

consideration. Ottawa has experienced the minimum year to year variation in the past; however, in the future, it is expected to see a huge increase in the year to year variation in average yearly precipitation. In conclusion, this graph makes it evident that wetter climatic conditions compared to the baseline climate are expected in the future for all cities under consideration.

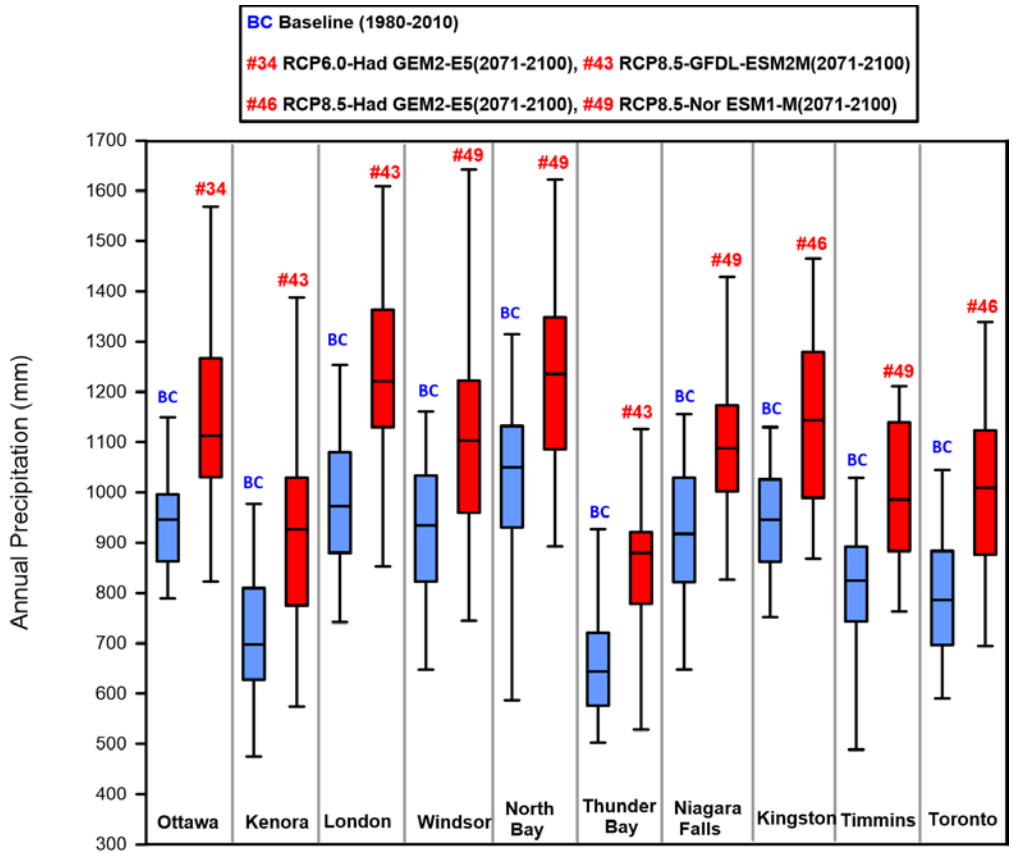

Figure 4.13 Annual precipitation for the past and the selected future ensemble for all locations

Similar to precipitation, descriptive statistical analyses were also carried out for temperature data for all of the locations under consideration. After review of these analyses, future climate ensembles with the maximum change in the average of mean annual temperature in comparison to the baseline were identified. These selected future ensembles and the baseline ensemble for all ten locations are presented in Figure 4.14.

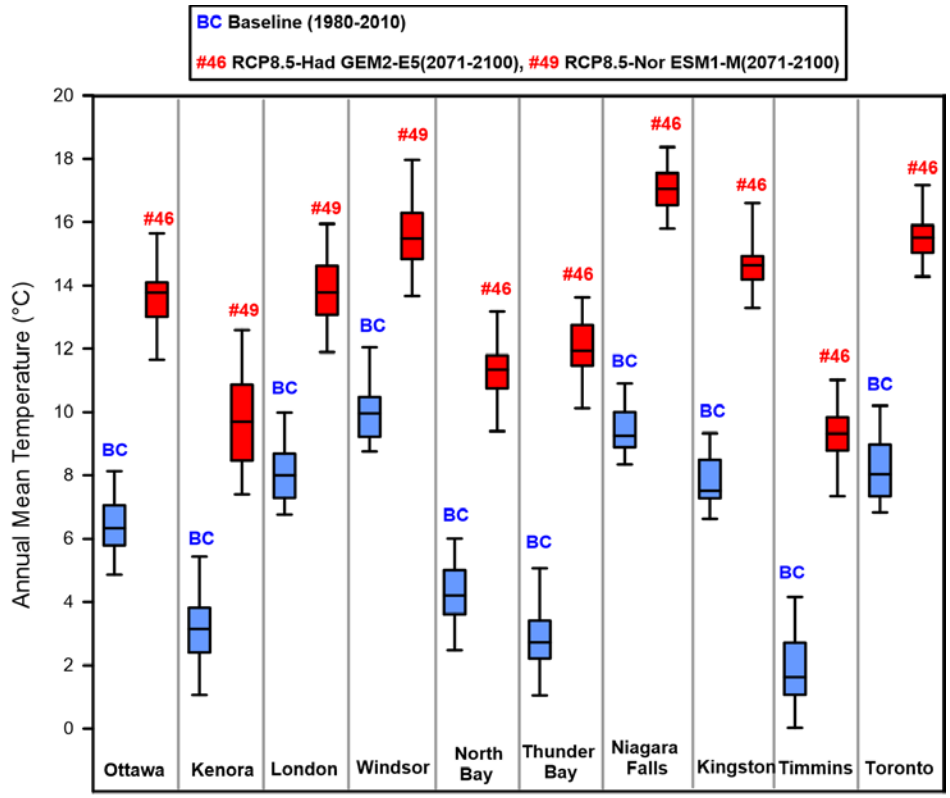

Figure 4.14 Annual mean temperature for the baseline and the selected future ensemble for all locations

Base on this figure, it is clear that the last thirty years of the century would experience the warmest conditions across Ontario. This increase in temperature would occur under RCP 8.5, which is the worst scenario in terms of greenhouse gas emissions. It can also be observed that the GCM Had GEM2 predicts the highest increase in temperature for most of the locations. A review of the baseline information indicates that among all locations, the city of Windsor has experienced the warmest historical period, while, during the same period, the city of Timmins had the lowest values of average annual temperatures. The graph also indicates that the future temperature of all ten locations could be noticeably higher when compared to the historical period, with cities of Thunder Bay and Niagara Falls are expected to see the largest changes.

It should be noted that in all ten locations, even the minimum values of temperature are higher than the maximum values of the historical period. For many of these cities, the minimum yearly future temperature is four degrees above the maximum of historical yearly average temperature.

Based on the above analysis and review, it is quite clear that Ontario would experience warmer days in the future. For the city of Windsor, which shows the lowest expected increase in temperature, the average yearly temperature could still see an increase by up to five degrees in the future.

In order to assess the water availability for the future climates, annual moisture indices were estimated for all ensembles using the Thornthwaite and Hare (1955) method. The results of Niagara Falls are presented in Figure 4.15. This figure compares the availability of moisture at the ground surface over 30 years of the historical period for all future climate ensembles. It can be observed that the median water availability for many future climate ensembles is less than the historical value. For a few of the future climate ensembles, the median I_m values are similar to historical value. This observation at first might seem surprising as precipitation increase is expected for almost all future climate ensembles for the city of Niagara Falls. However, it should be noted that a predicted considerable increase in temperature would also result in a proportional increase in potential evaporation and hence would offset the increased water availability. In terms of wetter condition, ensemble #8 indicates much wetter conditions than historical conditions, with a similar median value for I_m and higher values for the 75^{th} percentile and maximum. It should be noted that ensemble #8 corresponds to the GCM HadGEM2-E5 for RCP 2.6 for the period 2011-2031. In general, the moisture indices for most of the years fall within the dry sub-humid to humid; therefore, the future climate of Niagara Falls would be classified as moist-humid similar to the

baseline climate. A similar analysis was carried out for all the locations under consideration, and the results are available in Appendix B.

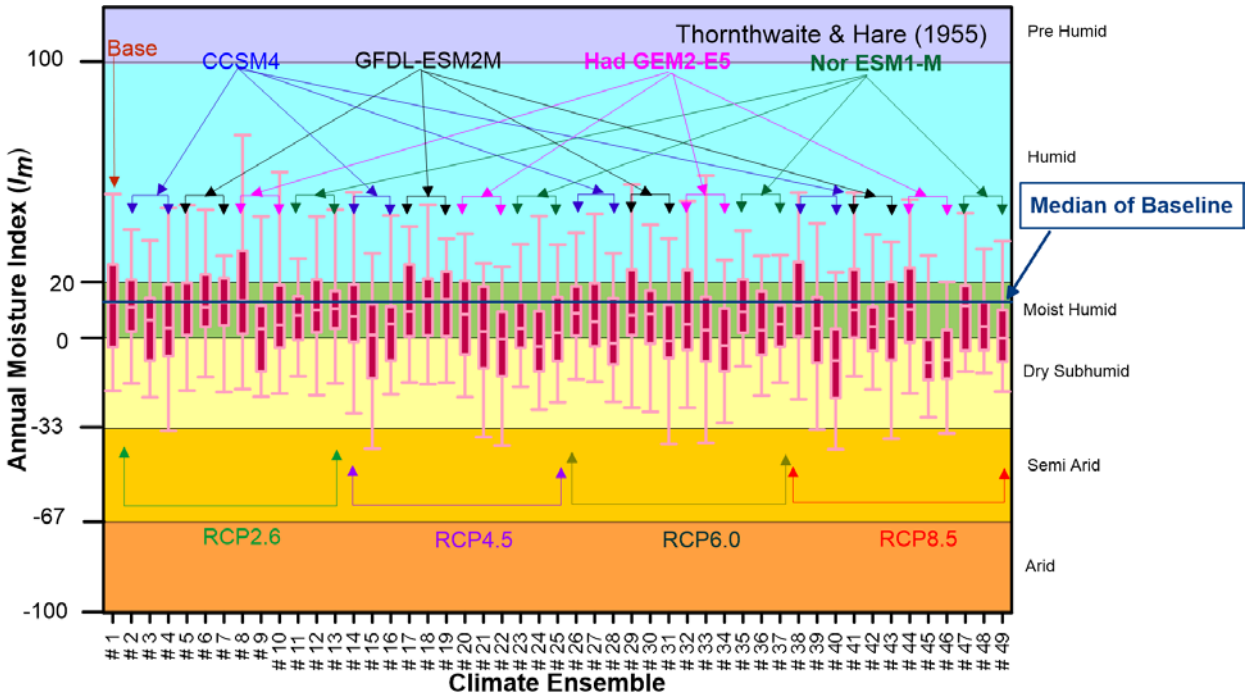

Figure 4.15 Yearly variation of the annual moisture index for Niagara Falls

Considering that the wetter climatic conditions can potentially be more detrimental to the stability of the embankment slopes, the annual moisture indices from wettest future climate ensembles are compared to the baseline conditions for all cities in Figure 4.16. It can be observed that among all the cities under consideration, North Bay is expected to have the wettest climatic conditions and hence the highest moisture availability in the future. In contrast, Thunder Bay would have the driest climatic conditions and the lowest moisture availability over the future 90 years. Furthermore, similar to the historical period, the city of North Bay could experience the maximum year to year variation while the city of Ottawa is expected to experience the lowest year to year variation in climate.

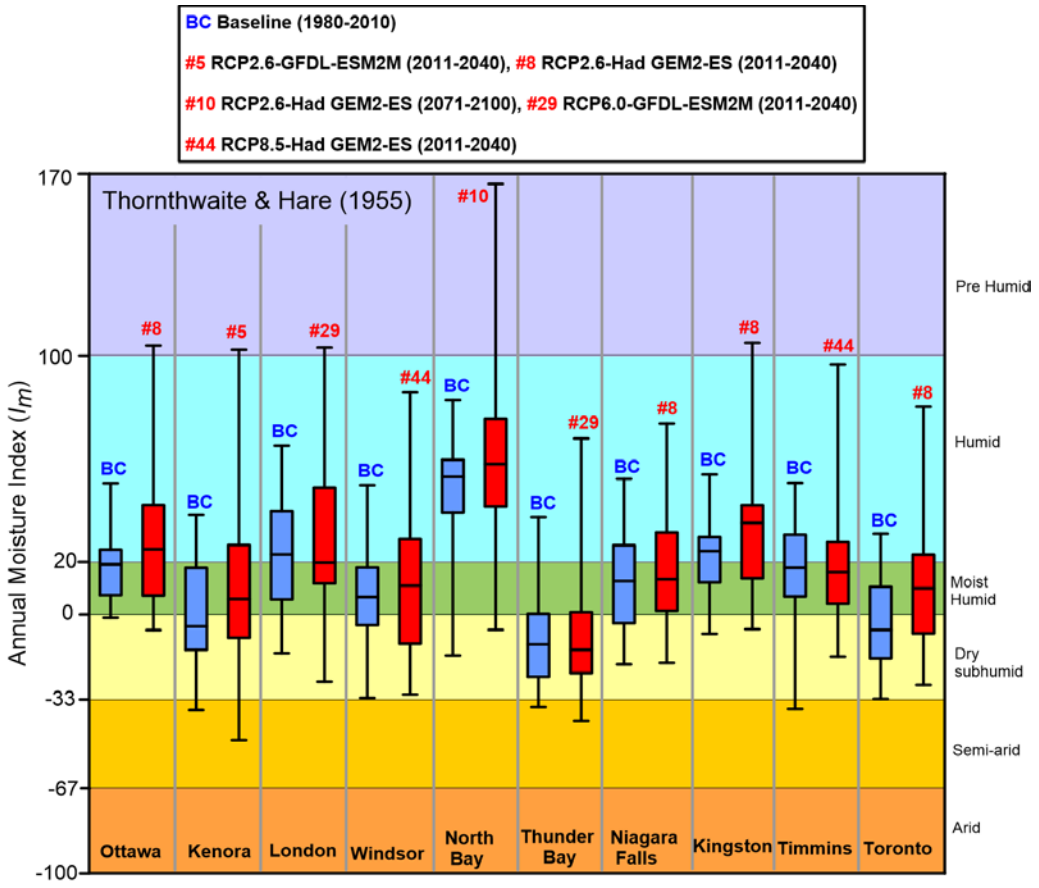

Figure 4.16 Climate classification for all locations in the past and future

4.2.3. Changes in seasonal considerations

The 90 years' future air temperature data was analyzed to estimate freezing and thawing dates in the future. The descriptive statistics of the future climate data is presented in the form of box and whisker plots to analyze the duration of active and inactive periods. These analyses were carried out for all ten locations, and corresponding graphs are available in Appendix B.

After review of these analyses, future climate ensembles with the maximum change in the median freezing and thawing dates in comparison to the baseline were identified. Figure 4.17 and Figure 4.18 show the baseline ensembles and selected future ensembles for freezing and thawing dates, respectively, for all ten locations.

It can be seen that for the cities under consideration, Niagara Falls would have a significant shift in both future freezing and thawing dates compared to the historical period. Based on this graph, this city would have a longer active period. Therefore, it is expected that in the future, the ground condition may remain thawed for a longer period, and potentially larger quantities of water can enter the ground surface.

By looking at the change in the freezing and thawing dates of all locations, it can be concluded that late freezing and early thawing conditions are expected across all locations under consideration. This would result in a longer active period in the future, which may cause more water to enter the ground surface and can be a potential influence on the embankment water balance.

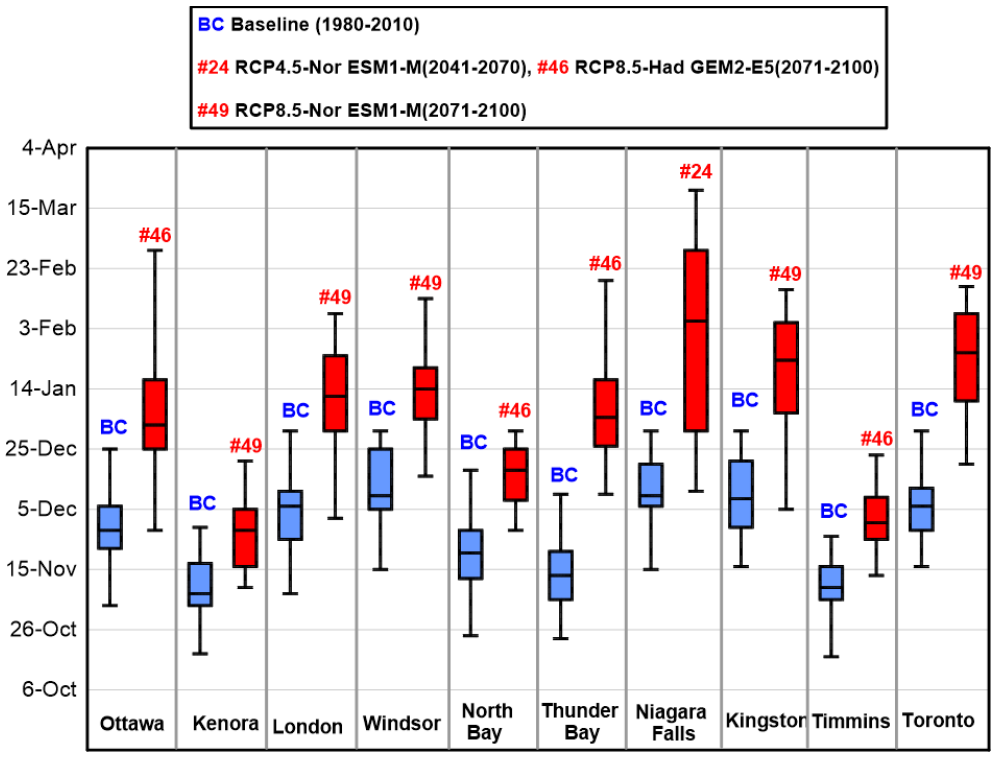

Figure 4.17 Comparison of historical and future freezing dates of all locations

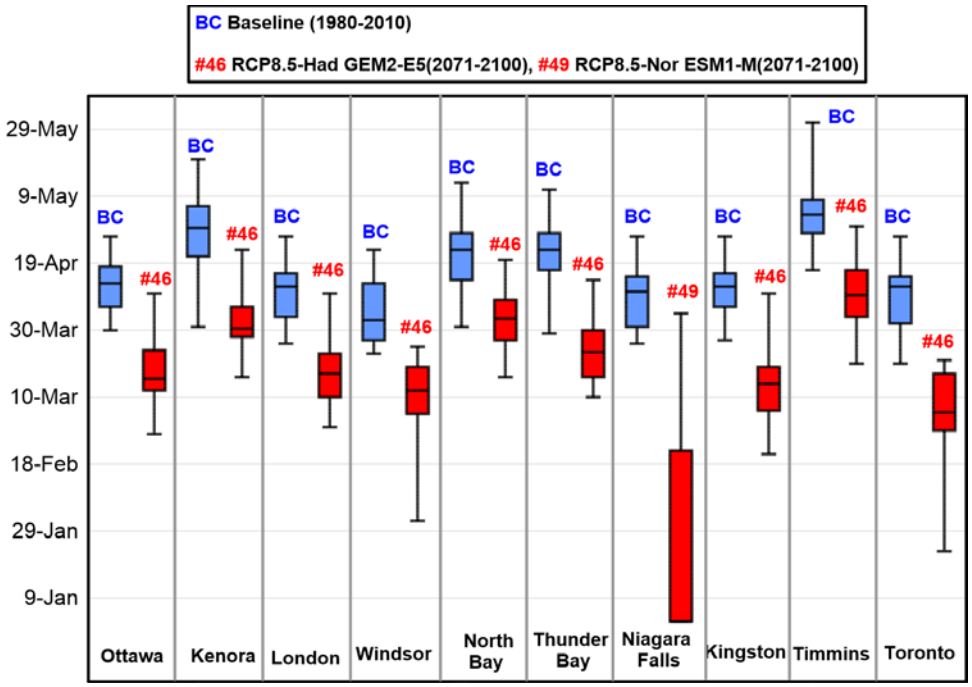

Figure 4.18 Comparison of historical and future thawing dates of all locations

4.3. Long-term design climate

As described earlier, forty-nine climate ensembles were assembled for each of the ten locations, as part of the future climate data compilation. Each of these ensembles contains daily climate data for a thirty-year period. This is rather a large number of projections based on various models and emissions scenarios. Ideally, all of these ensembles should be considered for the impact's studies, but for the current application, computational demands necessitate that only a limited set of ensembles be considered. It has been pointed out that selection can be based on two different criteria. The first is to select models that accurately depict the historical climate of the region of interest, and second, to select scenarios that span broad a range of future climate change as a much larger ensemble would (Salathe et al. 2007, and Lutz et al. 2016). As discussed earlier, the climate ensembles included in this study are from models that accurately depict the historical climate. Therefore the first criterion is met explicitly. The second criterion makes sense form a perspective

if one wants to see the range in probable impacts due to climate change. However, in the current study, the aim is to identify if the changing climate would result in a reduction of the factor of safety less than the allowable value against slope failure and to quantify this reduction. Therefore, the criterion needs to be somewhat adjusted. The factor of safety against slope failure is a function of pore pressure distribution within the embankment. Wetter climatic conditions, in general, result in higher pore pressure distributions and reduced suction strengths, resulting in lower factors of safety. Therefore, the criterion for the selection of climate ensembles should be to select ensembles that would produce wetter conditions in the embankment. A similar strategy has been used previously by Pk et al. (2018).

Wetter climatic conditions can be related to an increase in water availability at the ground surface. The water availability at the ground surface is a function of the availability of meteoric water and evaporative demand. Figure 4.19 shows the changes in precipitation and potential evaporation for the city of Niagara Falls. The values presented in this figure are based on the change in annual averages in relation to the baseline climatic conditions. An increase in precipitation values and a reduction in evaporative demand are expected to result in wetter conditions. A review of this figure indicates that the maximum increase in precipitation is expected for ensemble #49 associated with GCM NorESM1-M for RCP 8.5 for the later part of this century (2071-2100). One can select this ensemble, just based on this observation. However, there are other factors that also need to be considered. First, the data presented in Figure 4.19 (a) is the ensemble average; if one is to take into consideration the variation within each of the ensembles, a different selection can be made. For example, a review of Figure 4.12 indicates that although the median value of ensemble #49 has the largest increase from the baseline value, the largest overall increase and largest increase for the 75^{th} percentile can be observed for ensembles #8 and #43, respectively. Secondly, the

availability of water at the ground surface is not only dependent on the availability of meteoric water but also on the evaporative demand. A wetter climate in relation to the baseline would entail a maximum increase in precipitation and minimal increase or decrees in potential evaporation for the future in reference to the baseline conditions. A review of ensemble averages for potential evaporation in Figure 4.19 (b) indicates that, in general, there is an increasing trend in the *PE* for all ensembles when compared to baseline conditions. It can also be observed that increases are larger for higher radiative forcing and at later dates in the current century. The smaller increases in the amount of potential evaporation are all associated with RCP 2.6. However, these smaller increases in the amount of potential evaporation do not correspond to larger increases in precipitation values. Therefore, it is warranted that changes in precipitation and potential evaporation need to take into consideration in tandem. As described earlier, the annual moisture index is based on the ratio of precipitation and potential evaporation; therefore, a larger value of I_m for an ensemble would be representative of a wetter climate taking into consideration both the changes in precipitation and potential evaporation.

A similar approach was used by (Pk et al. 2018), where climate ensembles with the highest increase in precipitation and I_m values were selected as design climates to quantify the effect of climate change on embankment stability. However, this approach has two inherent shortcomings. First, the use of water availability as a criterion for scenario selection assumes that water balance at the ground surface is only based only on water availability dictated by atmospheric conditions. Numerous studies have shown that the water balance at the ground surface is also a function of hydraulic properties of the soil materials (e.g., Bashir et al. 2016 and Pk et al. 2018). The second shortcoming is related to the temporal scale at which one considers the water balance at the ground surface. As shown in the previous section, the identification of critical climate change scenarios is

dependent on whether one considers yearly or ensemble average. In reality, the water balance at the ground surface is a function of a sub-daily temporal scale. The intensity and frequency of the precipitation, together with the water-holding and conduction properties of the soil materials, would dictate the actual amount of water that enters the ground surface. For example, if one is to consider a daily resolution of precipitation data for water balance evaluation, the actual amount of water that enters the ground surface would be different if the sub-daily resolution of precipitation data is used. This is related to the infiltration capacity of the soil, which is a function of the hydraulic properties of the soil. Therefore, estimates of water balance are a function of temporal resolution of meteorological data, as also pointed out by others (Bashir and Pastora Chevez 2018, and Pk et al. 2018).

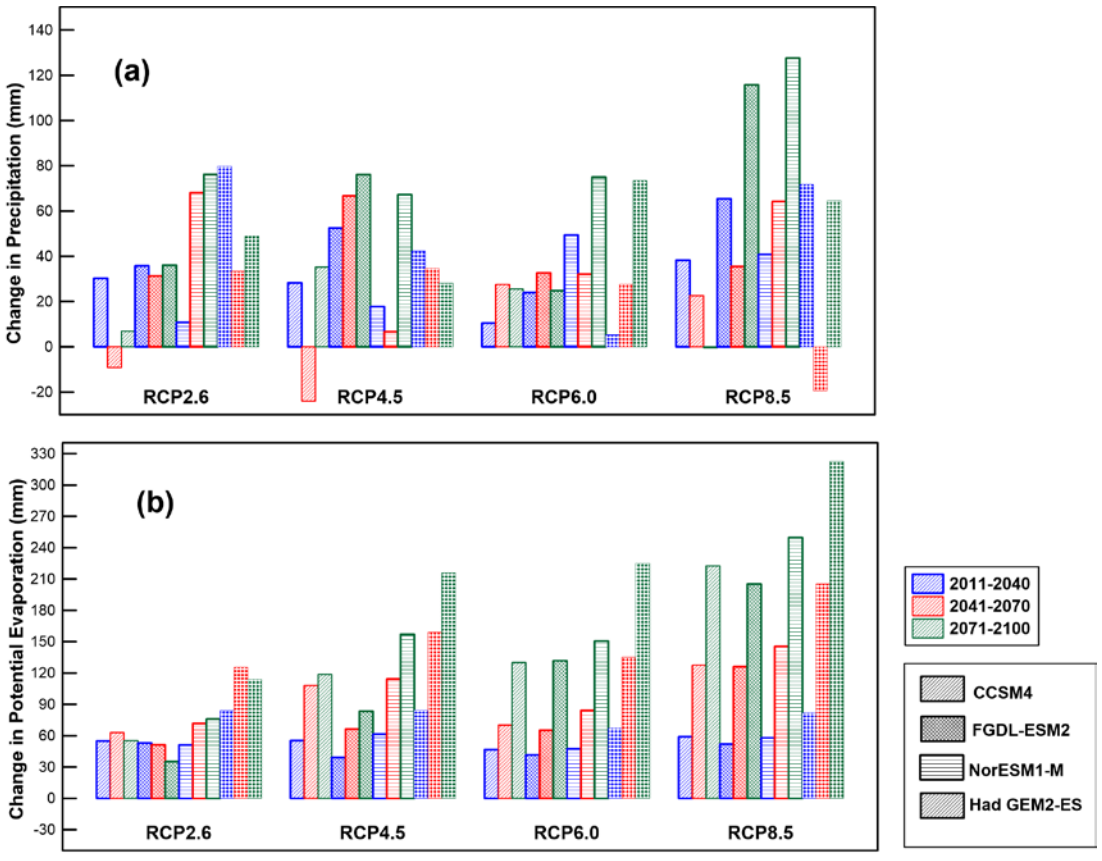

Figure 4.19 Change in (a) annual precipitation, and (b) potential evaporation over the active period in Niagara Falls

Taken into consideration the shortcomings mentioned above and the fact that there are no other guidelines for climate change scenario selection for geotechnical problems, an alternative methodology was used in the current research. This methodology is based on the water balance assessment using soil-atmosphere modelling and is presented in the following sections.

4.3.1. One-Dimensional water balance modelling

In this research, HYDRUS 1D was used to analyze the long-term variation of moisture in the soil embankment for different climatic conditions. HYDRUS 1D is a one-dimensional variably saturated finite element flow and transport model. The assessment was carried out by using the soil-atmosphere boundary with 30-year historical climate data and sixteen 90-year future climate datasets considering the selected soil materials that were discussed in detail in Chapter 3. This is to identify the design climates that can be applied in the 2D soil-atmosphere models.

One-dimensional simulations were carried out considering a 4 m high soil column. The column height was chosen based on the results of sensitivity analyses. These analyses were carried out to investigate the variation of moisture with depth by modelling a series of soil columns with different heights subjected to long term climate records. These simulations were performed for both types of materials, presented in chapter 3, and indicated that only the moisture in the upper 3 m depth of the soil column was affected by the soil-atmosphere boundary.

The groundwater level was applied at the bottom of the soil column using a constant head boundary (equal to zero). At the top of the soil column, a system-dependent boundary condition was applied to simulate the soil-atmosphere interaction at the ground surface. This boundary condition is capable of estimating actual evaporation, net infiltration, and surface runoff using climatic records of precipitation and potential evaporation together with model predicted transient soil-moisture conditions.

Thirty years of historical climate data and ninety years of future climate data, comprising of daily values of precipitation and potential evaporation, was applied as the soil-atmosphere boundary at the top of the soil column. In the numerical models, the daily precipitation records were uniformly distributed over the day. However, a sinusoidal shape distribution function was used for potential evaporation records to simulate the peak evaporation in the middle of the day (usually warmest hours of a day). The initial conditions for the models were assumed to be hydrostatic. This is a reasonable assumption, as numerical results indicated that the effect of the initial condition was minimal in the realm of long-term simulations.

4.3.2. Selection of appropriate design climate

Various outputs are available from HYDRUS 1D simulations. These include, but not limited to, the time history of pressure head and water content at each node, net infiltration, runoff and actual evaporation at the ground surface, outflow at the bottom boundary, and changes in water storage in the domain. For this study, the results of the numerical simulations in terms of the average degree of saturation through the soil column, time histories were found to be the most relevant. Average volumetric water content through the soil column can be simply obtained by calculating the water storage per unit volume of the domain. The degree of saturation can then be calculated as the ratio of volumetric water content to the saturated volumetric water content of the soil. In this study, the output time series were set to be reported on a daily basis. The results of the numerical simulations were analyzed in terms of variation of saturation over time for each location. The maximum degree of saturation during historical and future time periods was identified. In order to compare the long-term effects of different future climate scenarios, the frequency of high saturation occurrence (the number of days that saturation of the soil exceeds the maximum degree of saturation experienced during the historical period) was also determined.

Figure 4.20 shows the results of analyses for Niagara Falls. As can be seen, the maximum historical saturation for sand is 80%, while this value is 97% for the silt. This figure also indicates that the future climate data based on the GCM GFDL and RCP 2.6 has the highest values of saturation for both sand and silt materials. It can also be observed that for the same scenario, the number of events when this saturation occurs is also very high. Based on these observations, this scenario was chosen as the critical scenario for Niagara Falls.

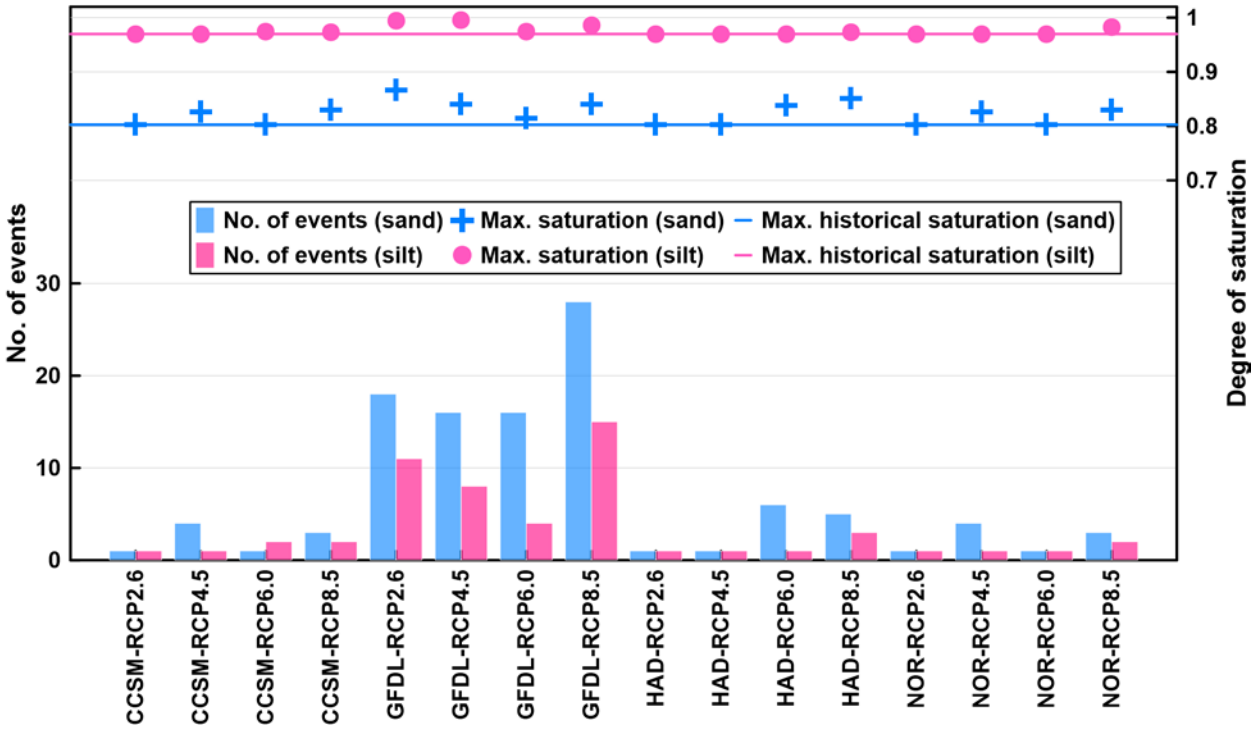

Figure 4.20 Maximum degree of saturation and frequency of high saturation occurrence in sand and silt material for Niagara Falls

Similar to Niagara Falls analyses, some analyses were also carried out for the nine other locations, which are available in Appendix C. Comparing the results for all locations shows that Kenora is the location with the largest increase in the saturation of the sand material. The city of Windsor appears to be the only location that the saturation for sand is above 90% for multiple climate

change scenarios, and even it is approximately equal to 100 % for one of the scenarios. For silt material, all locations would have a degree of saturation close or equal to 100% except Thunder Bay, with a saturation of 97%. Other notable observations are that the smallest increase in the future saturation relative to the maximum value in the historical period for the sand material would occur in the cities of Kingston and Niagara Falls for the selected scenarios; while, Toronto would have the smallest increase in saturation for the silt material.

Regarding the number of events for the selected scenario, London is the location with the most significant increase in the number of events for sand, while Windsor is the location with the lowest increase based on the selected scenario. On the other hand, Niagara Falls is the location with the lowest number of events for silt material, while Thunder Bay shows the greatest number.

Figure 4.21 and Table 4.2 present the summary of selected scenarios of all locations. It can be observed that climate scenarios under GCMs Had GEM and GFDL with RCP 8.5 have more potential to create the wettest conditions in the soil embankments compared to other GCMs and RCPs.

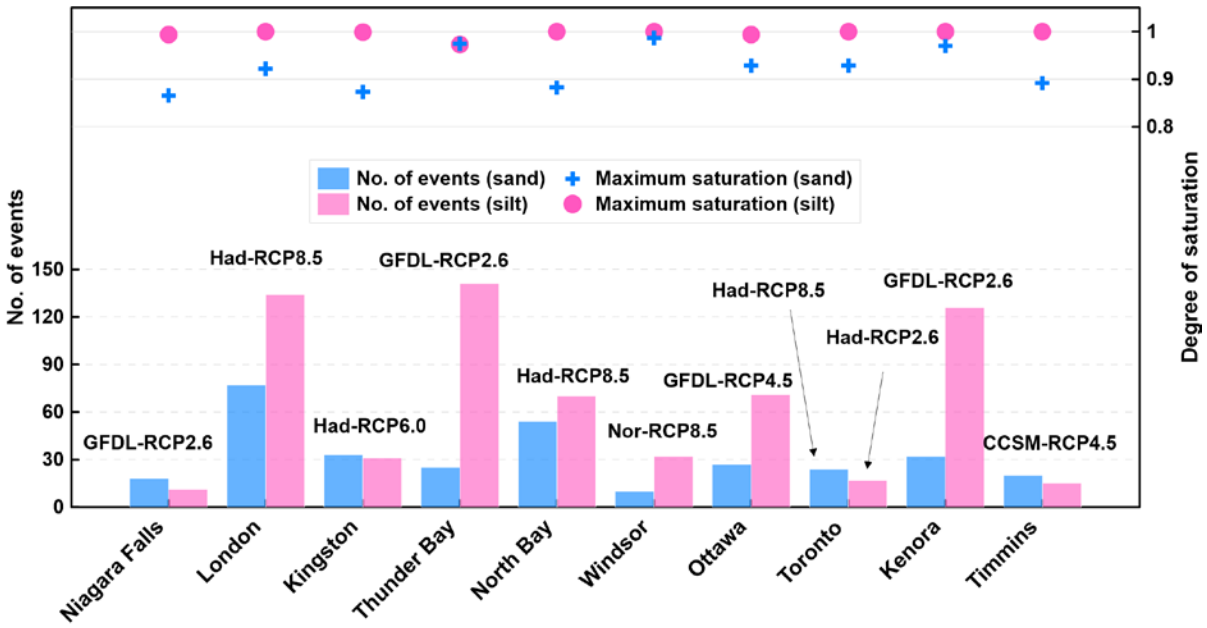

Figure 4.21 Result of analyses to determine the design climate for all locations

Table 4.2 Selected scenario for long term simulations of all locations

Location	Max. historical saturation (%)		Selected scenario				Increase in saturation (%)		No. of events	
			Sand embankment		Silt embankment					
	Sand	Silt	GCM	RCP	GCM	RCP	Sand	Silt	Sand	Silt
Niagara fall	80.3	95.2	GFDL	2.6	GFDL	2.6	7.9	4.4	18	11
London	80.6	96.3	Had	8.5	Had	8.5	14.5	3.8	77	134
Kingston	80.5	97.5	Had	6.0	Had	6.0	8.4	2.5	33	31
Thunder Bay	77.6	90.8	GFDL	2.6	GFDL	2.6	25.5	7.2	25	141
North bay	79.9	97.6	Had	8.5	Had	8.5	13.2	2.5	117	70
Windsor	81.0	96.3	Nor	8.5	Nor	8.5	21.8	3.8	10	32
Ottawa	80.6	95.9	GFDL	4.5	GFDL	4.5	15.3	3.7	27	71
Toronto	78.0	95.6	Had	8.5	Had	2.6	19.0	1.4	24	17
Kenora	76.8	91.0	GFDL	8.5	GFDL	8.5	26.3	9.9	32	126
Timmins	79.5	96.5	CCSM	4.5	CCSM	4.5	12.2	3.6	20	15

4.4. Design climate for extreme events

The Intergovernmental Panel on Climate Change (IPCC) has reported that as a result of the changing climate, it is expected that the frequency and intensity of the extreme precipitation events in North America would increase (IPCC 2013). Rainfall intensity-duration-frequency (IDF) curves express the probability of occurrence of extreme precipitation in a region and are a practical tool for the hydrological design of infrastructure. In Ontario, IDF curves are used as one of the significant criteria for designing infrastructure subjected to storms by regulatory organizations such as the Ministry of Transportation (MTO), Ministry of the Environment (MOE), Conservation and Parks, and Conservation Authorities (Coulibaly et al. 2016 and Switzman et al. 2017).

For assessment of climate change impact on future IDF curves, a baseline climate consisting of 30 years of historical climate data (i.e., 1981-2010) was considered as the datum in this research. Historical IDF curves for the province of Ontario can be obtained from Environment Canada

(Environment and Climate Change Canada 2014). Future IDF curves for Ontario are available from two different sources. Ministry of Transportation, Ontario (MTO 2018), and Ontario Climate Change Data Portal (CCDP 2018) provide future IDF curves for the province using different methodologies. Intensity-duration-frequency (IDF) curves by MTO have been developed by spatial and temporal interpolation techniques based on statistics of several weather stations within 150 km of Ontario (MTO 2018). Ontario Climate Change Data Portal provides future IDF curves for the province of Ontario based on both the fourth (AR4) and fifth Assessment Report (AR5) of the IPCC (IPCC 2007, IPCC 2013).

The IDF curves from CCDP have been developed based on two regional climate models, namely PRECIS and RegCM. They are driven by boundary conditions from the global climate model HadGEM2-ES considering three different emission scenarios, SRES A1Bfrom AR4, and RCP4.5, and RCP8.5 from AR5. Intensity-Duration-Frequency curves are available for the return periods of 2-year, 5-year, 10-year, 25-year, 50-year, and 100-year with durations of 5, 10,15, 30 minutes, and 1, 2, 6, 12, 24 hours (CCDP 2018). Figure 4.22 shows different sources that were used for compiling IDF curves for future climate.

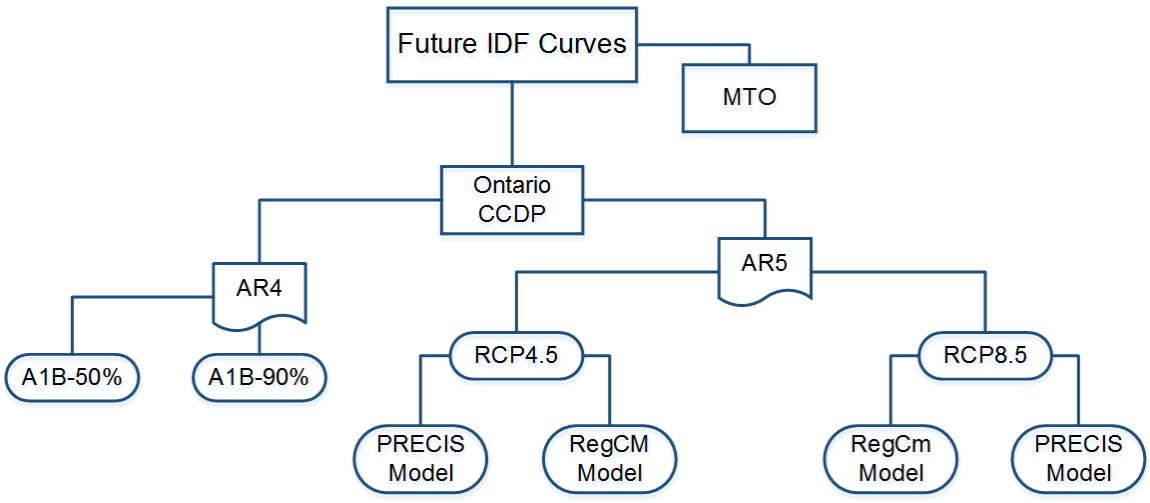

Figure 4.22 Future IDF Curves

4.4.1. Design IDF curves for Ontario

A review of both MTO and CCDP future IDF curves of all ten locations indicated that the most significant increase in future extreme precipitation is expected to occur during the last 30 years of this century (i.e., 2071-2100). Therefore, predicted IDF curves for this period were considered in the current study. The future IDF curves from CCDP and MTO for the city of Niagara Falls are shown in Figure 4.23, and Figure 4.24 shows the difference between the precipitation intensities for 60-minute and 24-hour durations. It can be observed that intensities for the A1B scenario for the 90^{th} percentile are the highest. The only exception is, that in some instances, for durations less than 10 minutes, and shorter return periods of 2 and 5 years, the MTO predicted IDF curves report slightly higher values than IDF curves from CCDP for the A1B scenario for the 90^{th} percentile. However, if emission scenarios from the latest assessment report (AR5) and the predictions from MTO are considered, the following observations can be made:

- For the majority of cases, the predictions from RCP8.5-RegCM predict higher intensities;
- For the 60-minute duration, the predictions for RCP8.5-RegCM are higher in 62% of the instances; and
- For the 24-hour duration, the predictions for RCP8.5-RegCM are higher in 87% of the instances.

Based on the above observations and for the sake of brevity, future IDF curves from CCDP based on RCP8.5-RegCM were selected for the city of Niagara Falls to investigate the effect of extreme rainfalls on the slope stability.

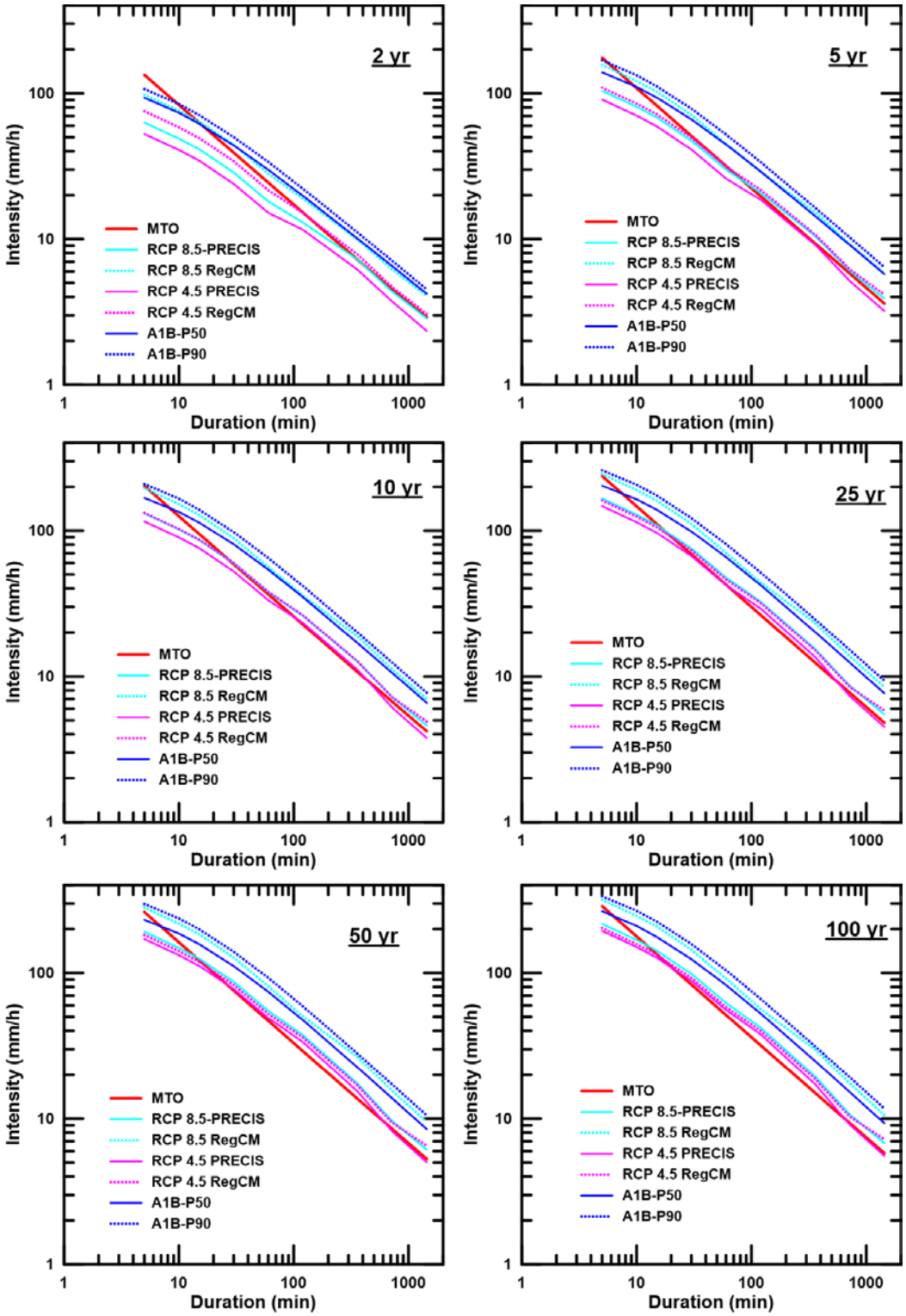

Figure 4.23 Comparison between future IDF curves-MTO (2085) and CCDP (2071-2100)

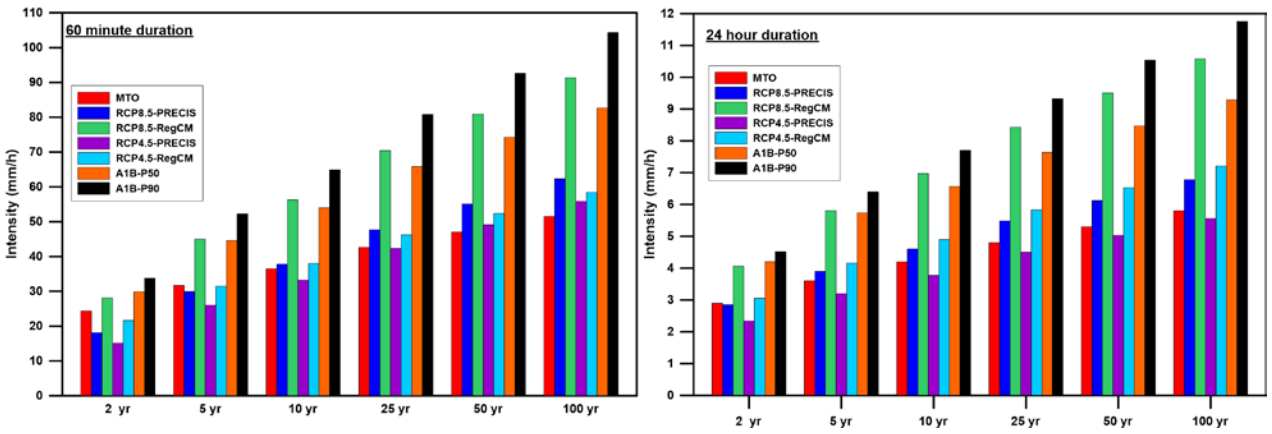

Figure 4.24 Future precipitation intensities for 60 minutes and 24 hours duration for the city of Niagara Falls

A similar evaluation was carried out for the other nine other locations across Ontario. Similar to the assessment for Niagara Falls, it was observed that the future IDF curves from CCDP for the A1B-P90% scenario predict higher intensities than all the other IDF curves for most durations and return periods. Also, for AR5, the predictions from RCP8.5-RegCM predicted higher intensities in most instances. Figure 4.25 shows the percentage change in intensities between the future predictions under RCP8.5-RegCM and the historical period for return periods of 2, 10, and 100-year intervals and durations of 1, 6, and 24 hours for all locations. This figure illustrates that a higher percentage change for most locations can be observed for 6- and 24-hour durations. It also shows that apart from the city of Kenora, the intensity of the extreme events is expected to increase for all other locations. The highest increase can be observed for Niagara Falls, where the 24-hour storm with the return period of 100 years could potentially increase in intensity by around 160%. It can also be observed that even for a one-hour rainfall event with a 2-year return period, a potential future increase of 30% can be expected. A similar observation can be made for the city of Kingston, where 24 hr storms with return periods of 2, 10, and 100 years could have an intensity

increase of around 120%. It is also worth noting that for both of these cities, a substantial increase in intensities for 1-hour and 6-hour storms is also predicted.

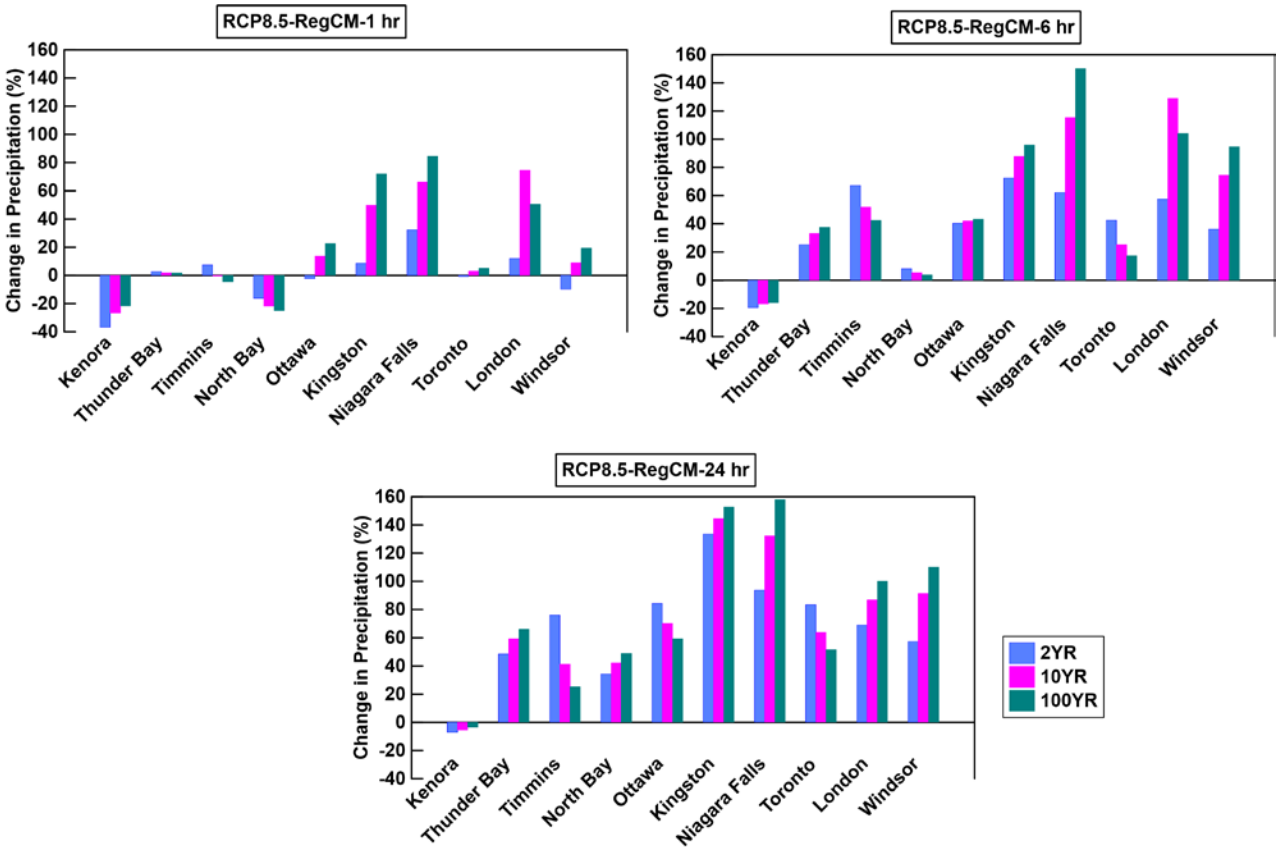

Figure 4.25 Percentage change in precipitation for 2071-2100 based on RCP8.5-RegCM

The predicted extreme precipitation intensities for all locations for the period 2071-2100 are shown in Figure 4.26. This graph shows that Niagara Falls would experience extreme rainfalls with higher intensity compared to other locations. For instance, this city would face rainfall with a 30 mm/hr intensity over 6 hours with a return period of 2 years.

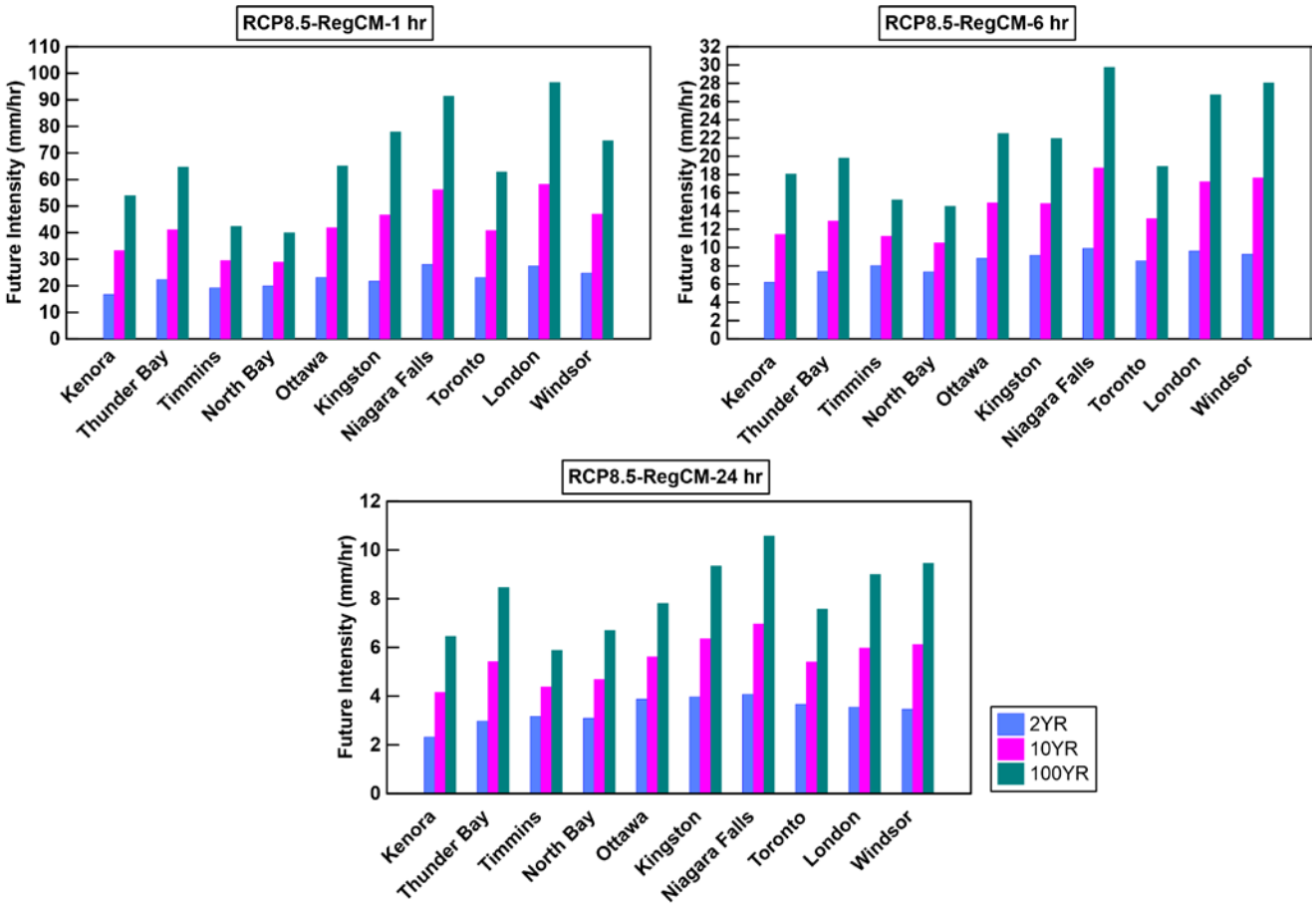

Figure 4.26 Extreme precipitation intensity for 2071-2100 based on RCP8.5-RegCM

Chapter 5: Model Setup for Numerical Modelling of Long-term Variation of Slope Moisture Conditions

Extreme precipitation events have the potential to destabilize manmade and natural slopes leading to slope failures. The destabilization effect depends on not only the intensity and duration of the extreme precipitation event but also the incipient soil moisture conditions within the slope at the onset of extreme events. For example, an initially dry slope can remain stable under high intensity and long duration extreme precipitation events. However, an event of similar intensity and duration can cause slope failure in a relatively wet slope. Therefore, a reasonable estimation of the slope's initial moisture condition just before the occurrence of the extreme event is required to assess their stability during the extreme precipitation events. In this part of the research, the estimation of long-term variation of slope moisture conditions was considered based on the time history of soil-atmosphere interactions.

Due to continuous exposure to the environment, slope moisture conditions are continuously affected by climate variables such as precipitation and evaporation. Consequently, an appropriate soil-atmosphere model is required to evaluate the water balance at the surface of embankments. This model should be capable of simulating two-dimensional variably saturated flow to determine the pore water pressure distribution within the embankment over time.

In this research, HYDRUS 2D (Šejna and Van Genuchten 2018) was employed for analyzing the long-term variation of slope moisture conditions. This software is capable of simulating the movement of water, heat, and multiple solutes in variably saturated media using finite element methods. Further, HYDRUS 2D also supports a soil–atmosphere boundary to estimate actual evaporation and the resulting influx of meteoric water into the embankment surface. HYDRUS 2D is computationally efficient and is capable of running long-term simulations in manageable time frames in an efficient manner (Pk et al. 2018).

For each location, thirty years of historical climate data and ninety years of future climate data based on the selected scenario for that location (see Chapter 4) were used for soil–atmosphere modelling of embankments with two different materials. An innovative approach was employed to generate sub-daily data for the soil-atmosphere boundary in the HYDRUS 2D model. The results included a spatial and temporal variation of moisture distribution within the embankment. Then, statistical analyses were conducted on the daily variation of average water content in the slope area. Based on the results, average and extreme slope moisture conditions were estimated for sand and silt embankments across Ontario.

5.1. Geometry and material

The embankment profile considered in this study represents a typical highway embankment in Ontario. Since the problem is symmetrical, only one-half of the domain, as shown in Figure 5.1, was simulated. The height of the embankment was considered to be 8 m. This height is the maximum allowable height for an earth-fill embankment without a berm in Ontario (OPSD 202.010). Side slopes of the embankment are 2H:1V, and a 3 m wide unpaved shoulder was considered at the top of the embankment. The distance between the slope toe and the right side of the model was set to be more than three times the height of the slope to minimize the influence of the side boundary condition (Rahardjo et al. 2010).

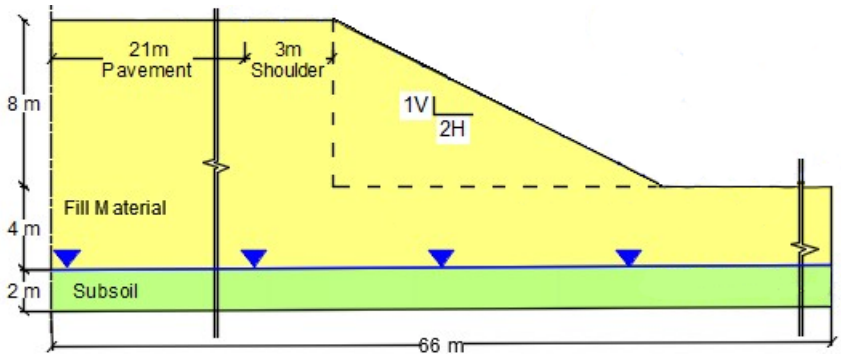

Figure 5.1 Design profile of the highway embankment

Two types of material have been considered in this study, silty sand and sandy silt, which are named sand and silt, respectively, after this. The hydraulic and geotechnical properties of these materials have already been presented in Chapter 3.

5.2. Finite element mesh

The finite element mesh in Hydrus 2D models was constructed by dividing the flow region into the quadrilateral and triangular elements. The program automatically subdivides the quadrilaterals into triangles, which are then treated as sub-elements (Šimůnek and Šejna 2018). The finite element mesh used in this study is shown in Figure 5.2. The global element size was targeted to be around 1 m. However, smaller mesh dimensions were considered at locations where large hydraulic gradients were expected. For instance, the finer mesh was generated in unpaved soil surface areas and the slope surface to provide an appropriate resolution within the infiltration zone. The mesh consists of a total number of 11146 elements.

It should be noted that the calculation of slope moisture content in this study was based on the water volume within the slope area, which is highlighted by red lines in Figure 5.2. Therefore, a corresponding sub-domain was considered in the mesh generation.

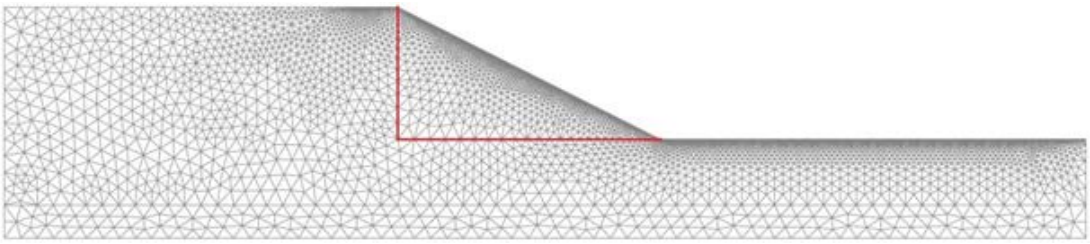

Figure 5.2 Finite Element Mesh used in HYDRUS 2D simulations

5.3. Boundary condition

The boundary conditions adopted in the finite element models are shown in Figure 5.3. A no-flow boundary was assigned to the left side and bottom of the domain. At the right-hand boundary, the

groundwater table was considered using a constant head boundary. At the top of the embankment, a no-flow boundary condition and soil-atmosphere boundary condition were assigned for the pavement and unpaved areas, respectively. Then, the runoff from the pavement was distributed over the soil embankment using the appropriate method described in section 5.4.

Thirty years of historical climate data and ninety years of future climate data based on the selected scenarios were considered as the soil-atmosphere boundary. Also, since the desired climate data is only available at the daily temporal resolution, an innovative approach was used to estimate sub-daily precipitation and potential evaporation data based on regional IDF curves. The details of this approach are presented in Section 5.6.

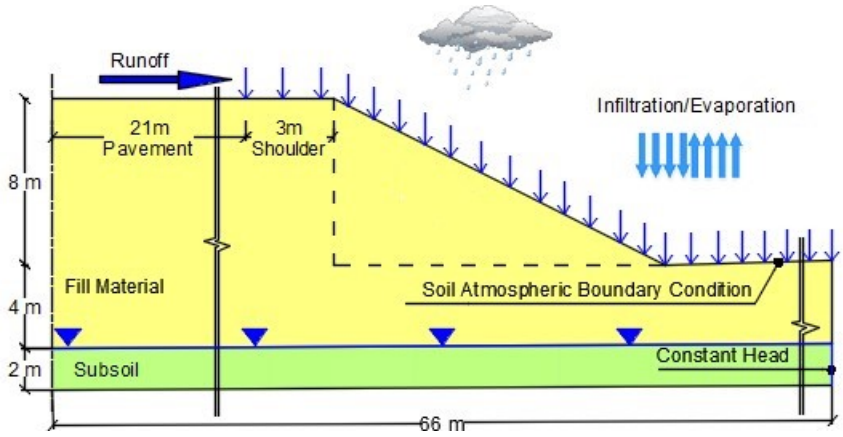

Figure 5.3 Boundary conditions of the embankment

5.4. Effect of pavement

The pavement surface is usually considered impermeable, and therefore a no-flow boundary condition can be used to model the pavement in numerical models of flow. The accumulated water at the paved surface can be modelled as runoff and distributed over the permeable part of the embankment adjacent to the impermeable pavement. It is essential for a conservative assessment of water balance at the ground surface (Pk 2017). This method has been successfully applied before by Coutinho et al. (2016) and Pk (2017) for simulating impervious materials in hydrological

models. The intensity of the rainfall imposed on the soil embankments (I_{SE}) is the actual rainfall intensity (*Irain*) increased by the ratio of the total length of paved area of the embankment (*TLE*) to the total length of the embankment (*TLSE*). Equation 5.1 shows total rainfall applied on unpaved areas of embankment:

$$I_{SE} = Irain \left(\frac{TLE}{TLSE} + 1 \right) \quad (5.1)$$

5.5. Initial conditions

The initial condition can affect the moisture content and pore water pressure in the embankment, which can influence the stability of the slope. In this study, several simulations were done to investigate the effect of initial condition on the moisture condition of the slope area. Comparison between the results of simulations with the hydrostatic condition above the water table and different initial conditions implied that since the simulations were run for 120 years, the effect of initial condition on the moisture condition of the slope area diminishes after a short period. Therefore, the hydrostatic condition above the water table was assumed as the initial condition for all 2D unsaturated flow simulation.

5.6. Climate data

Generally, historical and future climate data such as precipitation is only available at daily temporal resolution. However, previous research has shown that water entering the ground estimated by soil-atmosphere models is sensitive to the resolution of input climate data and can remarkably affect the performance of geotechnical structures (e.g., Pk 2017). Therefore, to have a realistic evaluation of the entering water, it is necessary to consider a sub-daily resolution for precipitation and potential evaporation.

5.6.1. Potential evaporation

Temperature is one of the main factors influencing the potential evaporation; therefore, it is reasonable to assume a distribution function for the potential evaporation during a day, which shows a peak in the middle of the day (warmest hours of a day). Fayer (2000) proposed a function for the distribution of potential evaporation based on this assumption. He considered that the potential evaporation value remains constant between the hours 00:00 to 06:00 and 18:00 to 24:00, and the total amount is about 11% of the total daily value. For the rest of the day, the distribution of the potential evaporation has a sinusoidal function. These functions are as follows and were used in this study:

$$T_p(t) = 0.24\overline{T_p} \qquad t < 0.264d\ ,\ t > 0.736d \tag{5.2}$$

$$T_p(t) = 2.75\overline{T_p}\sin\left(\frac{2\pi t}{1day} - \frac{\pi}{2}\right) \qquad 0.264d \leq\ t \leq 0.736d \tag{5.3}$$

Where $\overline{T_p}$ is the daily value of potential evaporation.

5.6.2. Precipitation

Some functions similar to the distribution of potential evaporation have been proposed for the daily distribution of precipitation (e.g., Simunek et al. 2009). However, since the actual duration of the precipitation can vary from a few minutes to hours, and it may occur at any time during the day, these functions might not appropriately represent the irregular nature of precipitation intensity and initiation. On the other hand, the intensity of the extreme precipitation events over a long period should be compatible with the intensity-duration-frequency (IDF) relationships. Given that IDF curves are estimated based on the long-term precipitation information for a region, using IDF curves for the generation of sub-daily data from an available time history of daily precipitation data is a viable approach. The probable number of rainfall events of equal duration with the intensities higher than a given value can be estimated from IDF curves. Further, as can be seen in

Figure 5.4, the general rule of IDF curves is that for a given duration, precipitation would be more intense as its frequency of exceedance decreases. In other words, for a constant duration, the intensity would increase as the return period increases (Musy et al. 2010). Considering these concepts, sub-daily data was generated based on the maximum precipitation value in the available daily data and using the well-known Sherman's equation (Equation 5.4) for the analytical representation of the IDF curves (Ghassemi, A. Personal communication, 2019).

$$i = \frac{kT^a}{(t+c)^b} \tag{5.4}$$

where *i* represents the intensity, T is the return period, t is the corresponding duration, and k, a, b, c are adjustment parameters which their values depend on the units considered for the other parameters.

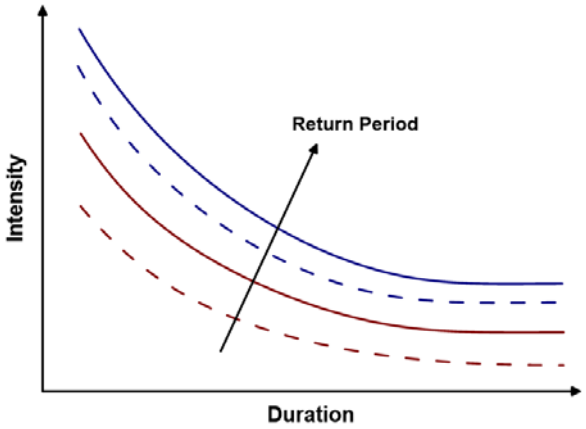

Figure 5.4 Schematic illustration of IDF curves, modified from (Musy et al. 2010)

5.7. Evaluation of moisture condition in the slope

Previous studies have shown that the factor of safety for slope stability is inversely related to the moisture content and depends on pore water pressure distribution (e.g., Pk 2017). In this research, the average degree of saturation within the slope area was calculated to assess slope moisture conditions. It was estimated by using cumulative water storage, which refers to the total amount of water in the slope area and is provided from Hydrus 2D results. Then, statistical analyses using

daily values of average saturation were conducted to determine the average and maximum moisture conditions in the slope to identify critical times at which pore water pressure (PWP) distribution puts the slope at risk because slope stability assessment for all times over the 120-year period is not practical. The results of slope stability analyses are presented in Chapter 6.

Using percentiles is common in hydrological studies. A percentile indicates the percentage of the distribution of degree of saturation below or equal to a specific value. In general, a percentile between 25 and 75 shows the normal value of the given data, a percentile higher than 75 (P75%) considered as above-normal value, and percentile P99% usually represents the extreme values. The values of historical and future daily degree of saturation of various percentiles for both sand and silt embankment in Niagara Falls are shown in Figure 5.5.

This figure shows that for intermediate percentiles (P50% and P75%), the historical data are slightly higher than the future. Conversely, the extreme saturation values (P99% and maximum) in the future are higher than historical. The differences between the historical and future data are more prominent in the sand rather than the silt embankment for the city of Niagra Falls.

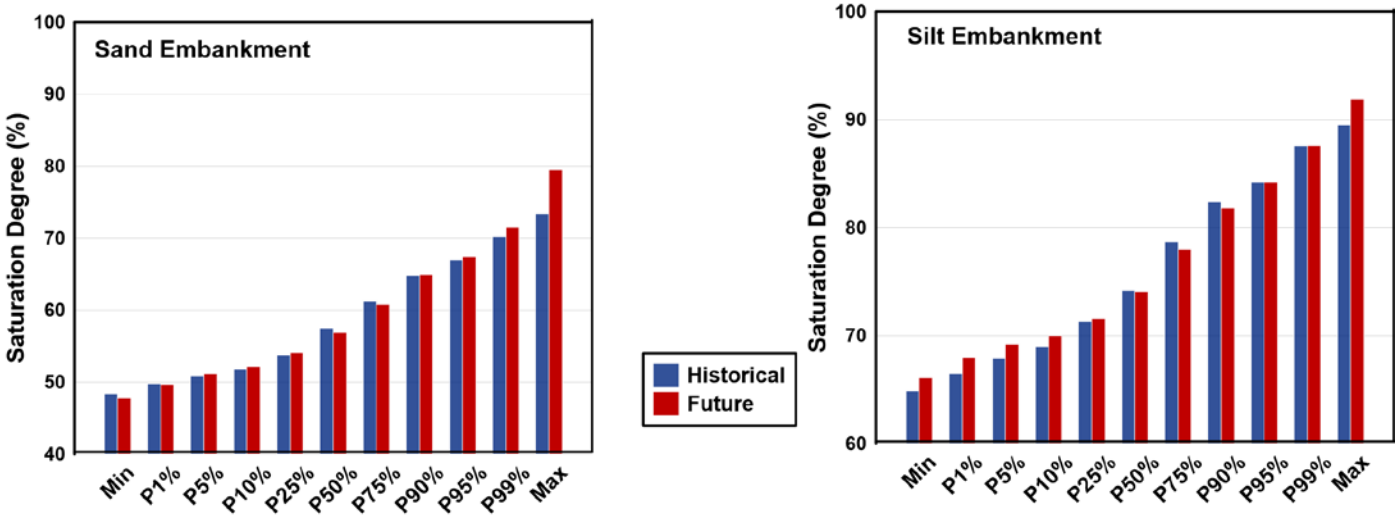

Figure 5.5 Historical and future saturation for sand and silt embankment in Niagara Falls

Figure 5.6 and Figure 5.7 illustrate the change in saturation of P50%, P75%, P90%, and maximum percentile in the future for sand and silt embankment, respectively. These figures indicate that the normal condition of slope moisture content (P50% or P75%) is not significantly influenced by climate change. It can also be observed that the degree saturation for the 90^{th} percentile would increase by around 5%. This observation is valid for both sand and silt slopes, for most instances, in the future time period. For the sand embankment, the extreme future degree of saturation could potentially increase up to 25% for some of the locations. However, for silt embankments, a 5% change in the future extreme degree of saturation can be expected for most locations.

In this research, degrees of saturation corresponding to the 50^{th} and 90^{th} percentiles (P50% and P90%) were considered as representatives for the normal range and above-normal range of saturation to define the initial conditions in slope stability analysis under extreme rainfalls. It should be noted that the P90% condition was favoured over maximum saturation because the occurrence of the extreme event at the time when the embankment is at maximum saturation is less probable.

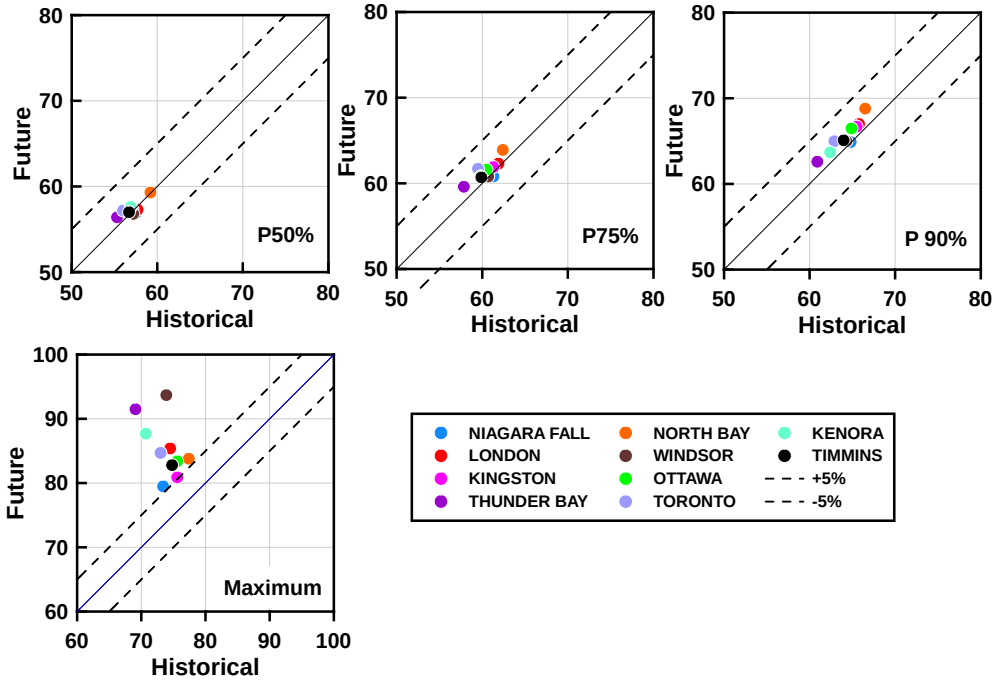

Figure 5.6 Comparison between historical and future saturation of various percentile in sand embankment for all locations

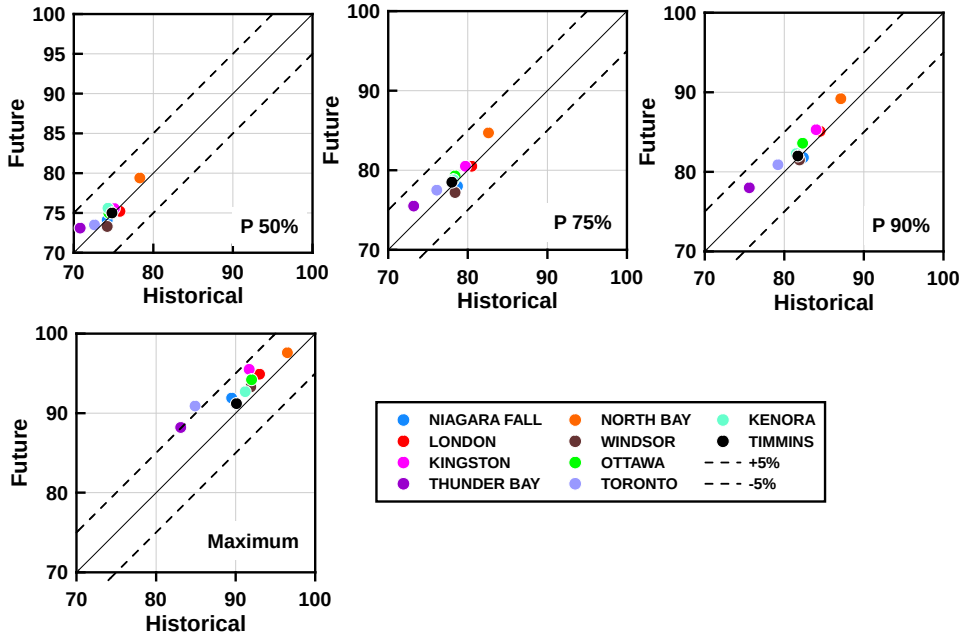

Figure 5.7 Comparison between historical and future saturation of various percentile in silt embankment for all locations

Figure 5.8 and Figure 5.9 show the degrees of saturation for 50th and 90th percentiles in different locations for sand and silt embankments, respectively. It can be observed from Figure 5.8, that for both historical and future time periods, the saturation of the sand embankment in North Bay is higher compared to all other locations, while Thunder Bay has the lowest values. This figure also shows that the maximum change in 50th and 90th percentile saturations for the sand embankment can be expected for the cities of Toronto and North Bay, respectively. Generally, it can be seen from this figure that the average saturation of sand embankment within the slope area is in the range of 55% to 70%.

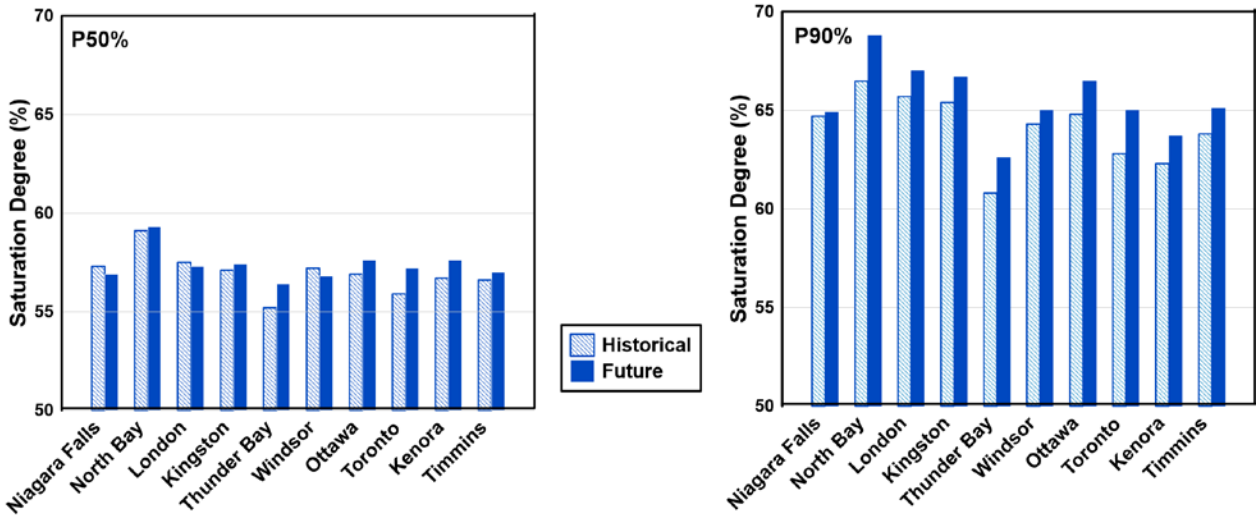

Figure 5.8 Historical and future saturation of P50% and P90% for sand embankment in different locations

According to Figure 5.9, similar to the sand, silt embankment has the highest saturation in North Bay and the lowest value in Thunder Bay for both historical and future time periods. The maximum change in the degree of saturation for P50% and P90% would occur in North Bay for both historical and future periods. Furthermore, the range of 70% to 90% for the degree of saturation in silt embankment can be observed from this graph.

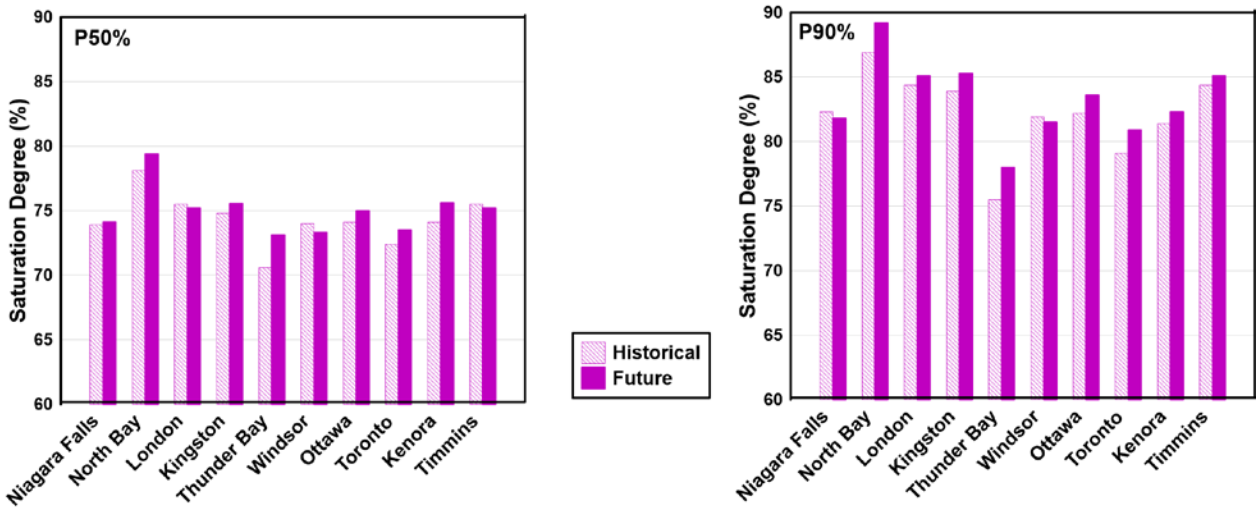

Figure 5.9 Historical and future saturation of P50% and P90% for silt embankment in different locations

Finally and most importantly, the answers to the following three main questions were pursued in this chapter:

- Is it more likely that for future extreme events, the initial conditions would be wetter?
- How does the saturation change in embankments during the historical and future climates?
- Is there a clear indication that some of the locations would see greater changes in saturation than then others?

Results presented above lead one to conclude that for some locations and certain percentiles, lower values of saturation in the future in comparison to historical conditions can be expected. However, in most instances, the future degree of saturation is expected to be higher than their historical counterparts. The most notable change in the future is expected for sand embankments for maximum saturation conditions. This change is expected for all the locations considered in this research. Of all the locations considered in this research, North Bay is expected to see large changes in the 50^{th} and 90^{th} percentile values of saturation.

Chapter 6: Slope Stability Analysis

As mentioned in the previous chapters, continuous exposure of the embankment to the environment can change the water balance in the embankment and affect the slope stability. Due to water seepage caused by meteoric conditions, the matric suction in the unsaturated soils could decrease, leading to shear strength reduction and subsequent slope instability (Fredlund and Rahardjo 1993; Rahardjo et al. 1995). Hence, it is necessary to consider the contribution of matric suction on the soil strength parameters in the slope stability analyses.

This study used limit equilibrium based software (SLOPE/W) using the Morgenstern-Price method (Morgenstern and Price 1965) for geotechnical models, and finite element seepage software SEEP/W for hydrological models. Both SLOPE/W and SEEP/W are modules of a software suite called GeoStudio (Geo-slope International Ltd. 2019) and are coupled. This coupling ensures that the factor of safety by SLOPE/W can be estimated for each time step for which pore pressure distribution is made available from the seepage assessment by SEEP/W. The factor of safety is defined as the ratio of available shear resistance along a potential plane of failure compared to the activating shear forces along the same plane.

6.1. Suction strength

From a classical soil mechanics perspective, lower shear strength is expected for fully saturated soils with positive pore water pressures. So, the increase in the degree of saturation could result in slope instability. For this reason, the average degree of saturation within the slope area was selected as the primary index to assess slope moisture conditions in this study, as discussed in Chapter 5.

Vanapalli et al. (1996) have proposed the following relationship for the shear strength of unsaturated soils:

$$\tau = c' + (\sigma - u_a)\tan\varphi' + [\frac{\theta-\theta_r}{\theta_s-\theta_r}](u_a - u_w)\tan\varphi' \quad (6.1)$$

where c' is effective cohesion, φ' is the effective angle of internal friction, and $(\sigma - u_a)$ and $(u_a - u_w)$ are the net normal stress and the soil suction, respectively. The second term of Equation (6.1) defines the suction strength of soils as:

$$\tau\_suction = [\frac{\theta-\theta_r}{\theta_s-\theta_r}](\ u_a\ \ -u_w)\tan\varphi' \qquad (6.2)$$

It can be seen from this equation that

the shear strength of unsaturated soils can be affected by the presence of negative pore water pressure (soil suction). Considering the presence of negative pore pressures within the embankment, the likelihood of instability due to soil-atmosphere interaction may either increase or decrease depending on the degree of saturation.

The contribution of suction in the soil strength for a range of soil saturation was estimated in the present study. For this purpose, the relationship between suction strength and degree of saturation can be estimated using the SWCC function by van Genuchten (1980) and equation (6.2). It should be noted that from a conservative perspective, it is desirable to not consider suction strength at low saturation (50% in this study). This can be accomplished by assuming a higher value of residual water content (θ_r) than the residual water content used in the SWCC function.

The relationship between saturation and suction strength, for the two soils considered in this research, is depicted in Figure 6.1. This figure shows that for both sand and silt, the maximum suction strength occurs around 70% saturation. From this figure, it is also quite clear that the contribution of suction in soil strength in silt is much higher than that for sand. It should also be noted that suction strength can play a significant role at shallower depths, as at these depths, changes in saturation due to atmospheric conditions are more prevalent.

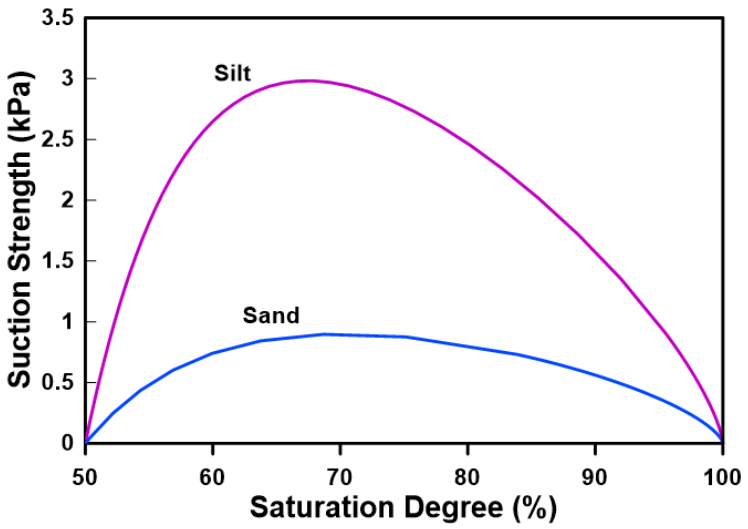

Figure 6.1 Relationship between saturation and suction strength for sand and silt materials

6.2. Types of slope failures

The slope instability may develop within the soil embankment as local, surficial (shallow), general, and deep-seated failure (Han et al. 2004). Figure 6.2 is a schematic of various failure types. Embankments are typically designed to satisfy a minimum factor of safety (FOS) against general (global) failures that would impact the operation of the roadway. On the other hand, the effect of soil-atmosphere interaction is more likely to induce shallow surface failures (Pk et al. 2018). Therefore, in this research, two types of failure were investigated. A minimum sliding mass depth can be defined in the limit equilibrium analyses to consider the depth of failure. In the present study, a minimum slip depths of 1m and 0.3m were assigned for general failure and shallow failure, respectively. The criterion for FOS is the allowable FOS of 1.3, which is recommended by MTO for the design of earth embankment slopes.

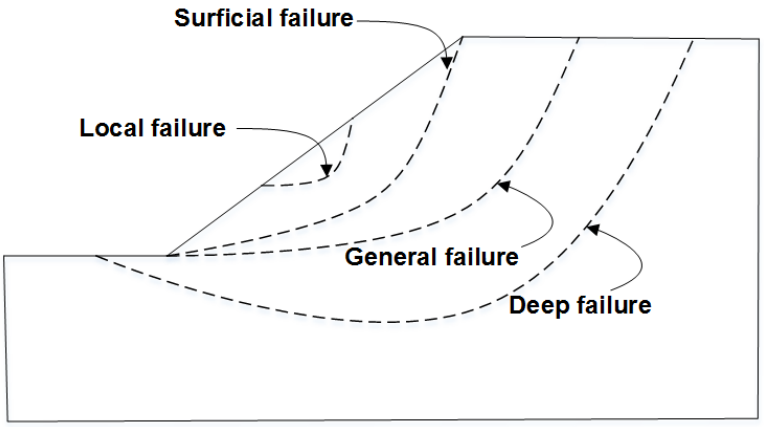

Figure 6.2 Potential slope stability failures modified from (modified from Han et al. 2004)

6.3. Long-term performance of embankments under changing climate

Slope stability assessment for all time steps over the 120 year period is not practical. Therefore, in this study, the results of statistical analyses on average saturation within the slope area were used for assessment of the long-term performance of slopes. The results of statistical analyses, presented in Chapter 5, indicated that the range of average saturation within the slope area is 55 to 70% for sand and 70 to 90% for silt embankments. Several spatial distributions of PWP within the embankments for the above-mentioned saturation range were exported from HYDRUS 2D to SLOPE/W to examine the values of FOS in the range of degrees of saturation mentioned above. The results are shown as the variation of the factor of safety over the degree of saturation in Figure 6.3 for sand and silt embankment. The reason for the different values of FOS for the same average degree of saturation can be attributed to the different spatial distribution of pore water pressure within the slope area. This is consistent with the observations that larger variation in FOS can be observed for similar saturation values in the sand embankment at a lower degree of saturation. This is related to the higher probability of differences in the spatial distribution of moisture in the sloped area at lower degrees of saturation.

Figure 6.3 also shows that for sand embankment, a rising trend in FOS with a degree of saturation from 55 to 70% can be seen. This trend is consistent with the variation of sand suction strength with saturation, as shown in Figure 6.1. On the other hand, the graph for silt embankment shows a decreasing trend in FOS with that increasing saturation. This is also consistent with the reduction in suction strength of silt with saturation in the range of 70 to 90%, which is consistent with the results shown in Figure 6.1.

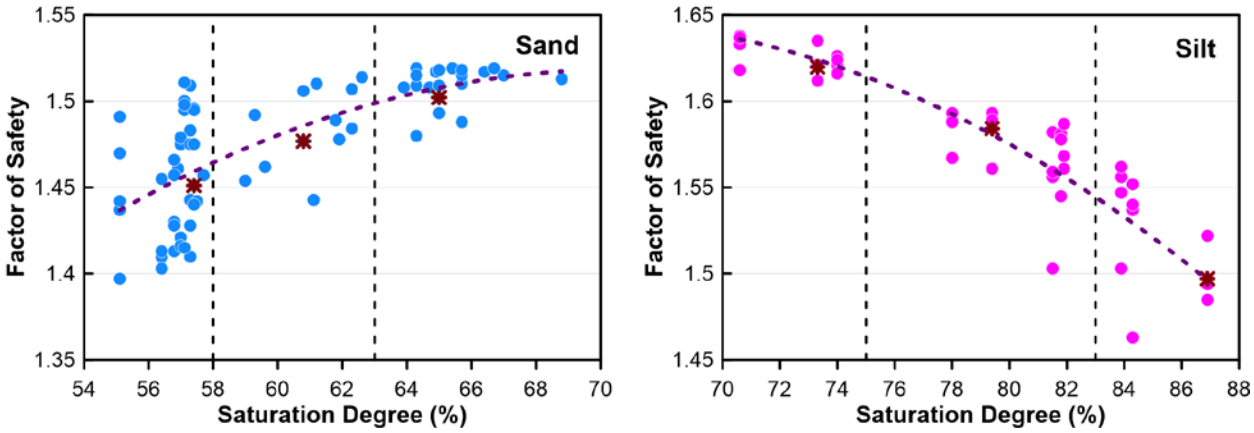

Figure 6.3 Variation of FOS with the degree of saturation in sand and silt embankment

6.4. Slope stability under extreme rainfall events

Assessment of slope stability during extreme events requires a hydro-geotechnical model in which the spatial distribution of pore water pressure from the hydrological model is consecutively introduced into the geotechnical model. In this study, SEEP/W and SLOPE/W have been used for the construction of coupled variably saturated flow and the limit equilibrium slope stability models.

It can be seen in Figure 6.4 that a finite element mesh containing 3761 nodes and a combination of 3551 quadrilateral and triangular elements was used in the SEEP/W models. A 1m global mesh was applied to the whole domain with 0.1m refinement along the flux boundary at the ground

surface. A no-flow boundary condition was applied at the pavement, on the left-hand side, and bottom of the embankment. At the right-hand side, the groundwater table was assumed at 4 m depth below the embankment surface, and the section above the groundwater table was considered as no flow. A flux boundary comprising of design storm records was applied at the soil-atmosphere interface. The details on the design storm are provided in section 6.4.2. A Non-ponding boundary condition was applied to prevent excessive accumulation of rainfall on the slope surface.

For the simulation of slope under extreme rainfall events, the evaporation was not taken into account. It is due to the fact that a large quantity of water is applied in a short period of 1 to 24 hours, and even the maximum evaporation over a 24-hour period is only a few millimetres. Therefore evaporation has a negligible effect on water balance on the ground surface during extreme rainfall events. This approach is similar to the one that has been used by Robinson et al. (2017) and Pk et al. (2018). It should also be noted that the initial conditions in the SEEP/W models were set up based on the long-term variation of moisture conditions within the slope, considering both participation and evaporation. This approach is explained in the following section. The hydraulic and geotechnical properties of the materials have already been presented in Chapter 3. The details of the SLOPE/W models are the same as explained in the previous sections.

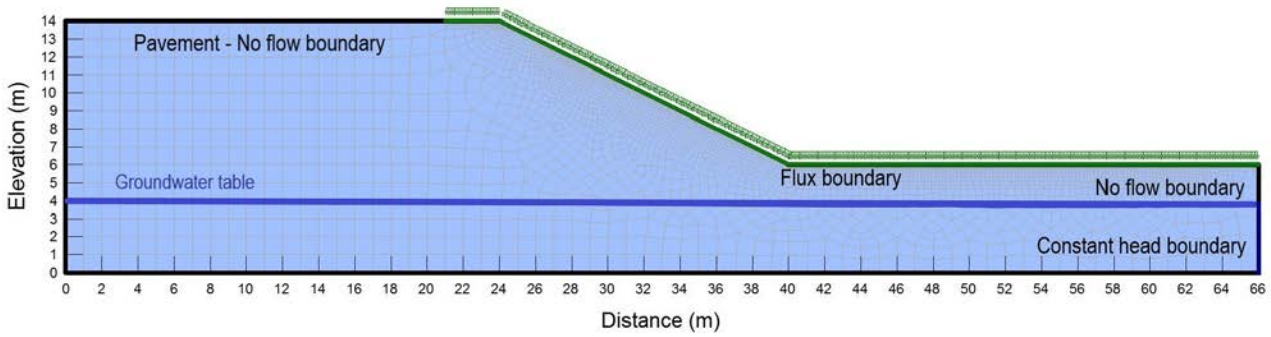

Figure 6.4 Meshing elements and boundary conditions for SEEP/W models

6.4.1. Initial conditions

It is a common practice to assume hydrostatic pore pressure distribution as the initial condition for the numerical simulation of a slope subjected to rainfall (Robinson et al. 2017). However, the hydrostatic conditions are a particular and rare case in reality at the field scale if it is under thermodynamic equilibrium (Lu and Godt, 2013).

In this research, the pore water pressure distribution corresponding to the saturation of P50% and P90% percentiles were considered as the initial conditions for slope stability analyses under extreme rainfalls. It should be noted that although different PWP distribution can exist for the same average saturation within the slope, this assumption is more reasonable than the hydrostatic condition, which does not commonly occur under average climate conditions.

According to Figure 6.3, the range of degree of saturation can be divided into three categories for each type of embankment for all locations under consideration and is presented in Table 6.1. This classification is based on the distribution of the FOS-Saturation relationship. A specific PWP distribution, as represented with a special symbol in Figure 6.3, was selected for each range of degree of saturation as the initial condition of stability analyses.

Table 6.1 Saturation classification for the initial conditions of slope stability analysis

	Degree of saturation (%)	
Category	Sand embankment	Silt embankment
1	≤ 58	≤ 76
2	58 - 63	76 - 83
3	≥ 63	≥ 83

The selected range of degrees of saturation for the initial conditions of slope stability assessments for sand and silt embankments in all locations can be seen in Figure 6.5. This figure shows that for

P50%, the initial condition for historical and future periods are in the same category. Additionally, all of them except the initial condition of North Bay is in the first category. On the other hand, as expected, all degrees of saturation for P90% are in the second or the third category. For most of the locations, historical and future degrees of saturation are in the same range, excluding Toronto and Kenora for the sand embankment and Thunder Bay and Ottawa for the silt embankment.

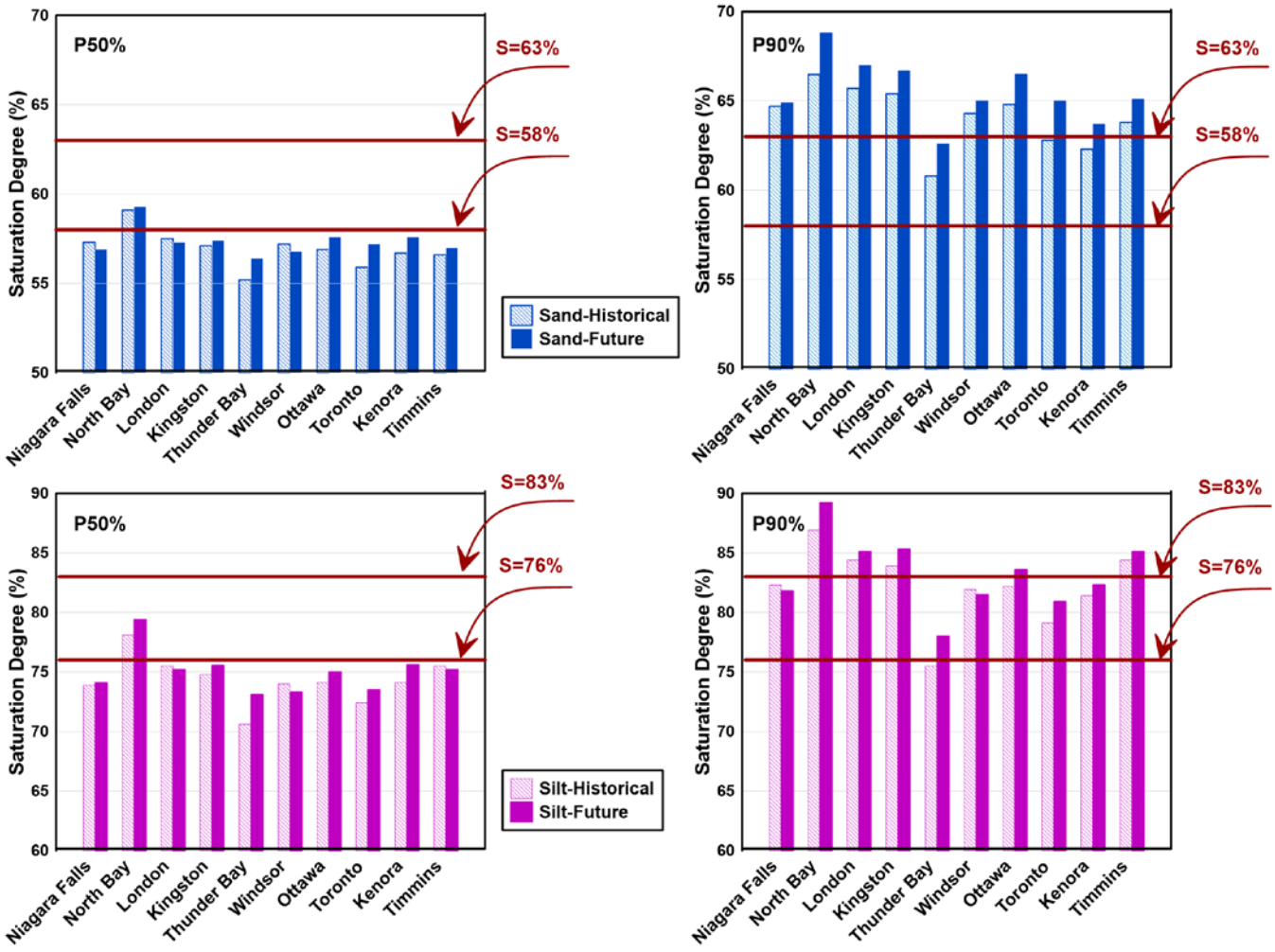

Figure 6.5 Status of saturation of all locations according to selected saturation categories

6.4.2. Atmospheric boundary conditions (Design storm)

Using an actual rainstorm (extreme rainfall) pattern is an ideal approach for hydrologic analysis (MTO 1997). However, actual storm records are not usually available for all locations. Also, such an approach is not feasible for studying the effects of future climate effects, as in most instances, the information on storm patterns is not available for future extreme events. Therefore, synthetic storm hyetographs were considered in this study. Several methods for generating design storm hyetographs have been reported in the literature (e.g., Prodanovic and Simonovic 2004, Yen and Chow 1980, and Watt et al. 1986). Some of these methods suggest a simple distribution shape, such as a rectangular hyetograph, for a single point of the IDF curve. For example, a uniform intensity throughout the rainfall duration is used for the establishment of a rectangular hyetograph (e.g., Prodanovic and Simonovic 2004). However, some hydrological analyses have demonstrated that this method underestimates the total precipitation volume of the rainfall events (Veneziano and Villani 1999). Geometric forms such as triangular hyetographs (e.g., Yen and Chow 1980) or linear/exponential hyetographs (e.g., Watt et al. 1986) are other options for hyetograph that have been proposed and have been used in previous studies. However, there are other different methods that consider the entire set of intensity-duration values for a particular return period and duration instead of a single point on an IDF curve (Keifer and Chu 1957 and USACE 2000). Among these methods, the method proposed by Keifer and Chu (1957), known as the Chicago design storm, has been widely used in the Canadian practice because it can be derived from available rainfall IDF relationships (McKelvie 1982, Marsalek and Watt 1984). This method has also been recommended by the Ministry of Transportation, Ontario, for the assessment of the storm impacts on the drainage systems (MTO 1997). In the current study, this method was used to represent intensity distribution over time for historical and future extreme rainfall events.

Figure 6.6 is an example of the design storms developed based on future IDF curves for 1-hour duration rainfall with the 100 years return period for the city of Niagara Falls. Historical and future design storms of all ten locations under consideration were developed for 1, 6, 24, and 48-hour durations with return periods of 2, 5, 10, 25, 50, and 100 years.

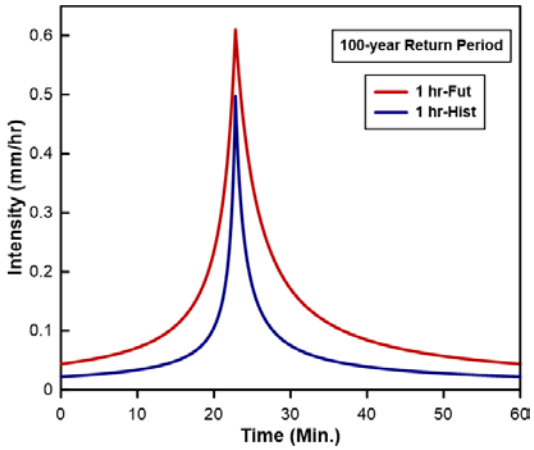

Figure 6.6 Sample Chicago curve for a 1-hour extreme rainfall for the city of Niagara Falls

6.5. Results and discussion

6.5.1. Variation of FOS over extreme rainfall

In this study, the effect of climate change on the stability of slopes subjected to extreme events was evaluated based on the critical (minimum) FOS overtime. For this purpose, the variation of FOS under historical and future rainstorms with six different return periods of 2, 5, 10, 25, 50, and 100 years was quantified. The stability of the slope was investigated for sand embankment under 1, 6, and 24-hour rainfall durations. On the other hand, since the extended rainfalls can make the low permeable soil embankment more vulnerable (Pk et al. 2018), 6, 24, and 48-hour durations were selected for stability assessment of silt embankments. For all cases, the simulations were continued beyond the duration of the rainfall event to ensure that the minimum FOS was obtained.

Figure 6.7 presents the variation of global FOS of sand embankment overtime under 1, 6, and 24-hour historical and future rainfalls for 1m minimum slip depth. These results are for the city of Niagara Falls. The graphs on the left demonstrate the variation of FOS with initial condition corresponding to P50%, and the graphs on the right correspond to initial conditions of P90%. Comparing these two sets of graphs for the general failure condition shows that the initial FOS for P90% is higher than P50%. One of the reasons could be the influence of water content on soil suction strength, as explained in section 6.1.

Observation of temporal FOS for global failure in the slope also shows that for 1-hour rainfall, there is a very minimal adverse effect on the FOS. The slight increase in FOS can be related to an increase in the water content and positive effect of PWP on the suction strength compared to the fairly dry initial condition. Additionally, this figure also shows that no reduction in FOS was observed for P50% initial conditions under 6-hour historical rainfalls. However, under 6-hour future rainfall, FOS decreases for P90% initial condition, although it is not a substantial decrease. It can also be observed that the factor of safety for 24-hour rainfall remains constant at the beginning of the rainfall event, but at about 10 hours into the 24-hour rainfall event, the FOS starts to decline. This reduction is more noticeable for future extreme rainfalls as opposed to the historical case, especially for P90% initial conditions.

Similar to Figure 6.7, Figure 6.8 shows the variation of global FOS of sand embankment overtime under different historical and future extreme rainfalls with the difference that this figure is for 0.3m minimum slip depth. This figure indicates that the reduction in FOS is higher and can be observed at earlier times, in comparison to the 1m minimum slip depth. This is not surprising as the shallower depth is expected to see larger changes in moisture contents over a shorter period of

time. Therefore, it can be concluded that the shallower depth of the slope is more affected by extreme rainfalls.

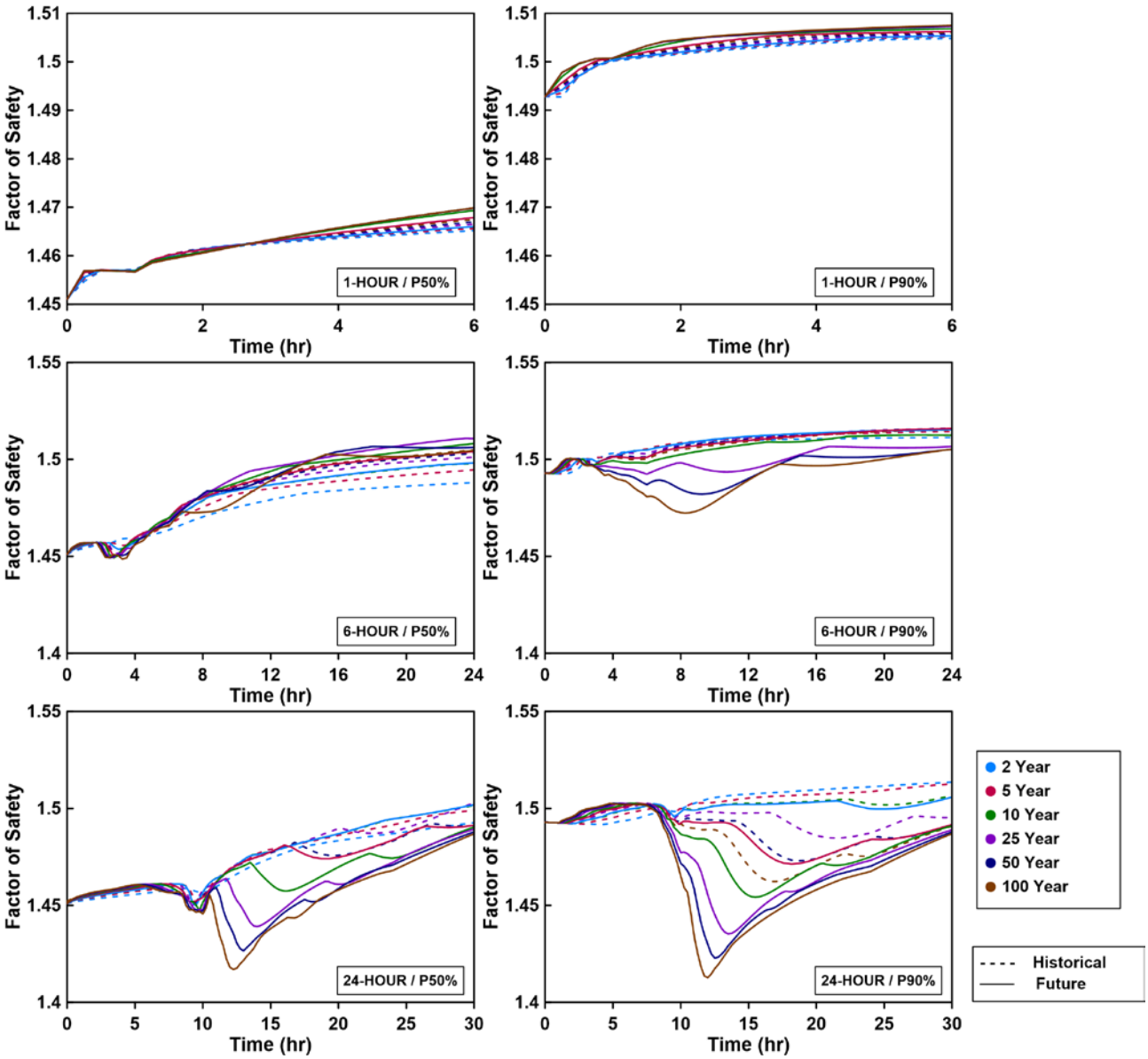

Figure 6.7 Temporal variation of FOS in the sand embankment for historical and future rainfalls with different return periods considering 1m minimum slip depth

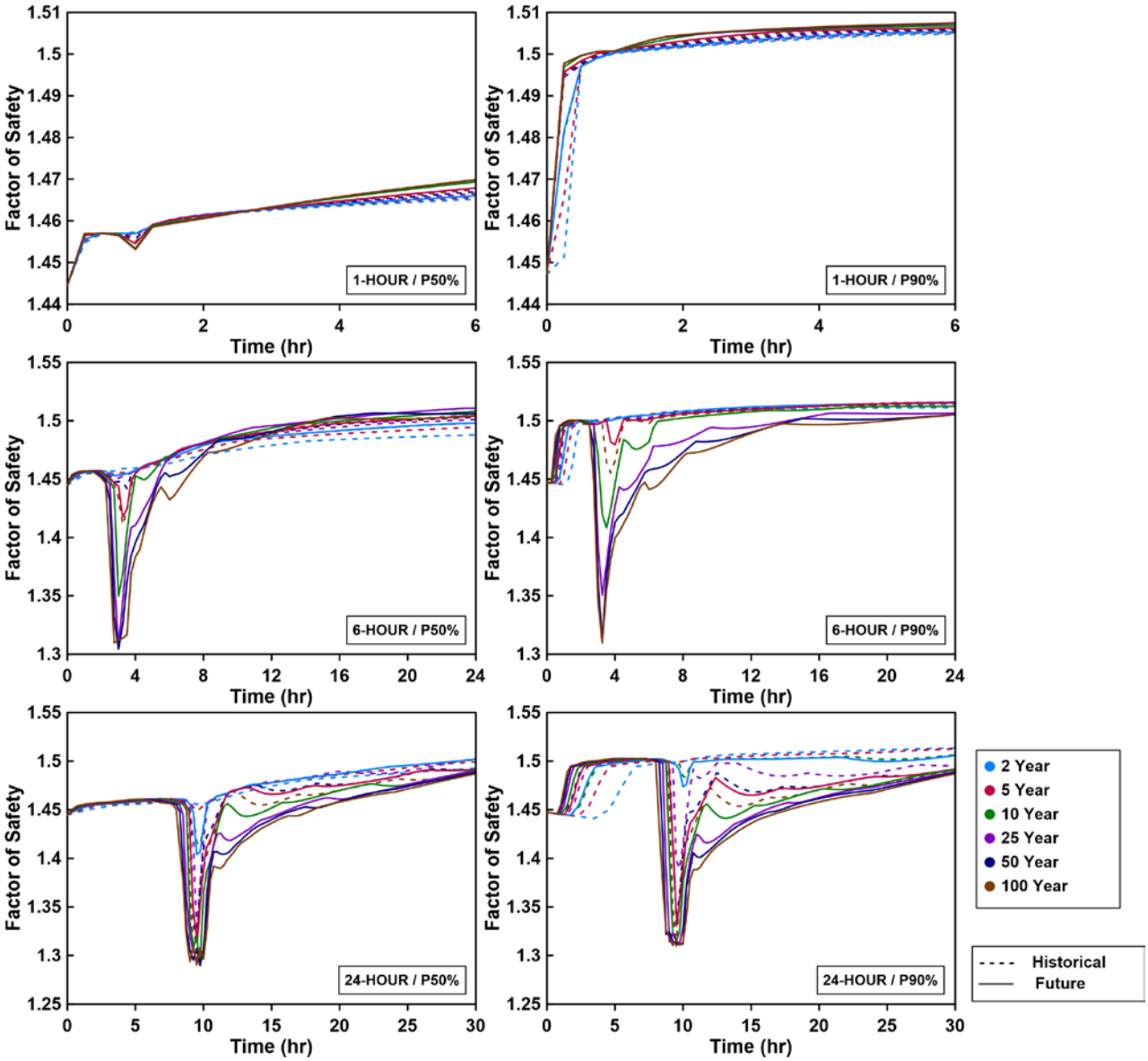

Figure 6.8 Temporal variation of FOS in the sand embankment for historical and future rainfalls with different return periods considering 0.3m minimum slip depth

Figure 6.9 and Figure 6.10 show the temporal distribution of FOS in silt embankment for historical and future rainfall of various durations. The results are of the city of Niagara Falls, for 1 and 0.3m minimum depths of failure, respectively. Similar to Figures 6.7 and 6.8, the graphs on the left are for P50% initial conditions, while on the right are for P90% initial conditions.

It can be observed from both the figures that 6-hour rainfall events do not influence the stability of the silt embankment for both types of failure. It can be inferred from Figure 6.9 that 24-hour rainfall would not change the PWP significantly for the minimum depth of 1m of the slope, with lower initial saturation. However, it can induce a moderate decline in FOS of the slope with a wetter initial condition, especially for future events, as the rainfall intensity is expected to be higher than the historical period. Additionally, it can be seen in this figure that the 48-hour rainfall reduces the FOS, even for P50%initial condition. It can also be observed that for wetter initial conditions (P90%), the reduction in FOS is more drastic. On the other hand, Figure 6.10 shows that in comparison to 1m depth, shallower depth of 0.3m is more adversely affected by 24-hour rainfall. This observation is valid for both P50% and P90% initial conditions. Similar observations can also be made for 48-hour rainfall events. This rainfall reduces the factor of safety in the silt embankment significantly and keeps the embankment remains in this critical condition for a longer time compared to other cases. Overall, it is evident that FOS reduction happens at earlier times for 0.3 m than for 1.0 m depth. This leads one to conclude that shallower depths seem to be more prone to the effects of climate change. Another point that can be inferred from comparing the graphs for sand and silt embankment is that reduction in FOS happens at later times in silt, which is consistent with the low permeability of silt compared to sand.

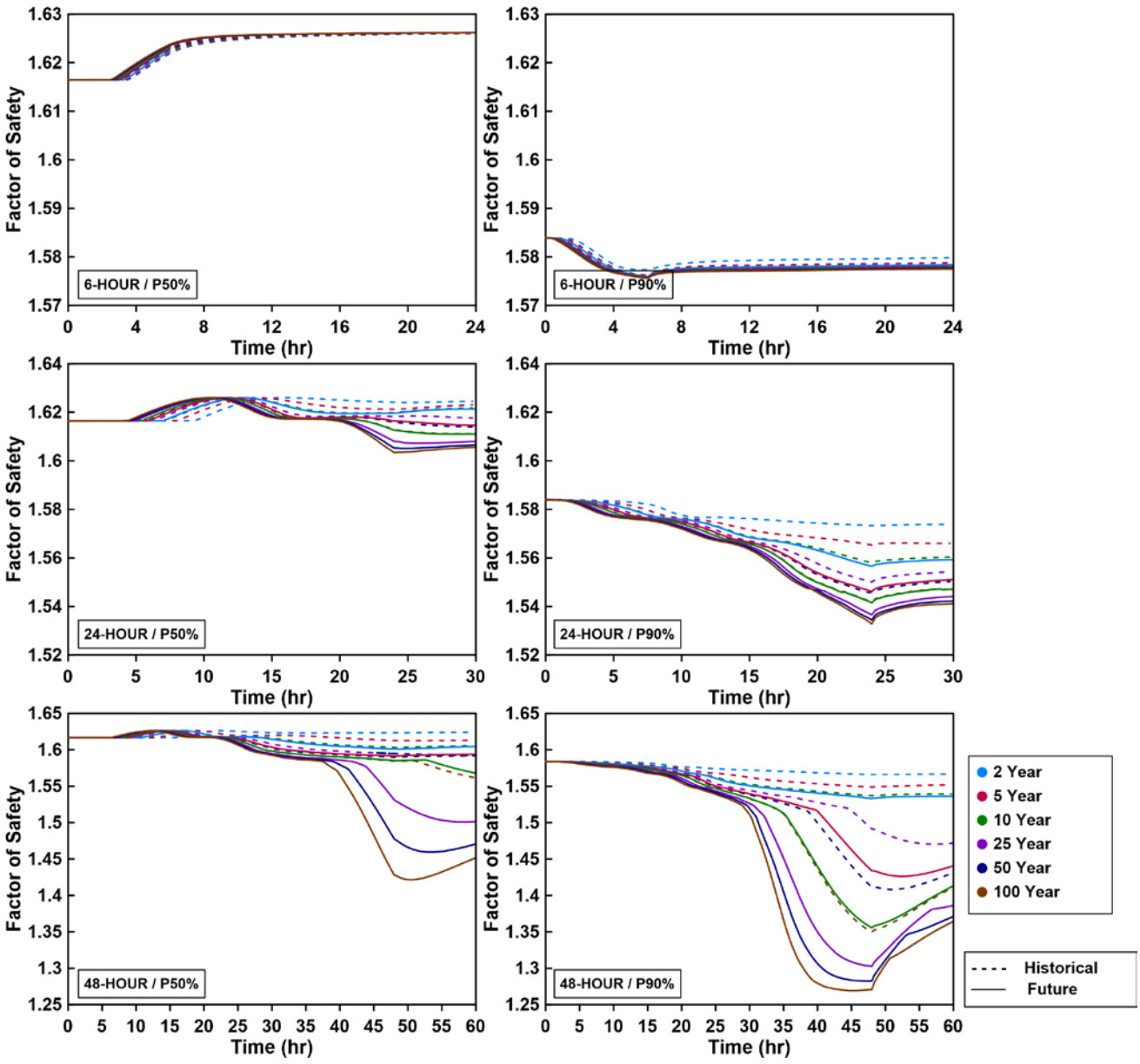

Figure 6.9 Temporal variation of FOS in the silt embankment for historical and future rainstorms with different return periods considering 1m minimum slip depth

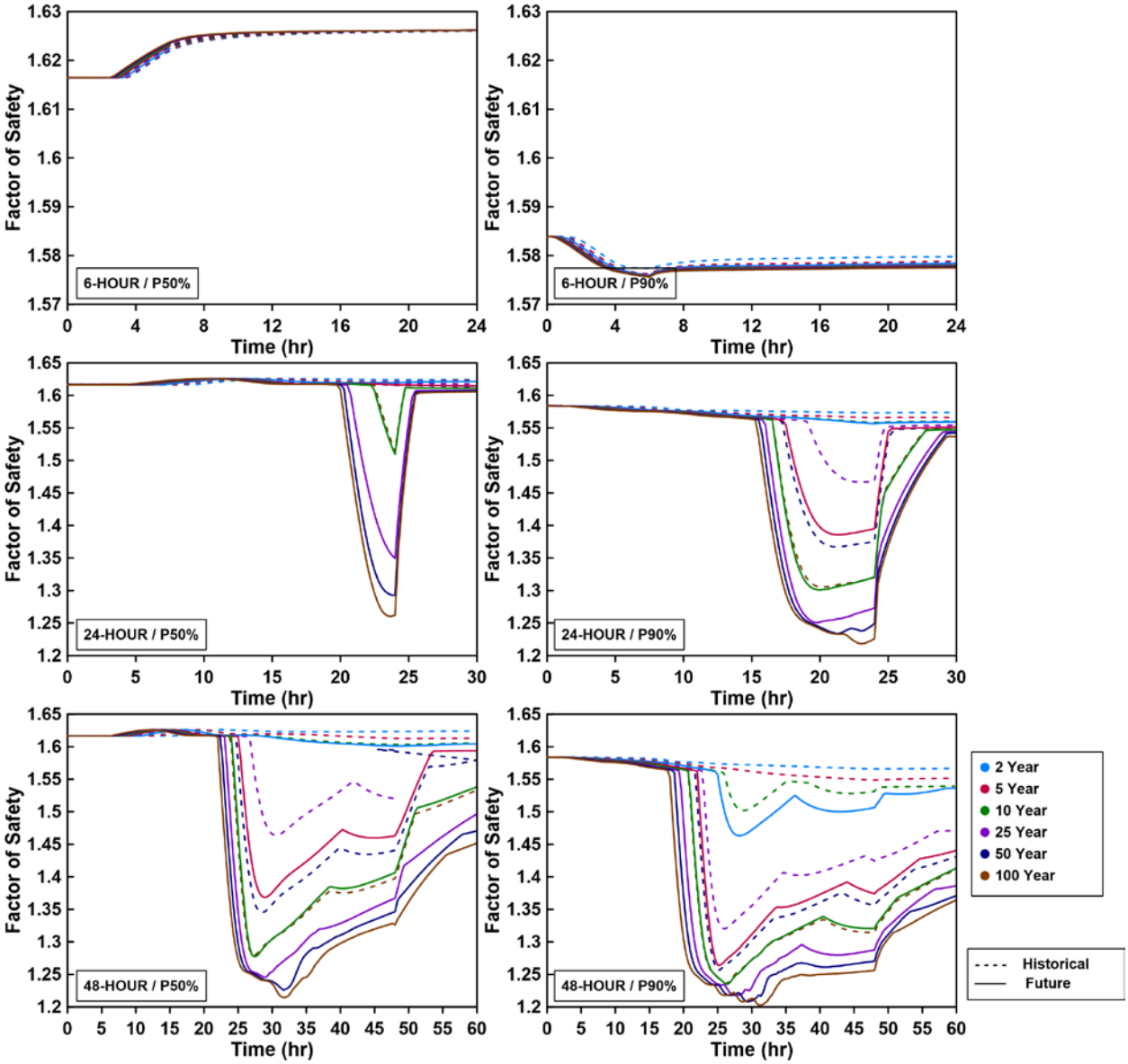

Figure 6.10 Temporal variation of FOS in the silt embankment for historical and future rainstorms with different return periods considering 0.3m minimum slip depth

Based on the review of the results presented in Figure 6.7 to Figure 6.10, it can be concluded that the extreme rainfalls with shorter return periods have less effect on the FOS, with rainfalls of 2-year return periods having no effect at all. Moreover, it can be concluded that in some instances, the FOS for both sand and silt embankments come close to the allowable value of FOS. However, two points should be noted here: 1) The embankments are mostly designed under dry conditions

that conservatively ignore the positive effect of suction on slope stability, and 2) The presented results have been obtained based on analyses assuming the estimated mean values for the geotechnical and hydraulic parameters. Therefore, the results presented here are only valid for the safety of embankment slopes without the considerations for likely variations and uncertainties in the soil parameters. For this reason, the effect of uncertainty in the values of hydraulic and geotechnical parameters on the probability of failure is discussed later in Chapter 7.

6.5.2. Critical FOS under extreme rainfall

Figure 6.11 shows the variation of critical FOS in sand embankment with P50% and P90% initial conditions under extreme rainfalls for different return periods. As described before, the critical FOS is the minimum FOS calculated over time for a given extreme rainfall. It can be seen that FOS changes only under future 24-hour rainfall events for the case of general failure. However, for shallow failure depths, both 6 and 24-hour rainfall events seem to have an effect on the FOS. It can also be observed that the FOS decreases with increasing return periods as the rainfall intensity increases. This reduction is more pronounced for future events as opposed to the historical rainfall events. It can also be observed that for shallower depth that FOS remains unchanged under rainfall with the return periods greater than or equal to 10 years. This can be attributed to the lower retention and higher conduction capacity of the sand. It is hypothesized that during the rainfall event, water infiltrates into the sand embankment, but a limited portion of it is retained at the shallower depth, and the remaining water drains to the deeper layers.

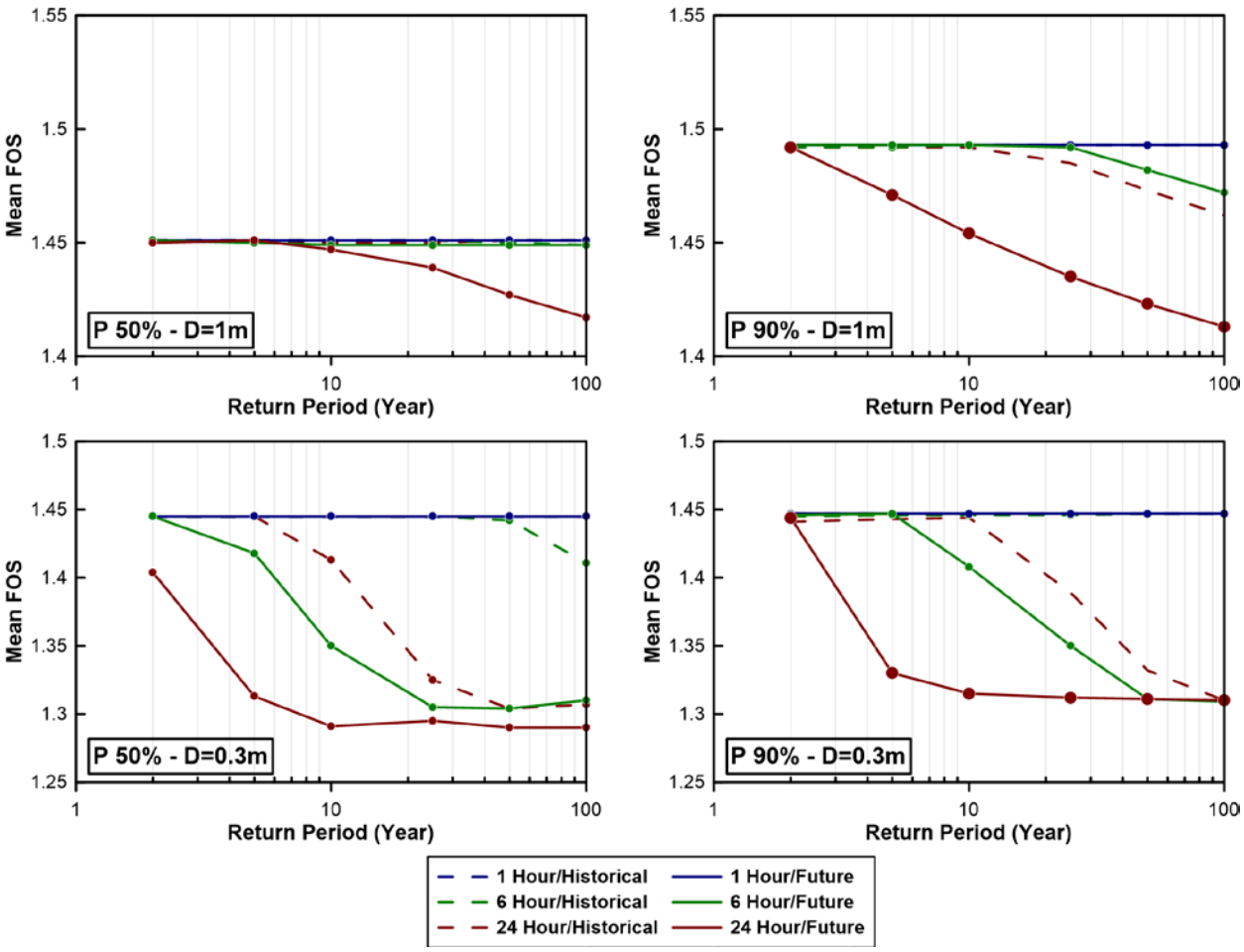

Figure 6.11 Critical FOS for sand embankment under various extreme events in Niagara Falls

Similar to Figure 6.11, Figure 6.12 presents the changes in critical FOS for the silt embankment with initial conditions of P50% and P90%, for extreme rainfalls with different return periods. The variation in FOS for both 0.3 and 1m minimum slip depths are presented in this figure. This figure shows that there are no changes in FOS for 6-hour rainfall events. This observation is valid for both 0.3 and 1m minimum slip depths. However, for larger duration rainfall events, a considerable decrease in the FOS can be observed. This observation is also consistent with results from others, where it has been reported that events of larger duration result in more water entering the silt embankment. This is due to lower intensities of shorter duration events and lower infiltration capacity of the silt material (Pk et al. 2018). Additionally, similar to the sand embankment, FOS

of silt embankment decreases with increasing the rainfall intensity, as it is evident that FOS decreases with increasing the return period, with lower values for future events. It can also be observed that the shallower depth of the slopes can be more affected by the extreme rainfall in comparison to deeper depths.

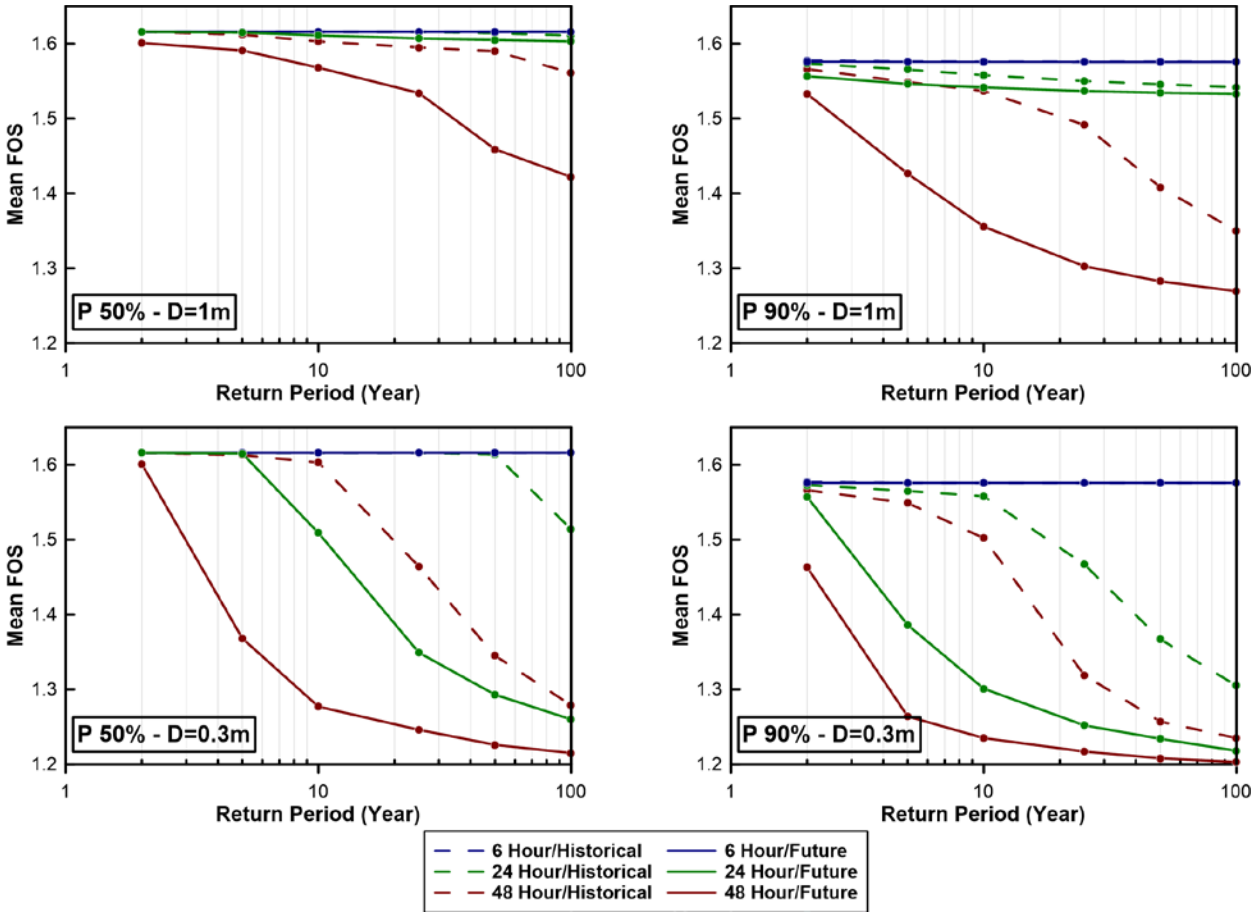

Figure 6.12 Critical FOS for silt embankment under various extreme events in Niagara Falls

Similar to Figure 6.7 to Figure 6.10, the variation of FOS over time was plotted for all other nine locations, and critical FOSs under different rainfall events were obtained. Figure 6.13 and Figure 6.14 show these critical FOSs for sand and silt embankment, respectively. These results are for

100-year extreme rainfall events of different durations. These figures present the critical FOSs for both general and shallow failures with both P50% and P90% initial conditions.

Based on Figure 6.13, it can be concluded that 1-hour rainfall would not change the stability of the sand embankment since the slope has almost similar values for critical FOS for both historical and future time periods. This observation is valid for both general and shallow failures for most of the locations. A small difference in FOS values can be observed for Toronto and Kenora for the P90% initial condition. This can be attributed to the difference between their initial saturation conditions, as presented in Figure 6.5 previously. The initial saturation for P90% in the historical period is in the first category and is lower than future saturation, which is in the second category.

For the 6-hour duration, in the case of global failure, the critical FOS of sand embankments remains relatively unchanged under P50% conditions. However, future FOS for sand embankments with 1m slip depth and P90% initial conditions is less than the historical condition for most of the locations. This is due to higher rainfall intensities in the future; however, the FOS values are still above the allowable value. Furthermore, FOSs for 0.3m minimum slip depths are, in general, lower than those observed for 1m minimum slip depth. This is not surprising as climatic loads are known to have more effect on shallower depths (Pk et al. 2018). It can also be seen that in the future, for shallower depth, the rainfall events have the potential to decrease the FOS quite close to the allowable value. This observation is true for most of the locations.

The graphs for 24-hour rainfall in Figure 3.13 indicate two salient points. One is that future FOS during a 24-hour rainfall event is almost similar for P50% and P90% initial conditions. One of the reasons for this similarity could be due to the fact that during the longer duration of rainfall, much larger quantities of water enter the embankment, and the effect of initial conditions get somewhat muted. Second, it can be noted that 24-hour rainfall would considerably affect the shallower depth

of sand embankments in the future. Future FOS for all locations come quite close or dip slightly below the MTO requirement of 1.3.

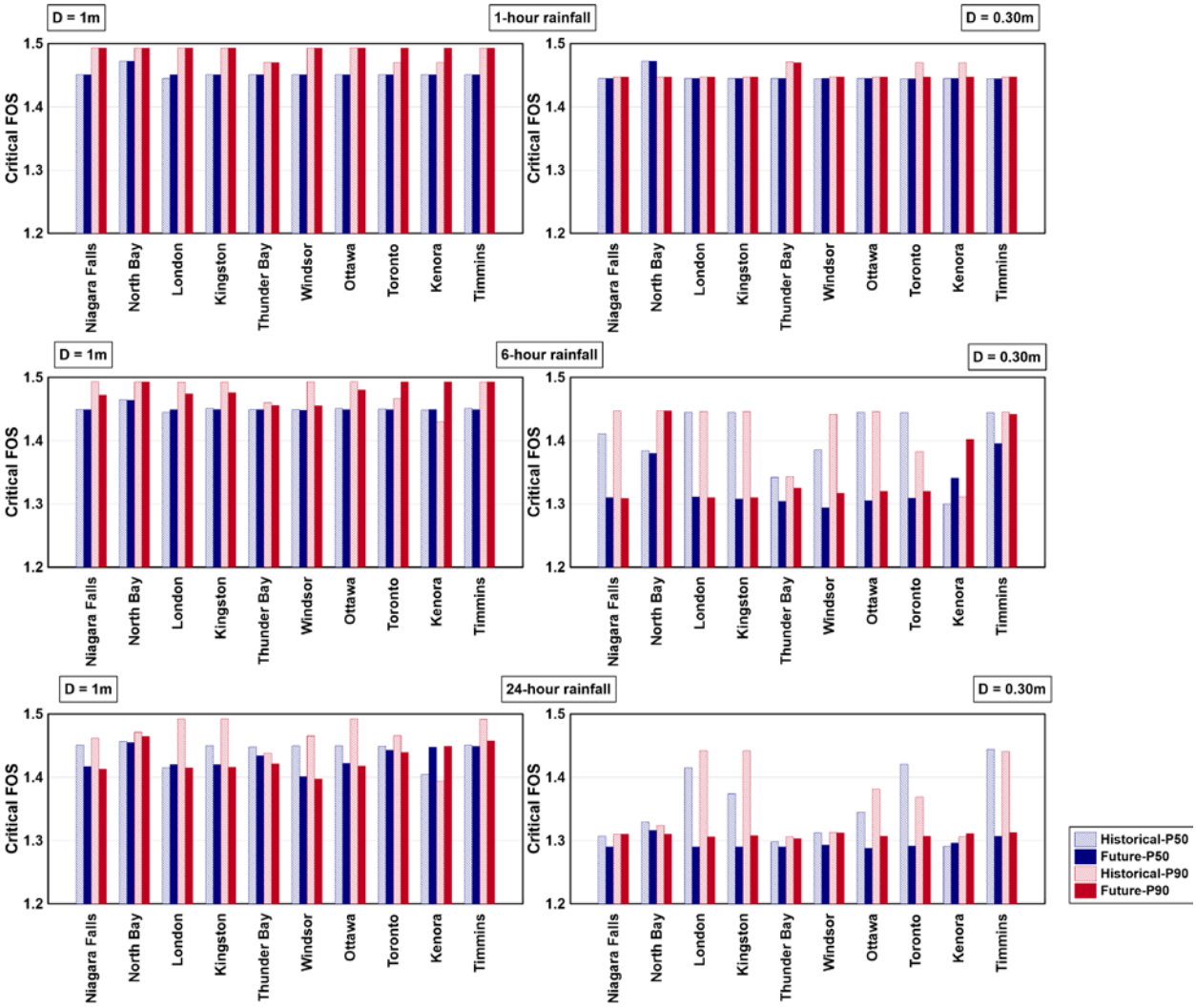

Figure 6.13 Critical FOS of sand embankment under different durations of 100-year rainfall in all locations

Figure 6.14 shows that the stability of the silt embankment would not be impacted by 6-hour rainfall events. Only critical FOSs of silt embankment in Ottawa in historical and future periods are slightly different because of different initial conditions in these periods. These rainstorms do not influence the shallower slope depths as well. Moreover, considering 1m minimum slip depth, values of historical and future FOS under 24-hour rainfall are similar for P50% initial conditions.

However, for P90% initial conditions, future FOS of the slope is expected to be similar or less than the historical FOS because of the wetter initial condition and/or higher rainfall intensities in the future. The maximum decrease in future FOS under 24-hour rainfall is observed for the city of Ottawa. This location not only has a higher rain intensity in the future but also has a wetter initial condition in comparison to the historical period. For the shallower minimum depth of 0.3m, 24-hour extreme rainfall events have the potential to considerably reduce FOS in the future. It can be seen that for most locations, even with the drier initial condition, future FOS for 24-hour events are expected to be less than the allowable value of FOS required by MTO.

Figure 6.14 also shows the notable impact of 48-hour rainfall events on the stability of silt embankments in the future, for both global and shallow failures. These extreme rainfall events can decrease the FOS of the slopes for 1m minimum slip depth, with FOS for slopes with wetter initial conditions below 1.3 in most cases. The values of FOS for 0.3m minimum slip depth also decrease in the future. It can be observed that critical FOS of all locations under future 48-hour rainfalls is below or equal to 1.2, which is less than the allowable FOS of 1.3.

Overall, it can be inferred from Figure 6.13 and Figure 6.14 that shallow failures are more likely to be triggered due to the changing climate. The comparison between the results of deep and shallow failure analyses confirms that extreme rainfall events may influence the shallow failures to a greater extent. Furthermore, it should also be noted that embankments built with fine materials such as silt appear to be more susceptible to extreme rainfall events in the future. Another notable observation from the results is the projected increase in future FOS for the sand embankments in the city of Kenora. This can be attributed to the expected lower intensity of future extreme rainfall events for Kenora in comparison to historical values, as described in chapter 4.

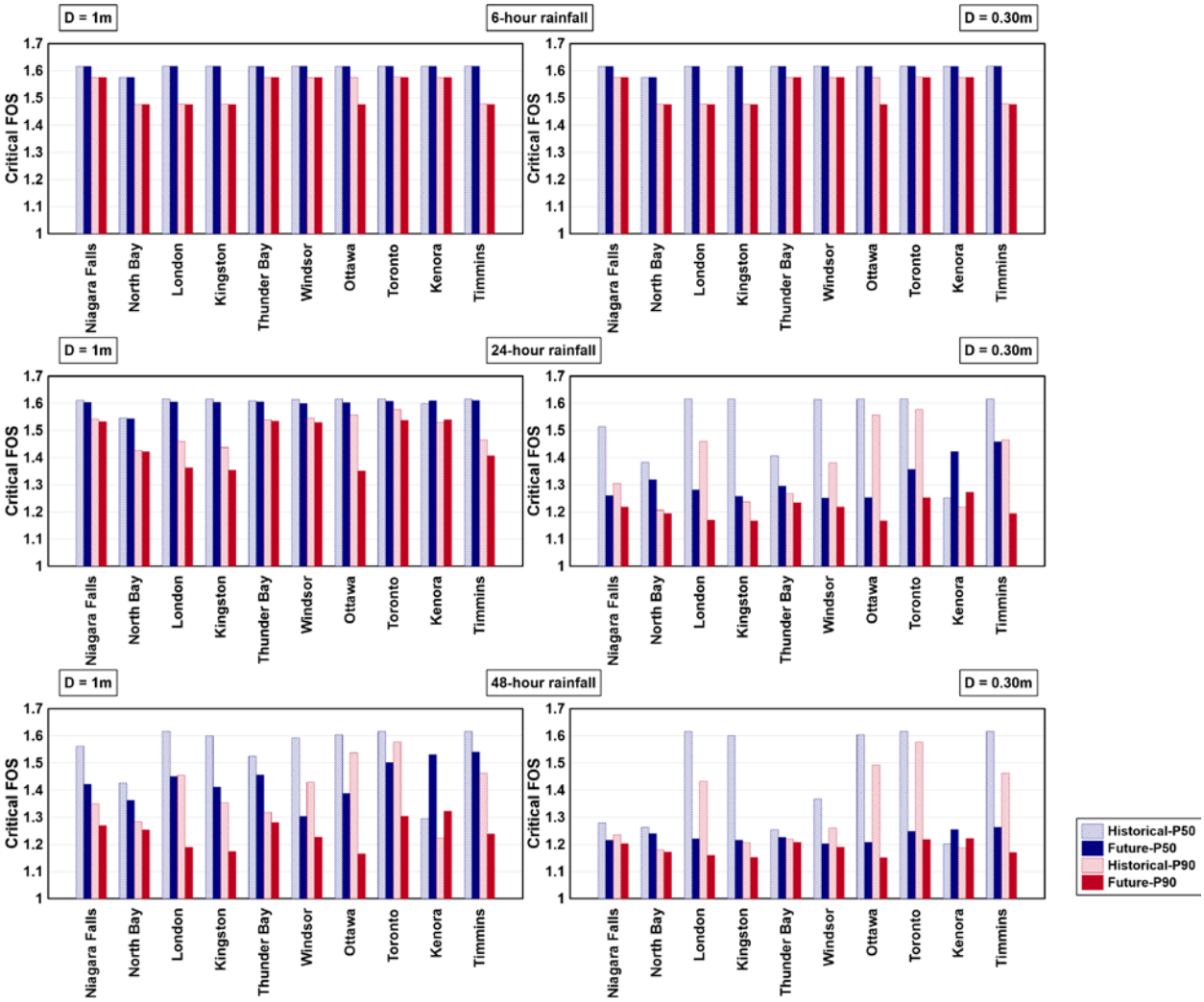

Figure 6.14 Critical FOS of silt embankment under different durations of 100-year rainfall in all locations

Chapter 7:Probabilistic analysis

There are inevitable uncertainties in various factors influencing the stability of slopes. These uncertainties may lead to uncertainty in the factor of safety, which is not considered in the conventional slope stability analyses. Uncertainties in soil strength, soil hydraulic properties, and rainfall characteristics are the most important sources of uncertainty that can affect the stability of embankment slopes, exposed to the environment. The reason is that soils are inherently heterogeneous materials. The natural spatial and temporal variation of soils, together with measurement errors and insufficient data, can make substantial alterations in soil properties such as strength parameters, saturated and unsaturated hydraulic conductivity, and soil retention parameters. All these properties are expected to play a crucial role in the stability of slopes subjected to rainfall events.

Along with the above-mentioned parameters, the indeterministic characteristics of the rainfall events can also make the stability assessments more complicated. Reliability analyses provide an option of evaluating the uncertainties and estimating their effects on the performance of slopes using the probabilistic concepts. In such analyses, by assigning a probability distribution function to the input parameters, engineers can evaluate the probability of a desired level of performance. In this study, a series of reliability analyses were carried out to evaluate the effects of the uncertainties in the geotechnical and hydraulic soil properties on the stability of slopes under various extreme rainfall events. The theoretical aspects of the employed method for reliability analysis are explained in the following section. The uncertainty in the occurrence of various rainfall events is estimated separately based on the IDF curves concept, which is also described in a later section.

7.1. Reliability analysis of slope stability

In reliability analysis, the level of uncertainties for a given FOS is normally estimated in terms of probability of failure (P_f) and the reliability index (β). The probability of failure is defined as the possibility of FOS less than the desired value (usually less than 1.0), considering uncertainties in values of the variables involved in its calculation. The reliability index represents the number of standard deviations that separate the mean FOS from a critical value (FOS=1). It is generally expected that a higher FOS implies a lower probability of failure; however, it is not always the case. For example, as can be seen in Figure 7.1, Lacasse (2016) has shown the results of two analyses for the same foundation that lead to different results. In the first analysis with limited information on soil properties and loads, a FOS of 2 was obtained. In the second analysis with more extensive information, a FOS of 1.4 was obtained, which is less than FOS calculated from the first analysis. The second analysis resulted in lower FOS; however, there is a higher safety margin (lower probability of failure) compared to the first analysis.

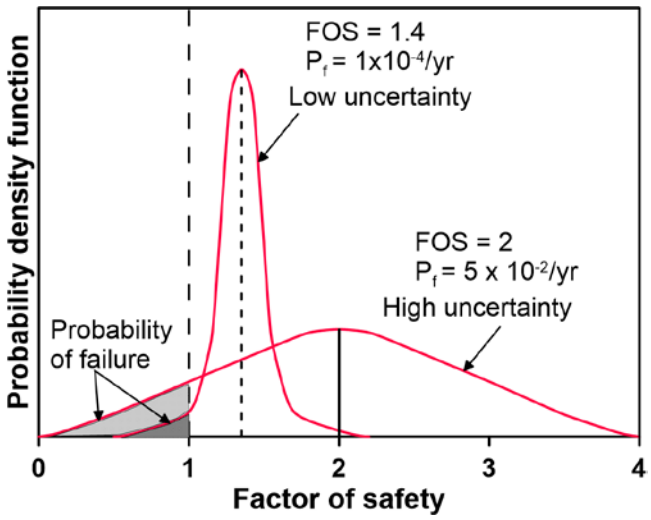

Figure 7.1 Factor of safety and probability of failure (modified from Lacasse 2016)

7.2. Reliability methods

The main objective of reliability analysis is to estimate the probability distribution of FOS. A probability distribution (density) function describes the relative likelihood that a random variable is within a given range, and is attributed to each parameter used in the reliability analysis. The normal (or Gaussian) and log-normal distributions are the most common types of probability distributions that are generally used for probabilistic studies in geotechnical engineering. In previous studies, the normal distribution has been suggested to be used for geotechnical strength parameters (e.g., Lumb 1966 and Hassan and Wolff 1999). While, log-normal distribution has been used for hydraulic conductivity and soil water retention parameters (e.g., Bennion and Griffiths 1966, Carsel and Parrish 1988, Phoon et al. 2010). Both normal and log-normal distribution functions can be defined in terms of mean value and standard deviation (or the coefficient of variation) for a given random variable.

Equation 7.1 is a common function to define the performance function G(X) related to FOS.

$$G(X) = FOS(X) - 1 \tag{7.1}$$

Where $X = (x_1, x_2, \dots, x_N)$ is a vector of the *N* random variables, with (x_i) representing various influencing parameters, which in this study are soil parameters affecting the slope stability. As mentioned before, safety within the context of a probabilistic analysis is typically expressed in terms of a probability of failure (P_f) and reliability index *(β)* as follows:

$$P_f = P[G(X) \leq 0] \tag{7.2}$$

$$\beta = E[G(X)]/\sigma[G(X)] \tag{7.3}$$

Where $E[G(X)]$ and $\sigma[G(X)]$ are the mean and standard deviation of the performance function, respectively. The definitions of P_f and β are illustrated in Figure 7.2, where P_f indicates the probability of slope failure (the area under the probability distribution of $G(X) \leq 0$), while β

represents the mean of the performance function in terms of its standard deviation. For a higher mean value of FOS and/or a lower standard deviation of the distribution, a higher reliability index is expected. It should be noted that the above definition is accurate if the performance function (or factor of safety equation) is linear, which is not always the case for slope analysis models (El-Ramly et al. 2002). However, Mostyn and Li (1993) have suggested that the performance functions of slopes are reasonably linear and have recommended ignoring the nonlinearity when calculating β.

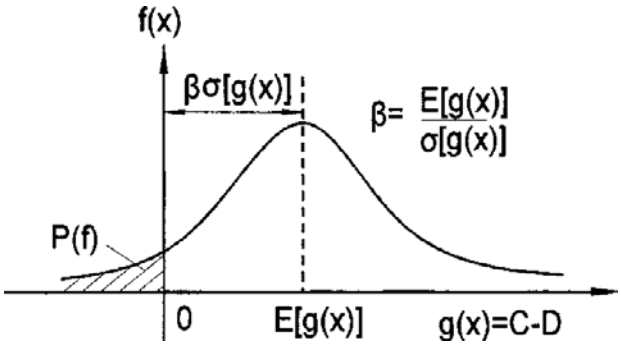

Figure 7.2 Definition of the probability of failure and reliability index for a normal distribution function (Xue and Gavin 2007)

In this study, the first-order second-moment method (FOSM) was used for reliability analysis. This method is based on Taylor's series expansion of the performance function around the mean vector of variables, and only first-order terms of the series are taken into account. If the input variables are not correlated, it can be shown that the mean and the variance of the performance function are given by the following equations:

$$E[G(X)] \approx G[E(x_1), E(x_2), \dots, E(x_N)] \quad (7.4)$$

$$\sigma^2[G(X)] \approx \sum_1^N (\frac{\partial G}{\partial x_i})\sigma^2[x_i] \quad (7.5)$$

If a probability distribution function is assumed for the performance function, its mean and standard deviation (Equations 7.4 and 7.5) can be used to calculate the probability for any of its

values. If input variables are not independent, the correlation has to be taken into account for the calculation of the variance. The assumption of the probability distribution function for the performance function is one of the limitations of the FOSM method. Also, the first-order partial derivatives in Equation 7.5 must be numerically estimated using a finite difference scheme. A common practice is to select two points over a range of plus and minus one standard deviation with respect to the mean value of the random variable x_i, in order to capture the nonlinear behaviour of the function in a range of likely values (Wolff 1994). Therefore, assuming *N* random variables, the number of simulations required to apply the FOSM method is *1+2N*. Monte Carlo simulation (MCS) is another technique that is often used to simulate the probability density function of a performance function and could have been used in this study. However, this method requires a large number of simulations, which is not practical for problems with small probabilities of failure and a large number of random variables such as this study (Phoon et al. 2008; Phoon and Ching 2015).

The application of the Taylor Series method in geotechnical engineering has been described in previous studies (e.g., Baecher and Christian 2005). It is common to use the following simple formula, which was derived from the Taylor series technique to estimate the standard deviation of the factor of safety (Wolff 1994; Duncan 2000; Baecher and Christian 2005):

$$\sigma = \sqrt{(\frac{\Delta FOS_1}{2})^2 + (\frac{\Delta FOS_2}{2})^2 + \cdots + (\frac{\Delta FOS_N}{2})^2} \quad (7.6)$$

Where $\Delta FOS_i = (FOS_i^+ - FOS_i^-)$ and FOS_i^+ and FOS_i^- are the factor of safety calculated with the value of the *i-th* parameter, respectively increased and decreased by one standard deviation from its mean value. In calculating FOS_i^+ and FOS_i^- the values of all other parameters are kept at their mean values. In this study, five soil hydraulic parameters (K_{sat}, α, n, θ_s and θ_r) and soil friction angle *(φ)* were considered as random variables. In this study, uncertainties in material

properties were estimated considering one standard deviation based on previous literature; however, they can also be estimated considering multiple standard deviations. The mean value of these variables and their mean ±1 standard deviation values for sand and silt material are presented in chapter four. In total, 37440 slope stability analyses were conducted under various historical and future rainfalls with six different return periods and three different durations to estimate the probability of both general and shallow failures, in all ten locations. These analyses were carried out for both sand and silt materials with the P50% and P90% initial conditions. The analyses were carried out for mean values of material parameters (as shown in Table 3.8), and also their values considering ±1 standard deviation. The results were assimilated by developing a series of fragility curves, as described in the following section.

7.3. Fragility curves

Fragility curves are developed when the probability of failure for various possible loading conditions needs to be evaluated in the slope stability analyses. Fragility curves are an appropriate tool for reliability-based analysis of slope stability as they relate the probability of failure (P_f) with the intensity of the applied loads. The advantages of developing fragility curves include the allowance for an explicit appraisal of the uncertainties associated with vulnerability modelling and the possibility of presenting results for a wide range of loadings. This makes fragility curves an attractive tool for carrying out risk assessments of large systems, such as major transport networks (Martinović et al. 2018).

In this study, the fragility curves were developed for both sand and silt embankments according to probabilistic analyses of slopes under different rainfall scenarios based on IDF curves for both historical and future periods. Instead of using intensity or duration, the return period was

considered as the primary independent variable for the fragility curve since it is a standard and important tool in hydrological engineering design.

7.3.1. Sand embankment

Figure 7.3 a and b show the fragility curves for sand embankment in the city of Niagara Falls under different historical and future rainfalls with P50% and P90% initial conditions. The results are presented for both general and shallow failures conditions, respectively. For a variably saturated soil embankment under rainfall, the probability of failure is mostly governed by the uncertainties in the variation of soil shear strength, which is controlled by soil suction as well as other soil shear strength parameters. The suction-related soil shear strength may increase or decrease with the increase in the soil moisture. Therefore, the fragility curves may significantly differ in trend depending on the changes in moisture distribution during the rainfall.

As presented in Figure 7.3a, a decreasing trend in the probability of general failure with increasing return period and duration of the event is observed for initial condition corresponding to the 50^{th} percentile. It can be observed that for this condition (P50%), the probability of general failure is lower for future conditions in comparison to historic conditions. It can also be seen that for a higher initial moisture condition (P90%), the probability of general failure is lower than that for lower initial moisture conditions (P50%) and remains almost constant with respect to increasing return period. This figure also shows that sand embankment stability may not be affected by a 1-hour rainfall event. It seems logical as for shorter duration events such as 1-hour, only a small quantity of water can infiltrate into the embankment, and this quantity of water would not percolate deeper into the embankment.

For 30 cm minimum slip depth (Figure 7.3b), the changes in the probability of failure are different from those observed for 1 m minimum slip depth. First, the probabilities of failure for shallower

depths are, in general, higher than those observed for deeper depths. This is not surprising as climatic loads are known to have more effect on shallower depths (Pk et al. 2018). Secondly, for 1-hour storms, the probability of failure does not seem to be affected by the changing climate, which is similar to the results for 1m depth. However, for storms of 6 and 24-hour durations, there are some differences between probabilities of failure for historical and future extreme precipitation events. Results indicate that for future events, some increase in the probability of failure can be expected for 6 and 24-hour events. An increase in the probability of failure can also be observed for historical storms of returns periods greater than 10 years for 24-hour events. This observation is consistent with the increase in intensities and is indicative that these intensity increases are to the extent that they may result in a reduction in the suction strength at shallower depths. However, these changes appear to be quite minimal.

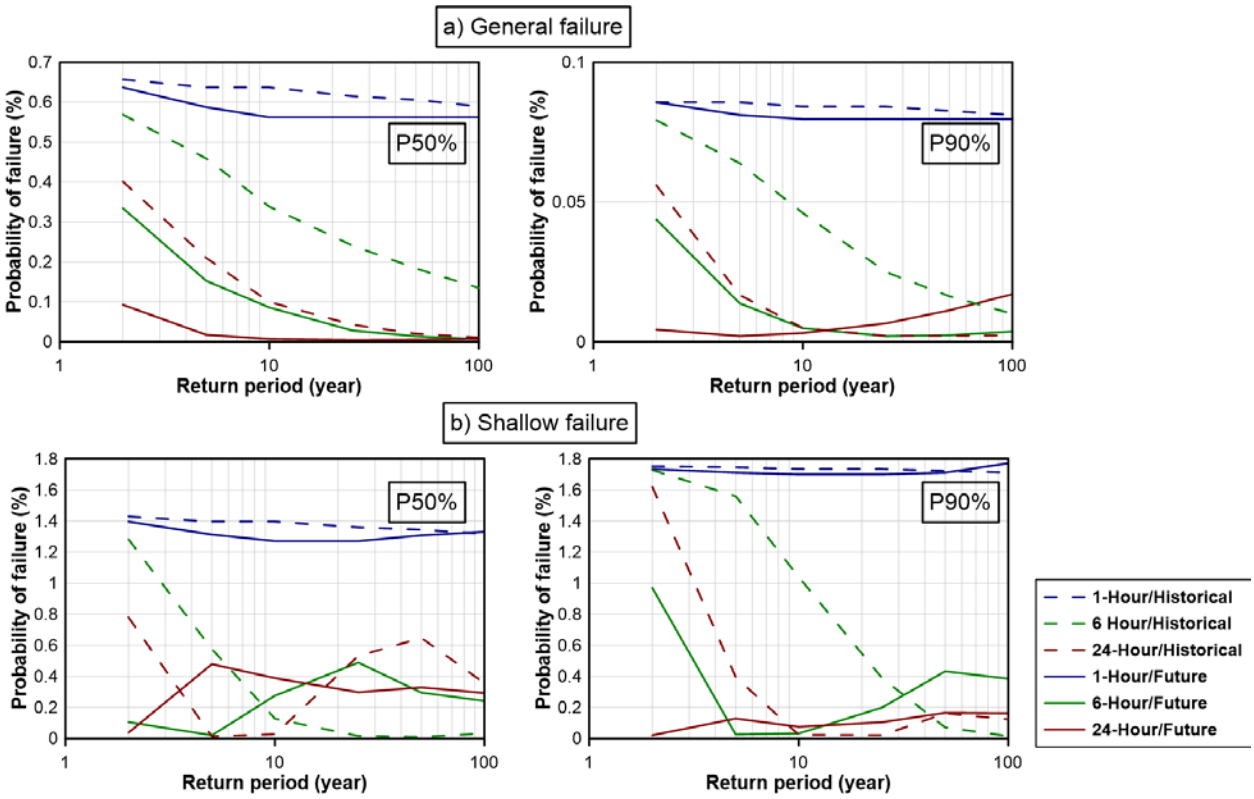

Figure 7.3 Fragility curves for sand embankment in Niagara Falls with P50% and P90% initial condition considering both types of failure

7.3.2. Silt embankment

Figure 7.4 a and b show the fragility curves developed for silt embankment in Niagara Falls under various historical and future rainfalls with different durations and return periods. These graphs are for P50% and P90% initial conditions considering both general and shallow failures. It is noticeable that the probabilities of failure are much larger for silt material as compared to sand material. This is consistent with the previous studies that have shown, in general, fine-grained materials are more prone to stability issues in comparison to coarse-grained materials under extreme rainfalls (Pk et al. 2018). It can also be observed that shallower soil depths are more vulnerable to historical and future climatic events, similar to the observations for the sand embankment.

Contrary to the sand embankment, the fragility curves for the silt embankment generally show an increasing trend in the probability of failure for higher return periods. This can be observed for both general and shallow failures. Moreover, the wetter initial conditions (P90%) result in a considerable increase in the probability of failure in comparison to the drier initial conditions (P50%). Additionally, more prolonged rainfall events can cause a considerable increase in the probability of failure. This observation is also consistent with results from others, where it has been reported that events of larger duration result in more water entering the silt embankment owing to their lower intensities in comparison to shorter duration events of higher intensities. This is attributed to the lower infiltration capacity of the silt material (Pk et al. 2018).

One of the reasons for the difference between the observations for embankments constructed with sand and silt materials can be attributed to the initial conditions. As shown in chapter 6, silt material tends to hold more water owing to its lower conduction and high retention properties in comparison to sand. Therefore, initial saturation conditions for the silt embankment are much higher than those

for sand for the same percentile of occurrence. As a result, for similar storms, silt embankments could potentially end up at higher saturation than the sand embankment. Besides, silt material, in general, gets a larger contribution from suction to its shear strength in comparison to sand (Lu and Likos 2006). Therefore, higher and larger increases in the probability of failure due to climatic events are expected for silt embankments. Accordingly, an increase in the probability of failure with increasing the return period (as rainfall intensity increases) along with a decrease in mean FOS for 24-hr and 48-hour rainfalls can also be observed in this figure.

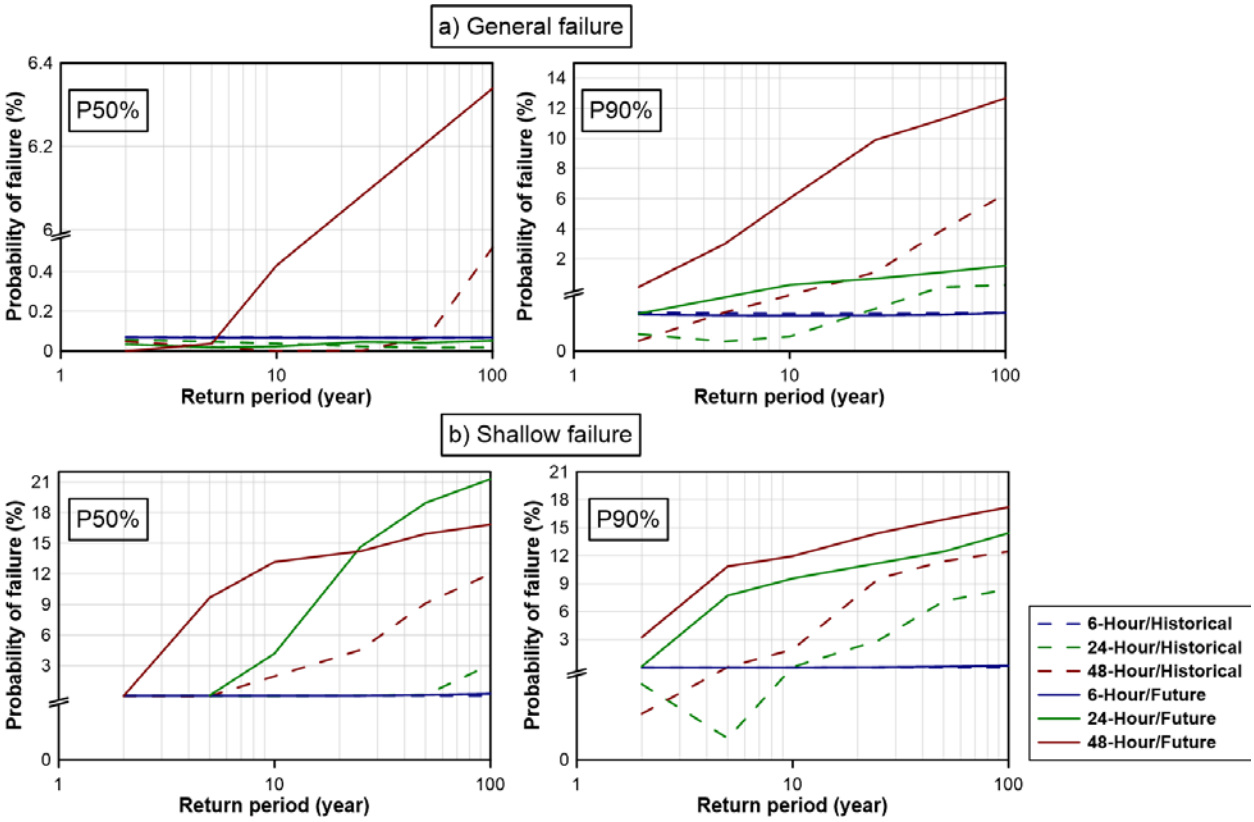

Figure 7.4 Fragility curves for silt embankment in Niagara Falls with P50% and P90% initial condition considering both types of failures

The abovementioned argument can also be extended to explain the difference between historical and future results. The substantial intensification of future rainfalls has an adverse effect on the safety of silt embankments in the future (as shown in chapter 6). For example, the probability of

general failure increases from less than 1% to around 6% for the 48-hr 100-year future rainfall event. Comparing fragility curves for shallow failure and general failure indicates that the probability of shallow failure is much higher than general failure. For example, the fragility curves for 24-hour rainfall events show that with P50%initial conditions, the probability of failure increases from almost negligible for general failure to 20% for shallow failures. The fragility curves for the other nine locations show similar trends for both sand and silt embankments. The fragility curves for these locations are shown in Appendix D.

7.4. Annual probability of failure

In order to evaluate the probability of failure for time-related problems, such as this study, considering a time frame to define is required to define a time period in which the probability of failure is determined. The probabilistic results are provided in terms of Annual Probability of Failure (APF) in the current state of practice in civil engineering projects.

Moreover, to consider the indeterministic nature of time-related problems such as rainfall when using fragility curves, the probability of load exceedance should also be taken into account. For this purpose, the Annual Probability of Failure is estimated to evaluate the probability of failure, taking into consideration the probability of load exceedance. The probability of load exceedance can be defined in terms of Annual Exceedance Probability (AEP). In this study, AEP was calculated based on the Poisson distribution model and related the exceedance probability of events to their corresponding return periods. Then, the fragility curves are combined with the AEP of extreme precipitation events to estimate the APF.

According to the IDF curves concept, extreme rainfalls can be identified in terms of three main characteristics: average intensity, duration, and return period (T). The return period, also known

as a recurrence interval, is an estimate of the average time between two extreme rainfall events and is equal to the inverse of the average frequency of occurrence at a specific location.

The Poisson distribution model is the most common model that has been used extensively to represent the temporal occurrence of random natural events such as earthquakes (e.g., Kramer 1996), landslides (e.g., Crovelli 2000) and extreme rainfall events (e.g., Smith and Karr 1990). This model is established for the events that follow a Poisson process where the average time between events is known, but the exact timing of events is random. Another assumption for this model is that the arrival of an event is independent of the event before; namely, the waiting time between events is memoryless. The temporal distribution of event recurrence using Poisson probability distribution can be given by:

$$P[N = n] = \frac{(\lambda t)^n}{n!} e^{-\lambda t} \tag{7.7}$$

The above equation gives the probability of n occurrence of a particular event during the time span of interest (t) for a given average rate of occurrence of the event λ (i.e., the inverse of return period). Therefore, the probability of occurrence of at least one event in a time interval can be easily derived:

$$P[N \geq 1] = 1 - P[N = 0] = 1 - e^{-\lambda t} = 1 - e^{-\frac{t}{T}} \tag{7.8}$$

where T is the return period of the event under consideration.

Based on the concept of IDF curves, the return period can be attributed to the probability of occurrence of rainfalls with intensity higher than a particular value for any given rainfall duration. Therefore, Equation (7.8) can be used to predict the probability of exceedance of rainfall with a given return period. The AEP value can then be calculated considering a time period of one year for a given return period. Figure 7.5 shows the annual exceedance probability curve considered in

this study. This curve indicates AEP values estimated by Equation (7.8) considering different return periods from 1 to 100 years. More details are provided in the following sections.

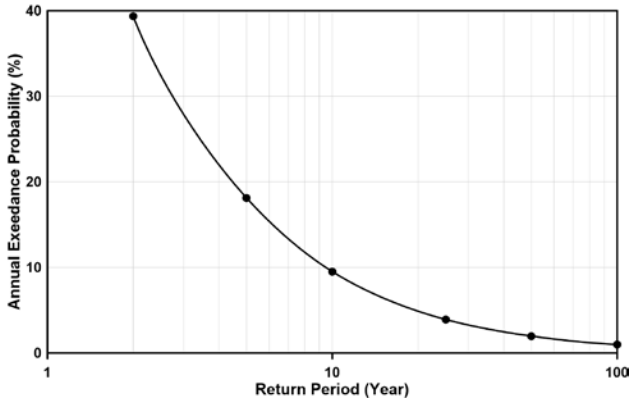

Figure 7.5 Annual Exceedance Probability curve in this study

In order to calculate the annual probability of failure (APF), the fragility curves (P_f vs. T) can be combined with the annual exceedance probability curve (AEP vs. T) (Phoon and Ching 2015). As shown in Figure 7.6, the annual exceedance probability curve can be discretized at several intervals to obtain a representative value. The annual probability of occurrence of each load interval can be estimated using the following equation:

$$P_{Oi} = P_{Li} - P_{Ui} \tag{7.9}$$

where P_{Oi} is the annual occurrence probability on a load interval i, P_{Li} is the AEP of the lower bound of the interval i, and P_{Ui} is the AEP of the upper bound of the interval i.

The probability of failure for each interval can be obtained by multiplying the annual occurrence probability of that interval (P_{Oi}) by its conditional probability of failure (P_{fi}). This conditional probability of failure can be obtained directly from the fragility curves. Adding the probability of failure of all the intervals of interest yields the annual probability of failure as given by:

$$APF = \sum_1^M P_{Oi} \,.\, P_{f,i} \tag{7.10}$$

where M is the number of considering intervals.

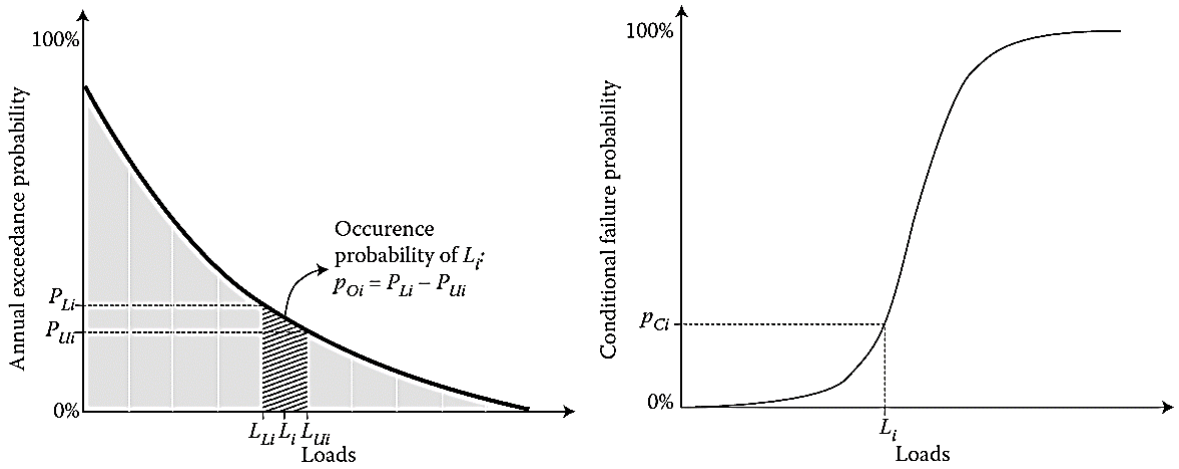

Figure 7.6 Estimation of APF using fragility curves (Phoon and Ching 2015)

7.4.1. Sand embankment

Figure 7.7 shows the estimated historical and future APF for sand embankment under different initial conditions and rainfall durations, considering both types of failures. It can be observed that under all three rainfall durations, the annual probability of general failure decreases in the future in all locations except for the city of Kenora. In this location, the drier initial condition (P50%) coinciding with lower rainfall intensity result in reducing the FOS due to lower values of water content and decreasing the suction strength of soil, which raises the probability of failure in the future. The graphs for shallow failure show that only APFs in Toronto and Kenora with the wetter initial condition (P90%) are higher in the future when compared to the historical period. The estimated increase in the future APF is 19% and 55% for the cities of Kenora and Toronto, respectively. This can be related to the higher saturation of their initial conditions in the future, as it was shown in Figure 6.5 in chapter 6.

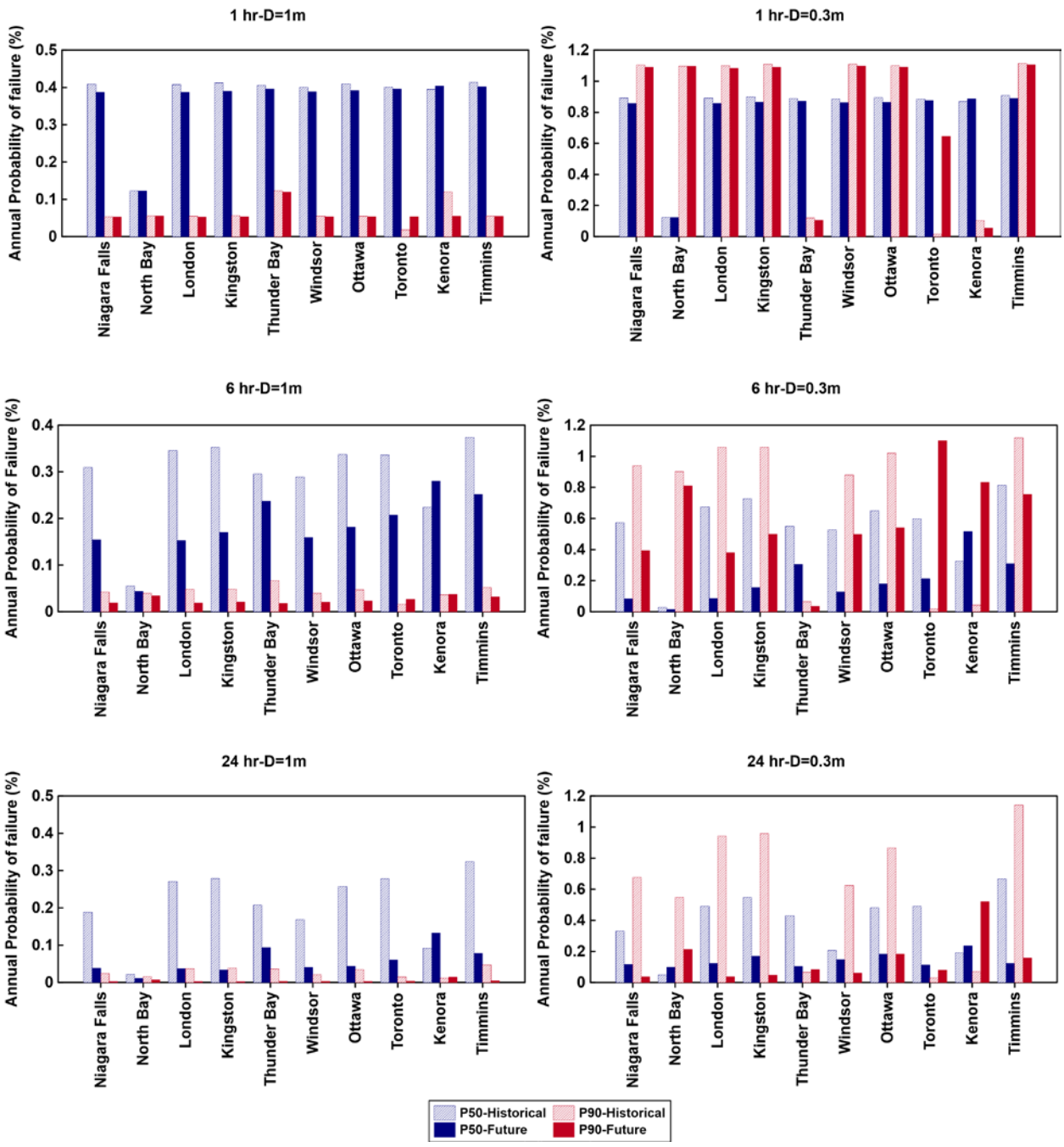

Figure 7.7 Annual probability of general and shallow failure for sand embankment under different extreme rainfall with P50% and P90% initial conditions

7.4.2. Silt embankment

Similar to Figure 7.7, Figure 7.8 shows the historical and future APF for silt embankment under different initial conditions and rainfall duration for both types of failures. This figure shows that

APFs for silt embankment are quite different from the sand embankment. It can be observed that unlike the sand embankment, the APFs for future climatic conditions are mostly higher than historical values. Considering all the cases at all the locations, the range of APF is between 0% to 3.5% in the historical period; however, future APF varies from 0.001% to 8%. The greatest future APF increase can be expected for the city of London, with a 47% increase. The 6-hour rainfall does not change the annual probability of general failure in the future; however, for shallow failures, the APF is expected to increase for many cities in the future. For 24-hour rainfall events, the APF is expected to increase for both general and shallow failures, especially for the wetter initial conditions (P90%). It should also be noted that the effect of future climate is more pronounced for shallower failures, especially for the cities of Northbay, London, Kingston, Ottawa, and Timmins.

APF due to 48-hour future rainfall events are also expected to be higher compared for both initial conditions, especially for shallower failures. For general failure, the most remarkable increase is expected for the city of Kingston, where the annual probability of general failure is expected to increase from 0.2% in the historical period to 7% in the future.

A review of the figure also indicates that for shallow failures, APFs are expected to increase for all future rainfall events of 6, 24, and 48-hours. As expected, these increases are more pronounced for wetter initial conditions for most of the locations. Many of these locations are expected to see a significant increase in APF, especially for wetter initial conditions. The city of Kenora is an exception where a decrease in APF for the future is expected. However, this result is not surprising since, as mentioned in chapter 6, future FOS of silt embankment in the city of Kenora is expected to increase because of lower future rainfall intensities compared to the historical values. Therefore, it can be concluded that future APFs can potentially be lower for this location. Overall, it can be

concluded that embankments built with silt are more susceptible to an increase in the probability of failures during prolonged rainfall events, and the occurrence of a shallow failure in silt embankments is more probable than general failure.

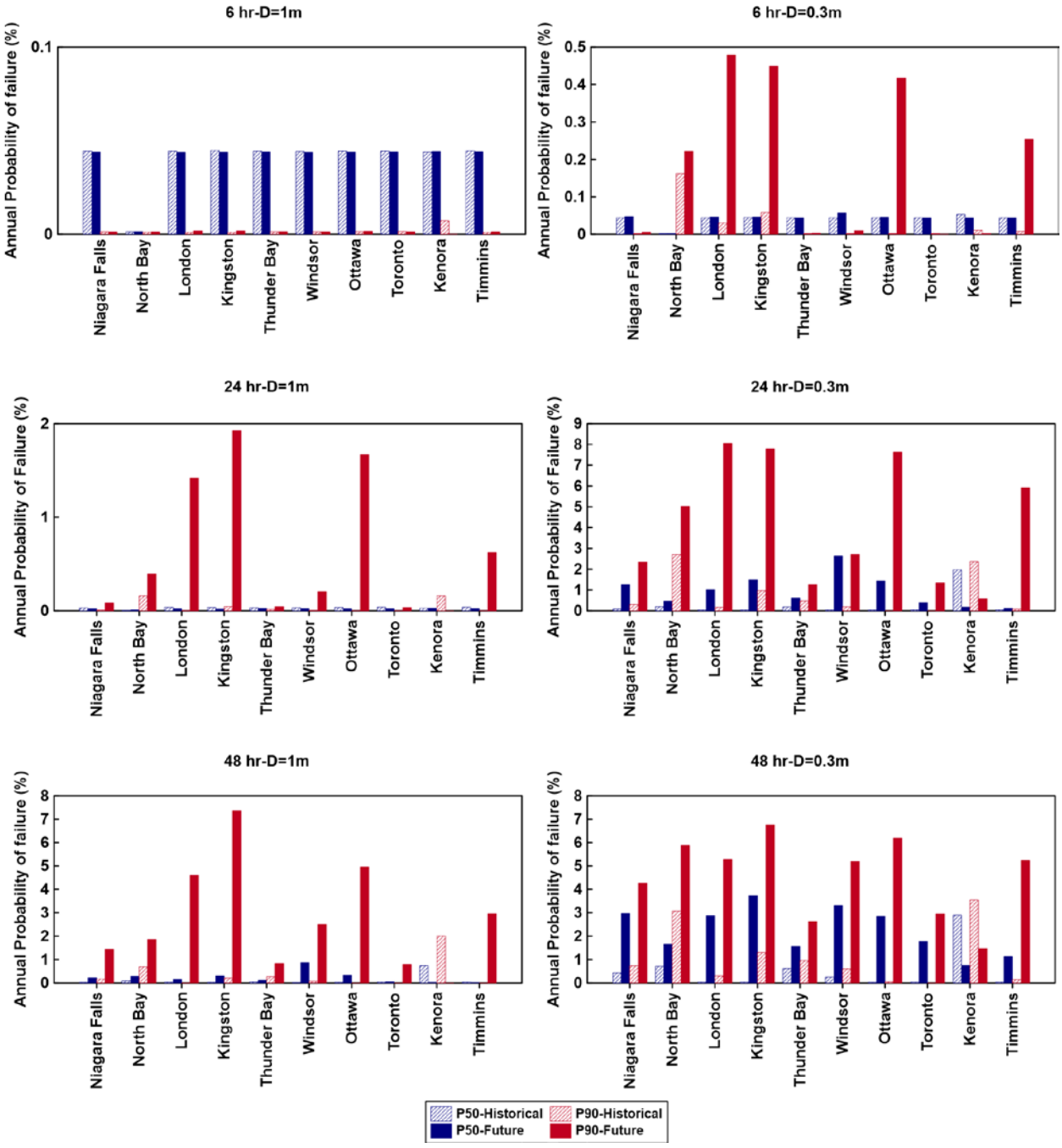

Figure 7.8 Annual probability of general and shallow failure for silt embankment under different extreme rainfall with P50% and P90% initial conditions

Chapter 8: Summary, Conclusions, and Recommendations for future research

This research aims to quantitatively assess the impact of future extreme rainfall events on the stability of typical highway soil embankments across Ontario. The quantification has been done by making use of numerical modelling techniques. Furthermore, probabilistic analyses have been performed to evaluate the effect of uncertainties in important parameters.

The research can be divided into four distinct sequential parts. In the first part, future climate changes were evaluated by calculating how climate variables would change over the next 90 years. Then, an appropriate long-term design climate for slope stability assessments was selected, and design IDF curves for slope stability assessments under future extreme rainfalls were identified. In the next part, spatial and temporal variation of moisture distribution within the embankment was evaluated. Subsequently, average and extreme slope moisture conditions were estimated for both sand and silt embankments based on statistical analyses that were carried on the basis of daily variation of average water content in the slope area. In the third part, the slope stability of sand and silt embankments during extreme precipitation events was assessed, and the impact of future climate change was quantified. This was accomplished by comparing the future stability condition of embankments with their historical performance. The last part is comprised of the probabilistic analyses to investigate the effects of uncertainties in soil parameters and extreme rainfall events on the slope stability of the embankments. A series of fragility curves representing the conditional probability of slope failure under various extreme rainfall events were developed and combined with the annual probability of extreme events occurrence to estimate the annual probability of failure.

8.1. Conclusions

8.1.1. Climate change

The review of the historical and future climate variables, including precipitation, potential evaporation, temperature, and annual moisture index data, indicates that future climate would change considerably across Ontario. An increasing trend in future precipitation has been predicted for all locations considered in this research. The precipitation data analysis shows that for all locations, the median value of average yearly precipitation is expected to increase more than the 75^{th} percentile of the historical value. Moreover, the descriptive statistical analyses of temperature data indicate that the future temperatures at all ten locations considered in this study could be noticeably higher than the temperatures recorded during the historical period. It was also observed that the future predicted values of the minimum temperature could potentially be higher than the maximum values of the historical period. Furthermore, the comparison of the availability of moisture at the ground surface over historical and future periods shows that for all locations, the median water availability for many future climate ensembles could potentially be less than the historical values. The reason for this is the predicted considerable increase in temperature, which would result in a proportional increase in potential evaporation and would offset the increased precipitation. Moreover, the review of the freezing and thawing dates shows that late freezing and early thawing conditions are expected across all locations under consideration. This would result in a longer active period in the future, which may cause more water to enter the ground surface and can be a potential influence on the embankment water balance and stability.

The review of the predicted future IDF curves from two different sources indicated that the intensity of the extreme rainfall events is expected to increase for most locations considered in this research. The only exception was found to be the city of Kenora, where the intensities are expected

to remain near or less than the historical values. The review also indicated that the modelling based on the more recent fifth Assessment Report (AR5) of the IPCC (IPCC 2007, IPCC 2013) predicts a lower increase in future extreme rainfall intensities in comparison to the modelling based on the fourth Assessment Report (AR4). This leads one to conclude that the effect of future extreme rainfall events might need to be revaluated as more recent modelling results become available.

8.1.2. Selection of appropriate climate ensembles

The compilation of future climate data results in rather a large number of climate ensembles based on various global climate models and emissions scenarios. Computational demand to take into account all of these ensembles in impact studies can be time and cost-prohibitive. As described in the thesis, no specific criteria for the selection of climate ensembles for geotechnical and geo-environmental problems currently exist in the literature. It has been shown in this research that the criteria used by others for selections based on annual water availability and/or increase in precipitation quantities is not adequate. This inadequacy is related to the temporal scale of climatic parameters and associated water balance in the embankment, which is a function of soil hydraulic properties. To address these inadequacies, an alternate approach was developed as part of the current research. This approach takes into consideration the intensity and frequency of the precipitation, together with the water-holding and conduction properties of the soil materials. This approach is based on the water balance assessment using soil-atmosphere modelling to analyze the long-term variation of moisture in the soil embankment for different climatic conditions. The results of one-dimensional water balance simulations were analyzed in terms of variation of saturation over time for each location. The maximum degree of saturation during historical and future time periods was identified. The selection of the climate ensembles was made based on the long-term effects of different future climate scenarios and the frequency of high saturation

occurrence. Therefore, it can be concluded that for the selection of climate change scenarios for slope stability assessments, consideration should be given criteria based on water balance as opposed to water availability at the ground surface. Moreover, the temporal scale of water balance should preferably be considered at a daily resolution.

8.1.3. Long term slope moisture conditions

The destabilization effect of extreme rainfalls on embankment slopes depends on not only the intensity and duration of the extreme rainfall events but also the incipient soil moisture conditions within the slope at the onset of extreme events. Therefore, the slope's initial moisture conditions just before the occurrence of the extreme event were estimated based on the time history of soil-atmosphere interactions. Statistical analyses using calculated daily values of average saturation were conducted to determine the average and maximum moisture conditions in the slope to identify critical times at which pore water pressure (PWP) distribution puts the slope at risk. The comparison between historical and future degree of saturation indicated that the initial conditions would be wetter in the future for most of the locations, although the changes are modest in most instances. In this research, saturation corresponding to P50% and P90% were considered respectively as representatives for the normal range and above-normal range of saturation to define the initial conditions in slope stability analysis under extreme rainfalls. In conclusion, the effect of incipient soil moisture conditions within the slope at the onset of extreme events is extremely important and needs to be quantified appropriately.

8.1.4. Slope stability under extreme rainfall events

The stability of the embankment's slope under extreme rainfall events was assessed by using hydrological and geotechnical models, where the spatial distribution of pore water pressure from the hydrological models was introduced into the geotechnical models. For this purpose, the

temporal variation of FOS and variation of critical FOS over the return period were quantified for all locations considering both historical and future rainfalls with different return periods.

The comparison between the results of deep and shallow failure analyses confirms that extreme rainfall events are expected to influence the shallow failures to a greater extent. Furthermore, the results also show that embankments built with fine materials such as silt are more susceptible to extreme rainfall events in the future. Moreover, it has also been concluded that wetter initial conditions have a higher potential to trigger the failure in the embankment.

8.1.5. Probabilistic analyses of slope stability

In this study, probabilistic analyses have been carried out to assess the influence of uncertainties in soil hydraulic properties, soil strength, and rainfall characteristics on the factor of safety of the embankment. In order to accomplish this, five soil hydraulic parameters (K_{sat}, α, n, θ_s, and θ_r) and soil friction angle (φ) were considered as random variables. More than thirty-seven thousand slope stability analyses were conducted under various historical and future rainfalls with six different return periods and three different durations to estimate the probability of both general and shallow failures for all ten locations. The analyses were done for both sand and silt materials with P50% and P90% initial conditions. The analyses were carried out for mean values of material parameters and also their values considering ±1 standard deviation. The results were assimilated by developing a series of fragility curves and the determination of the annual probability of slope failure.

It was found out that the fragility curves significantly differ in trend depending on the changes in moisture distribution during the rainfall. A higher probability of failure is expected for extreme events with longer return periods. It can also be concluded that fine-grained materials are more prone to failure in comparison to coarse-grained materials. Based on the results, for sand

embankments, only in Toronto and Kenora, the future annual probability of shallow failure is expected to be greater than the values in the historical period. The maximum expected value is 1.2% for the sand embankment in Toronto. However, silt embankments in all ten locations except Kenora are expected to experience a significant increase in APF in the future, especially for wetter initial conditions. An increase in APF from 0.1% in the historical period to 8% in the future was observed for the silt embankment. The comparison between general and shallow failure shows that shallower failures are more susceptible to climatic events. For example, in London, the annual probability of shallow failure in silt embankment is more than five times greater than the annual probability of general failure. Generally, although a maximum value of around 8% was estimated for the annual probability of both types of failures, more cities would experience this maximum value considering shallow failure. Kingston is the only location with an 8% annual probability of general failure, while the annual probability of shallow failure in London, Kingston, and Ottawa is expected to be 8%.

8.2. Contributions of the research

This study has made a number of contributions that would be of considerable value for both practicing engineers and researchers. Some of these contributions are as follows:

- This is the very first study that has compiled, classified, and assessed changing climatic conditions for ten different locations across Ontario. This was accomplished for both long term changes as well as for extreme precipitation events. The systematic quantification of the changes in various climatic parameters will be of interest and use for researchers and practitioners aiming to quantify the effect of climate change on other infrastructure projects.

- This study has used a novel approach based on daily water balance using soil-atmosphere modelling to identify critical climate ensembles from a slope stability perspective. This was accomplished for two different embankment materials. This approach is a significant improvement on previous approaches, that only rely on annual water availability at the ground surface based on atmospheric conditions only, without any consideration to soil hydraulic properties.
- As a part of this research, a comprehensive framework for estimating unsaturated soil hydraulic properties is presented. This framework uses soil properties databases, published values, and pedotransfer functions to estimate soil hydraulic properties for embankment materials. This framework not only estimates the soil hydraulic properties but also quantifies uncertainty in parameter estimation using established procedures. It is envisioned that this framework will be of great value to practitioners and researchers to estimate unsaturated soil hydraulic properties as measured values are not available in most instances.
- In terms of soil-atmosphere modelling, this study has made a number of enhancements to the modelling approaches that have been reported in the literature. Some of these enhancements are as follows:
    - Previous modelling attempts have used the same duration of active periods for historical and future time periods. In the current research, a detailed analysis of the future climate data was carried out to identify the changes in the start and duration of the active period. Different active periods were used for historical and future simulations
    - In soil-atmosphere modelling, it is common to assume that potential evaporation (*PE*) is uniformly distributed over the twenty-four hour period. However, it is well known

that *PE* follows a daily diurnal cycle. In the current study, a novel approach is used to take into account the daily diurnal cycle of *PE*. This approach provides a better representation of the physical process.

- In previous modelling attempts, either daily precipitation data is used in simulations, or daily data is distributed over a single sub-daily interval. The current research effort used an innovative approach to generate sub-daily data from an available time history of daily precipitation data and IDF curves.
- In order to quantify the effect of extreme precipitation events, it is common to assume a constant intensity during a particular storm. In this research, Chicago storm distributions, which have been widely used in Canadian practice, were used. These distributions were derived from available rainfall IDF relationships for all locations considered in this research. These distributions were used to simulate the effect of extreme precipitation events on embankment stability. It is expected that these storm distributions provide a more realistic representation of extreme precipitation events as opposed to the assumption of constant intensity storms.
- This research has also provided a framework for probabilistic assessment of slope stability using fragility curves and estimating the annual probability of failure. One of the novel features of this research is that the probability of load exceedance is taken into account explicitly.

8.3. Recommendations for future research

The intent of the current study was to develop a design methodology to carry out slope stability assessments for highway embankments across Ontario from a climate change perspective. Overall, the study results have revealed that climate change affects the hydrology and stability of the

highway embankments, although not necessarily negatively in all instances. The following is a list of recommendations for future research.

- This study was carried out for ten locations in Ontario. To gain a better understanding of the effect of climate change on the embankment stability across the province of Ontario, it is suggested to expand the number of locations. Similarly, the geometry of the embankment profile was held constant in this study, created based on a review of multiple MTO reports. Therefore, a parametric study on the embankment design parameters such as the height, slope, geology, and material properties would provide an additional understanding of embankment behaviour under changing the climate.
- In this study, the results of statistical analyses on average saturation within the slope area were used for assessment of the long-term performance of slopes. The pore water pressure distribution corresponding to the saturation of P50% and P90% percentiles were considered as the initial conditions for slope stability analyses under extreme rainfalls. It was observed that different PWP distributions exist for the same average saturation within the slope. Therefore, it is recommended to investigate the stability of slope considering different average saturation values with various PWP distributions as the initial conditions.
- Risk assessment analysis is recommended to complement probabilistic analyses that have been carried out as part of this research. In order to ensure the long-term safety and serviceability of the current and future highway embankments exposed to changing climate, a risk register based on the probability and impact of failure should be developed.

Bibliography

Ahmad, F. 2018. Effect of Climate Change on a Monolithic Desulphurized Tailing Cover. York University. Canada.

Baecher, G.B., and Christian, J.T. 2005. Reliability and Statistics in Geotechnical Engineering. John Wiley & Sons,.

Bashir, R., Ahmad, F., and Beddoe, R. 2020. Effect of Climate Change on a Monolithic Desulphurized Tailings Cover. Water, **12**(9): 2645. Multidisciplinary Digital Publishing Institute. doi:10.3390/w12092645.

Bashir, R., Fiaz, A., and Beddoe, R. 2019. Effect of Climate Change on a Monolithic Soil Cover in a Moist Humid Climate. *In* 15th International Conference on Geotechnical Engineering. Lahore, Pakistan.

Bashir, R., and Pastora Chevez, E. 2018. Spatial and Seasonal Variations of Water and Salt Movement in the Vadose Zone at Salt-Impacted Sites. Water, **10**(12): 1833. MDPI AG. doi:10.3390/w10121833.

Bashir, R., Sharma, J., and Stefaniak, H. 2016. Effect of hysteresis of soil-water characteristic curves on infiltration under different climatic conditions. Canadian Geotechnical Journal, **53**(2): 273–284. Canadian Science Publishing. doi:10.1139/cgj-2015-0004.

Batali, L., and Andreea, C. 2016. Slope Stability Analysis Using the Unsaturated Stress Analysis. Case Study. Procedia Engineering, **143**: 284–291. Elsevier Ltd. doi:10.1016/j.proeng.2016.06.036.

Bennion, D.W., and Griffiths, J.C. 1966. A Stochastic Model for Predicting Variations in Reservoir Rock Properties. Society of Petroleum Engineers Journal, **6**(01): 9–16. Society of Petroleum Engineers (SPE). doi:10.2118/1187-pa.

Bo, M.W., Fabius, M., and Fabius, & K. 2008. IMPACT OF GLOBAL WARMING ON STABILITY OF NATURAL SLOPES.

Calamak, M., and Yanmaz, A.M. 2014. Probabilistic Assessment of Slope Stability for Earth-fill Dams Having Random Soil Parameters. : 25–27. doi:10.14264/uql.2014.16.

Carsel, R.F., and Parrish, R.S. 1988. Developing joint probability distributions of soil water retention characteristics. Water Resources Research, **24**(5): 755–769. John Wiley & Sons, Ltd. doi:10.1029/WR024i005p00755.

CCDP. 2018. CCDP - Ontario Climate Change Data Portal. Available from http://www.ontarioccdp.ca/. [accessed 26 February 2020].

Ciabatta, L., Camici, S., Brocca, L., Ponziani, F., Stelluti, M., Berni, N., and Moramarco, T. 2016. Assessing the impact of climate-change scenarios on landslide occurrence in Umbria Region, Italy. Journal of Hydrology, **541**: 285–295. Elsevier B.V. doi:10.1016/j.jhydrol.2016.02.007.

Coe, J.A., and Godt, J.W. 2012. Review of approaches for assessing the impact of climate change on landslide hazards. *In* Landslides and Engineered Slopes: Protecting Society through Improved Understanding - Proceedings of the 11th International and 2nd North American Symposium on Landslides and Engineered Slopes, 2012. [publishername] CRC Press/Balkema. pp. 371–377.

Collison, A., Wade, S., Griffiths, J., and Dehn, M. 2000. Modelling the impact of predicted climate change on landslide frequency and magnitude in SE England. Engineering Geology, **55**(3): 205–218. Elsevier Science Publishers B.V. doi:10.1016/S0013-7952(99)00121-0.

Comegna, L., Picarelli, L., Bucchignani, E., and Mercogliano, P. 2013. Potential effects of incoming climate changes on the behaviour of slow active landslides in clay. **10**: 373–391. doi:10.1007/s10346-012-0339-3.

Coutinho, A.P., Lassabatere, L., Montenegro, S., Antonino, A.C.D., Angulo-Jaramillo, R., and Cabral, J.J.S.P. 2016. Hydraulic characterization and hydrological behaviour of a pilot permeable pavement in an urban centre, Brazil. Hydrological Processes, **30**(23): 4242–4254. John Wiley and Sons Ltd. doi:10.1002/hyp.10985.

Crovelli, R.A. 2000. Probability Models for Estimation of Number and Costs of Landslides Open-File Report 00-249. Denver, Colorado.

Dai, S.., and Wang, M. 1992. Reliability Analysis in Engineering Applications. Van Nostrand Reinhold, New York, NY.,.

Dikau, R., and Schrott, L. 1999. The temporal stability and activity of landslides in Europe with respect to climatic change (TESLEC): Main objectives and results. Geomorphology, **30**(1–2): 1–12. Elsevier. doi:10.1016/S0169-555X(99)00040-9.

Dixon, N., and Brook, E. 2007. Impact of predicted climate change on landslide reactivation: Case study of Mam Tor, UK. Landslides, **4**(2): 137–147. doi:10.1007/s10346-006-0071-y.

Duncan, J.M. 2000. Factors of Safety and Reliability in Geotechnical Engineering. Journal of Geotechnical and Geoenvironmental Engineering, **126**(4): 307–316. American Society of Civil Engineers. doi:10.1061/(ASCE)1090-0241(2000)126:4(307).

Duncan, J.M., and Sleep, M.D. 2018. Evaluating reliability in geotechnical engineering. : 161–210. CRC Press. doi:10.1201/B17970-10.

El-Ramly, H., Morgenstern, N.R., and Cruden, D.M. 2002. Probabilistic slope stability analysis for practice. doi:10.1139/T02-034.

Environment and Climate Change Canada. 2014. Engineering Climate Datasets - Climate - Environment and Climate Change Canada. Available from https://climate.weather.gc.ca/prods_servs/engineering_e.html. [accessed 13 June 2020].

Environment and Climate Change Canada. 2018. Historical Climate Data - Environment and Climate Change Canada. Available from https://climate.weather.gc.ca/historical_data/search_historic_data_e.html. [accessed 25 February 2020].

Environment and Climate Change Canada. 2019. Canadian Climate Normals - Climate - Environment and Climate Change Canada. Available from https://climate.weather.gc.ca/climate_normals/index_e.html. [accessed 15 June 2020].

Fayer, M.J. 2000. UNSAT-H Version 3.0:Unsaturated Soil Water and Heat Flow Model Theory, User Manual, and Examples. Richland, WA (United States).

FHWA. 2002. Subsurface Investigations-Geotechnical Site Characterization Reference Manual National Highway Institute Archived Document.

Fowler, A.M., and Hennessy, K.J. 1995. Potential impacts of global warming on the frequency and magnitude of heavy precipitation. Natural Hazards, **11**(3): 283–303. Kluwer Academic Publishers. doi:10.1007/BF00613411.

Fredlund, D.G. (Delwyn G.., and Rahardjo, H. (Harianto). 1993. Soil mechanics for unsaturated soils. Wiley.

Fredlund, D.G., Rahardjo, H., and Fredlund, M.D. 2012. Unsaturated Soil Mechanics in Engineering Practice.

Fredlund, D.G., and Xing, A. 1994. Equations for the soil-water characteristic curve. *In* Canadian Geotechnical Journal.

Gariano, S.L., and Guzzetti, F. 2016. Landslides in a changing climate. Elsevier B.V.

van Genuchten, M.T. 1980. A Closed-form Equation for Predicting the Hydraulic Conductivity of Unsaturated Soils. Soil Science Society of America Journal, **44**(5): 892–898. Wiley.

doi:10.2136/sssaj1980.03615995004400050002x.

Geo-slope International Ltd. 2019. Stability Modeling with SLOPE/W: An Engineering Methodology (Computer Program). GEOSLOPE/W International Ltd., Calgary, Alberta, Canada.

Goswami, B.N., Venugopal, V., Sangupta, D., Madhusoodanan, M.S., and Xavier, P.K. 2006. Increasing trend of extreme rain events over India in a warming environment. Science, **314**(5804): 1442–1445. doi:10.1126/science.1132027.

Gupta, S.C., and Larson, W.E. 1979. Estimating soil water retention characteristics from particle size distribution, organic matter percent, and bulk density. Water Resources Research, **15**(6): 1633–1635. John Wiley & Sons, Ltd. doi:10.1029/WR015i006p01633.

Han, J., Sheth, A.R., Porbaha, A., and Shen, S.-L. 2004. Numerical Analysis of Embankment Stability over Deep Mixed Foundations. *In* Geotechnical Engineering for Transportation Projects. American Society of Civil Engineers, Reston, VA. pp. 1385–1394.

Harr, M.. 1984. Reliability-based design in civil engineering. Henry M. Shaw Lecture, Dept. of Civil Engineering, North Carolina State University, Raleigh, NC.,.

Hassan, A.M., and Wolff, T.F. 1999. Search Algorithm for Minimum Reliability Index of Earth Slopes. Journal of Geotechnical and Geoenvironmental Engineering, **125**(4): 301–308. ASCE. doi:10.1061/(ASCE)1090-0241(1999)125:4(301).

IPCC. 2007. Climate Change 2007: Synthesis Report. Contribution of Working Groups I, II and III to the Fourth Assessment Report of the Intergovernmental Panel on Climate Change. Geneva, Switzerland.

IPCC. 2013. Climate Change 2013 The Physical Science Basis Working Group I Contribution to the Fifth Assessment Report of the Intergovernmental Panel on Climate Change.

IPCC. 2015. Synthesis Report - Climate Change 2014.

Jasim, F.., Vahedifard, F., Ragno, E., AghaKouchak, A., and Ellithy, G. 2017. Effects of Climate Change on Fragility Curves of Earthen Levees Subjected to Extreme Precipitations Reusing Abandoned Natural Gas Storage Sites for Compressed Air Energy Storage View project Soil stabilization for road subgrade View project. doi:10.1061/9780784480724.045.

Keifer, C.J., and Chu, H.. 1957. Synthetic Storm Pattern for Drainage Design. Journal of the Hydraulics Division, **83**(4): 1–25.

Kramer, S.L. 1996. Geotechnical earthquake engineering. Prentice Hall, Upper Saddle River, N.J.

Kulhawy, F.H. 1992. On the Evaluation of Soil Properties. Geotechnical Special Publication, **31**: 95–115.

Lacasse, S. 2016. Norwegian Geotechnical Institute (NGI) Digital Archive: Hazard, Reliability and Risk Assessment - Research and Practice for Increased Safety. Available from https://ngi.brage.unit.no/ngi-xmlui/handle/11250/2465332. [accessed 6 May 2020].

Liu, W., Luo, X., Huang, F., and Fu, M. 2017. Uncertainty of the Soil–Water Characteristic Curve and Its Effects on Slope Seepage and Stability Analysis under Conditions of Rainfall Using the Markov Chain Monte Carlo Method. Water, **9**(10): 758. MDPI AG. doi:10.3390/w9100758.

Lu, N., and Godt, J. 2012. Hillslope hydrology and stability.

Lu, N., and Likos, W.J. 2006. Suction Stress Characteristic Curve for Unsaturated Soil. Journal of Geotechnical and Geoenvironmental Engineering, **132**(2): 131–142. American Society of Civil Engineers. doi:10.1061/(ASCE)1090-0241(2006)132:2(131).

Lumb, P. 1966. The Variability of Natural Soils. Canadian Geotechnical Journal, **3**(2): 74–97. Canadian Science Publishing. doi:10.1139/t66-009.

Lutz, A.F., ter Maat, H.W., Biemans, H., Shrestha, A.B., Wester, P., and Immerzeel, W.W. 2016. Selecting representative climate models for climate change impact studies: an advanced envelope-based selection approach. International Journal of Climatology, **36**(12): 3988–4005. John Wiley and Sons Ltd. doi:10.1002/joc.4608.

Marsalek, J., and Watt, W.E. 1984. Design storms for urban drainage design. Canadian Journal of Civil Engineering, **11**(3): 574–584. NRC Research Press Ottawa, Canada . doi:10.1139/l84-075.

Martinović, K., Gavin, K., and Reale, C. 2016. Assessing the Vulnerability of Irish Rail Network Earthworks. *In* Transportation Research Procedia. Elsevier B.V. pp. 1904–1913.

Martinović, K., Reale, C., and Gavin, K. 2018. Fragility curves for rainfall-induced shallow landslides on transport networks. Canadian Geotechnical Journal, **55**(6): 852–861. Canadian Science Publishing. doi:10.1139/cgj-2016-0565.

Mbonimpa, M., Aubertin, M., Chapuis, R.P., Bussie`re, B., and Bussie`re, B. 2002. Practical pedotransfer functions for estimating the saturated hydraulic conductivity. Geotechnical and Geological Engineering,: 235–259.

McInnes, R., Jakeways, J., Fairbank, H., and Mathie, E. 2007. Landslides and Climate Change: Challenges and Solutions: Proceedings of the International Conference on Landslides and Climate Change, Ventnor, Isle of.

McKelvie, S.. 1982. Preparing a design storm. Proceedings of Stormwater and Water Quality Management. Athens, GA.

Morgenstern, N.R., and Price, V.E. 1965. The Analysis of the Stability of General Slip Surfaces. Géotechnique, **15**(1): 79–93. Thomas Telford Ltd . doi:10.1680/geot.1965.15.1.79.

Mostyn, G.., and Li, K.. 1993. Probabilistic slope analysis - State-of-play. *In* Conference on

probabilistic methods in geotechnical engineering. A.A. Balkema, Rotterdam, Netherlands. pp. 89–109.

MTO. 1997. Drainage Management Manual. Ronin House Publishing, under contract from Ministry of Transportation of Ontario, Ottawa, Ontario, Canada.

MTO. 2018. IDF Curve Look-up - Ministry of Transportation. Available from http://www.mto.gov.on.ca/IDF_Curves/map_acquisition.shtml. [accessed 26 February 2020].

Mualem, Y. 1976. A new model for predicting the hydraulic conductivity of unsaturated porous media. Water Resources Research, **12**(3): 513–522. John Wiley & Sons, Ltd. doi:10.1029/WR012i003p00513.

Musy, A., Higy, C., and Higy, C. 2010. HYDROLOGICAL REGIMES. : 291–294. CRC Press. doi:10.1201/B10426-74.

Muzik, I. 2002. A first-order analysis of the climate change effect on flood frequencies in a subalpine watershed by means of a hydrological rainfall-runoff model. Journal of Hydrology, **267**(1–2): 65–73. doi:10.1016/S0022-1694(02)00140-3.

NAVFAC. 1982. Foundations and earth structures. Design manual, 7.

Ontario Regions Map. 2011. Available from http://map-canada.blogspot.com/2012/04/ontario-regions-map.html. [accessed 19 April 2020].

Otálvaro, I., and Cordao-Neto, M. 2013. Probabilistic analyses of slope stability under infiltration conditions. doi:10.1201/b14393-84.

Park, H.J., Lee, J.H., and Woo, I. 2013. Assessment of rainfall-induced shallow landslide susceptibility using a GIS-based probabilistic approach. Engineering Geology, **161**: 1–15. Elsevier. doi:10.1016/j.enggeo.2013.04.011.

Peck, A., Prodanovic, P., and Simonovic, S.P.P. 2012. Rainfall Intensity Duration Frequency Curves Under Climate Change: City of London, Ontario, Canada. Canadian Water Resources Journal / Revue canadienne des ressources hydriques, **37**(3): 177–189. doi:10.4296/cwrj2011-935.

Penman, H.L. 1948. Natural evaporation from open water, hare soil and grass. Proceedings of the Royal Society of London. Series A, Mathematical and physical sciences, **193**(1032): 120–145. doi:10.1098/rspa.1948.0037.

Phoon, K.-K., Asce, M., Santoso, A., and Cheng, Y. 2008. Probabilistic Analysis of Soil Water Characteristic Curves from Sandy Clay Loam.

Phoon, K.-K., Santoso, A., and Quek, S.-T. 2010. Probabilistic Analysis of Soil-Water Characteristic Curves. Journal of Geotechnical and Geoenvironmental Engineering, **136**(3): 445–455. American Society of Civil Engineers. doi:10.1061/(ASCE)GT.1943-5606.0000222.

Phoon, K.., and Ching, J. 2015. Risk and Reliability in Geotechnical Engineering. Taylor & Francis Group 6000 Broken Sound Parkway NW, Suite 300 Boca Raton, FL 33487-2742.

Pk, S. 2017. Effects of Climate Change on Soil Embankments. York University. Canada.

Pk, S., Bashir, R., and Beddoe, R. 2018. Effect of Climate Change on Earthen Embankments in Southern Ontario. Environmental Geotechnics,.

Powers, P. 1992. Construction Dewatering: New Methods and Applications - J. Patrick Powers - Google Books. *In* 2nd edition. John Wiley & Sons.

Prodanovic, P., and Simonovic, S. 2004. Generation of Synthetic Design Storms for the Upper Thames River Basin. Water Resources Research Report,.

Rahardjo, H., Lim, T.T., Chang, M.F., and Fredlund, D.G. 1995. Shear-strength characteristics of

a residual soil. Canadian Geotechnical Journal, **32**(1): 60–77. NRC Research Press Ottawa, Canada . doi:10.1139/t95-005.

Rahardjo, H., Nio, A.S., Leong, E.C., and Song, N.Y. 2010. Effects of Groundwater Table Position and Soil Properties on Stability of Slope during Rainfall. Journal of Geotechnical and Geoenvironmental Engineering, **136**(11): 1555–1564. doi:10.1061/(ASCE)GT.1943-5606.0000385.

Rawls, W.J., Brakensiek, D.L., and Saxtonn, K.E. 1982. Estimation of Soil Water Properties. Transactions of the ASAE, **25**(5): 1316–1320. American Society of Agricultural and Biological Engineers. doi:10.13031/2013.33720.

Rianna, G., Zollo, A., Tommasi, P., Paciucci, M., Comegna, L., and Mercogliano, P. 2014. NC-ND license (http://creativecommons.org/licenses/by-nc-nd/3.0/). Selection and peer-review under responsibility of Dipartimento di Ingegneria Civile The Third Italian Workshop on Landslides Evaluation of the effects of climate changes on landslide activity of Orvieto clayey slope ScienceDirect. Procedia Earth and Planetary Science, **9**: 54–63. doi:10.1016/j.proeps.2014.06.017.

Robinson, J.D., Vahedifard, F., and AghaKouchak, A. 2017. Rainfall-triggered slope instabilities under a changing climate: comparative study using historical and projected precipitation extremes. Canadian Geotechnical Journal, **54**(1): 117–127. NRC Research Press. doi:10.1139/cgj-2015-0602.

Salathe, E.P., Mote, P.W., and Wiley, M.W. 2007. Review of scenario selection and downscaling methods for the assessment of climate change impacts on hydrology in the United States pacific northwest. International Journal of Climatology, **27**(12): 1611–1621. John Wiley & Sons, Ltd. doi:10.1002/joc.1540.

Schaap, M.G., Leij, F.J., and Van Genuchten, M.T. 2001. Rosetta: A computer program for estimating soil hydraulic parameters with hierarchical pedotransfer functions. Journal of Hydrology, **251**(3–4): 163–176. Elsevier. doi:10.1016/S0022-1694(01)00466-8.

Schmidt, J., and Dikau, R. 2004. Modeling historical climate variability and slope stability. Geomorphology, **60**(3–4): 433–447. doi:10.1016/j.geomorph.2003.11.001.

Šejna, M., and Van Genuchten, M.T. 2018. New features of version 3 of the HYDRUS (2D/3D) computer software package. J. Hydrol. Hydromech, **66**: 133–142. doi:10.1515/johh-2017-0050.

Sharma, R.K. 2016. Reliability Analysis of Slope Stability using Monte Carlo Simulation and Comparison with Deterministic Analysis. The 7th International Conference on Computational Methods (ICCM2016),.

Simunek, J., Van Genuchten, M., and Sejna, M. 2009. THE HYDRUS-1D SOFTWARE PACKAGE FOR SIMULATING THE ONE-DIMENSIONAL MOVEMENT OF WATER, HEAT, AND MULTIPLE SOLUTES IN VARIABLY-SATURATED MEDIA.

Šimůnek, J., and Šejna, M. 2018. Notes on Spatial and Temporal Discretization (when working with HYDRUS).

Smith, J.A., and Karr, A.F. 1990. A statistical model of extreme storm rainfall. Journal of Geophysical Research, **95**(D3): 2083. John Wiley & Sons, Ltd. doi:10.1029/JD095iD03p02083.

SVOffice. 2009. SVSLOPE - 2D/3D LEM Slope Stability Analysis | Bentley Systems.

Switzman, H., Razavi, T., Traore, S., Coulibaly, P., Burn, D.H., Henderson, J., Fausto, E., and Ness, R. 2017. Variability of Future Extreme Rainfall Statistics: Comparison of Multiple IDF Projections. Journal of Hydrologic Engineering, **22**(10): 04017046. American Society of

Civil Engineers (ASCE). doi:10.1061/(ASCE)HE.1943-5584.0001561.

Tegos, A., Efstratiadis, A., Malamos, N., Mamassis, N., and Koutsoyiannis, D. 2015. Evaluation of a Parametric Approach for Estimating Potential Evapotranspiration Across Different Climates. Agriculture and Agricultural Science Procedia, **4**: 2–9. Elsevier BV. doi:10.1016/j.aaspro.2015.03.002.

Thornthwaite, C.W. 1948. An Approach toward a Rational Classification of Climate. Geographical Review, **38**(1): 55. JSTOR. doi:10.2307/210739.

Thornthwaite, C.W., and Hare, F.K. 1955. Climatic classification in forestry. Unasylva, **9**: 51–59.

Tsubaki, R., David Bricker, J., Ichii, K., and Kawahara, Y. 2016. Development of fragility curves for railway embankment and ballast scour due to overtopping flood flow. Hazards Earth Syst. Sci, **16**: 2455–2472. doi:10.5194/nhess-16-2455-2016.

USACE. 1984. Hydrologic Modeling System HEC-HMS Technical Reference Manual CPD-74B.

USDA. 2018. National Soil Survey Handbook (NSSH) | NRCS Soils. Available from https://www.nrcs.usda.gov/wps/portal/nrcs/detail/soils/ref/?cid=nrcs142p2_054242. [accessed 6 March 2020].

Vanapalli, S.K., Fredlund, D.G., Pufahl, D.E., and Clifton, A.W. 1996. Model for the prediction of shear strength with respect to soil suction Characterization of the Mechanistic-Empirical Pavement Design Guide Input Parameters for the Resilient Modulus of Ontario Subgrade Soils View project Model for the prediction of shear. Article in Canadian Geotechnical Journal,. doi:10.1139/t96-060.

Veneziano, D., and Villani, P. 1999. Best linear unbiased design hyetograph. Water Resources Research, **35**(9): 2725–2738. American Geophysical Union. doi:10.1029/1999WR900156.

van Vuuren, D.P., Edmonds, J.A., Kainuma, M., Riahi, K., and Weyant, J. 2011. A special issue

on the RCPs. Climatic Change, **109**(1): 1–4. doi:10.1007/s10584-011-0157-y.

Watt, W.E., Chow, K.C.A., Hogg, W.D., and Lathem, K.W. 1986. A 1-h urban design storm for Canada. Canadian Journal of Civil Engineering, **13**(3): 293–300. NRC Research Press Ottawa, Canada . doi:10.1139/l86-041.

Whetton, P.H., Fowler, A.M., Haylock, M.R., and Pittock, A.B. 1993. Implications of climate change due to the enhanced greenhouse effect on floods and droughts in Australia. Climatic Change, **25**(3–4): 289–317. Kluwer Academic Publishers. doi:10.1007/BF01098378.

Wolff, T.F. 1994. Evaluating the reliability of existing levees.

Xue, J.F., and Gavin, K. 2007. Simultaneous determination of critical slip surface and reliability index for slopes. Journal of Geotechnical and Geoenvironmental Engineering, **133**(7): 878–886. doi:10.1061/(ASCE)1090-0241(2007)133:7(878).

Yen, B.C., and Chow, V.T. 1980. DESIGN HYETOGRAPHS FOR SMALL DRAINAGE STRUCTURES. Journal of the Hydraulics Division, **106**(HY6).

Zhang, J., and Huang, H.W. 2016. Risk assessment of slope failure considering multiple slip surfaces. Computers and Geotechnics, **74**: 188–195. Elsevier Ltd. doi:10.1016/j.compgeo.2016.01.011.

Appendices

Appendix A: Material Properties

Table A.1 Descriptive statics for saturated water content (modified from Carsel and Parrish 1988)

Soil Type	Saturated water content θ_s			
	x	SD	CV	n
Clay*	0.38	0.09	24.1	400
Clay loam	0.41	0.09	22.4	364
Loam	0.43	0.10	22.1	735
Loamy sand	0.41	0.09	21.6	315
Silt	0.46	0.11	17.4	82
Silt loam	0.45	0.08	18.7	1093
Silt clay	0.36	0.07	19.6	374
Silty clay loam	0.43	0.07	17.2	641
Sand	0.43	0.06	15.1	246
Sandy clay	0.38	0.05	13.7	46
Sandy clay loam	0.39	0.07	17.5	214
Sandy loam	0.41	0.09	21.0	1183

x: Mean value, SD: Standard deviation, CV: Coefficient of variation (%), and n: sample size. *Agricultural soil: less than 60%clay.

Table A.2 Descriptive statics for residual water content (modified from Carsel and Parrish 1988)

Soil Type	Residual water content θ_r			
	x	SD	CV	n
Clay*	0.068	0.034	49.9	353
Clay loam	0.095	0.010	10.1	363
Loam	0.078	0.013	16.5	735
Loamy sand	0.057	0.015	25.7	315
Silt	0.034	0.010	29.8	82
Silt loam	0.067	0.015	21.6	1093
Silt clay	0.070	0.023	33.5	371
Silty clay loam	0.089	0.009	10.9	641
Sand	0.045	0.010	22.3	246
Sandy clay	0.100	0.013	12.9	46
Sandy clay loam	0.100	0.006	6.0	214
Sandy loam	0.065	0.017	26.6	1183

x: Mean value, SD: Standard deviation, CV: Coefficient of variation (%), and n: sample size. *Agricultural soil: less than 60%clay.

Table A.3 Descriptive statics for retention parameter α (modified from Carsel and Parrish 1988)

Soil Type	α (1/cm)			
	x	SD	CV	n
Clay*	0.008	0.012	160.3	400
Clay loam	0.019	0.015	77.9	363
Loam	0.036	0.021	57.1	735
Loamy sand	0.124	0.043	35.2	315
Silt	0.016	0.007	45.0	82
Silt loam	0.020	0.012	64.7	1093
Silt clay	0.005	0.005	113.6	126
Silty clay loam	0.010	0.006	61.5	641
Sand	0.145	0.029	20.3	246
Sandy clay	0.027	0.017	61.7	46
Sandy clay loam	0.059	0.038	64.6	214
Sandy loam	0.075	0.037	49.4	1183

x: Mean value, SD: Standard deviation, CV: Coefficient of variation (%), and n: sample size. *Agricultural soil: less than 60%clay.

Table A.4 Descriptive statics for retention parameter α (modified from Carsel and Parrish 1988)

No.	PTF	SWCC model	Soil properties used in PTF				
			Sand (%)	Silt (%)	Clay (%)	OC[1]	DD[2]
1	Gupta and Larson 1979	WH[3]/VG[4]	+	+	+	+	+
2	Rawls et al. 1982	WH/VG	+	+	+	+	+
3	Rawls et al. 1983	WH/VG	+	+	+	+	+
4	Rajkaj and Varallyay 1992	WH/VG	+		+	+	+
5	Vereecken et al. 1989	VG	+	+	+	+	+
6	Tomasellla and Hodnett 1998	WH/VG		+	+	+	
7	Wosten et al. 1999	VG	+	+	+		
8	Schaap et al. 2001	VG	+	+	+		

OC[1]: Organic content, DD[2]: Dry density, WH[3]: Water content at fixed capillary pressure, VG[4]: van Genuchten model

Appendix B: Climate data

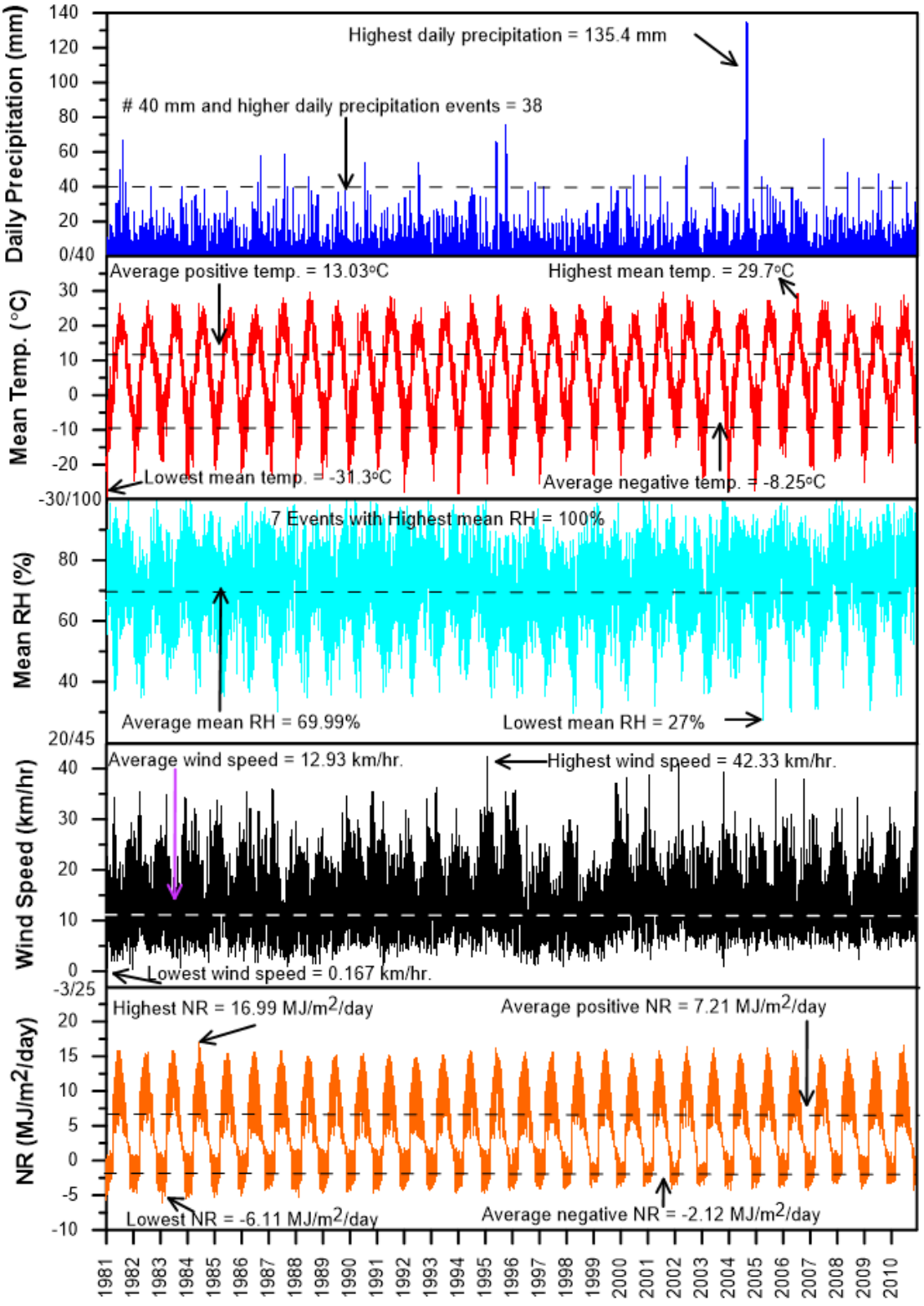

Figure B.1 Historical climate data for Ottawa

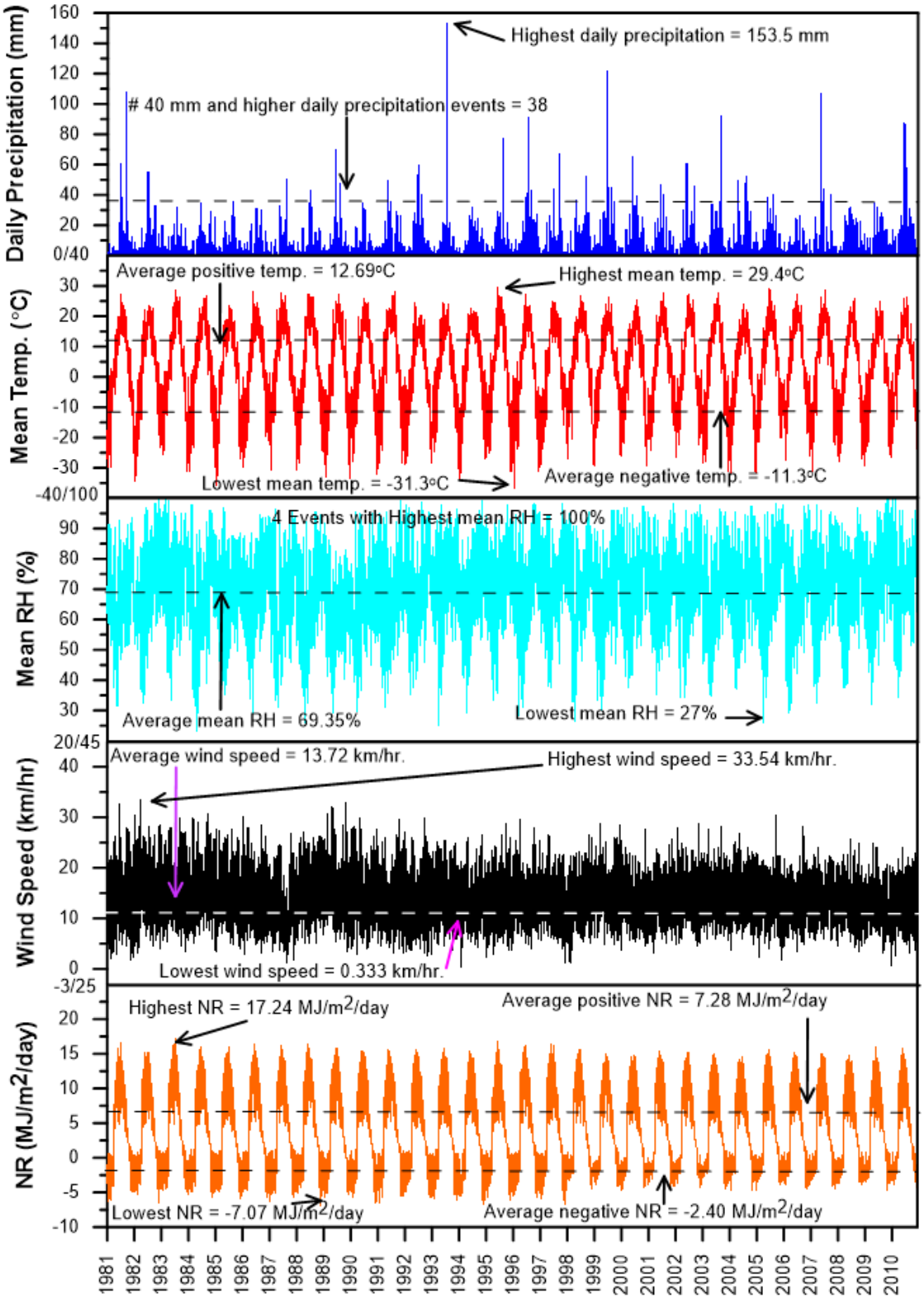

Figure B.2 Historical climate data for Kenora

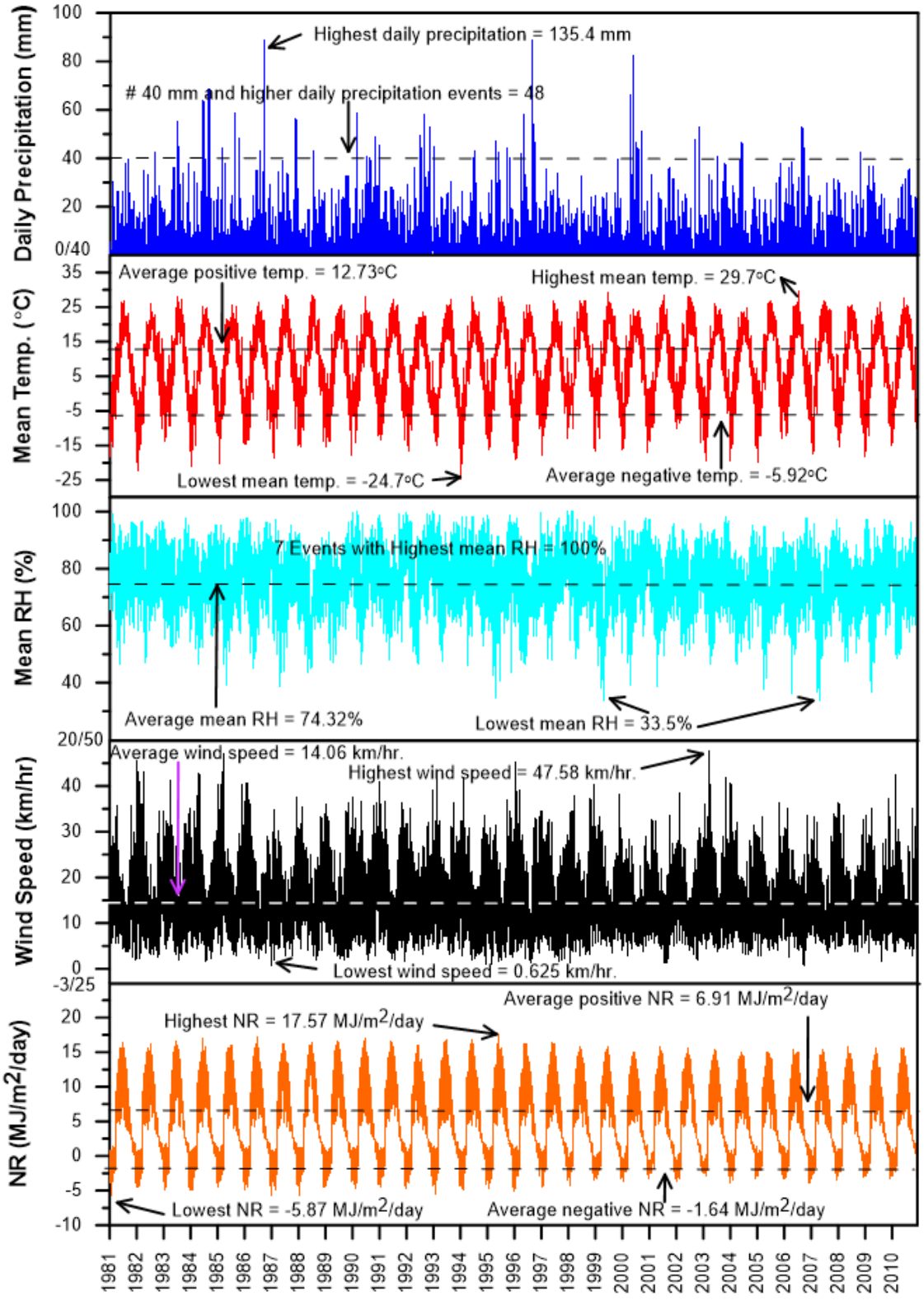

Figure B.3 Historical climate data for London

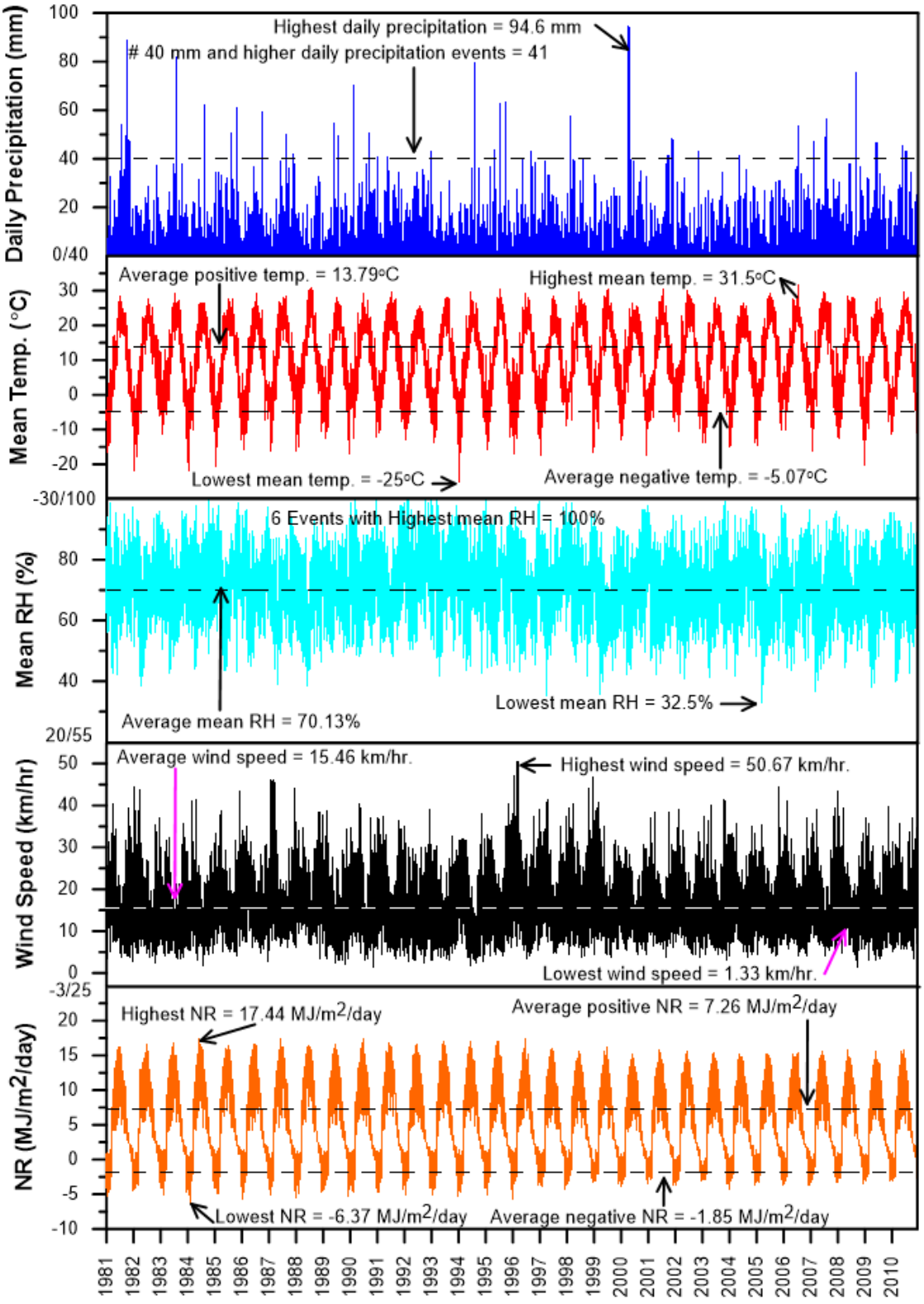

Figure B.4 Historical climate data for Windsor

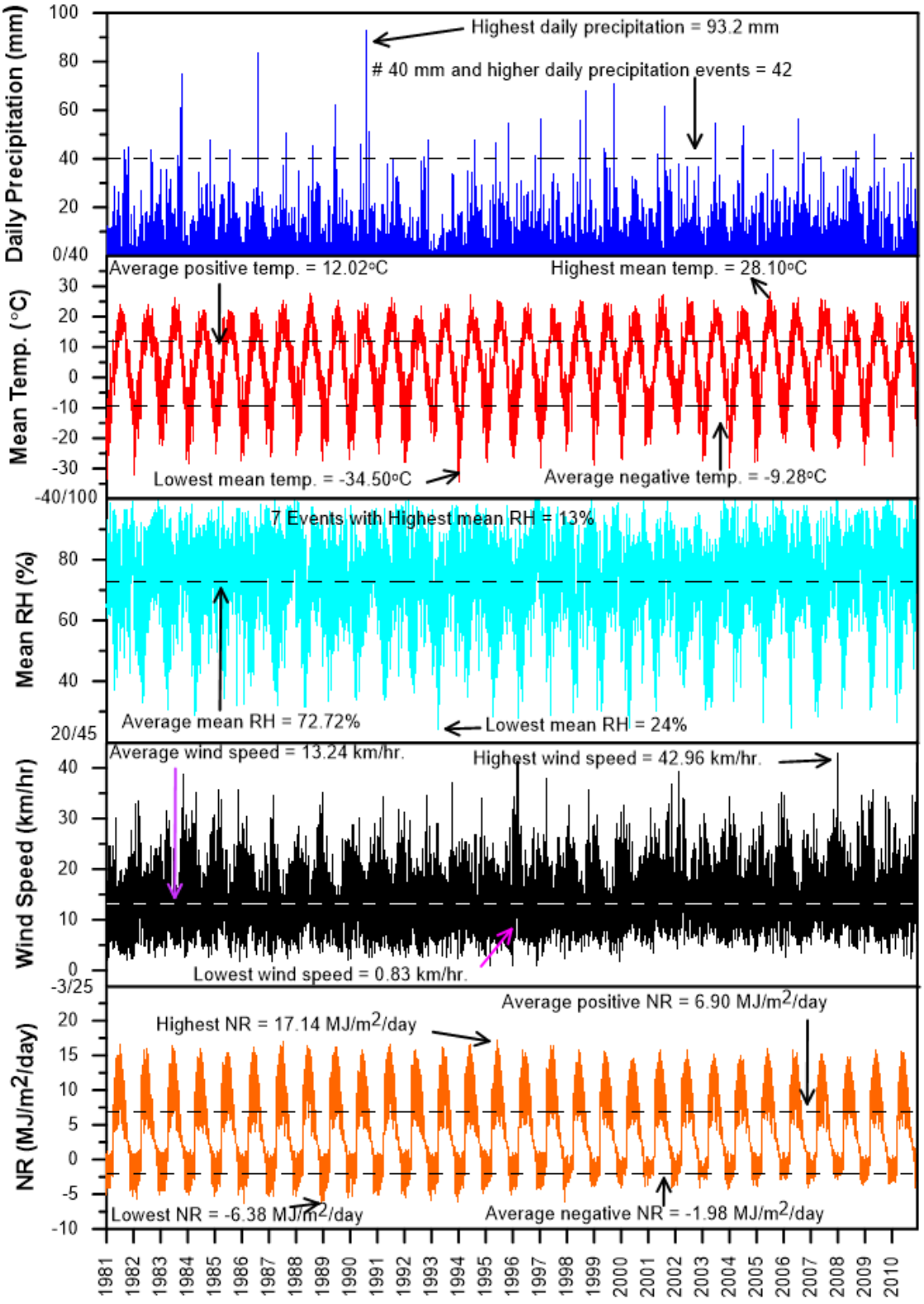

Figure B.5 Historical climate data for North Bay

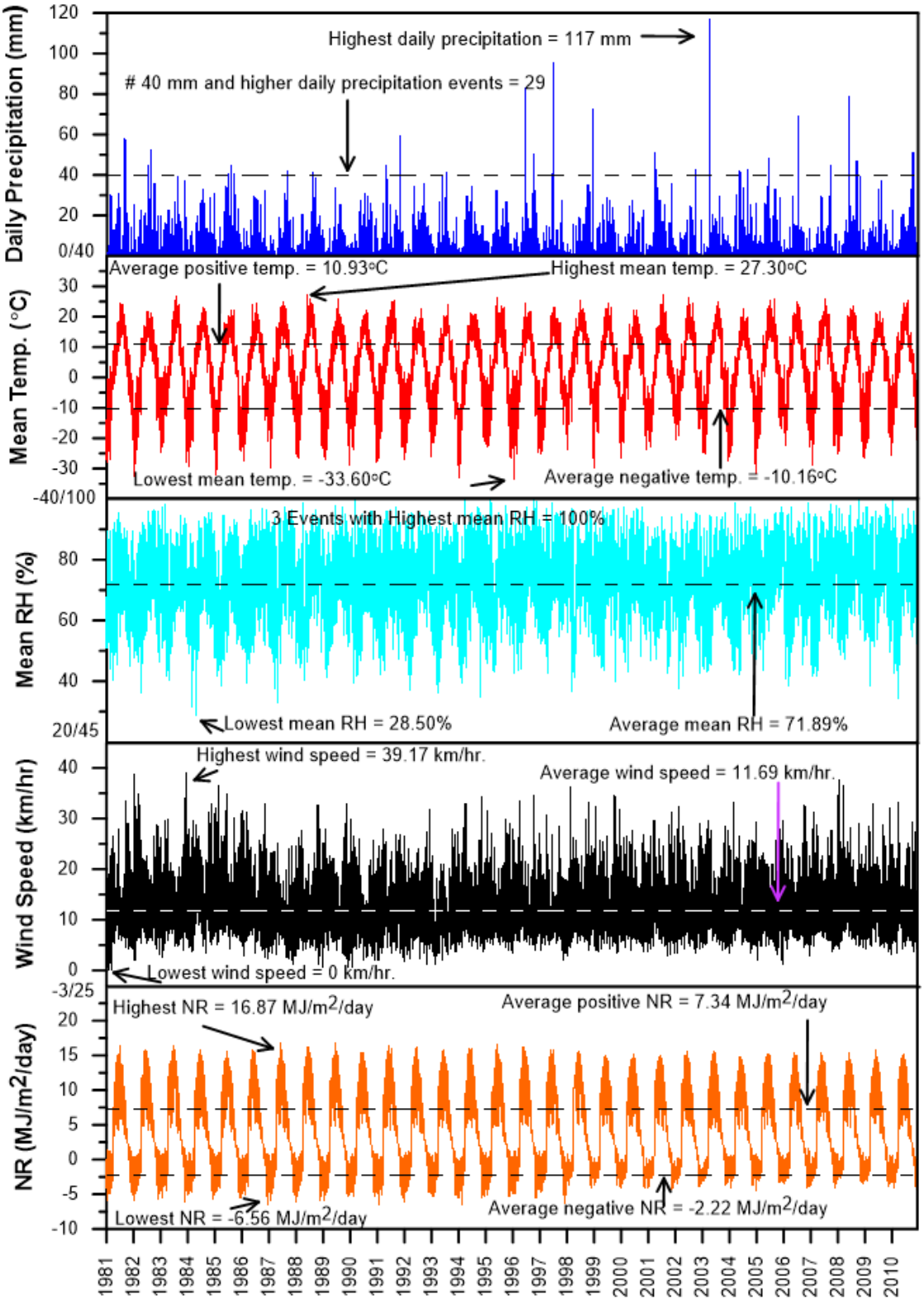

Figure B.6 Historical climate data for Thunder Bay

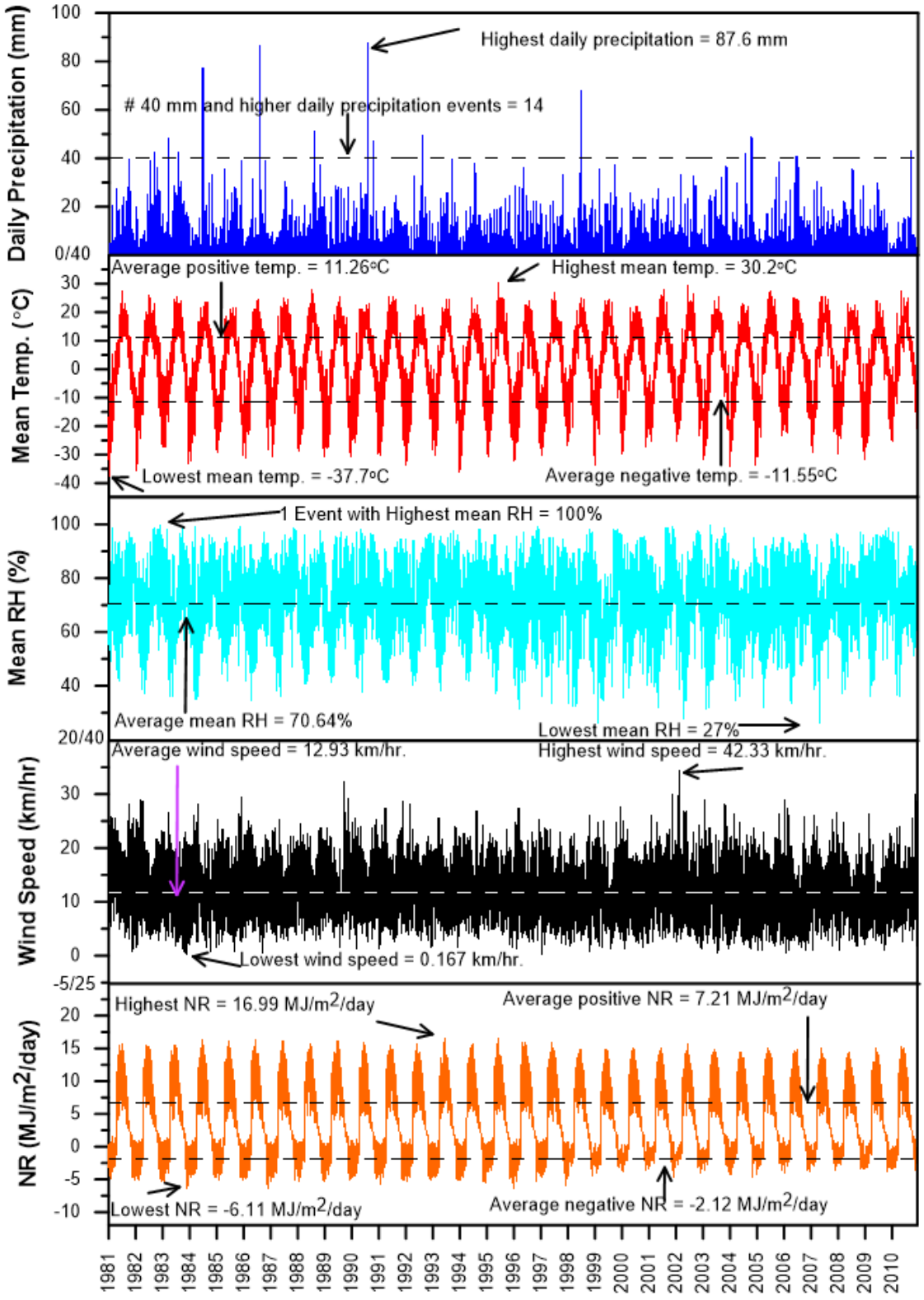

Figure B.7 Historical climate data for Timmins

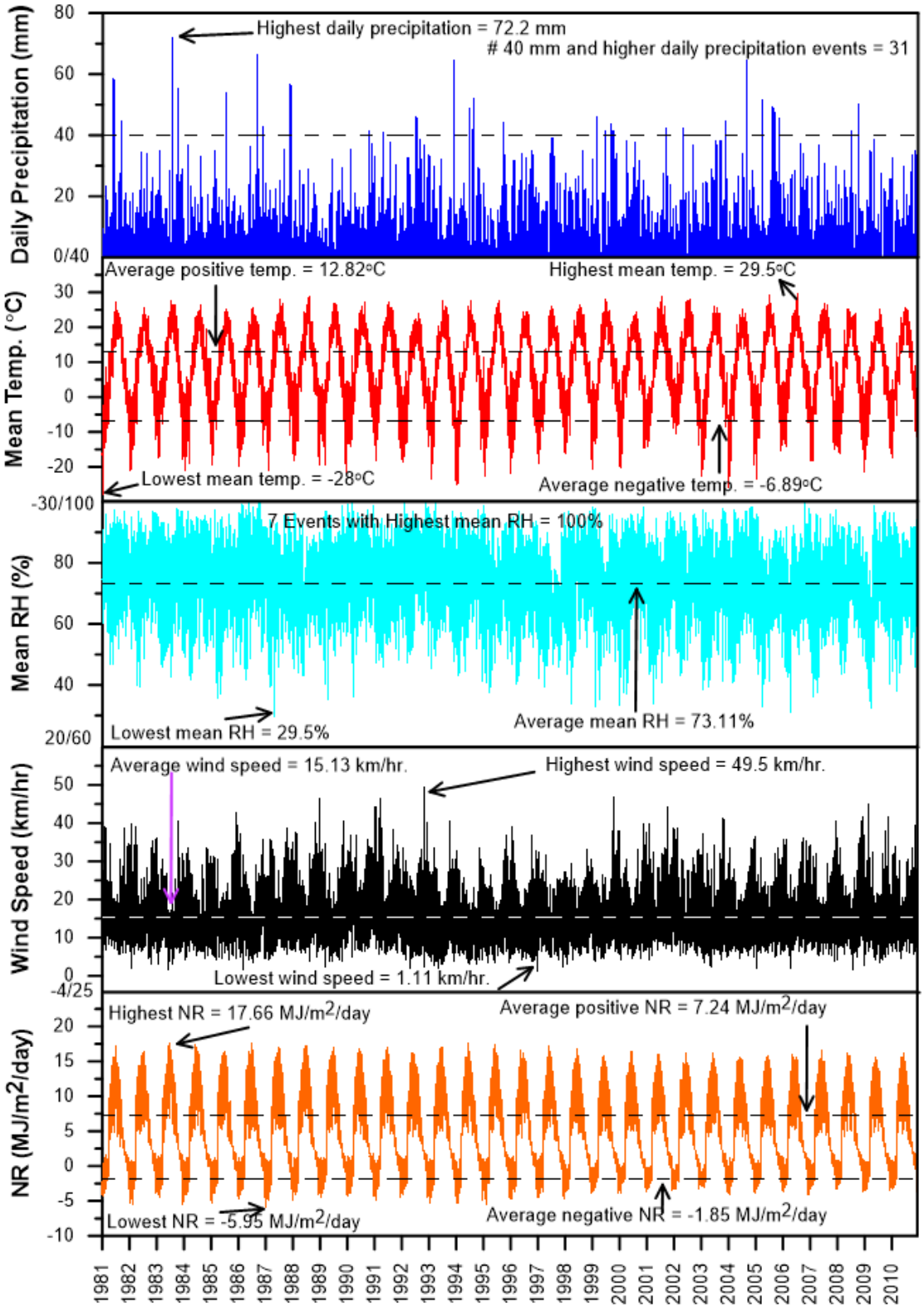

Figure B.8 Historical climate data for Kingston

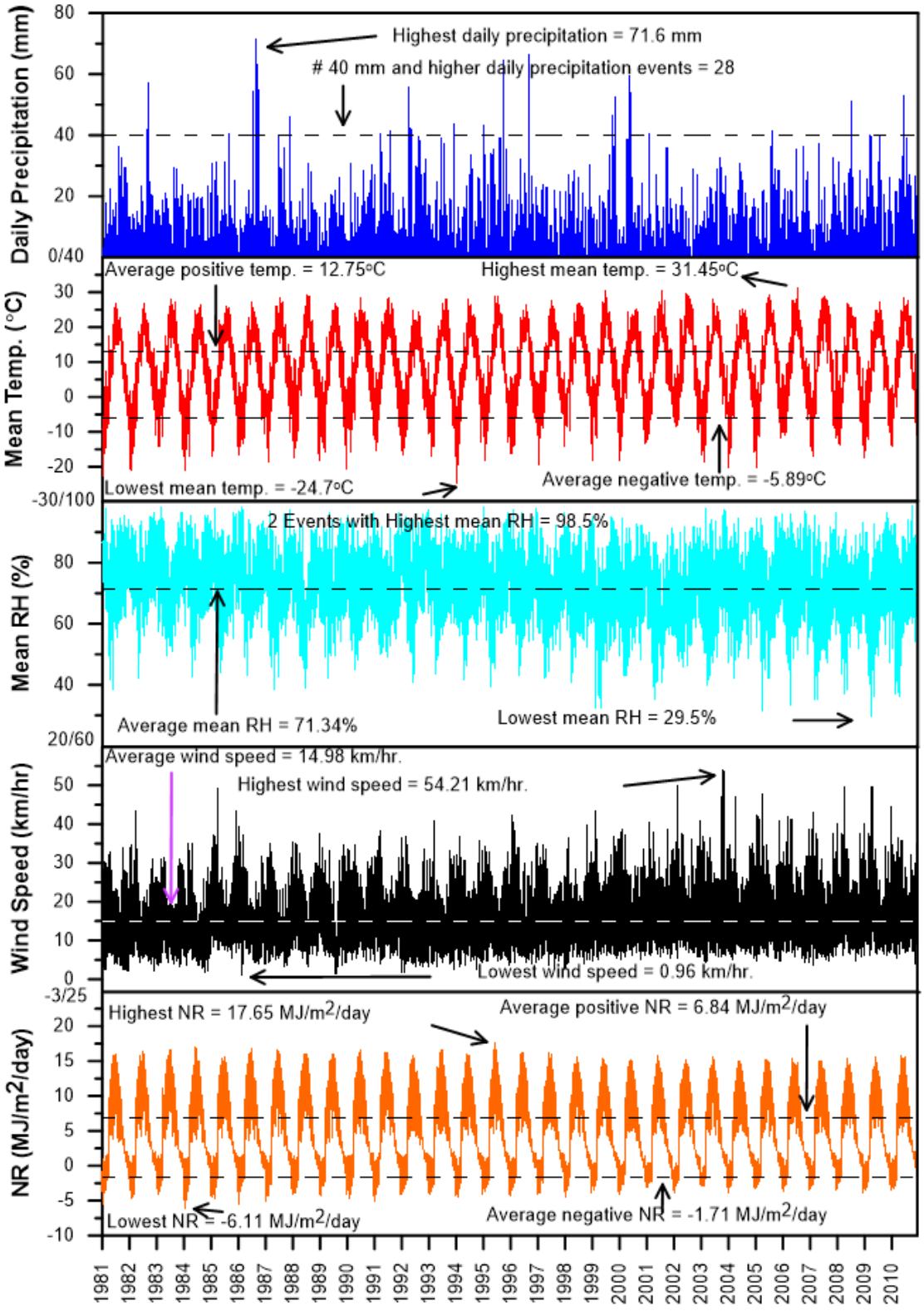

Figure B.9 Historical climate data for Toronto

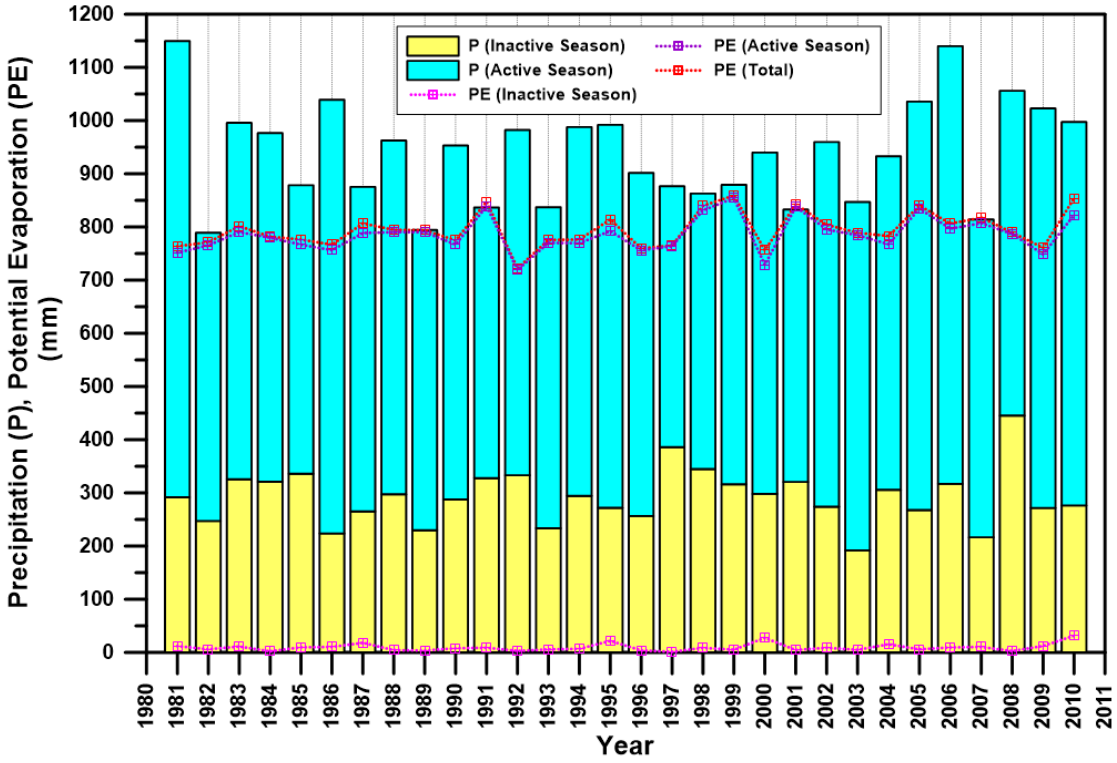

Figure B.10 Precipitation during active and inactive periods, and PE during the active period for Ottawa

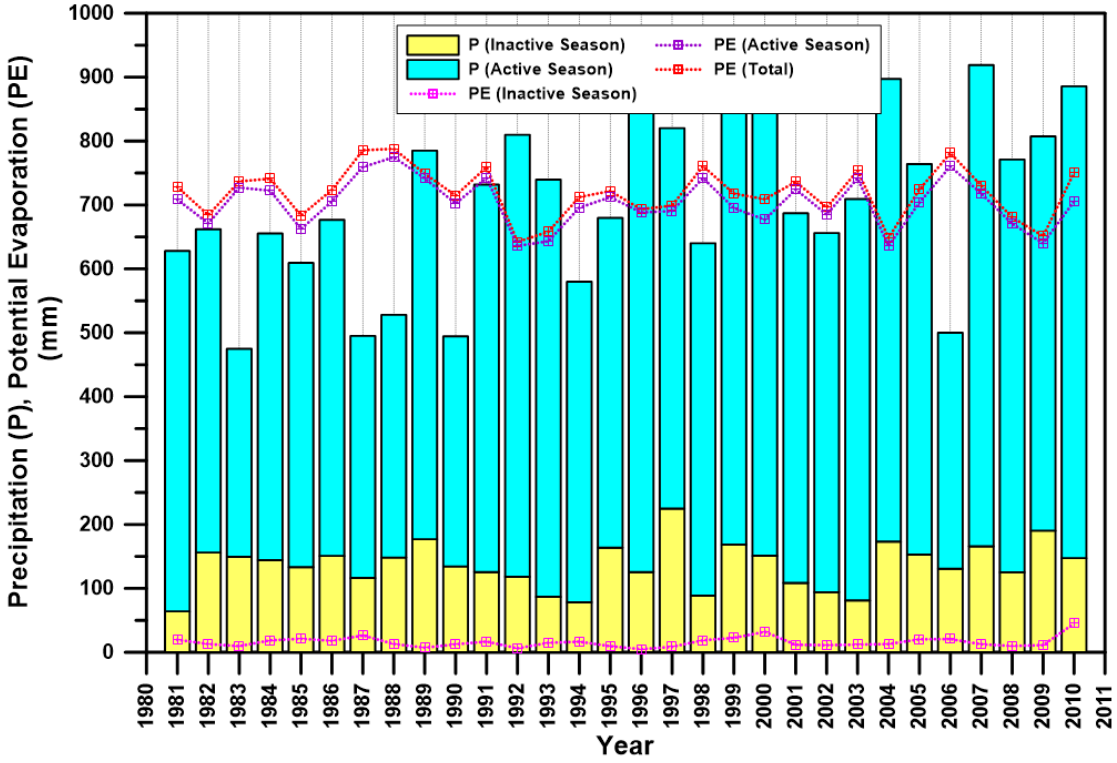

Figure B.11 Precipitation during active and inactive periods, and PE during the active period for Kenora

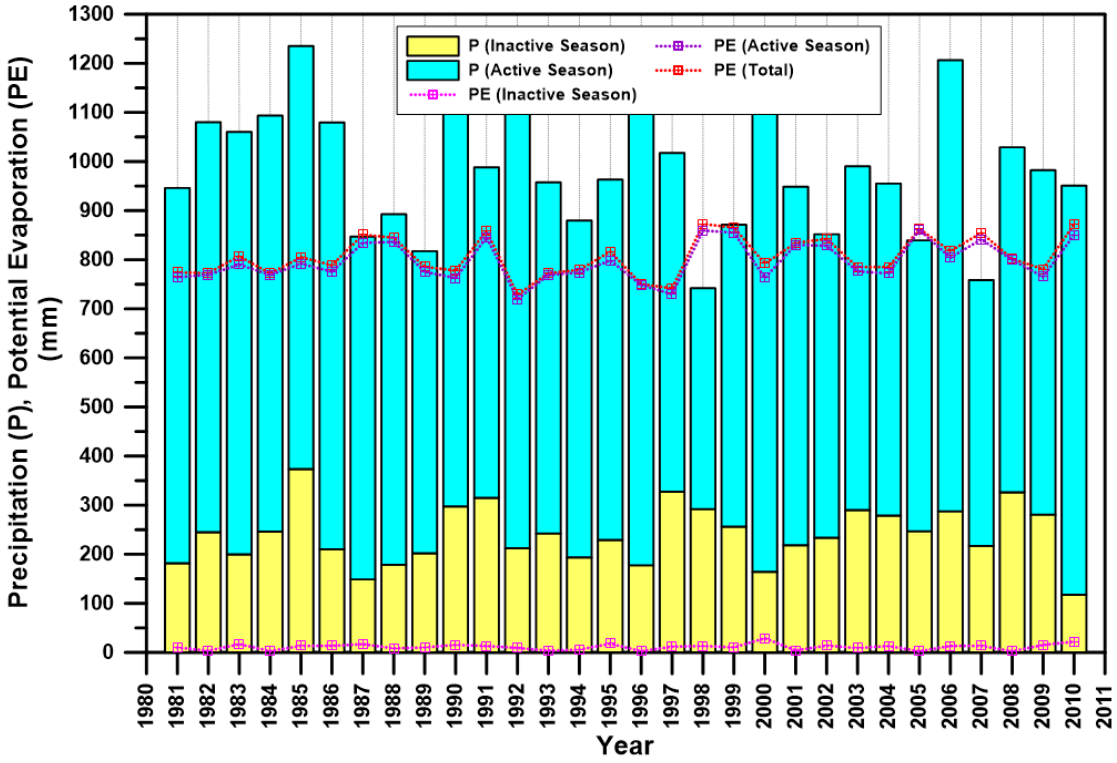

Figure B.12 Precipitation during active and inactive periods, and PE during the active period for London

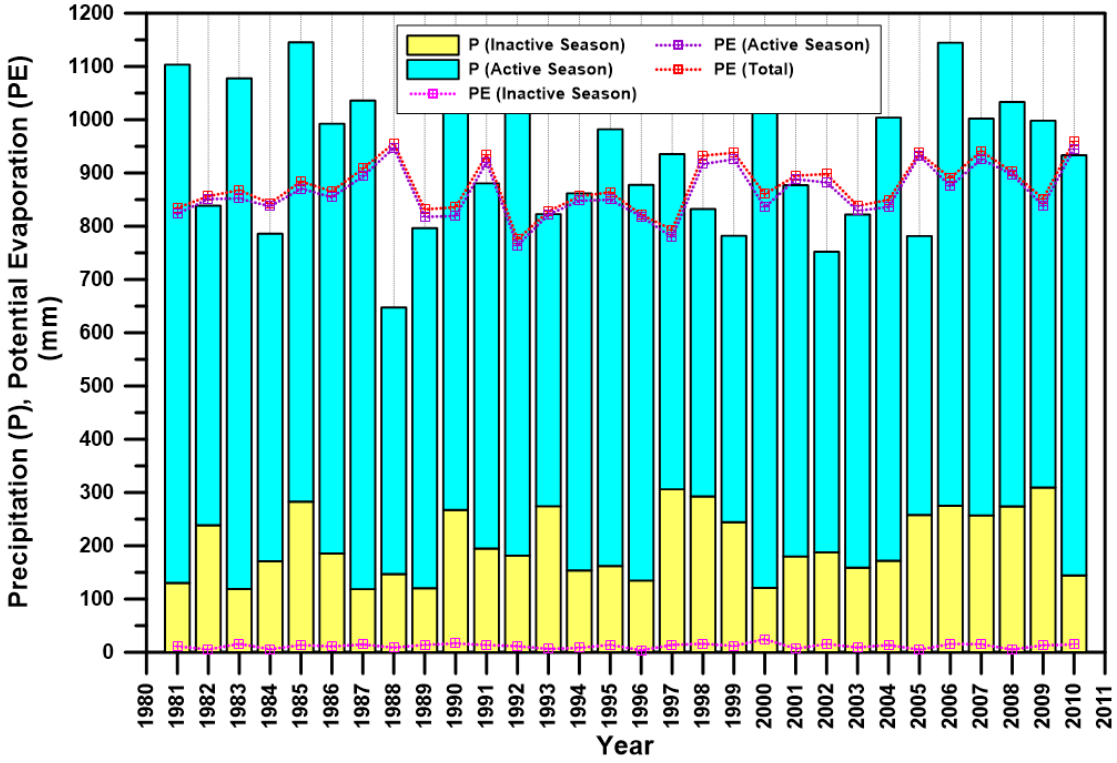

Figure B.13 Precipitation during active and inactive periods, and PE during the active period for Windsor

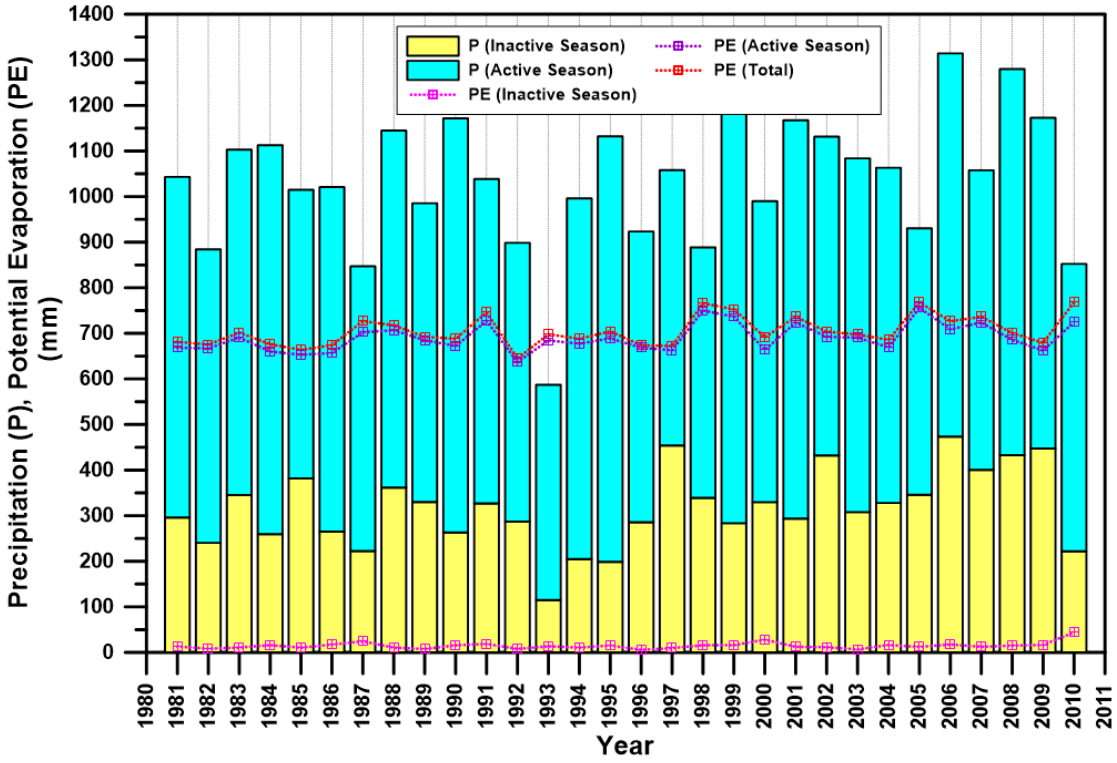

Figure B.14 Precipitation during active and inactive periods, and PE during the active period for North Bay

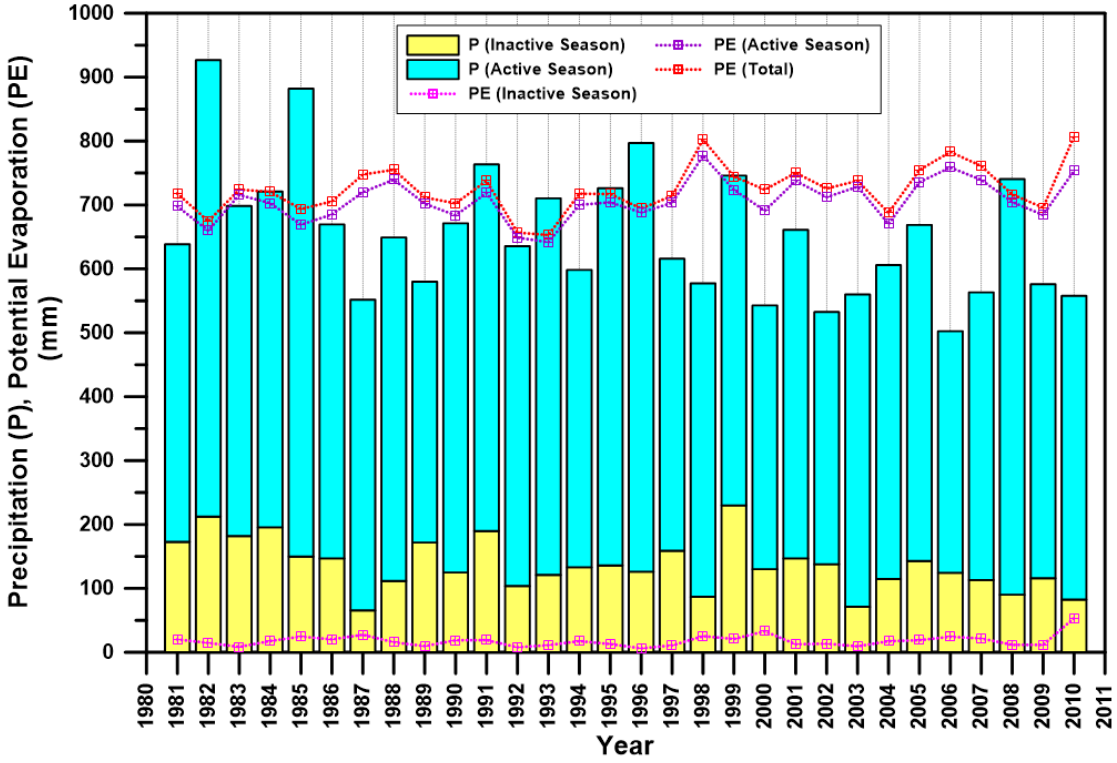

Figure B.15 Precipitation during active and inactive periods, and PE during the active period for Thunder Bay

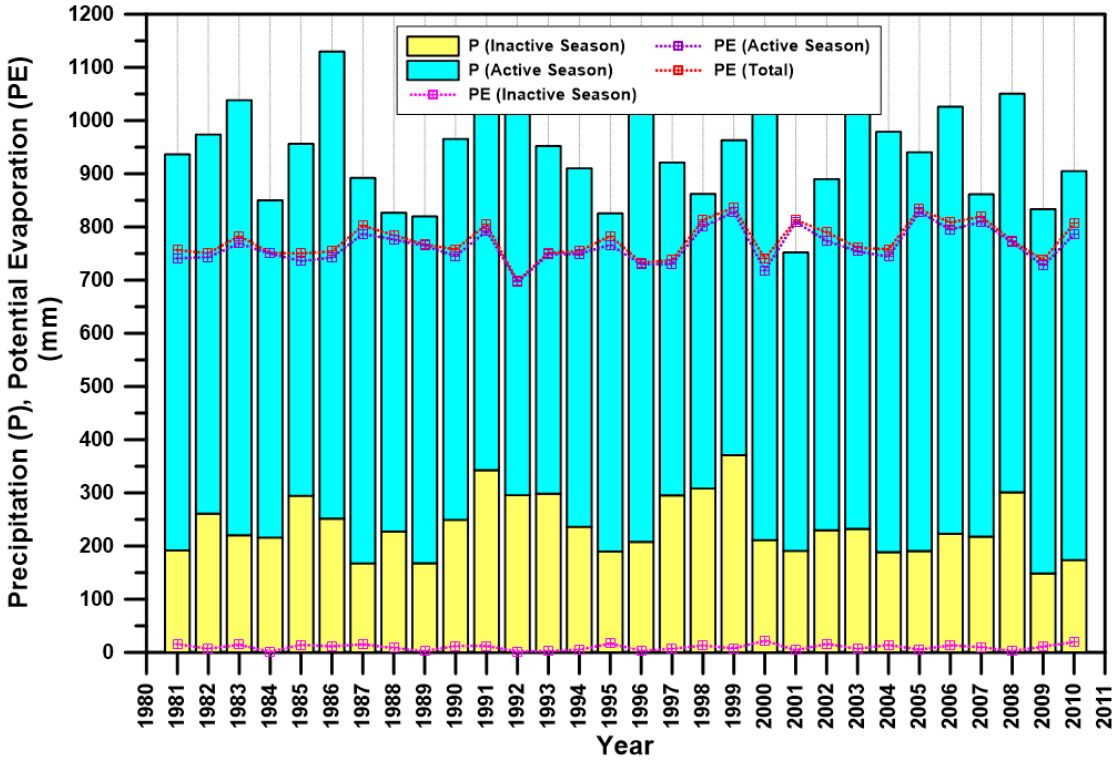

Figure B.16 Precipitation during active and inactive periods, and PE during the active period for Kingston

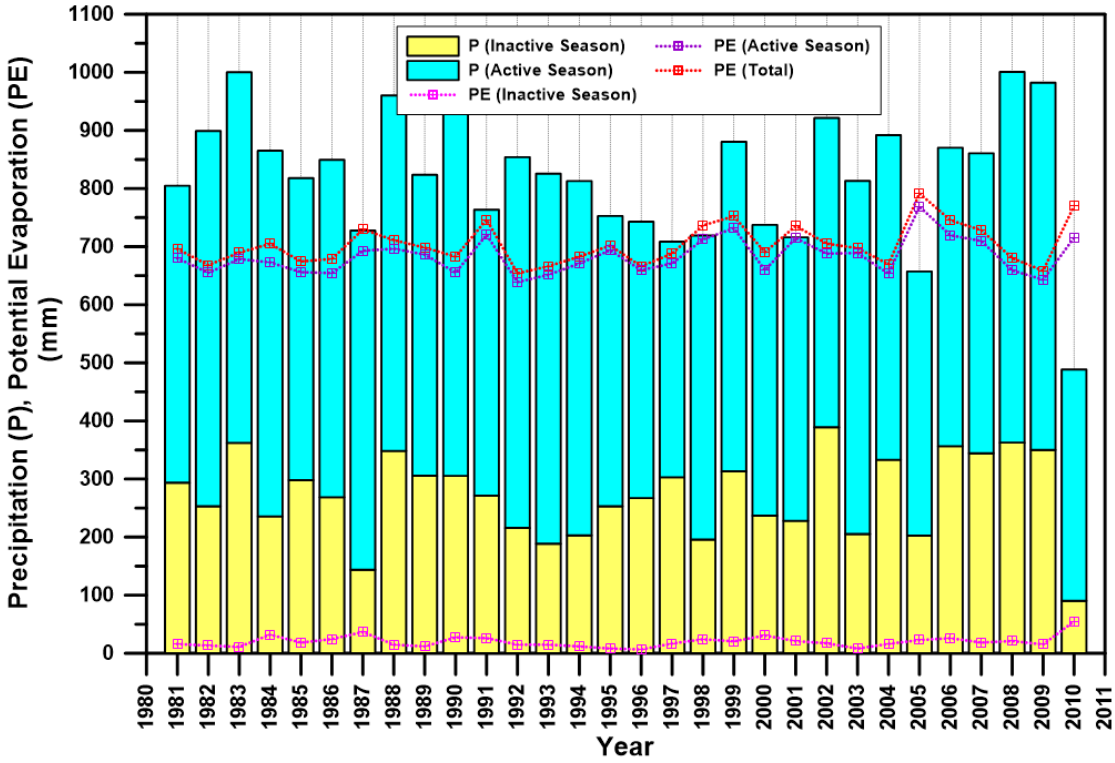

Figure B.17 Precipitation during active and inactive periods, and PE during the active period for Timmins

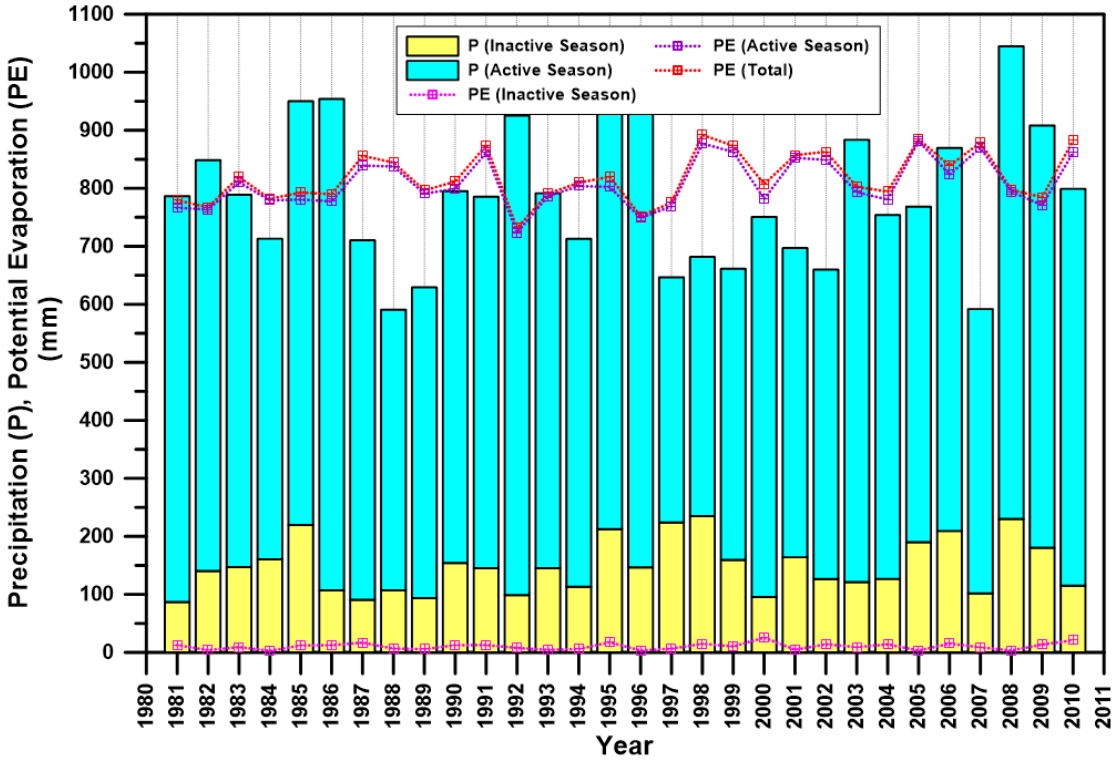

Figure B.18 Precipitation during active and inactive periods, and PE during the active period for Toronto

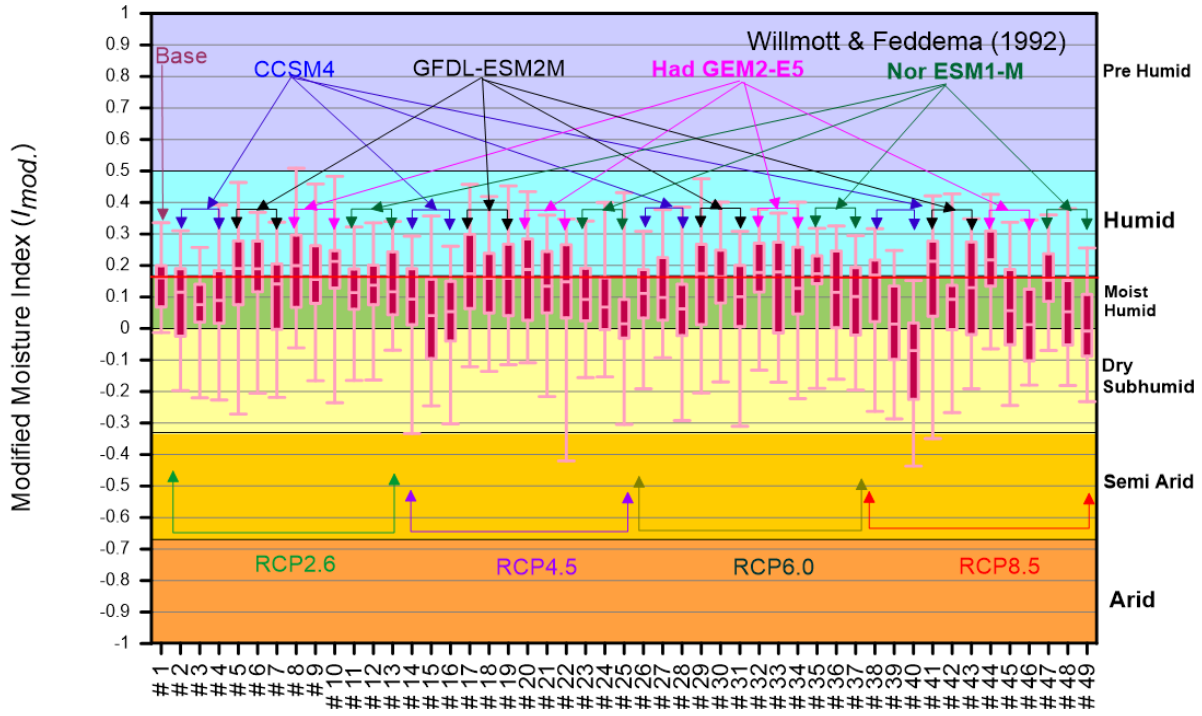

Figure B.19 Yearly variation of the annual moisture index for Ottawa

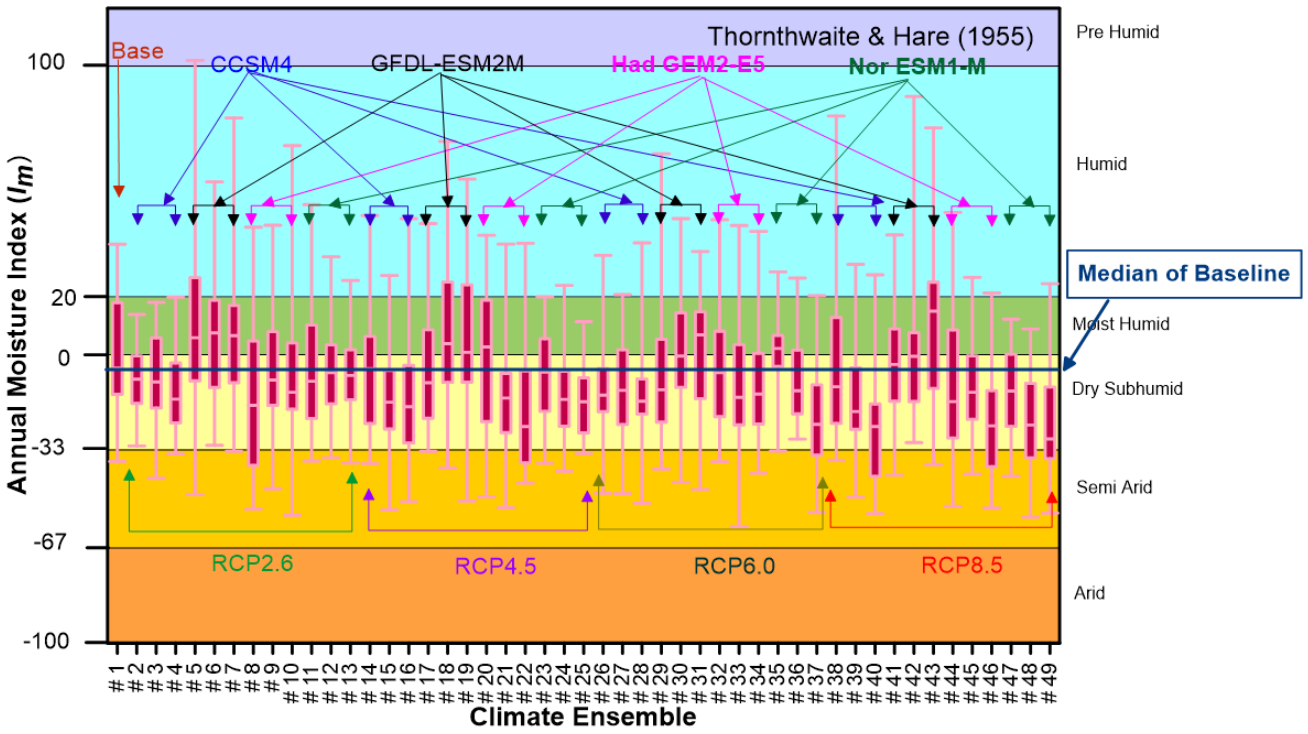

Figure B.20 Yearly variation of the annual moisture index for Kenora

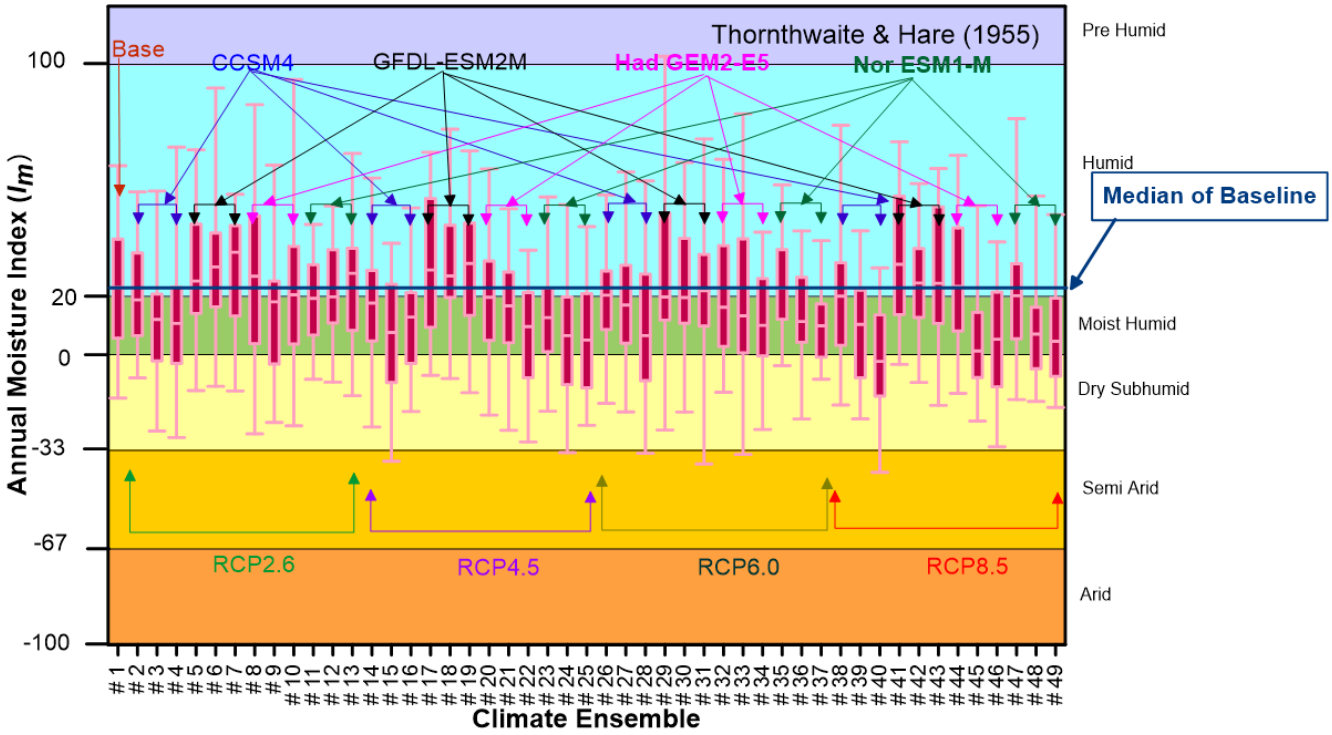

Figure B.21 Yearly variation of the annual moisture index for London

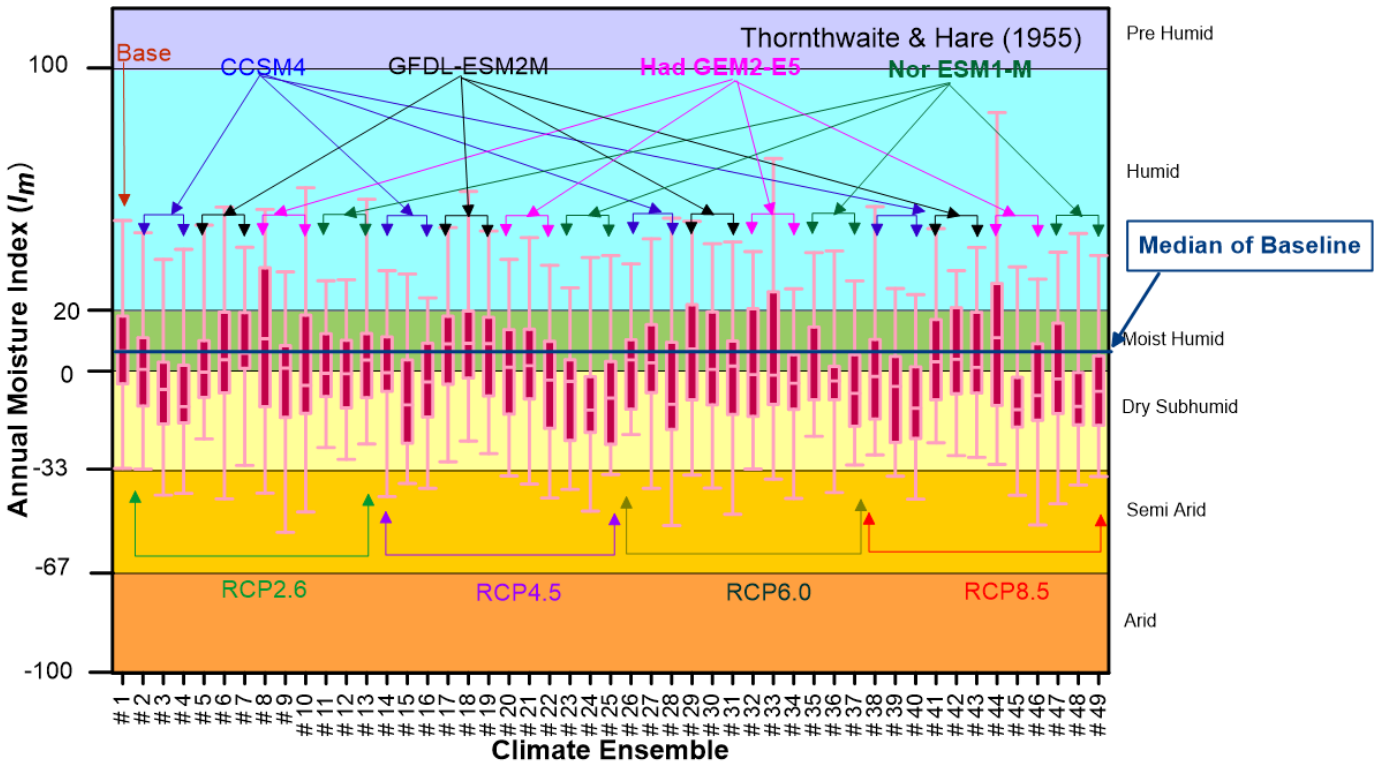

Figure B.22 Yearly variation of the annual moisture index for Windsor

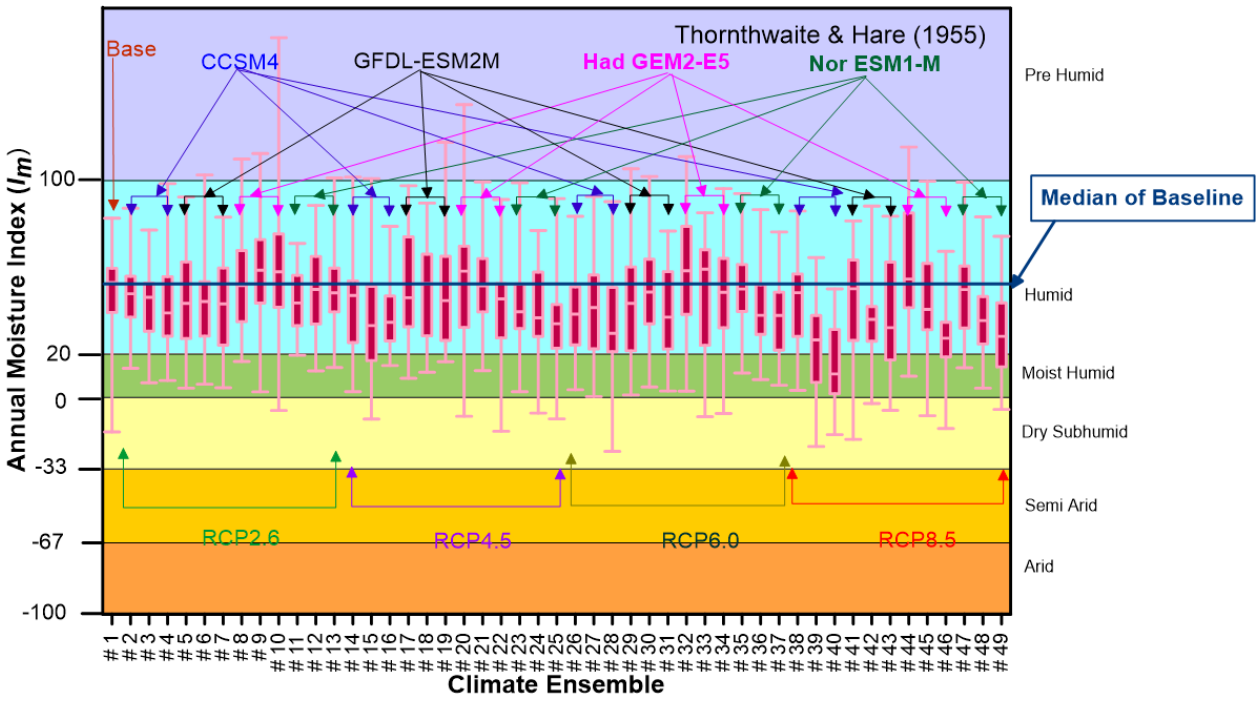

Figure B.23 Yearly variation of the annual moisture index for North Bay

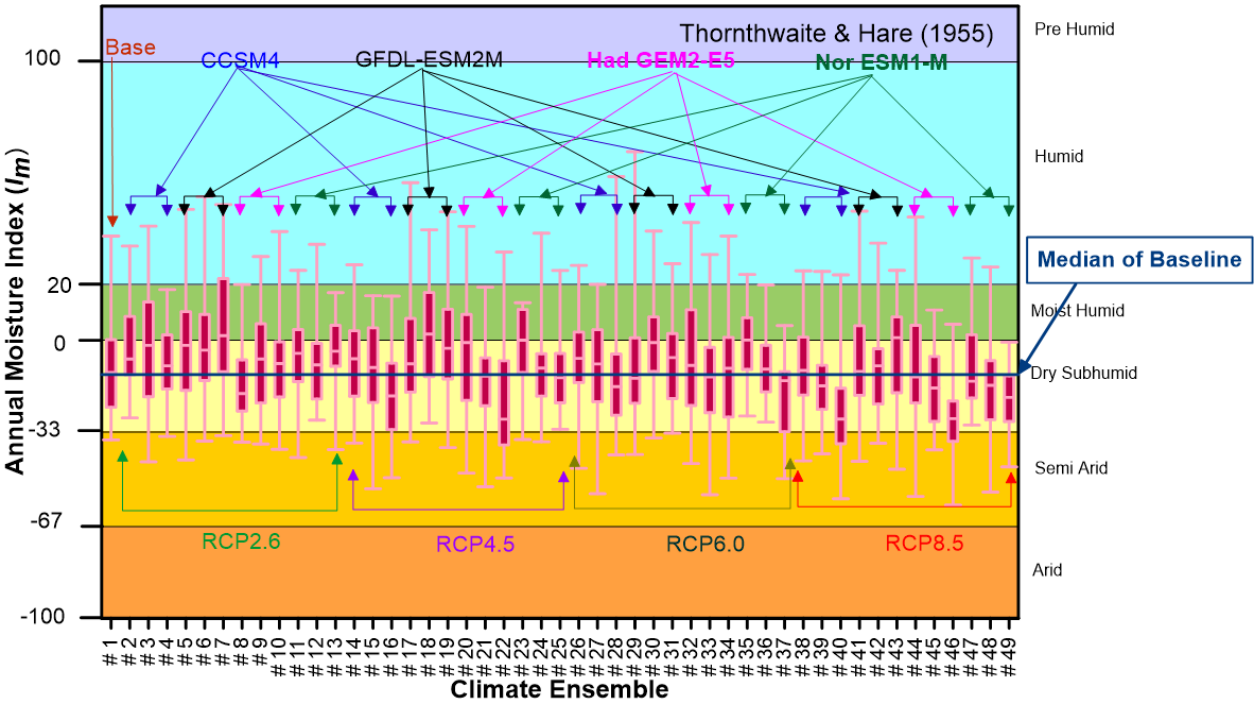

Figure B.24 Yearly variation of the annual moisture index for Thunder Bay

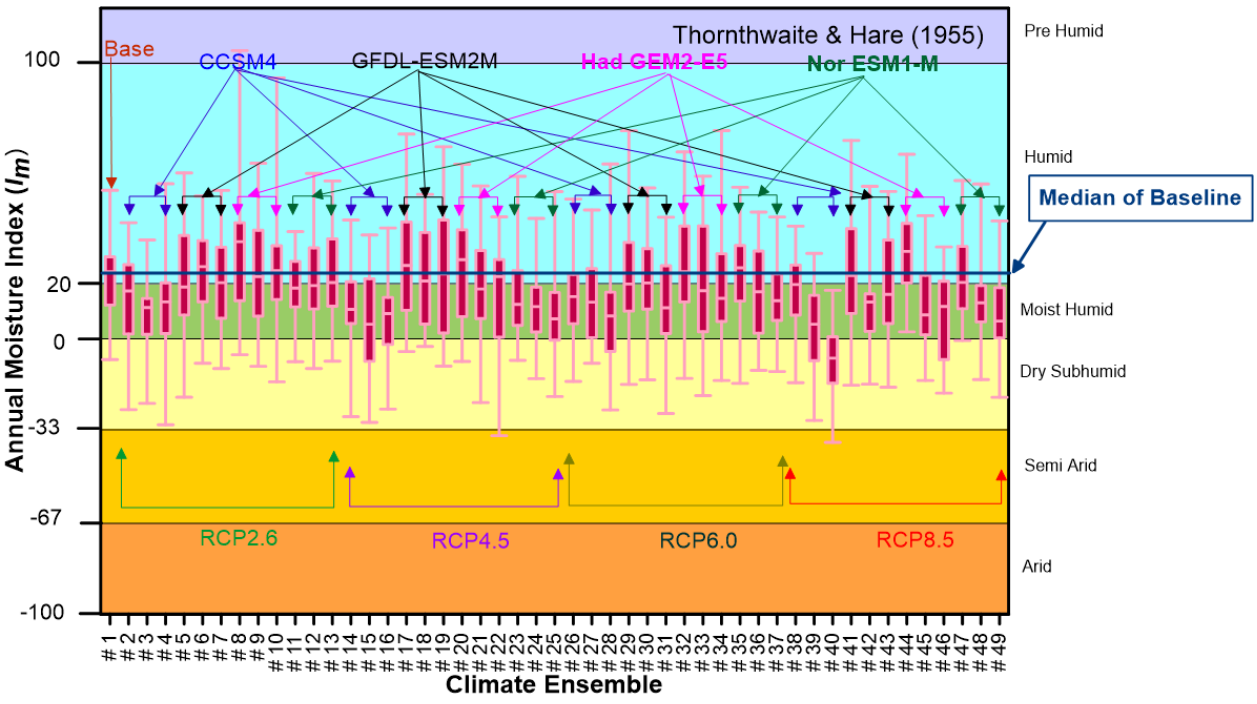

Figure B.25 Yearly variation of the annual moisture index for Kingston

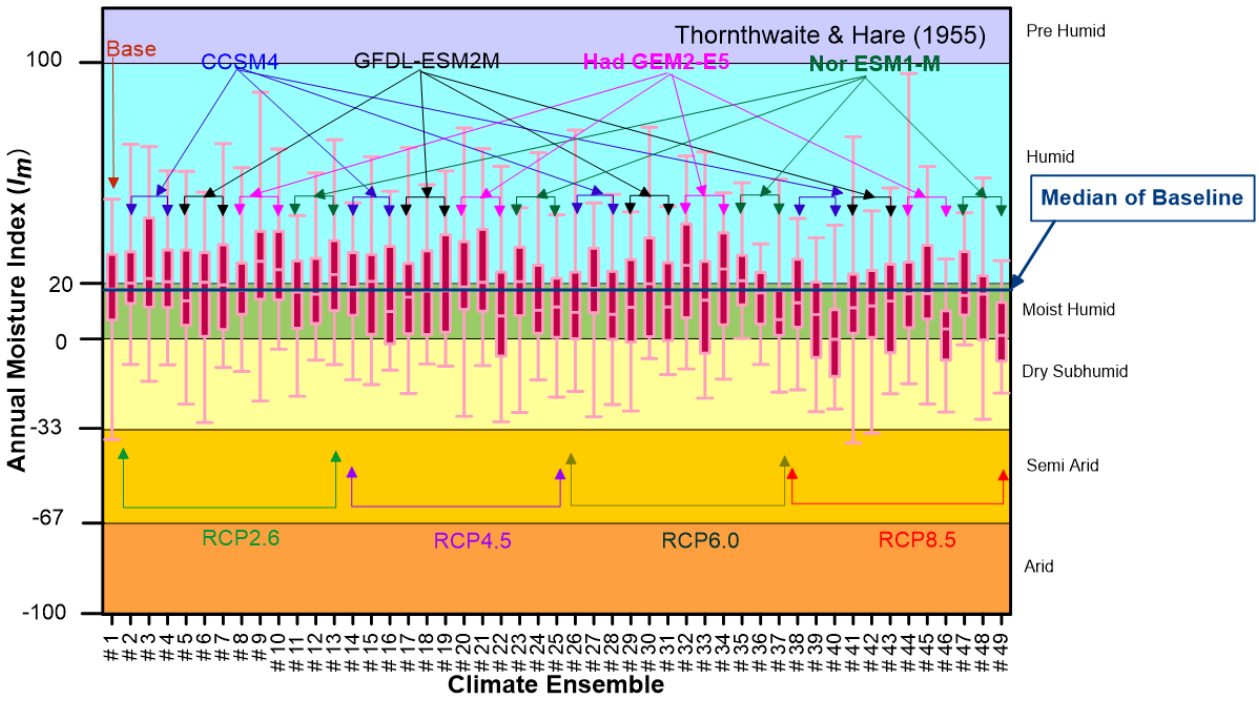

Figure B.26 Yearly variation of the annual moisture index for Timmins

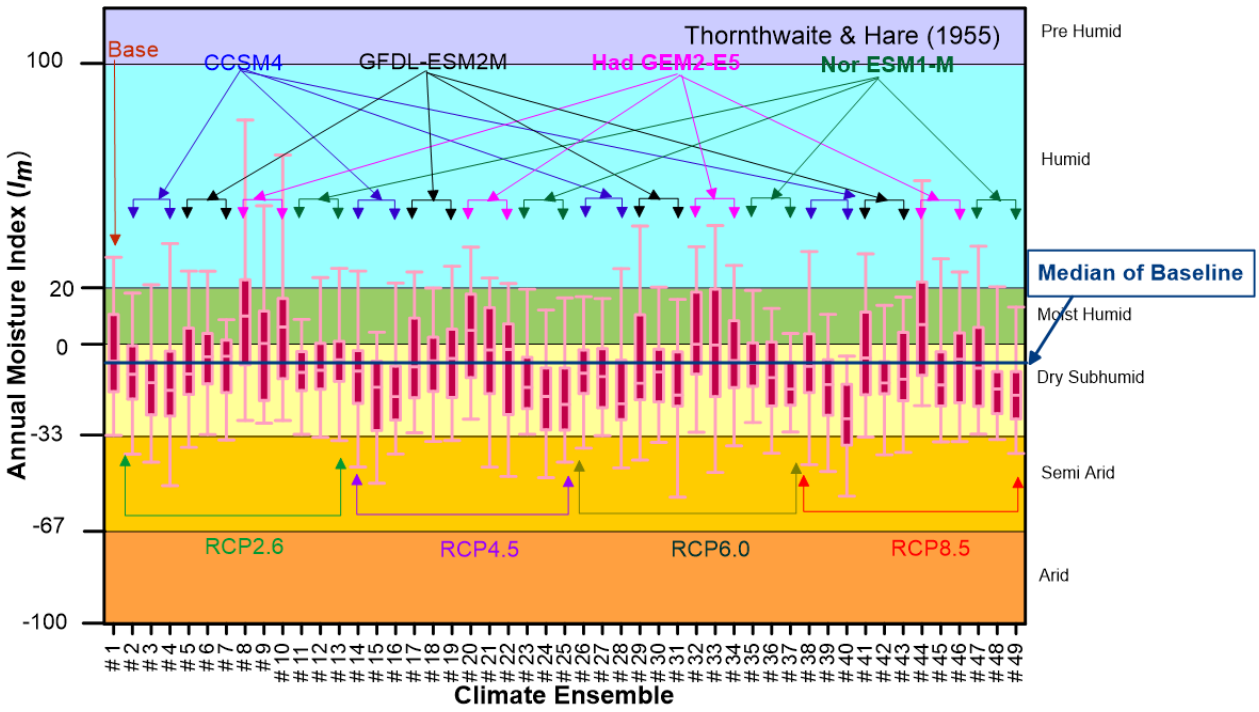

Figure B.27 Yearly variation of the annual moisture index for Toronto

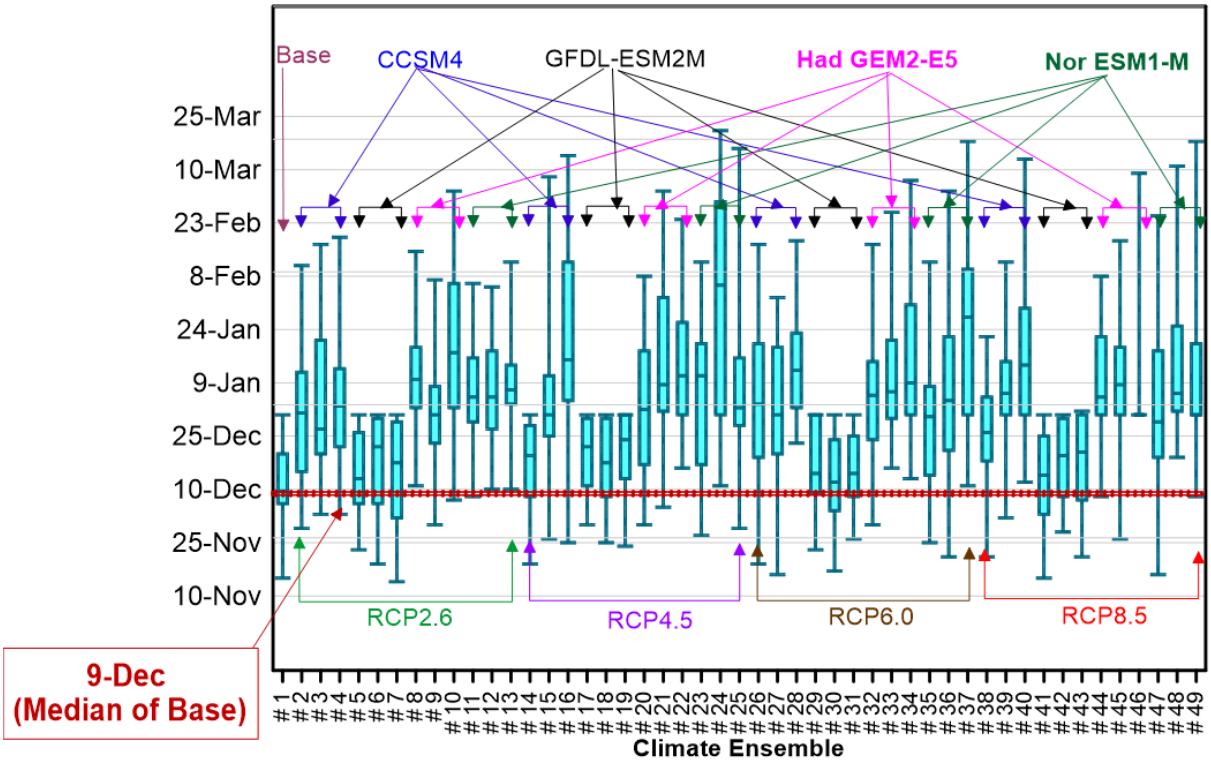

Figure B.28 Freezing dates based on all ensembles for Niagara Falls

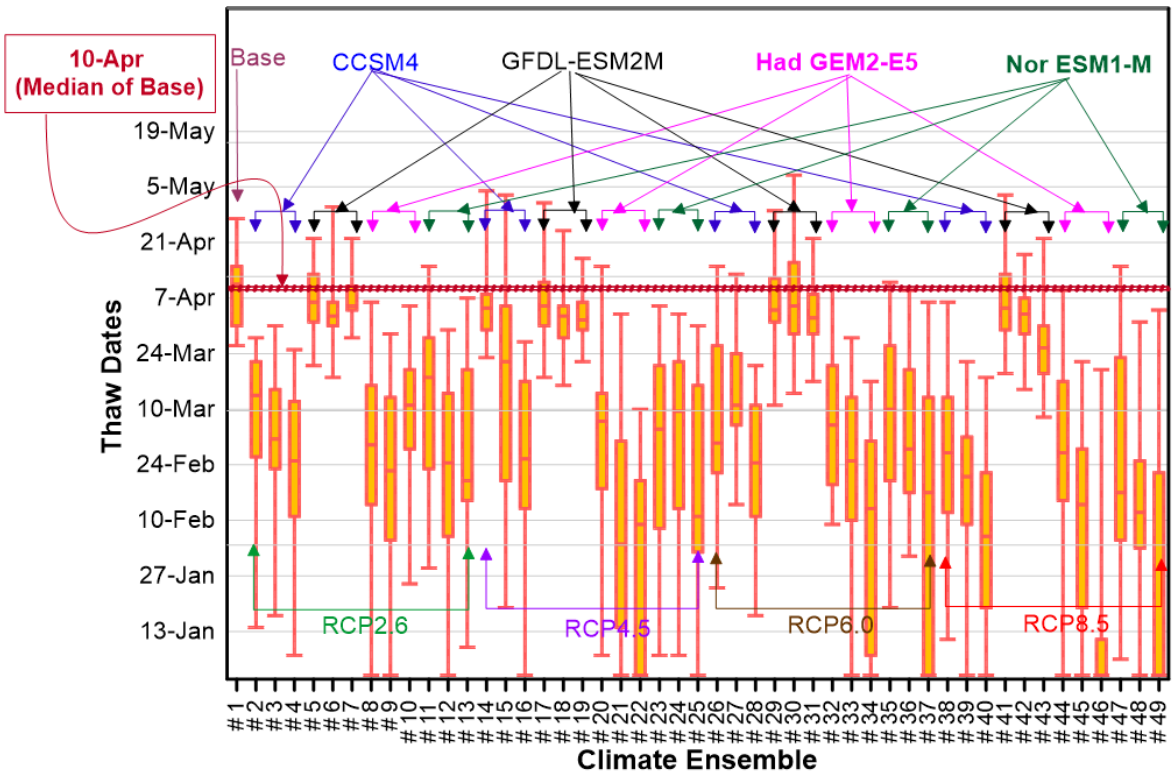

Figure B.29 Thaw dates based on all ensembles for Niagara Falls

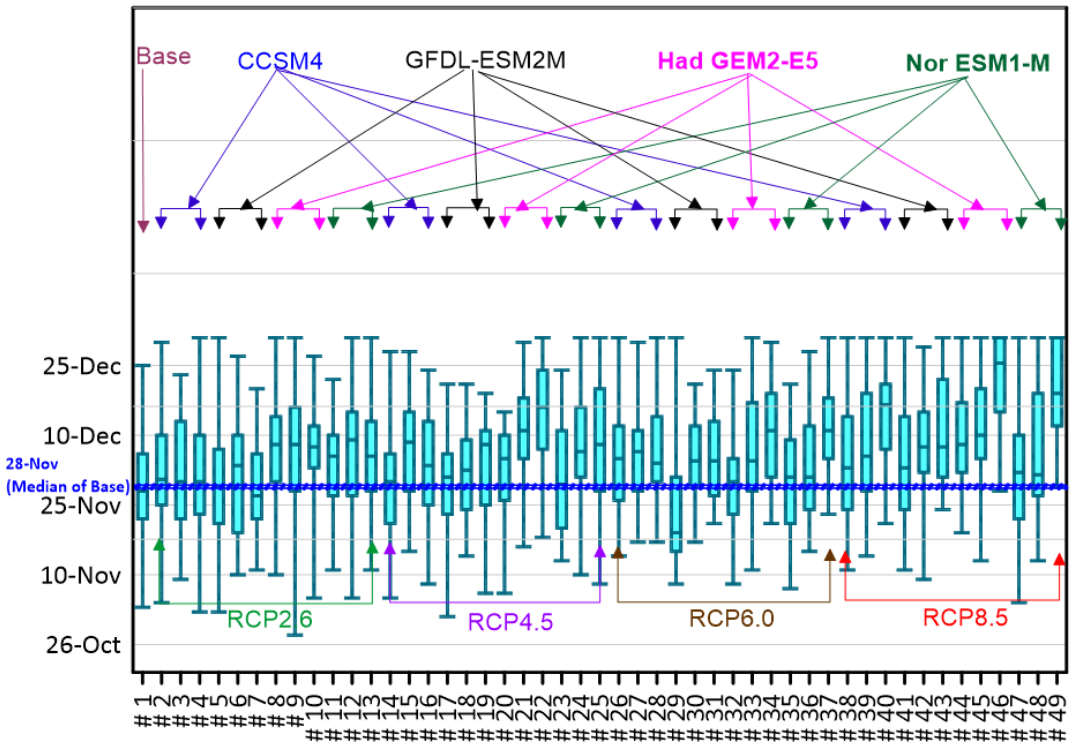

Figure B.30 Freezing dates based on all ensembles for Ottawa

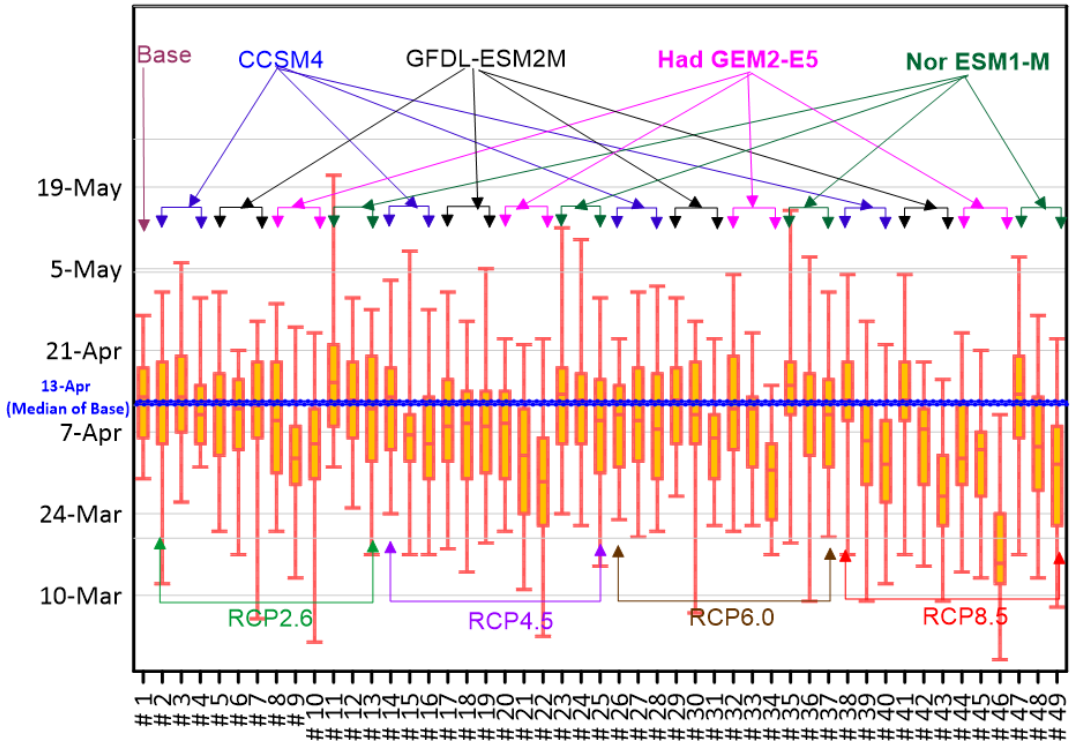

Figure B.31 Thaw dates based on all ensembles for Ottawa

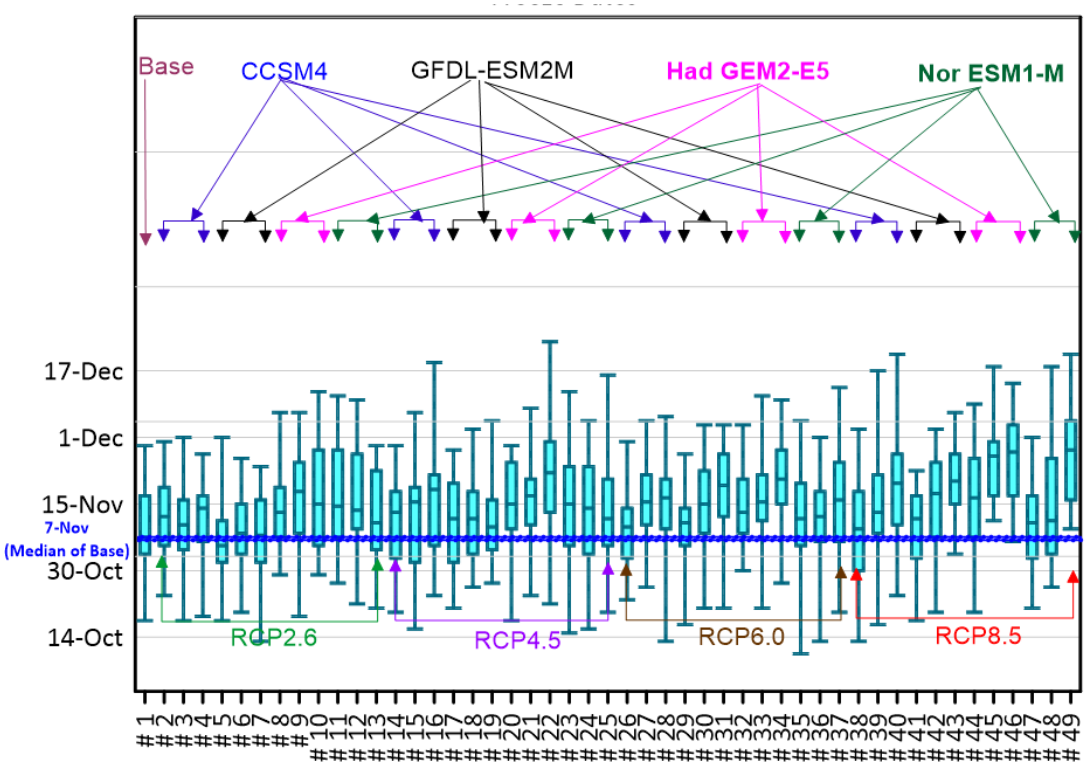

Figure B.32 Freezing dates based on all ensembles for Kenora

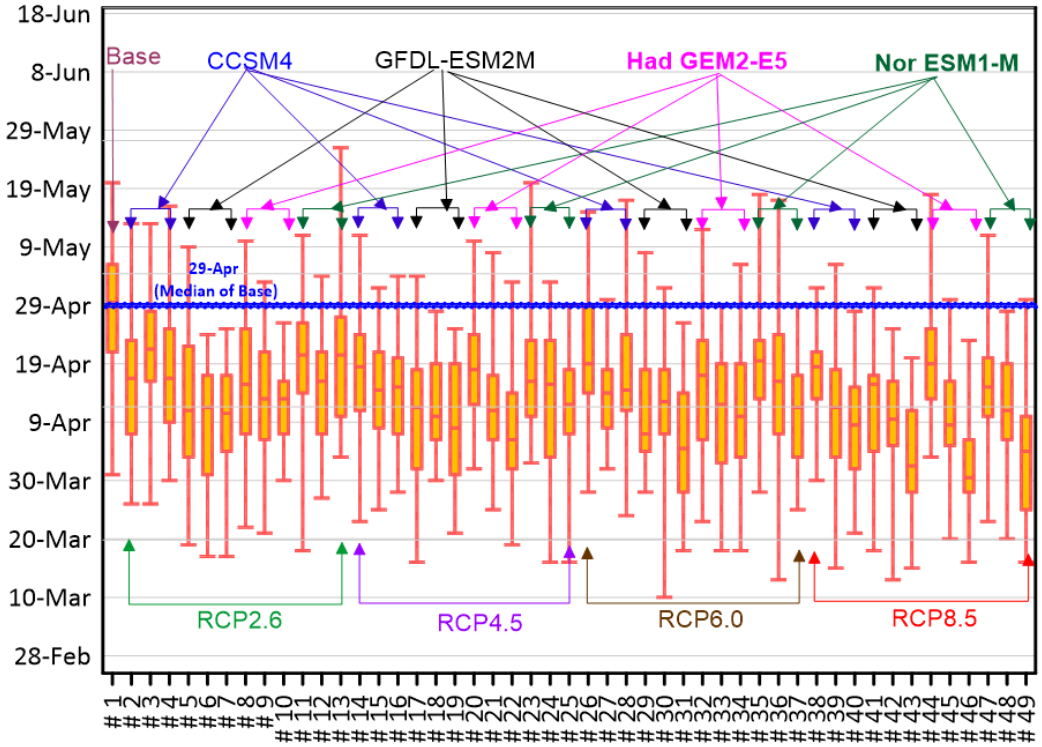

Figure B.33 Thaw dates based on all ensembles for Kenora

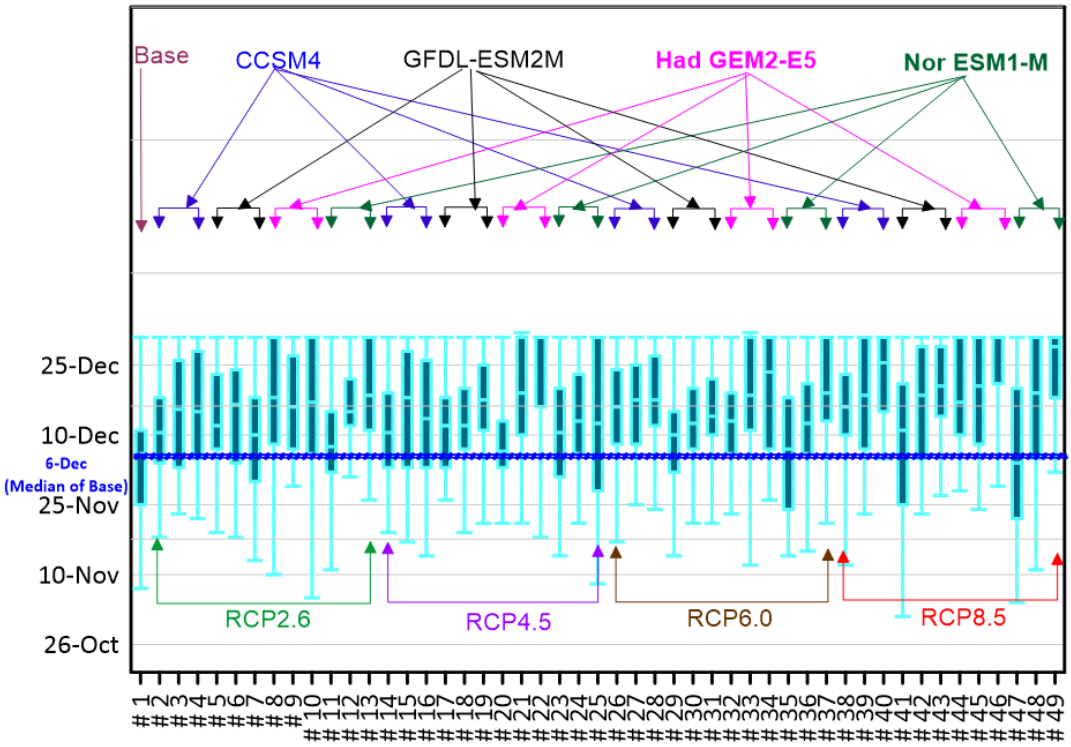

Figure B.34 Freezing dates based on all ensembles for London

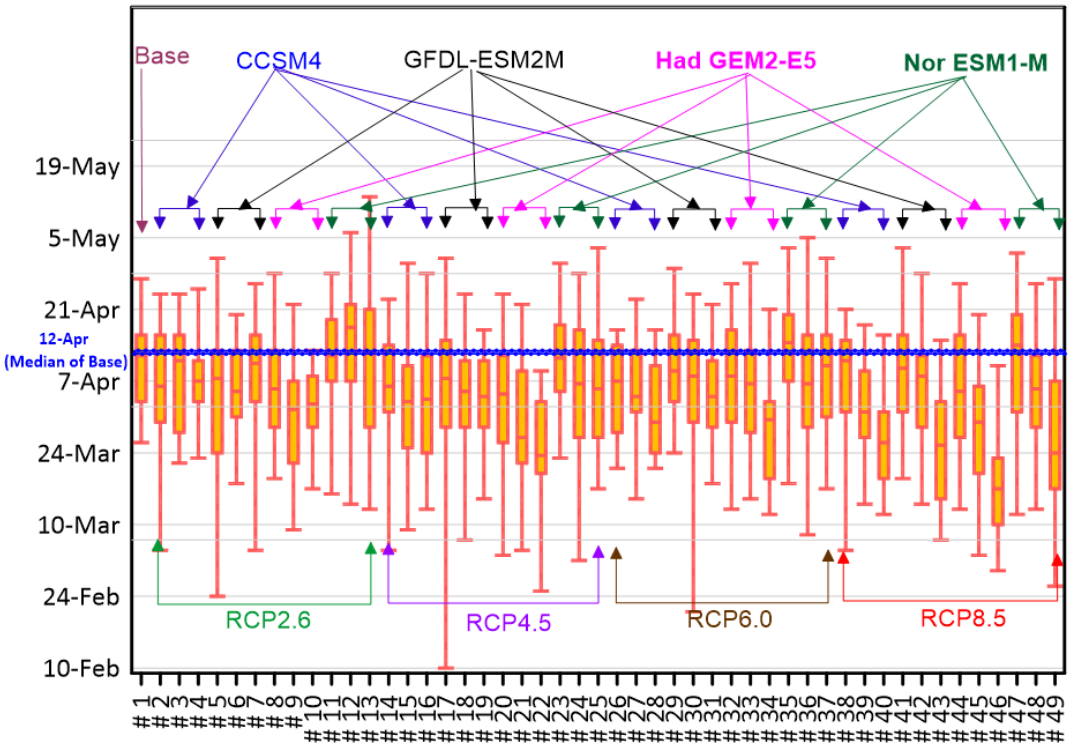

Figure B.35 Thaw dates based on all ensembles for London

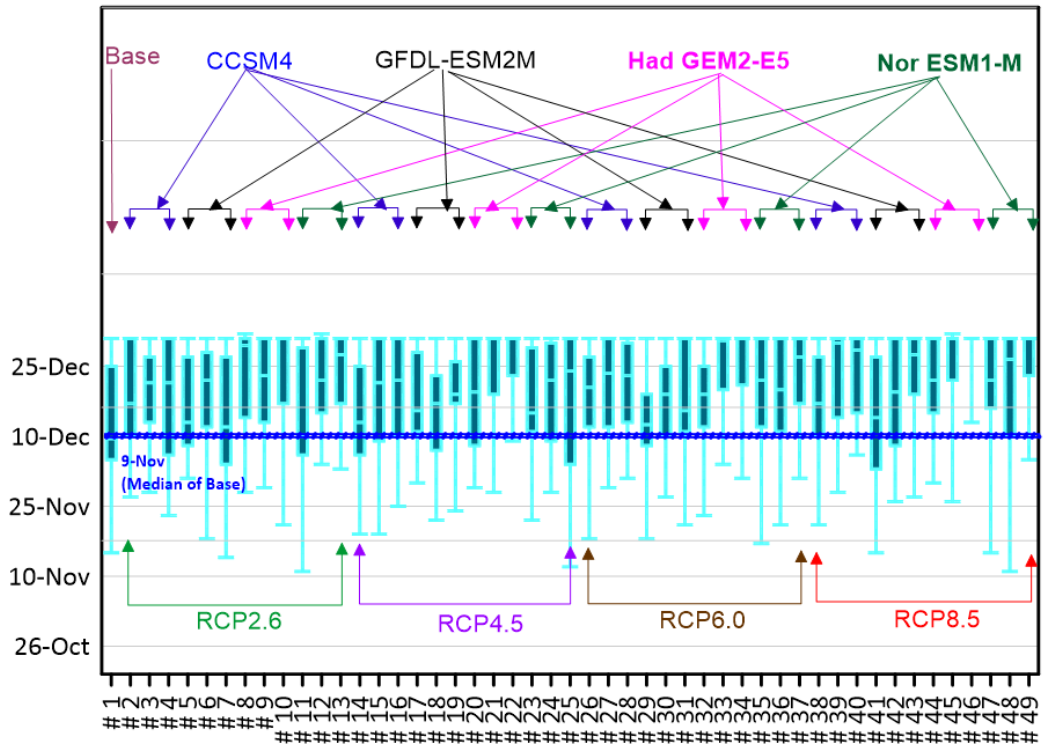

Figure B.36 Freezing dates based on all ensembles for Windsor

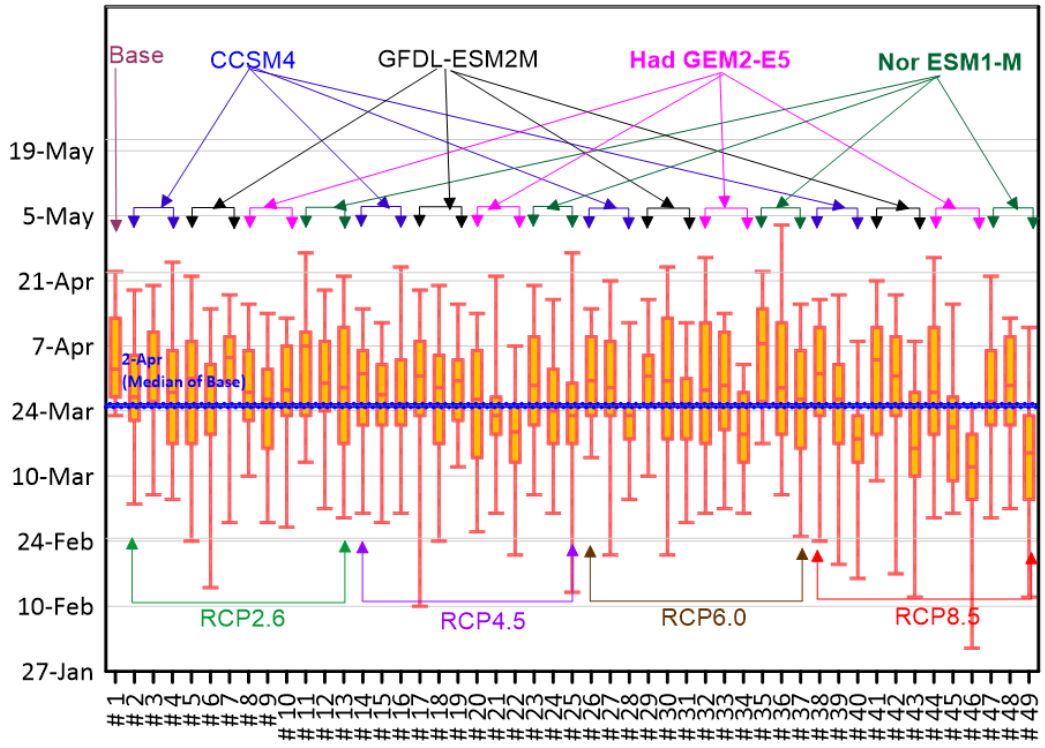

Figure B.37 Thaw dates based on all ensembles for Windsor

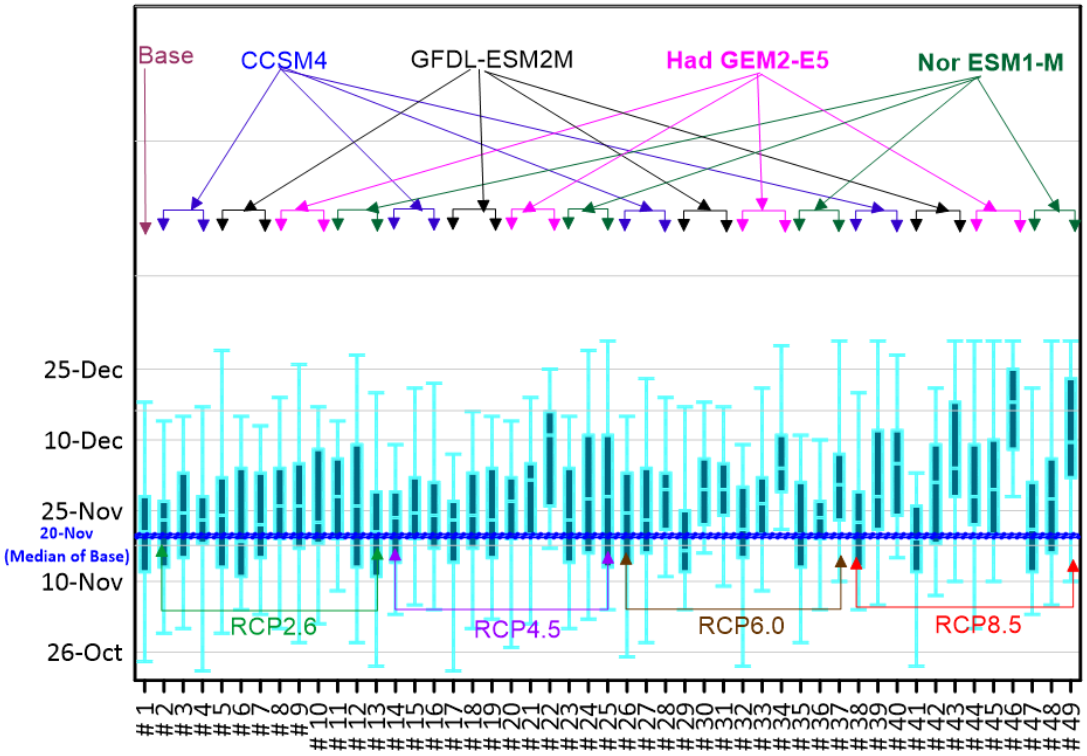

Figure B.38 Freezing dates based on all ensembles for North Bay

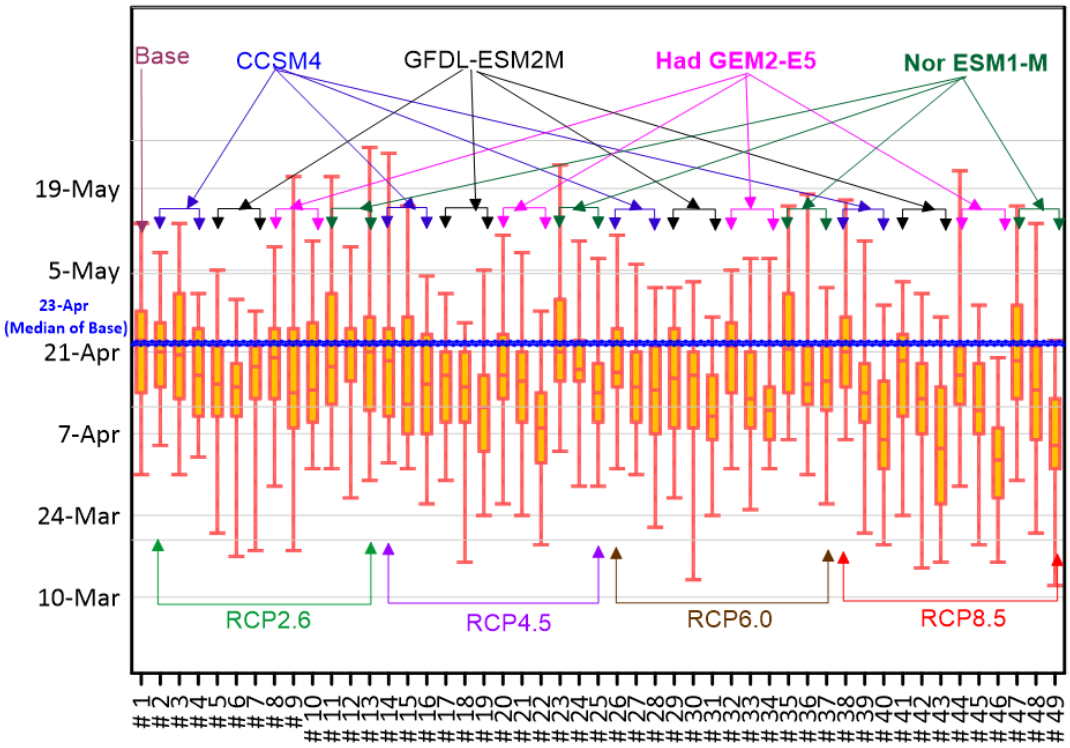

Figure B.39 Thaw dates based on all ensembles for North Bay

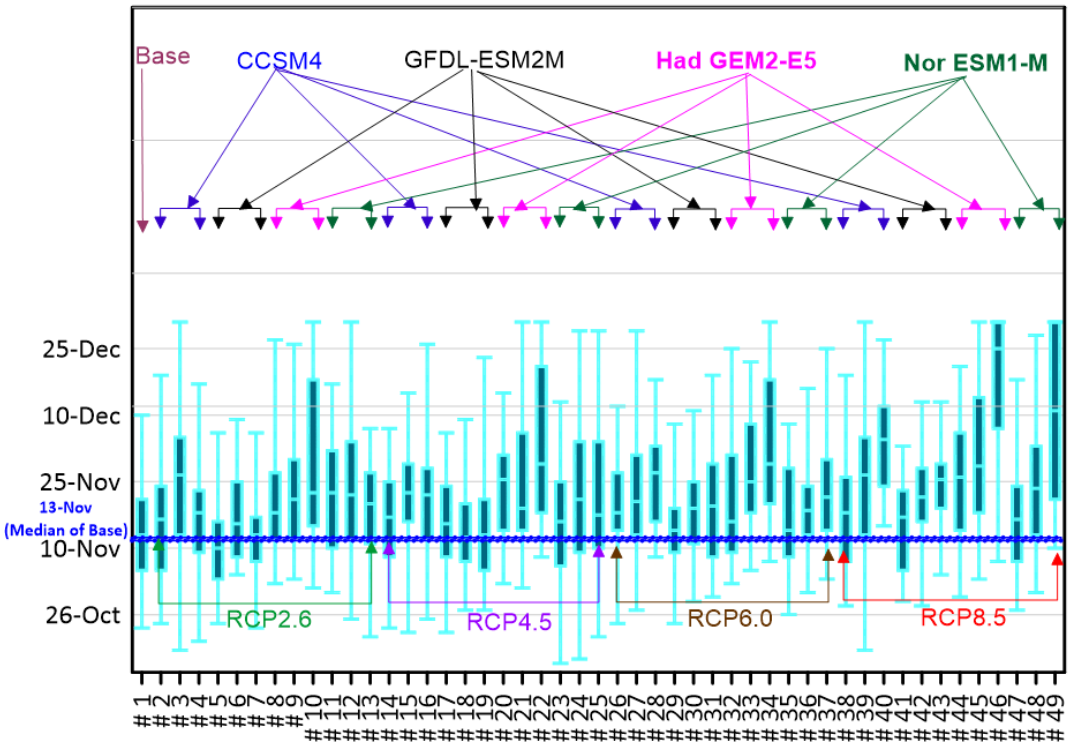

Figure B.40 Freezing dates based on all ensembles for Thunder Bay

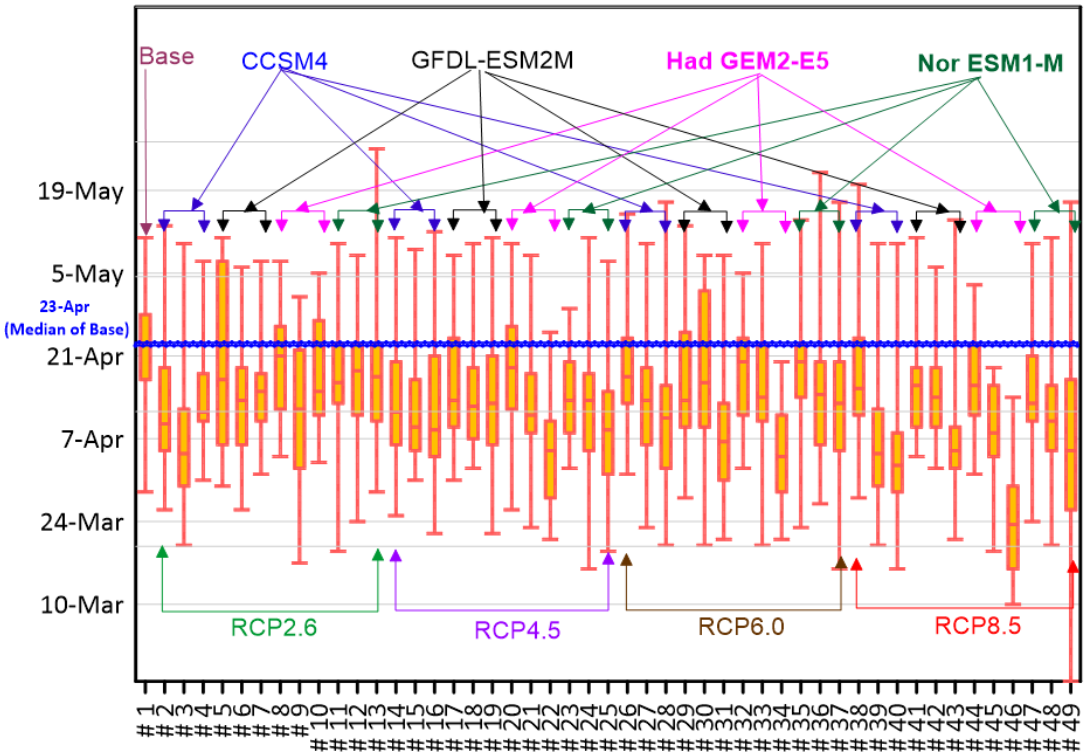

Figure B.41 Thaw dates based on all ensembles for Thunder Bay

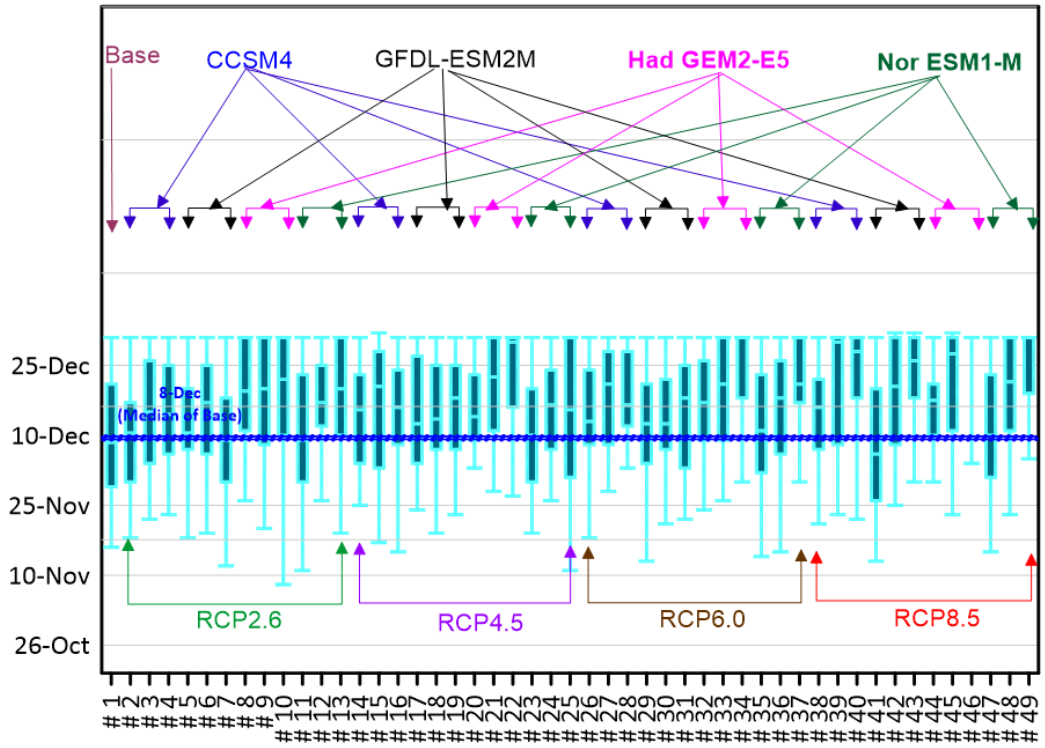

Figure B.42 Freezing dates based on all ensembles for Kingston

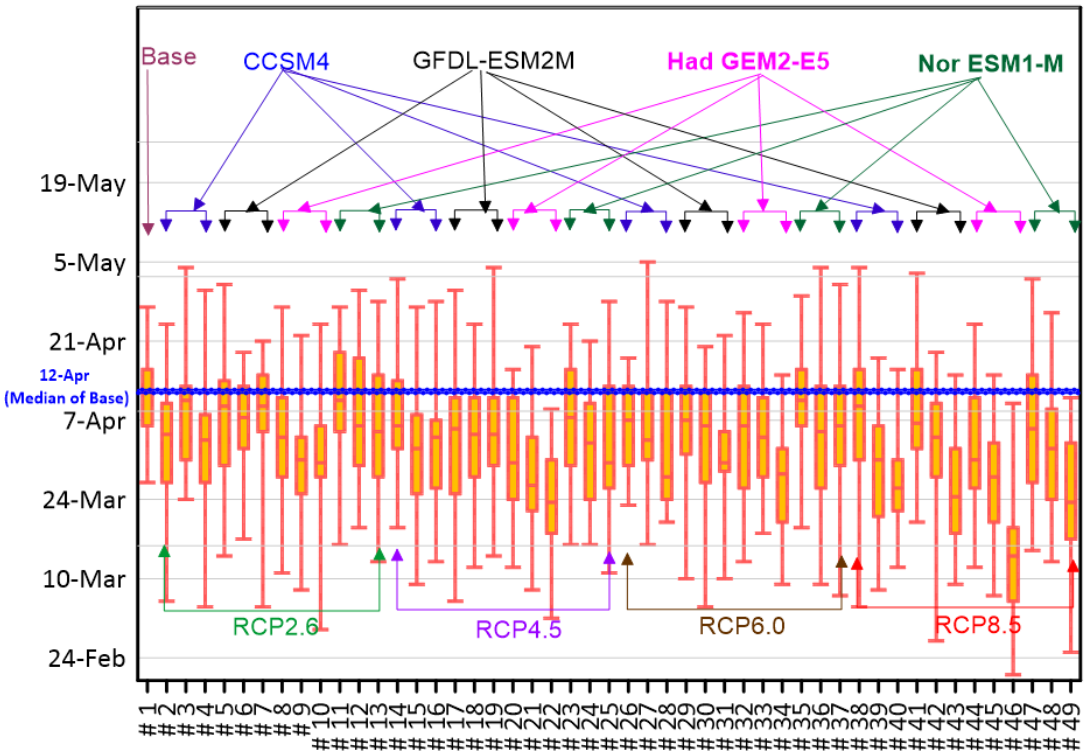

Figure B.43 Thaw dates based on all ensembles for Kingston

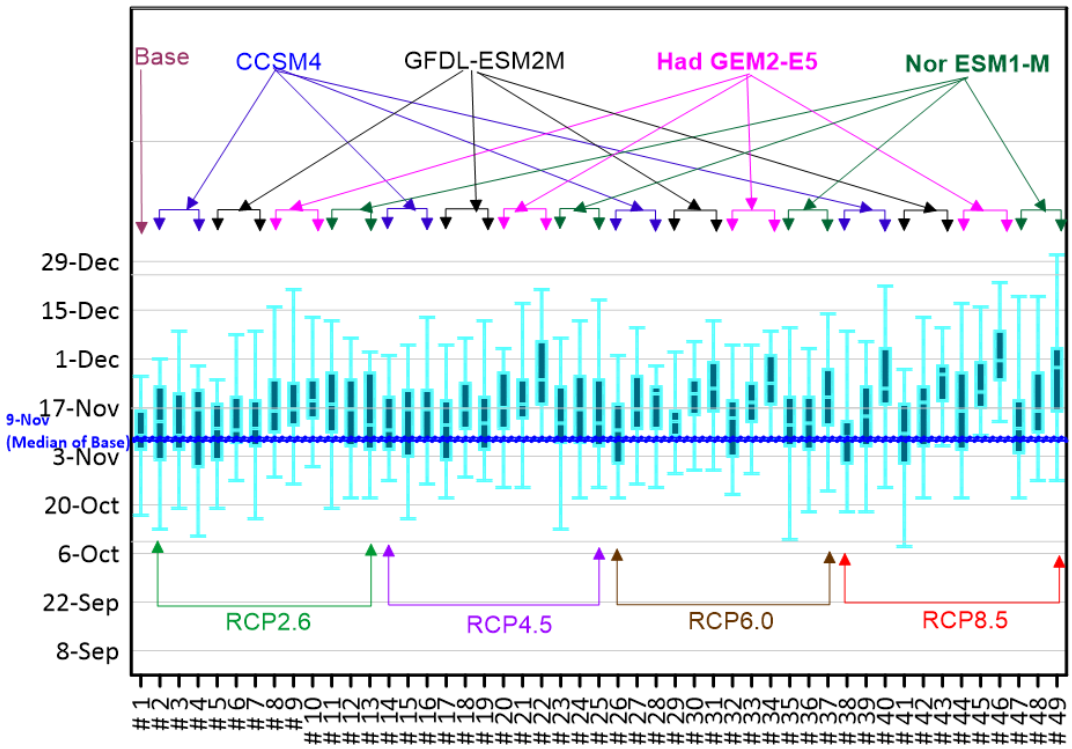

Figure B.44 Freezing dates based on all ensembles for Timmins

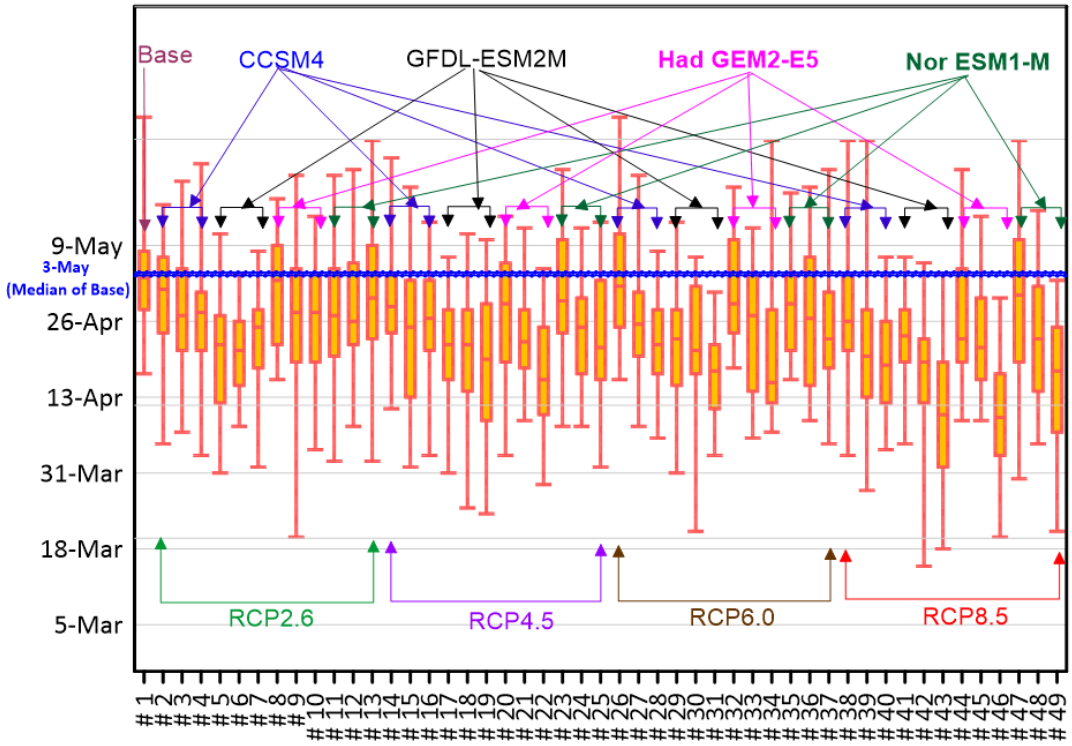

Figure B.45 Thaw dates based on all ensembles for Timmins

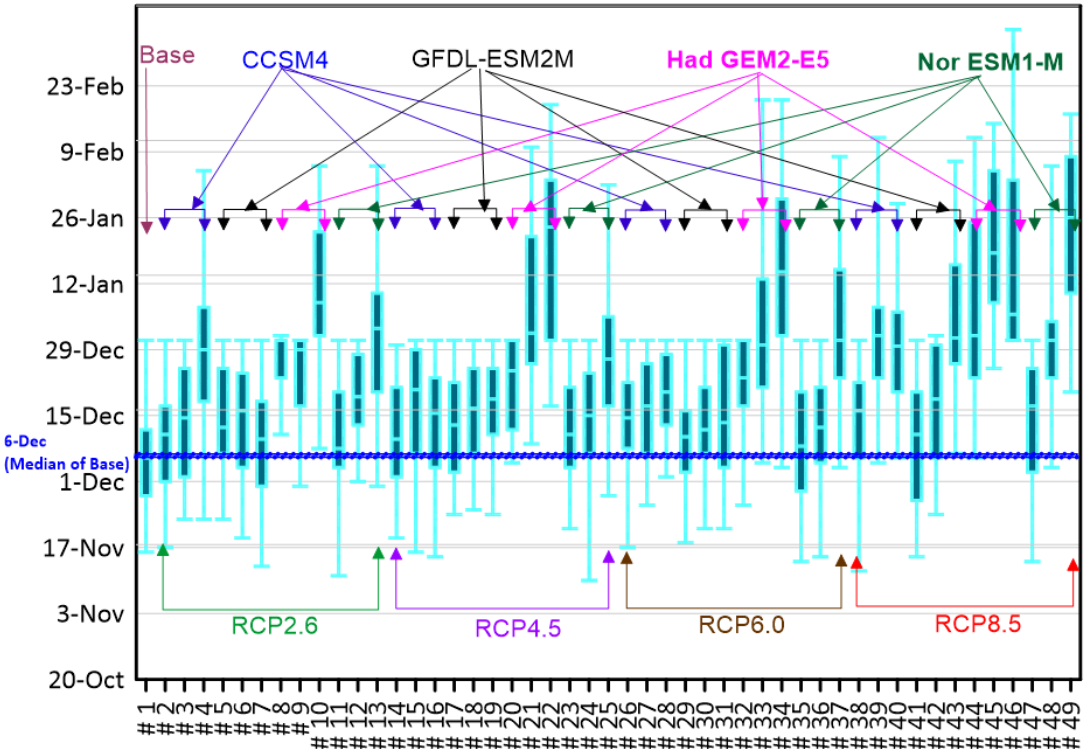

Figure B.46 Freezing dates based on all ensembles for Toronto

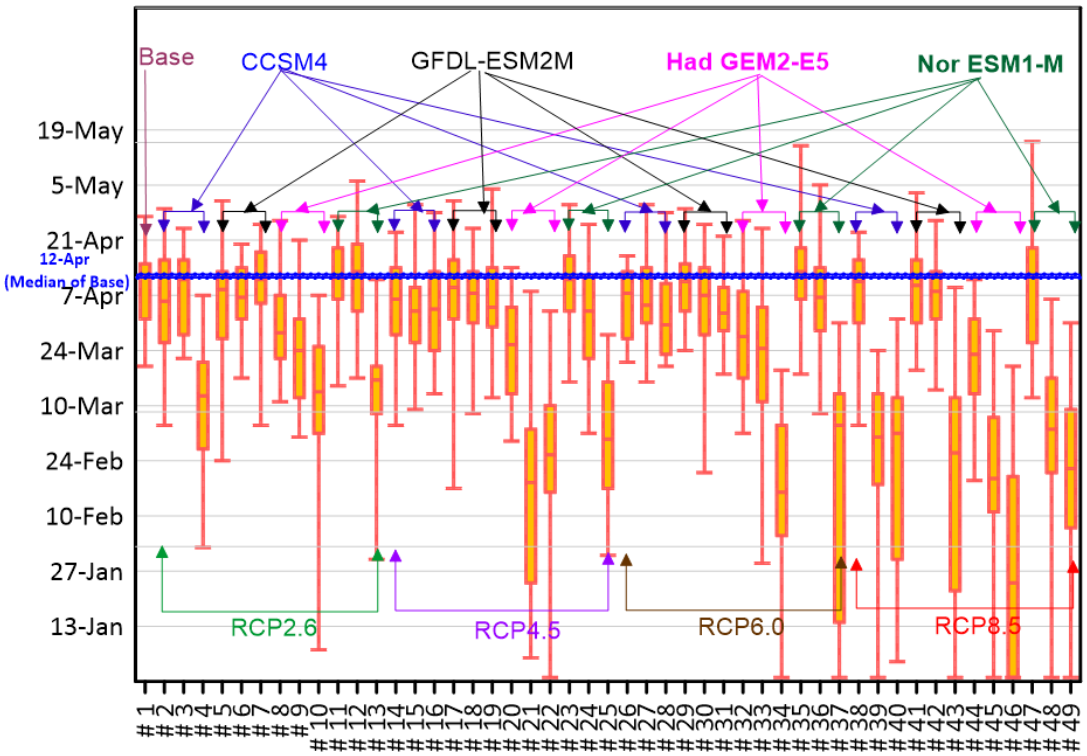

Figure B.47 Thaw dates based on all ensembles for Toronto

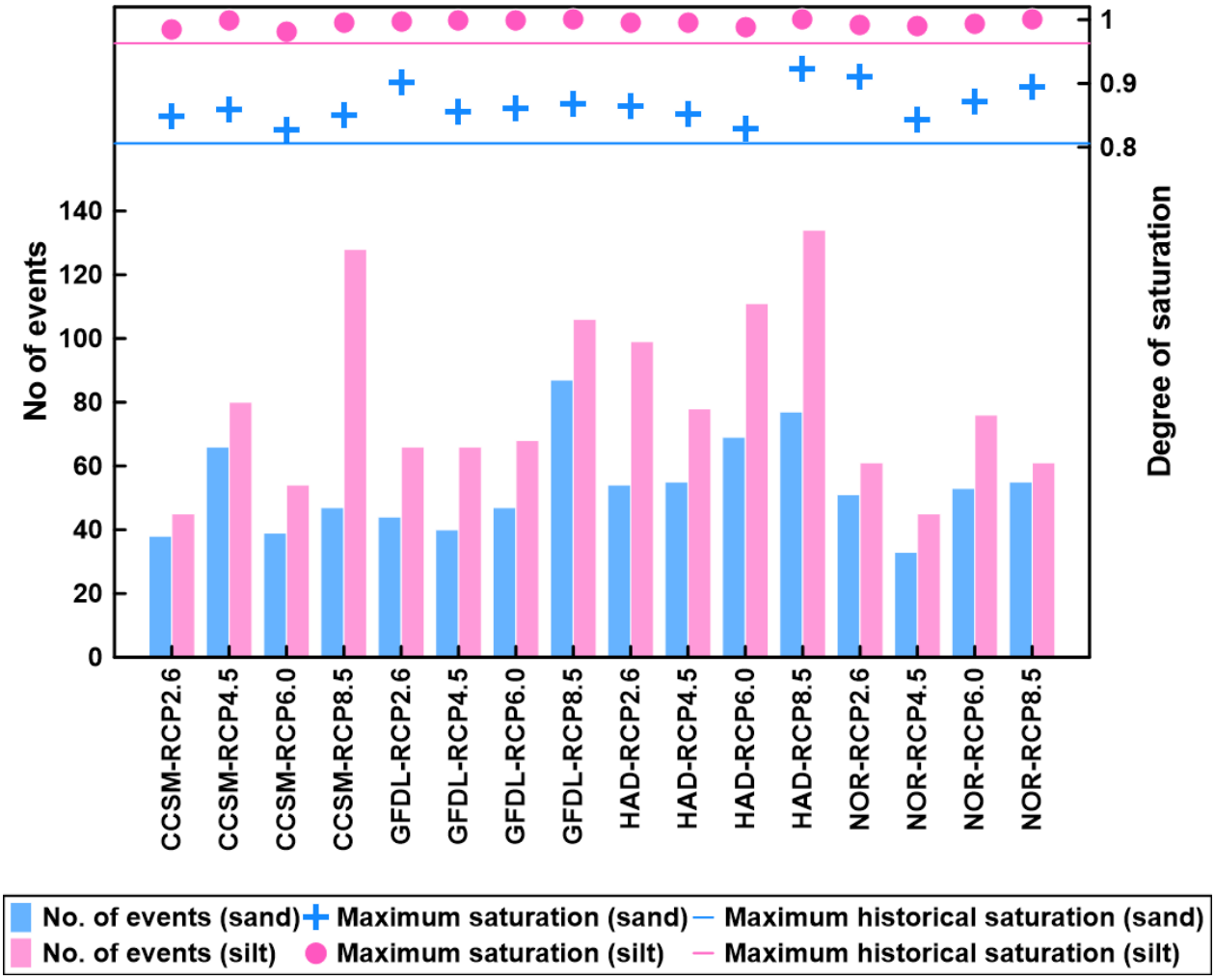

Figure C.48 Maximum degree of saturation and frequency of high saturation occurrence in sand and silt material for London

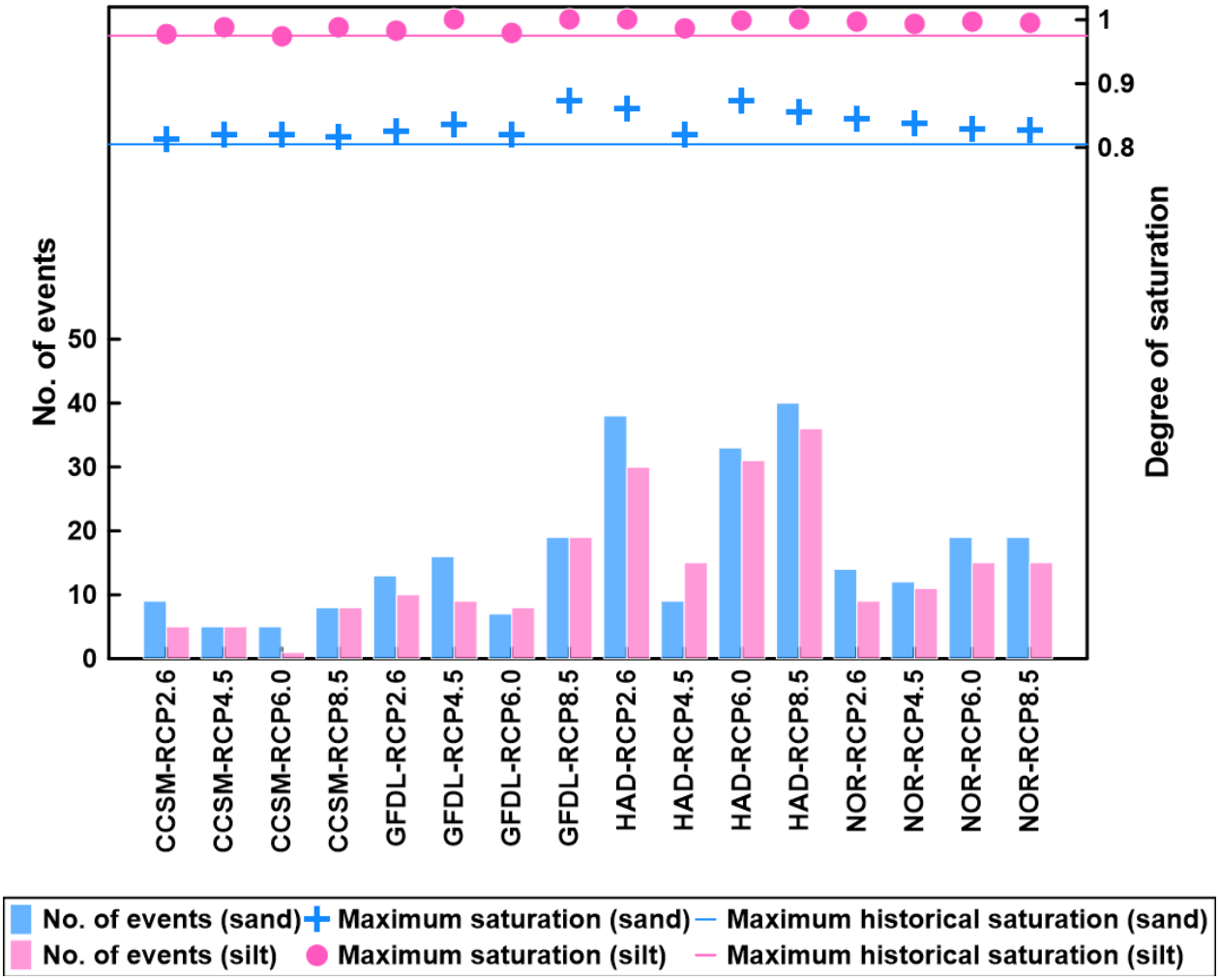

Figure C.49 Maximum degree of saturation and frequency of high saturation occurrence in sand and silt material for Kingston

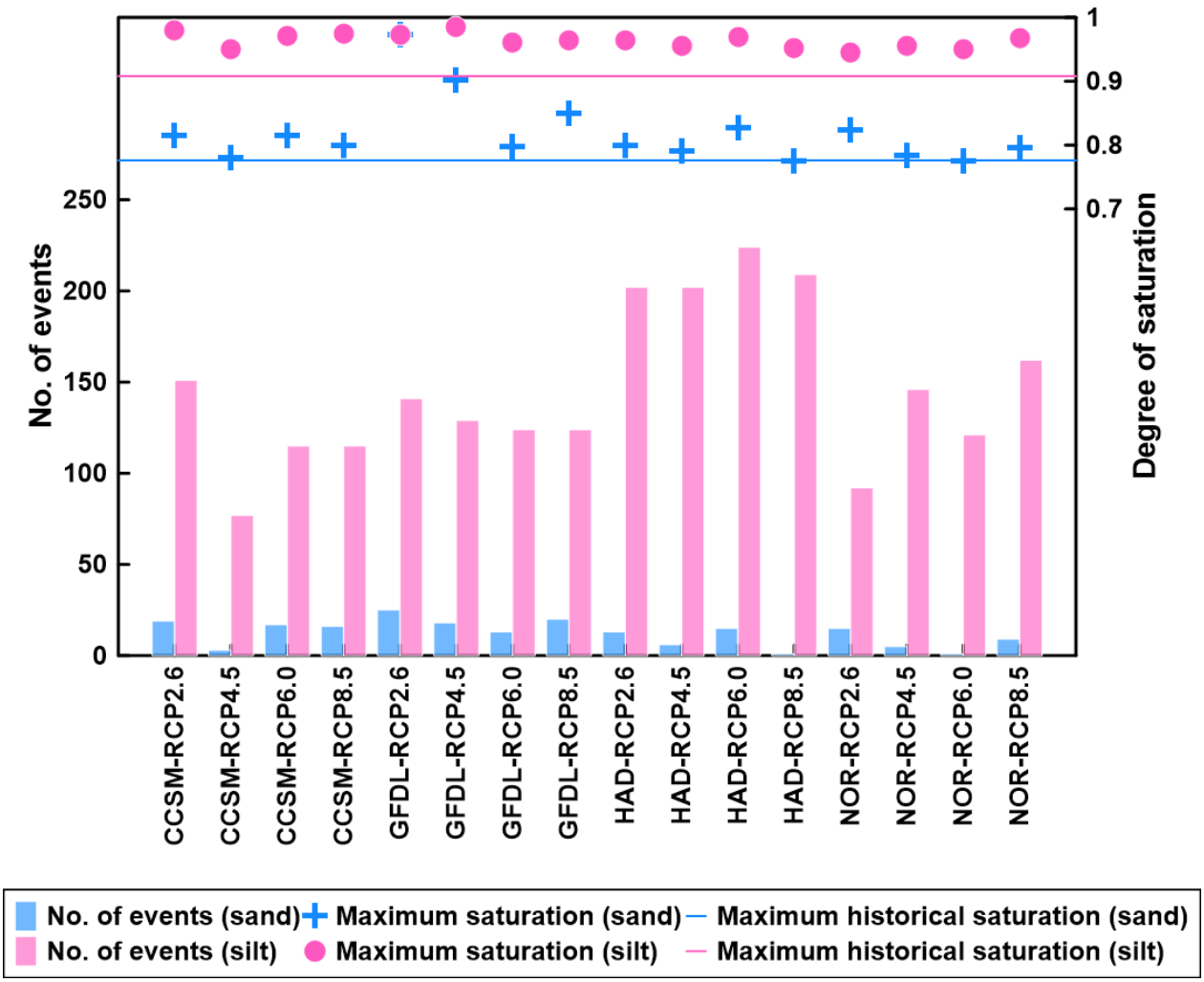

Figure C.50 Maximum degree of saturation and frequency of high saturation occurrence in sand and silt material for Thunder Bay

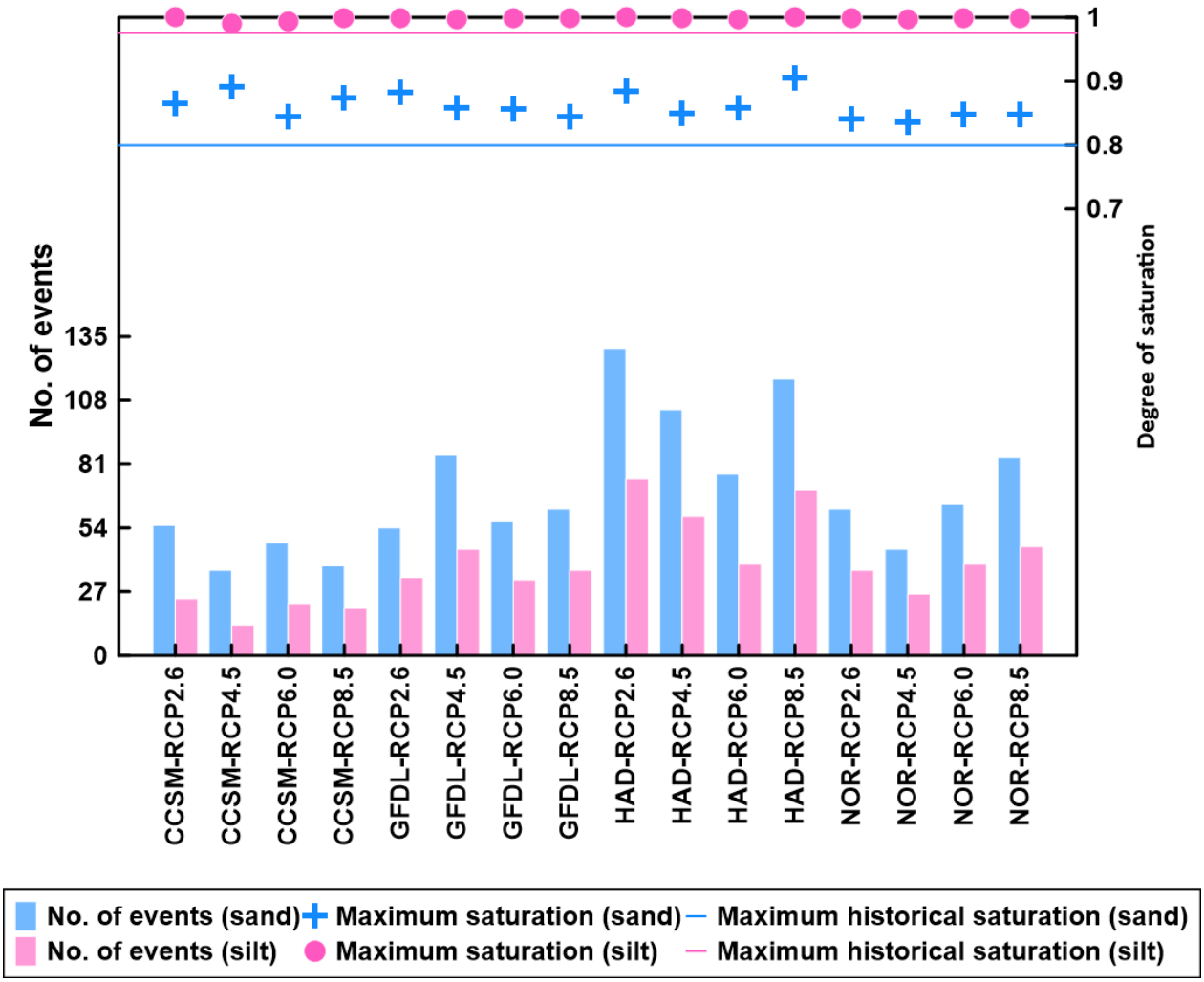

Figure C.51 Maximum degree of saturation and frequency of high saturation occurrence in sand and silt material for North Bay

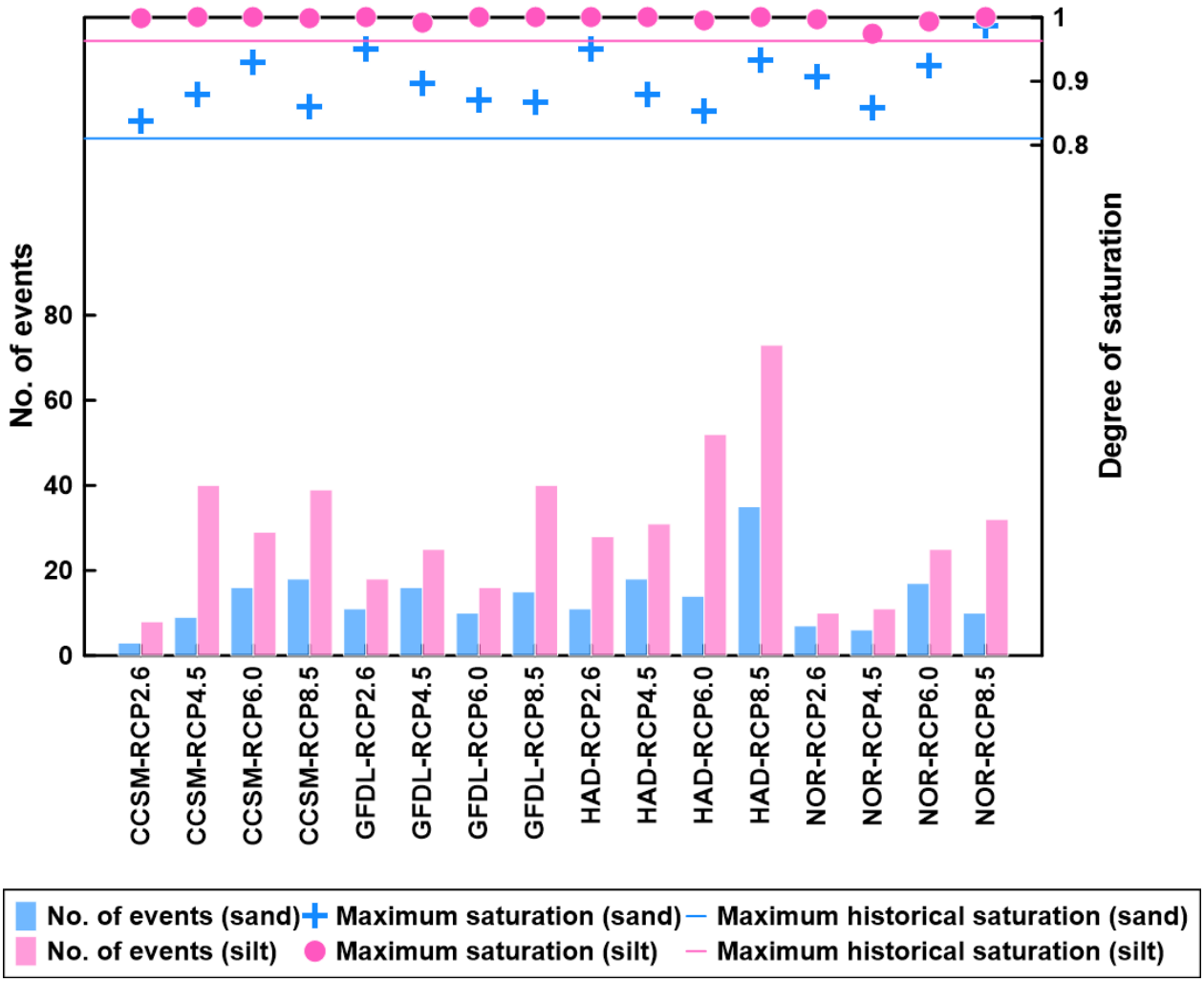

Figure C.52 Maximum degree of saturation and frequency of high saturation occurrence in sand and silt material for Windsor

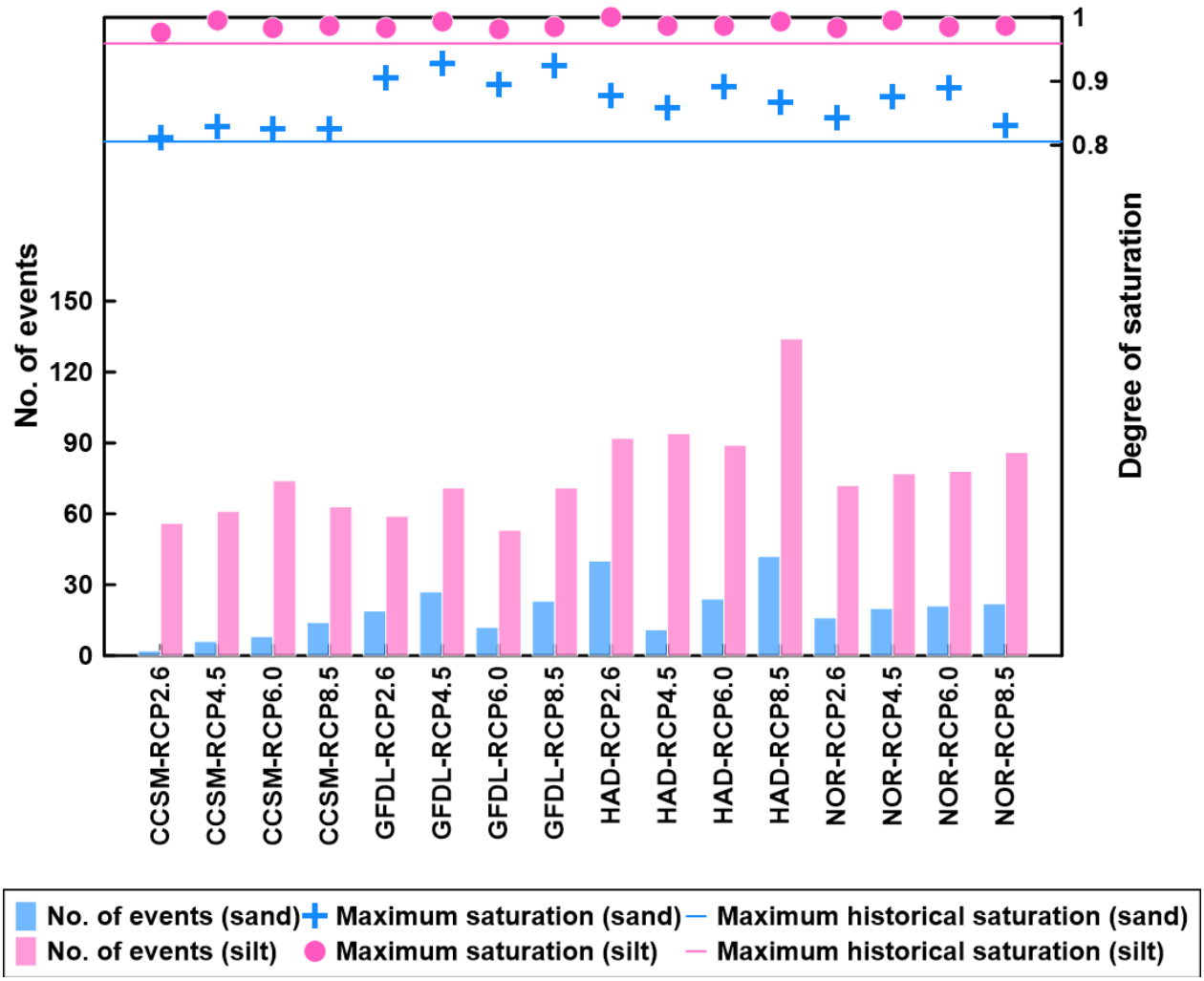

Figure C.53 Maximum degree of saturation and frequency of high saturation occurrence in sand and silt material for Ottawa

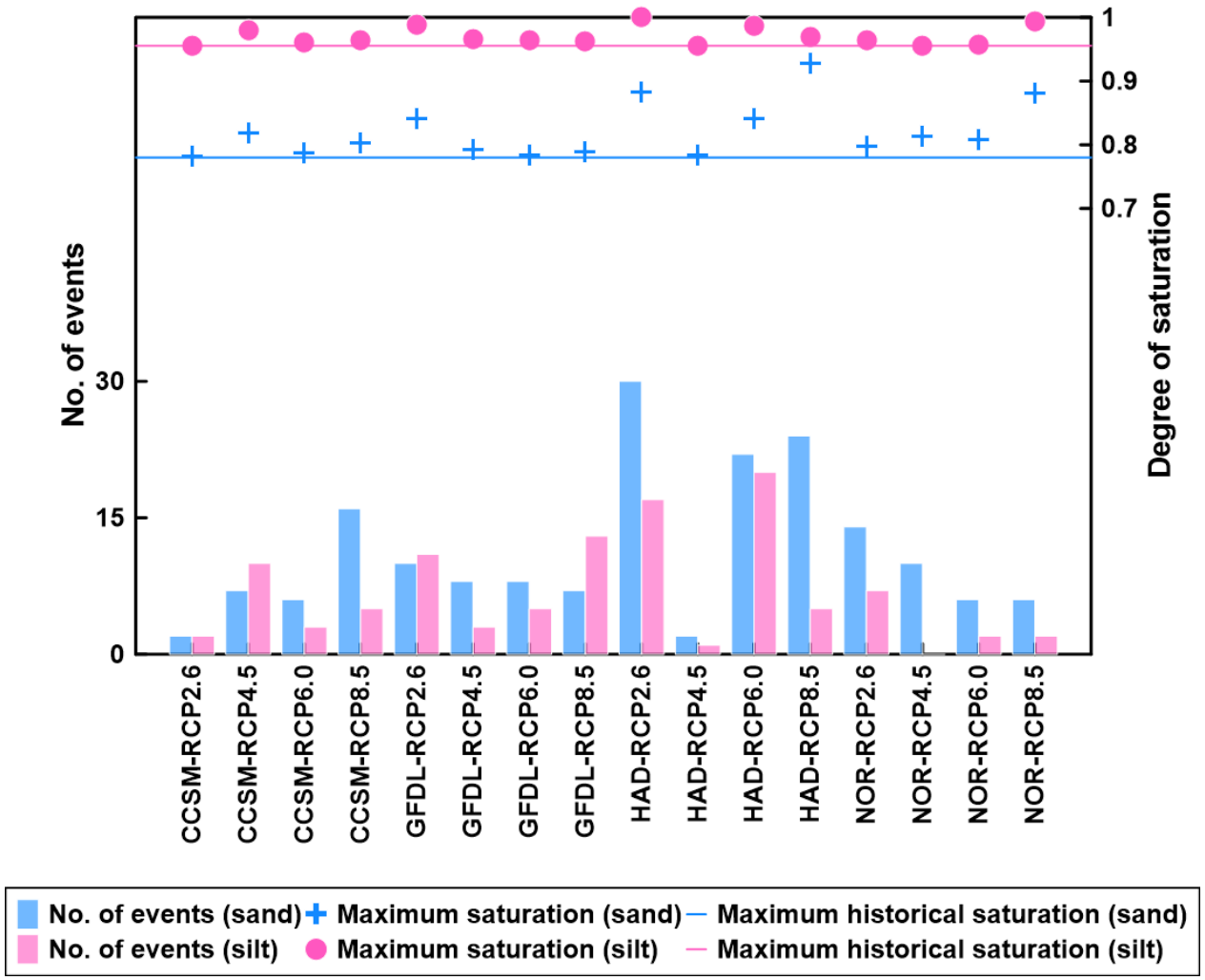

Figure C.54 Maximum degree of saturation and frequency of high saturation occurrence in sand and silt material for Toronto

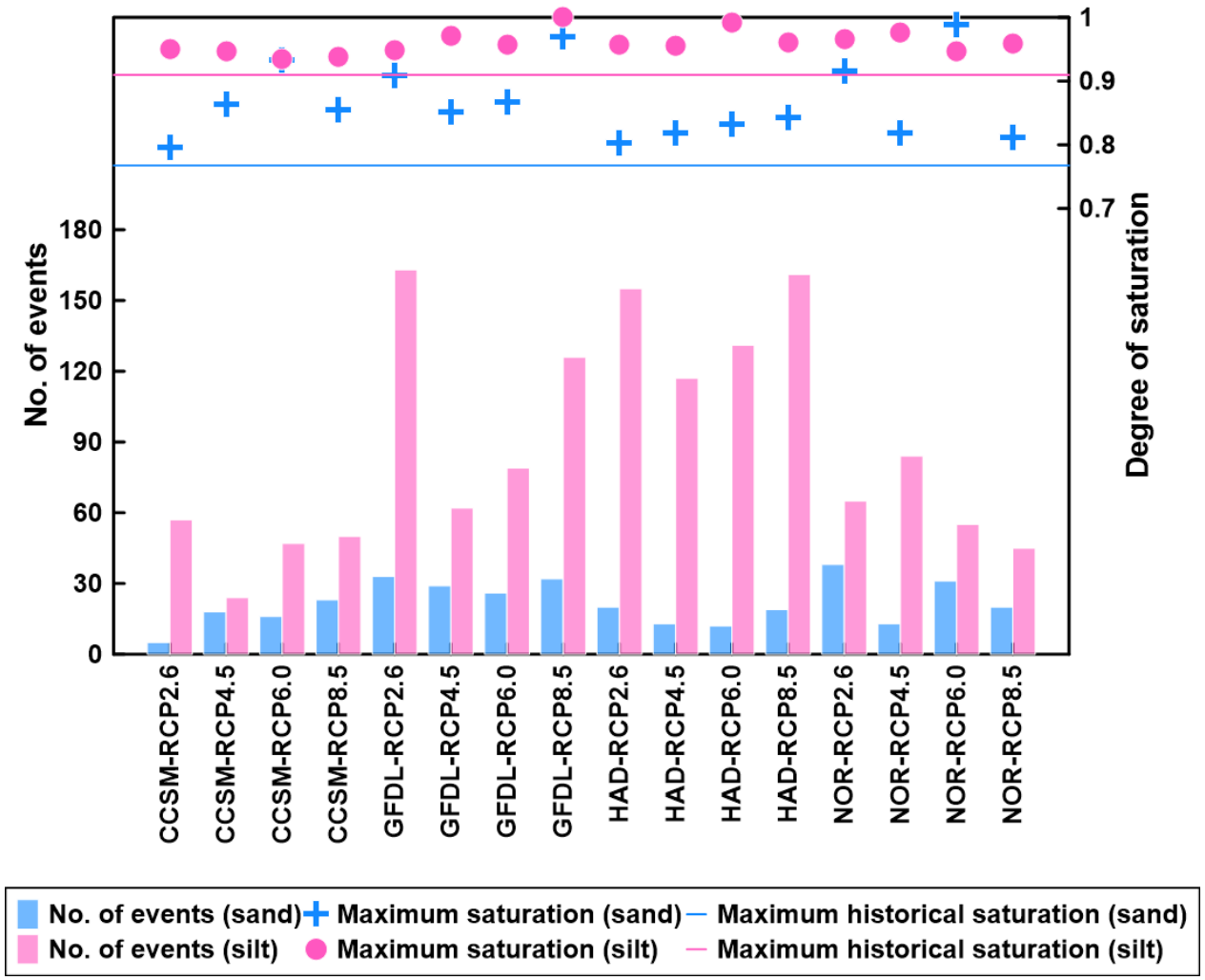

Figure C.55 Maximum degree of saturation and frequency of high saturation occurrence in sand and silt material for Kenora

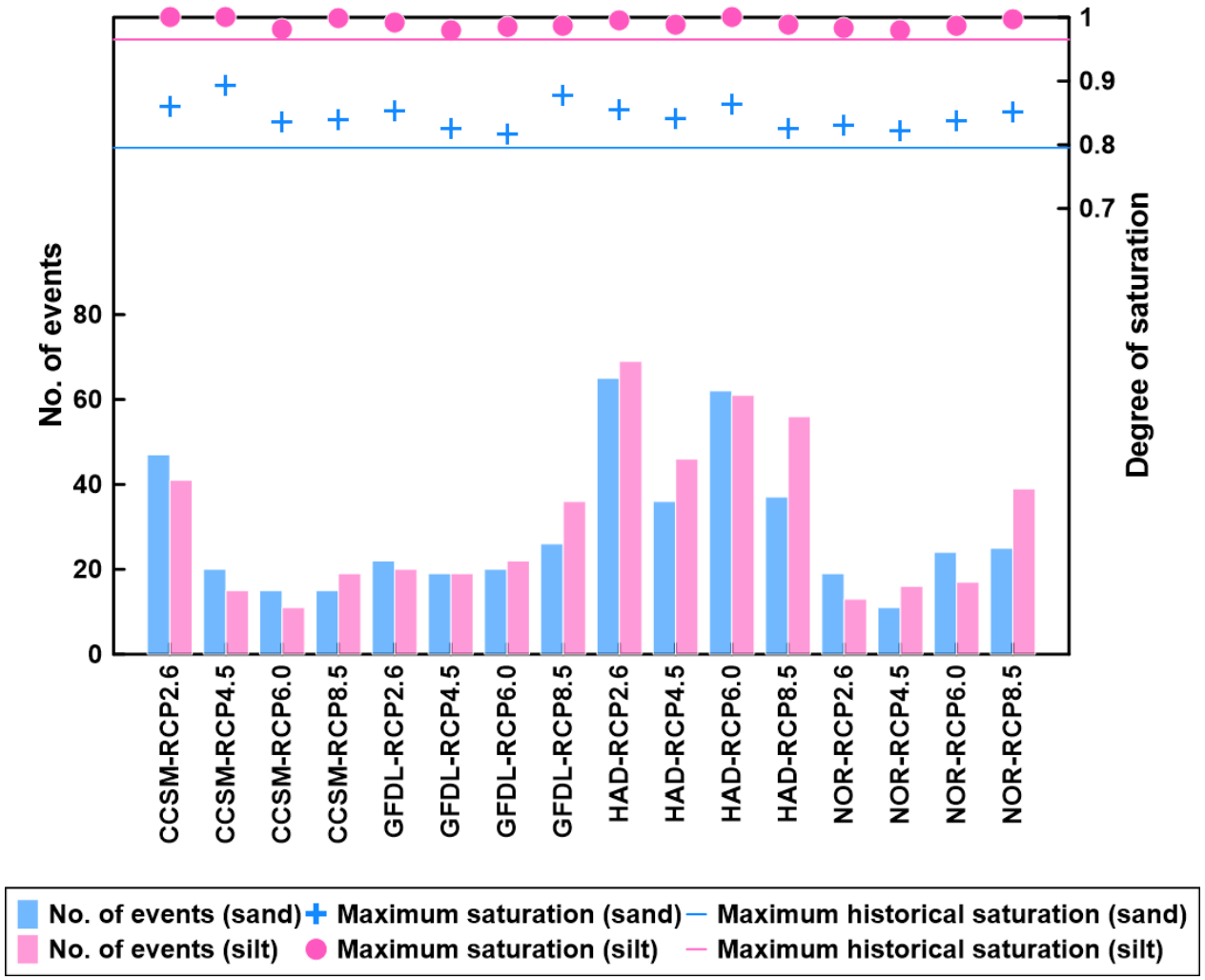

Figure C.56 Maximum degree of saturation and frequency of high saturation occurrence in sand and silt material for Timmins

Appendix D: Fragility curves

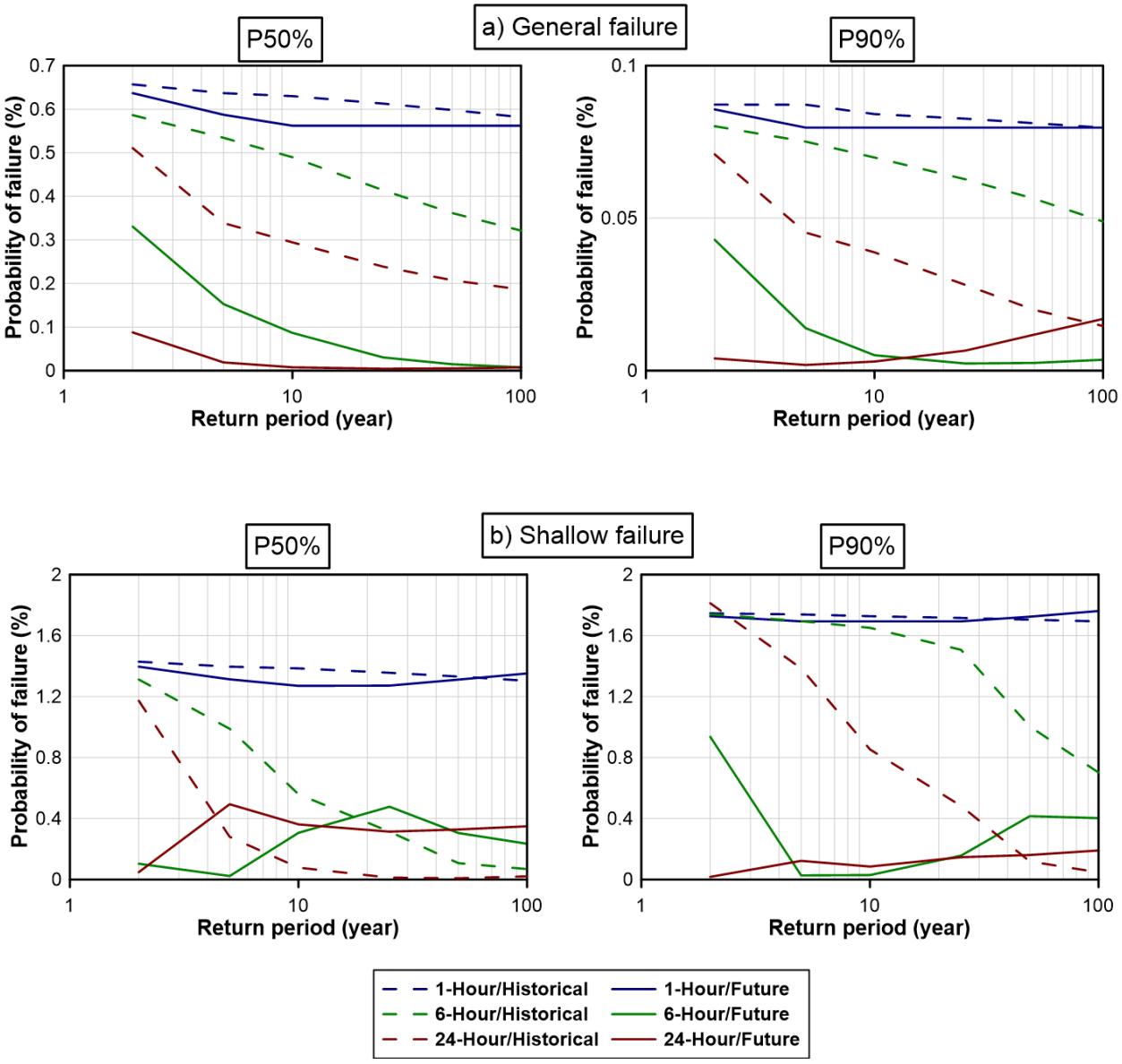

Figure D.57 Fragility curves for sand embankment in London with P50% and P90% initial condition considering both types of failures

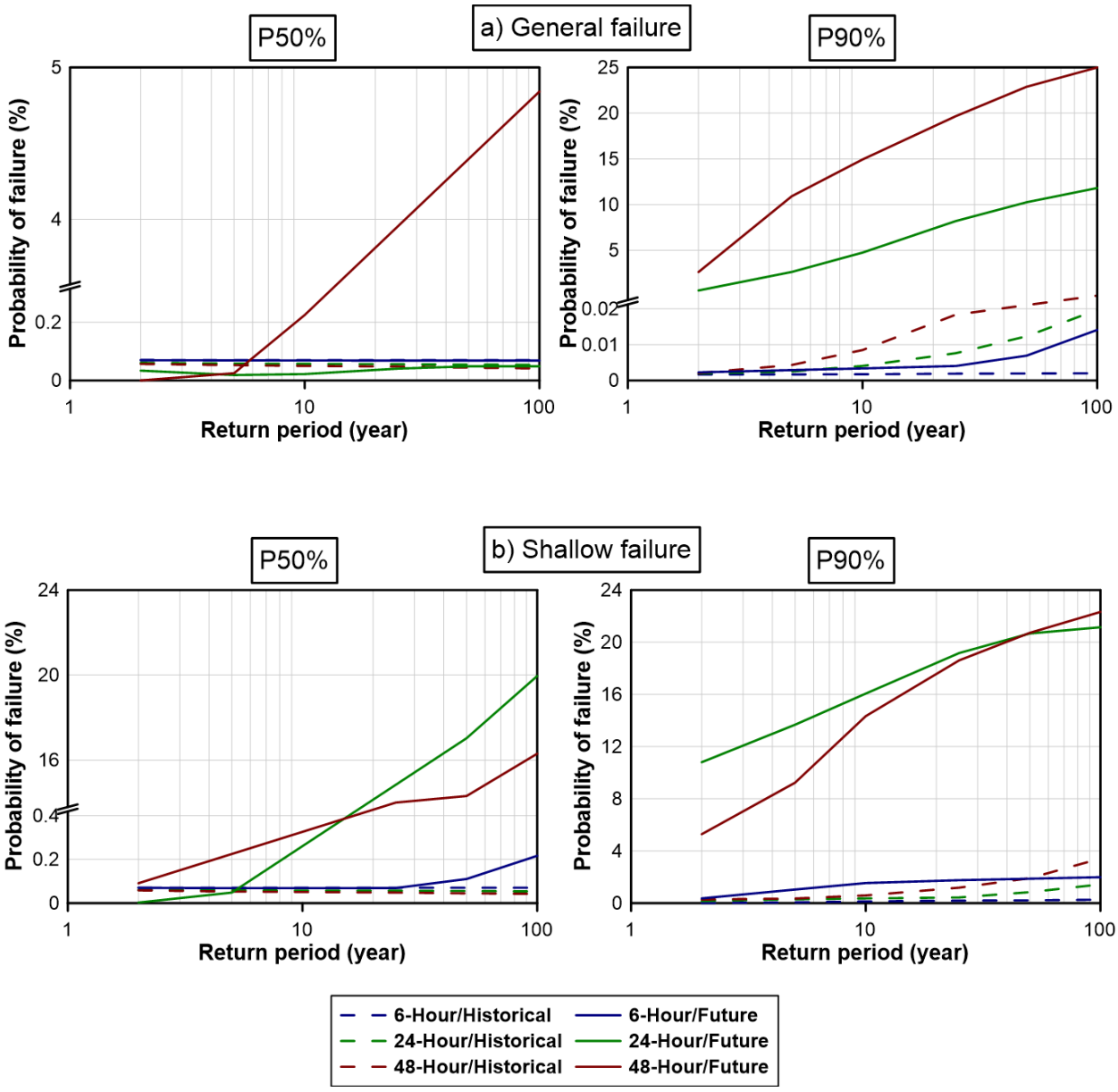

Figure D.58 Fragility curves for silt embankment in London with P50% and P90% initial condition considering both types of failures

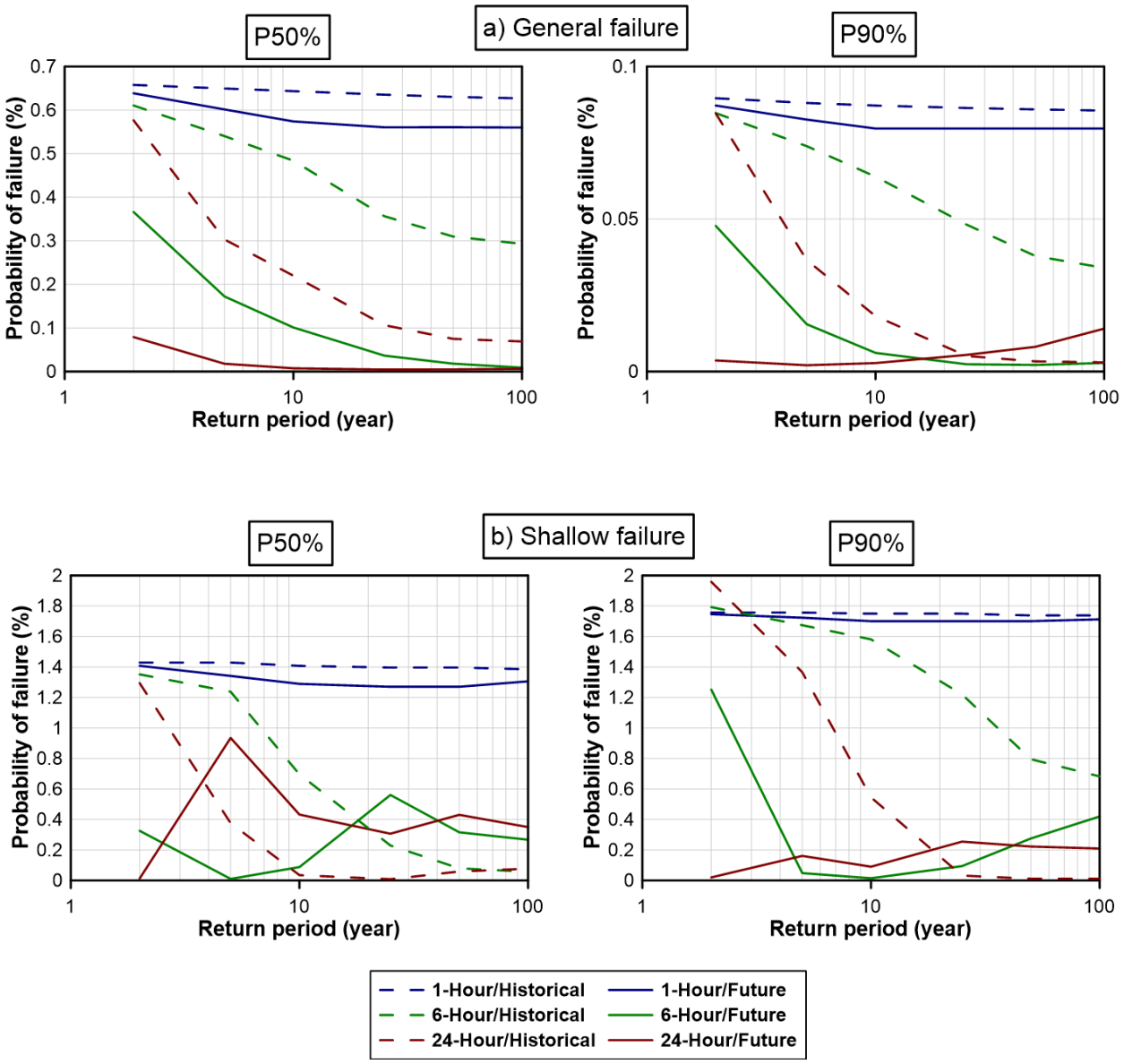

Figure D.59 Fragility curves for sand embankment in Kingston with P50% and P90% initial condition considering both types of failures

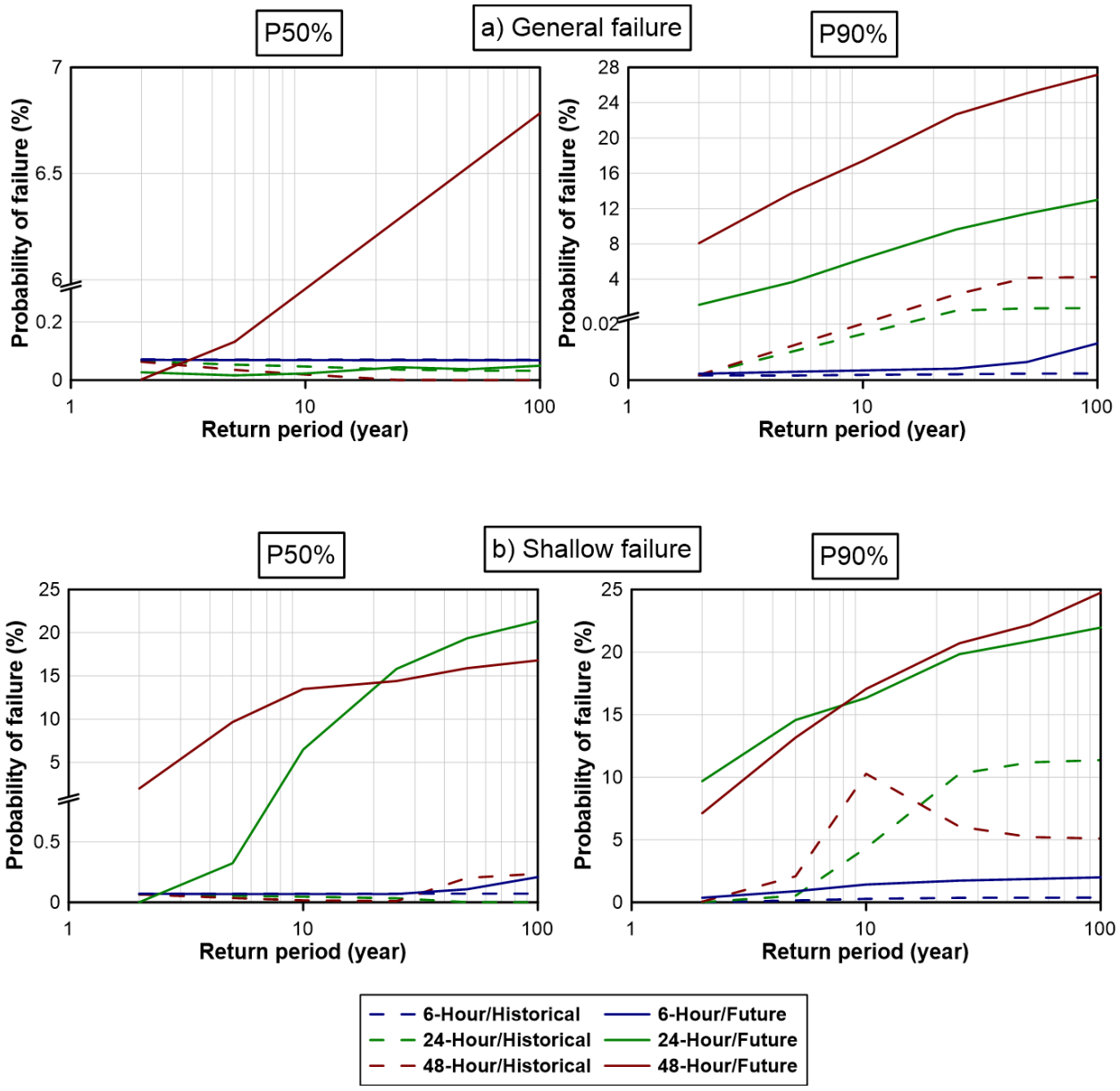

Figure D.60 Fragility curves for silt embankment in Kingston with P50% and P90% initial condition considering both types of failures

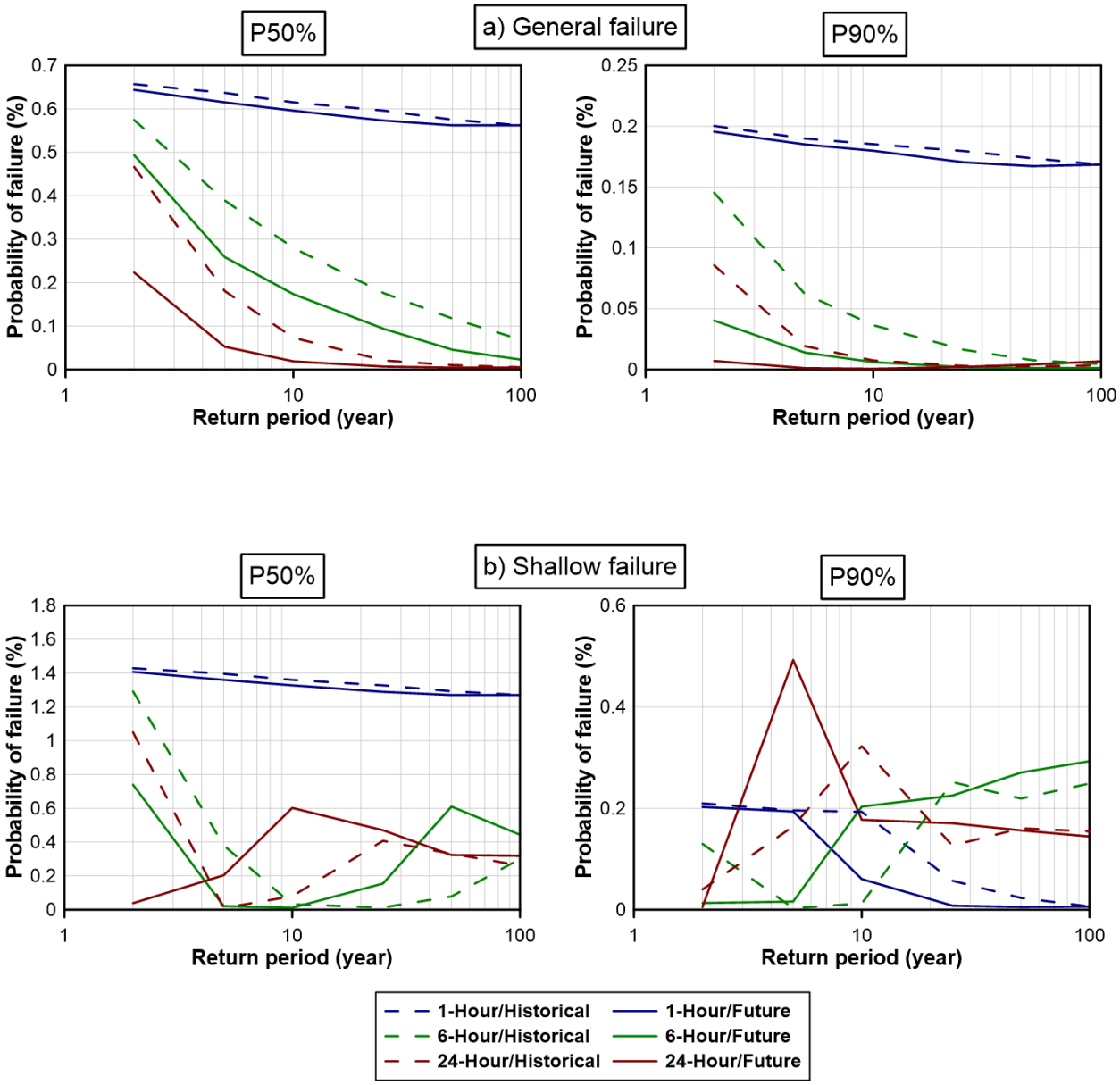

Figure D.61 Fragility curves for sand embankment in Thunder Bay with P50% and P90% initial condition considering both types of failures

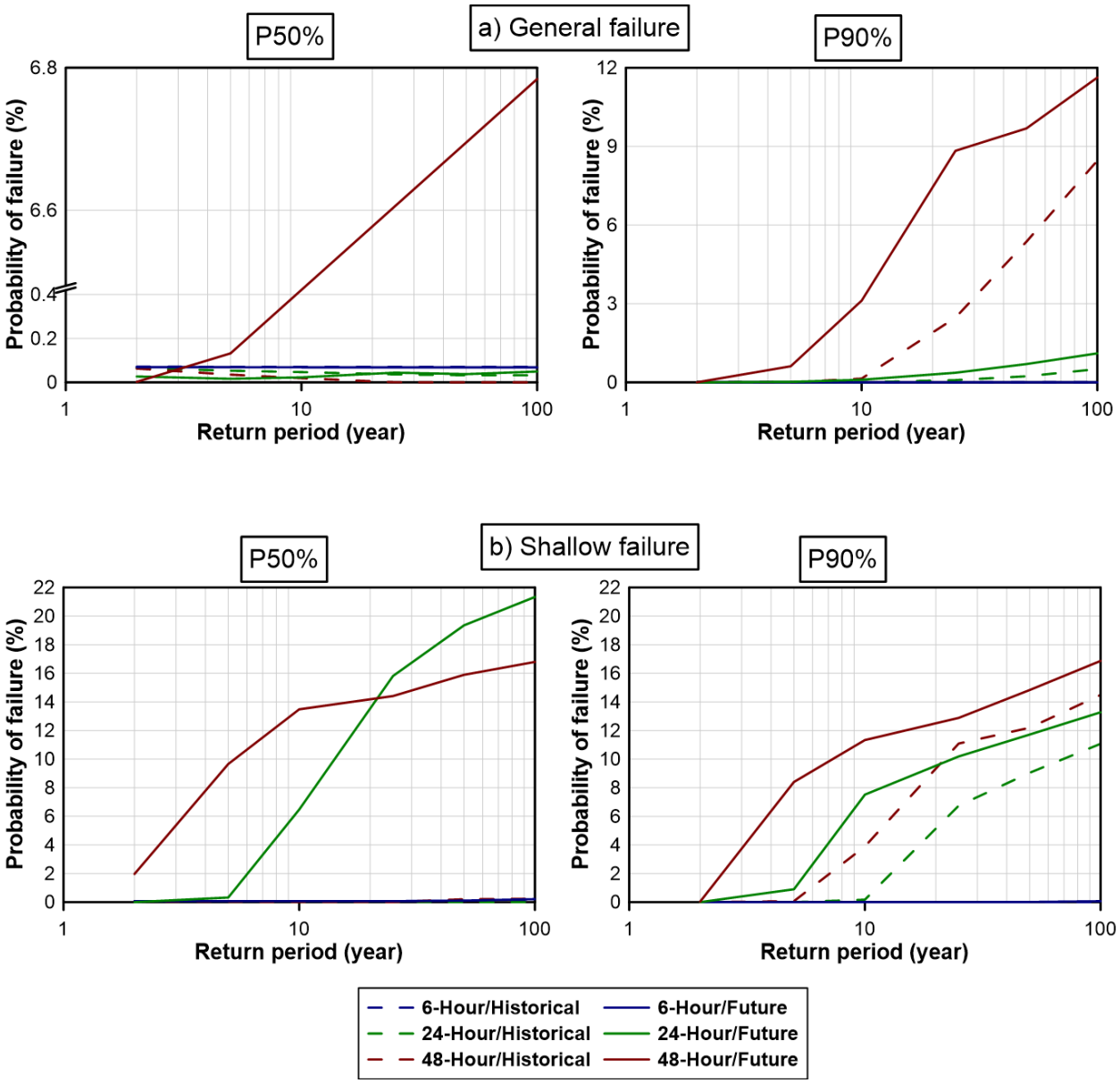

Figure D.62 Fragility curves for silt embankment in Thunder Bay with P50% and P90% initial condition considering both types of failures

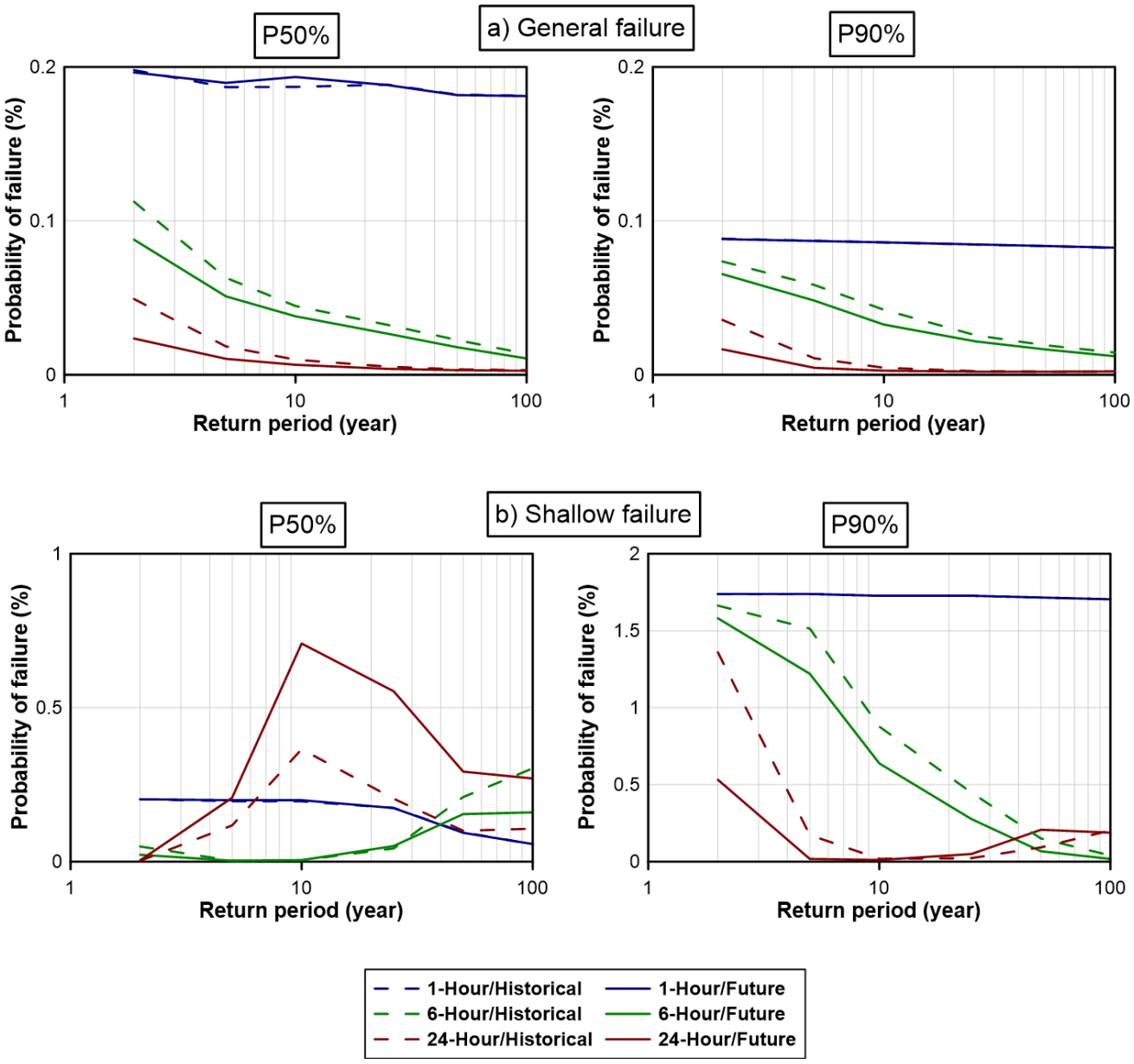

Figure D.63 Fragility curves for sand embankment in North Bay with P50% and P90% initial condition considering both types of failures

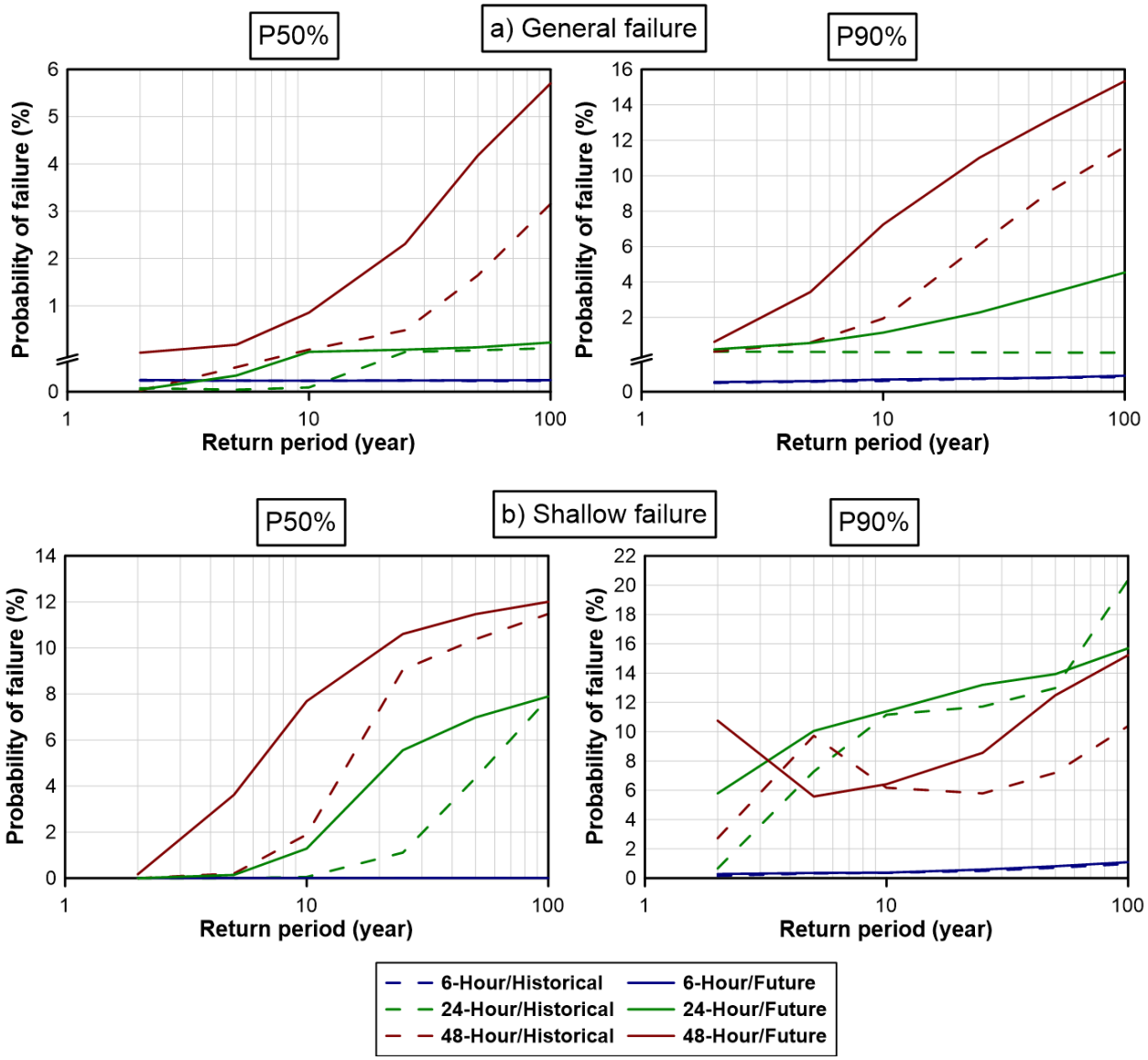

Figure D.64 Fragility curves for silt embankment in North Bay with P50% and P90% initial condition considering both types of failures

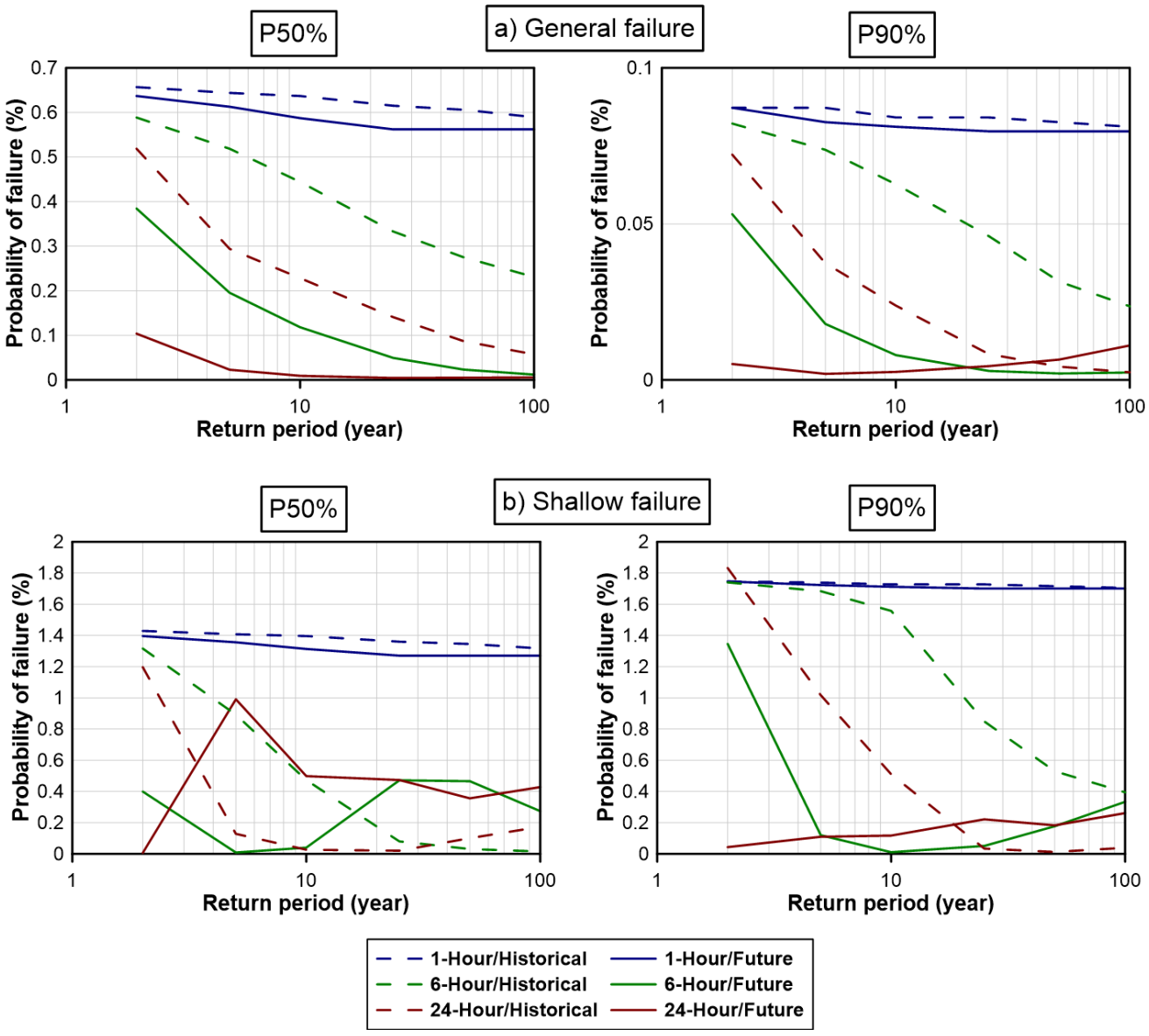

Figure D.65 Fragility curves for sand embankment in Ottawa with P50% and P90% initial condition considering both types of failures

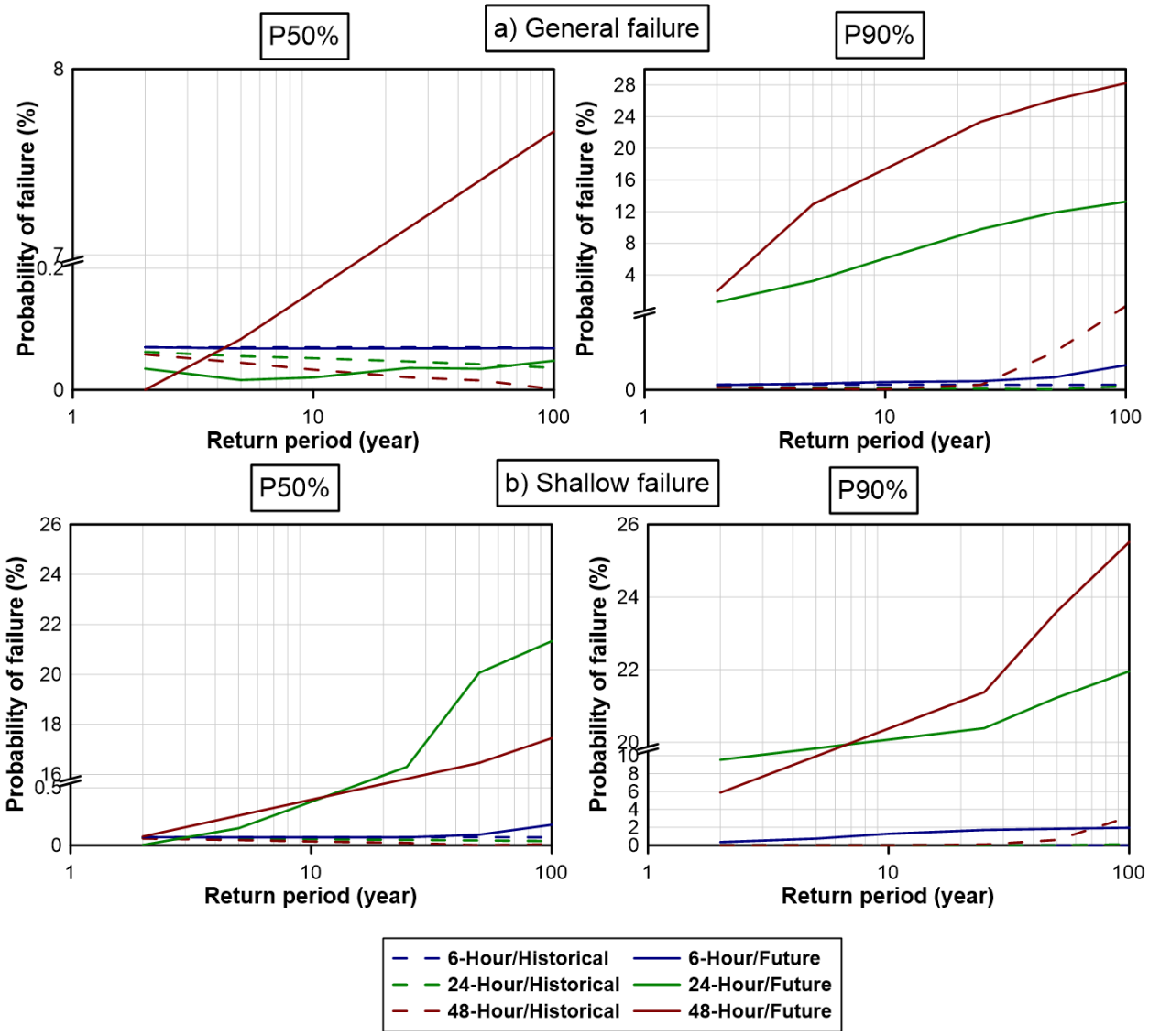

Figure D.66 Fragility curves for silt embankment in Ottawa with P50% and P90% initial condition considering both types of failures

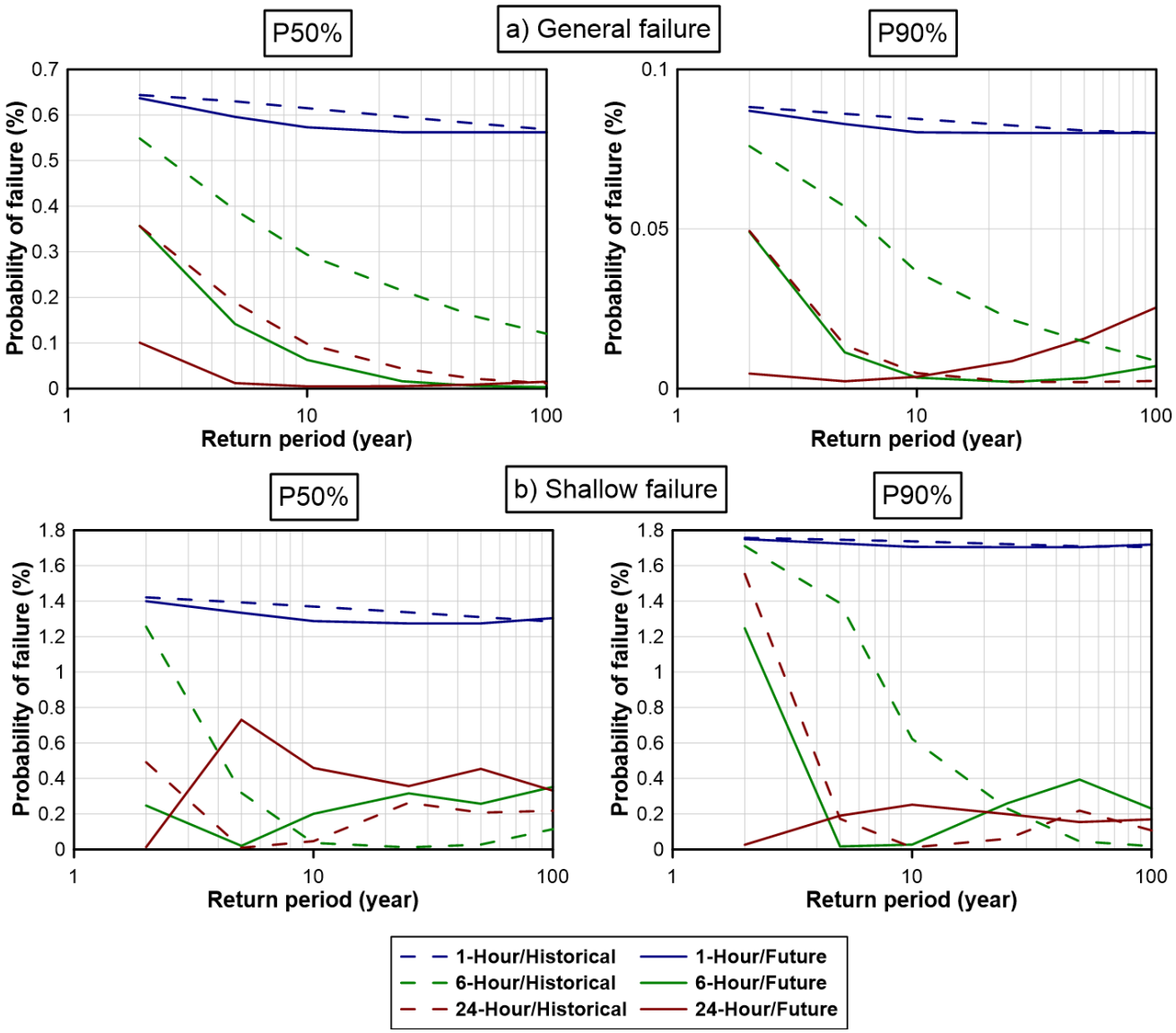

Figure D.67 Fragility curves for sand embankment in Windsor with P50% and P90% initial condition considering both types of failures

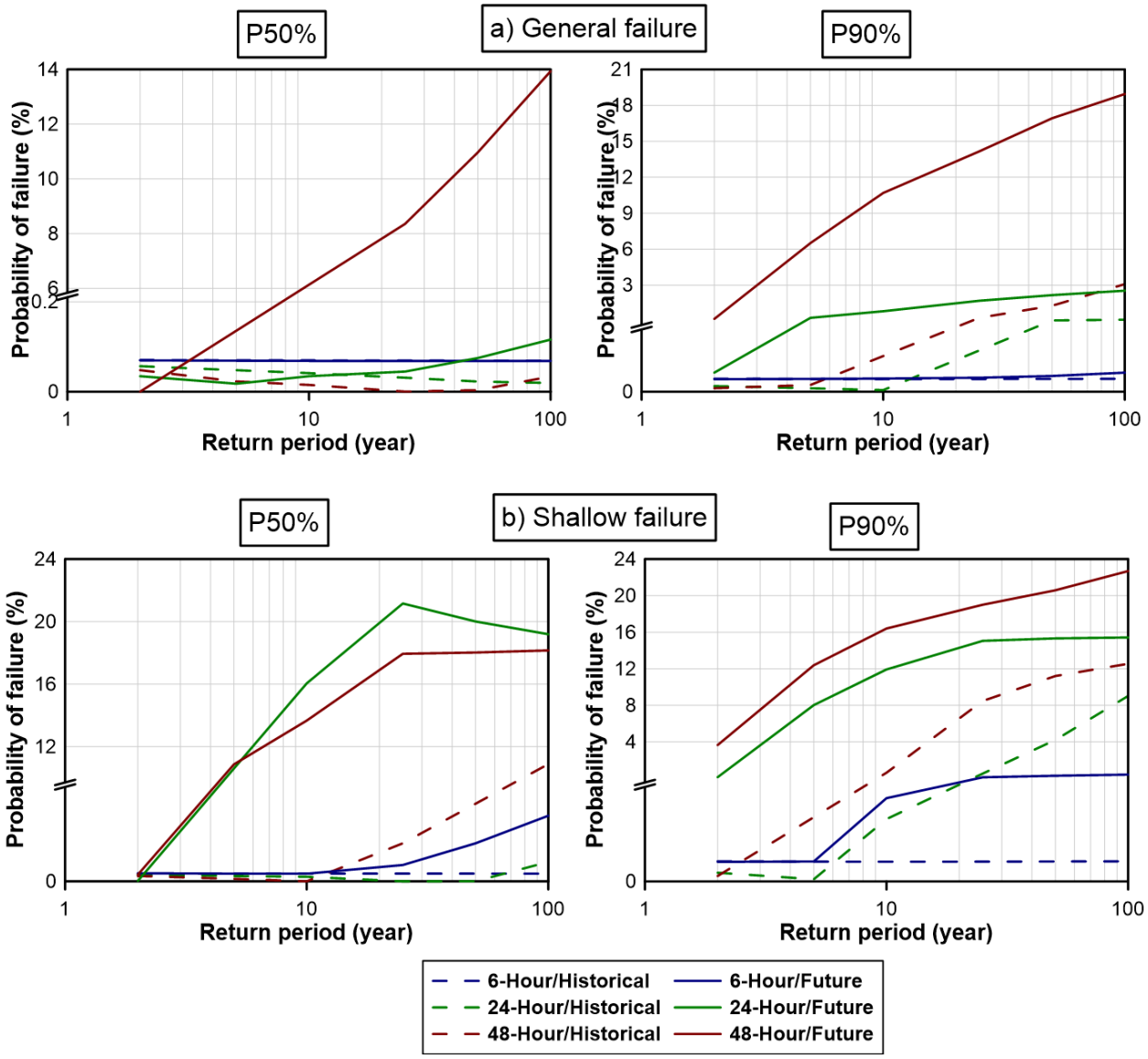

Figure D.68 Fragility curves for silt embankment in Windsor with P50% and P90% initial condition considering both types of failures

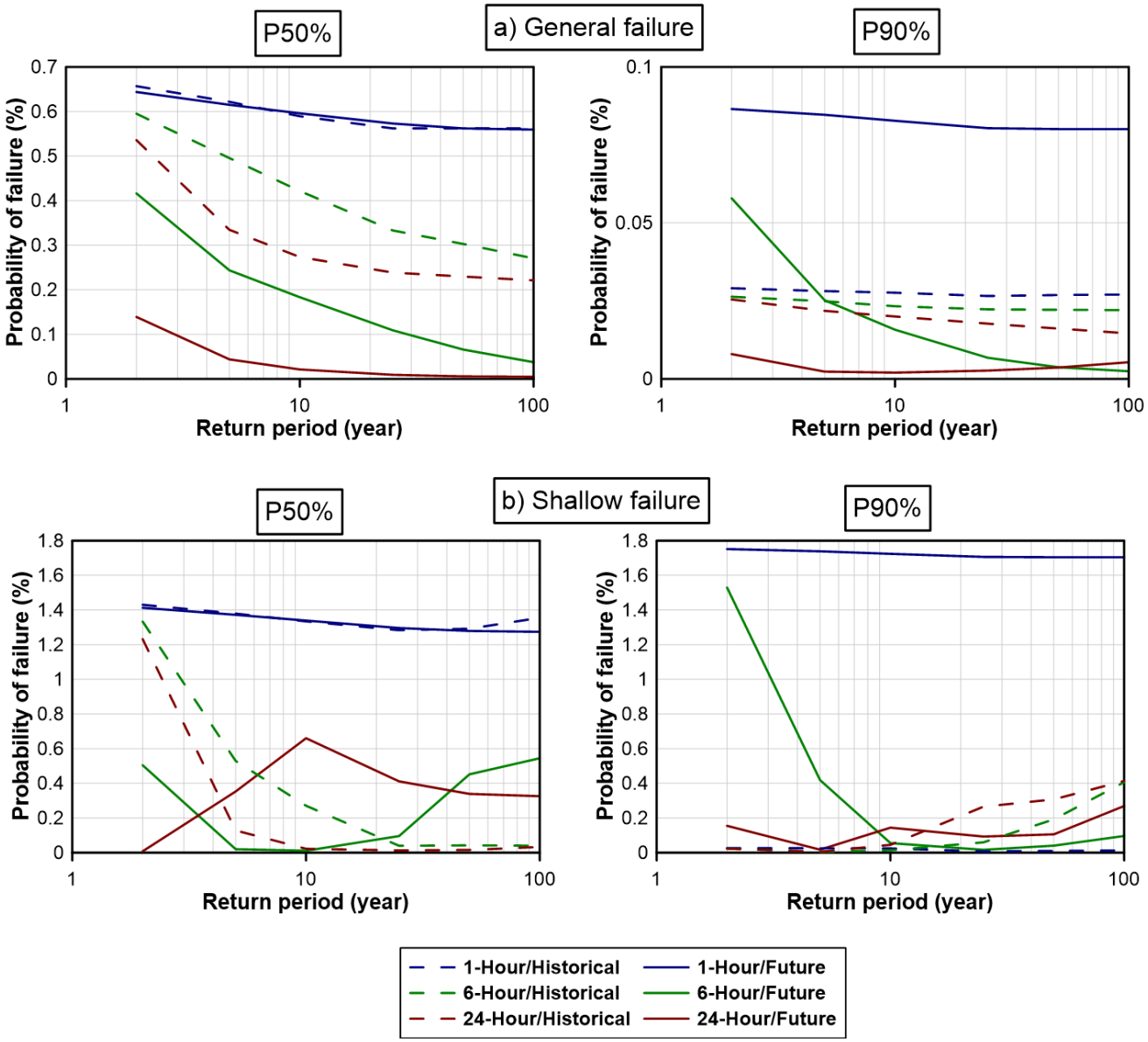

Figure D.69 Fragility curves for sand embankment in Toronto with P50% and P90% initial condition considering both types of failures

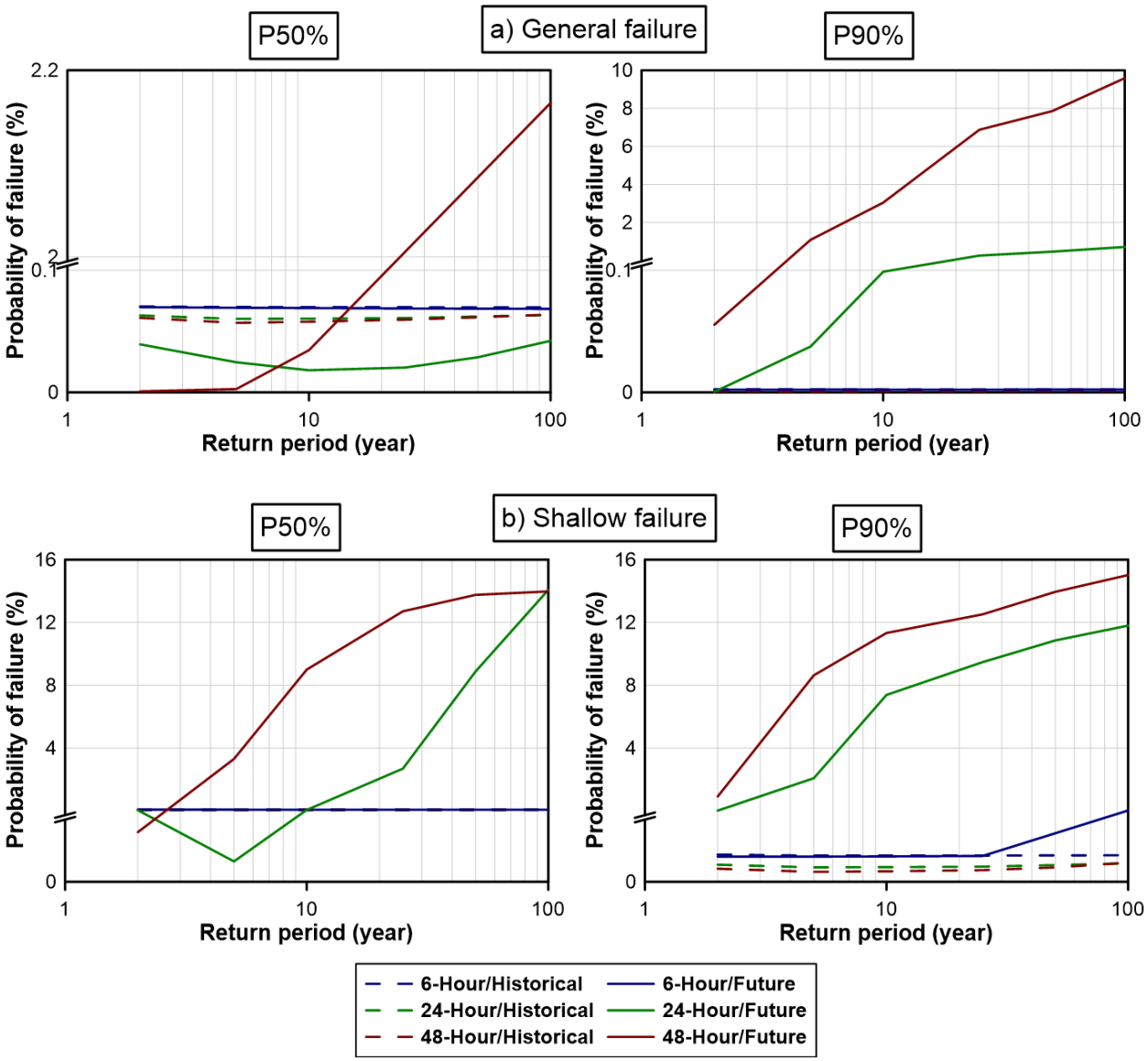

Figure D.70 Fragility curves for silt embankment in Toronto with P50% and P90% initial condition considering both types of failures

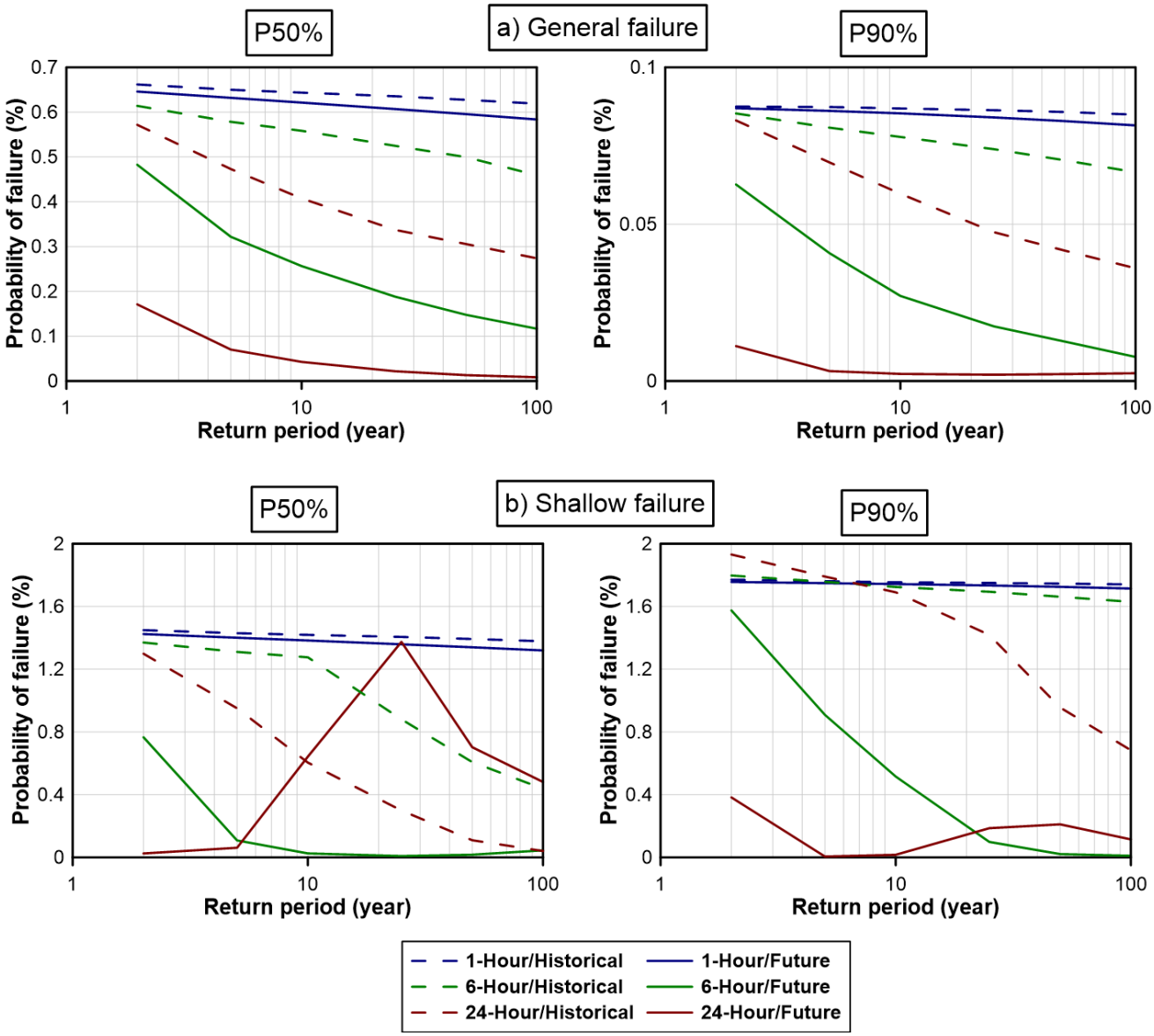

Figure D.71 Fragility curves for sand embankment in Timmins with P50% and P90% initial condition considering both types of failures

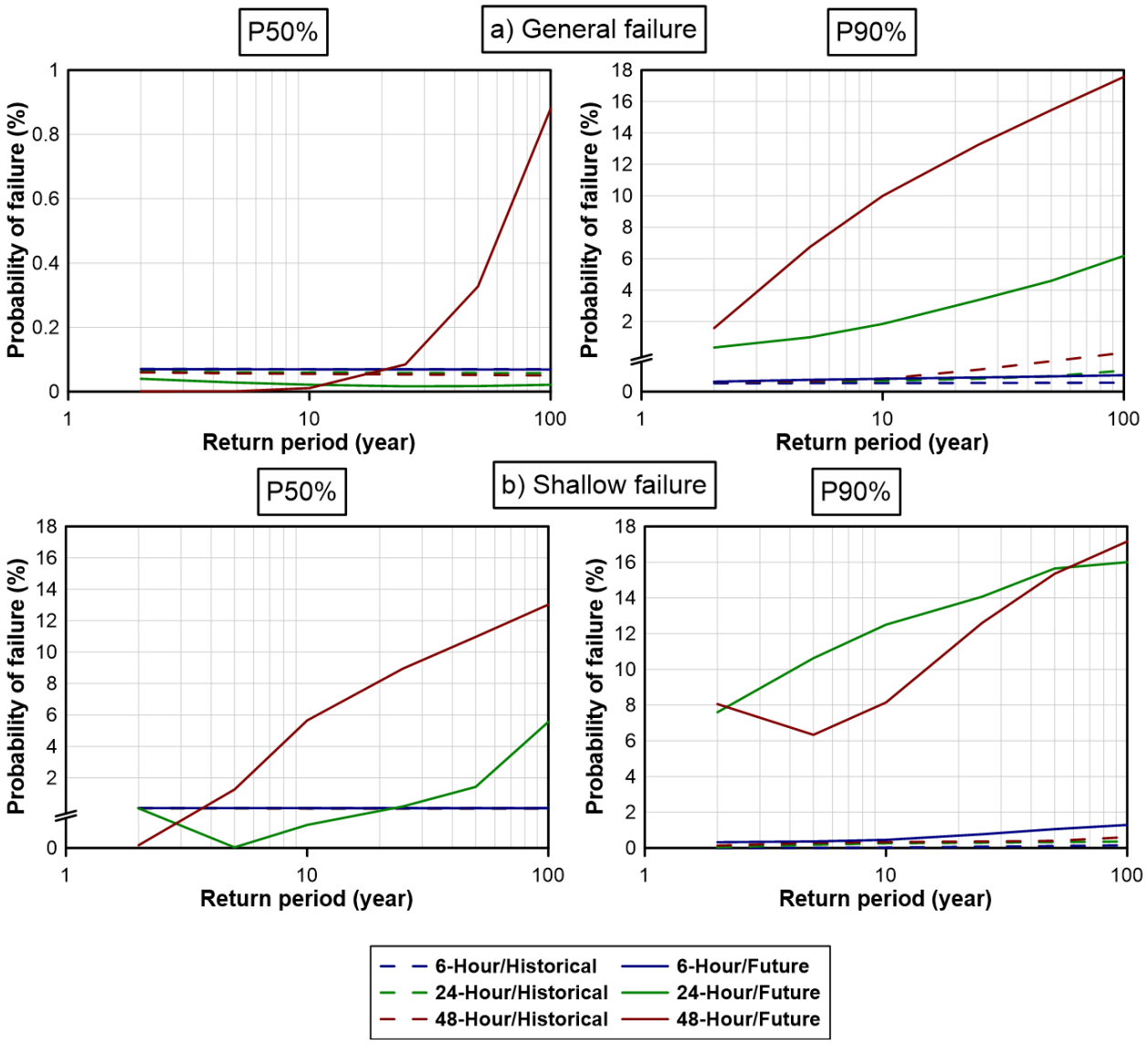

Figure D.72 Fragility curves for silt embankment in Timmins with P50% and P90% initial condition considering both types of failures

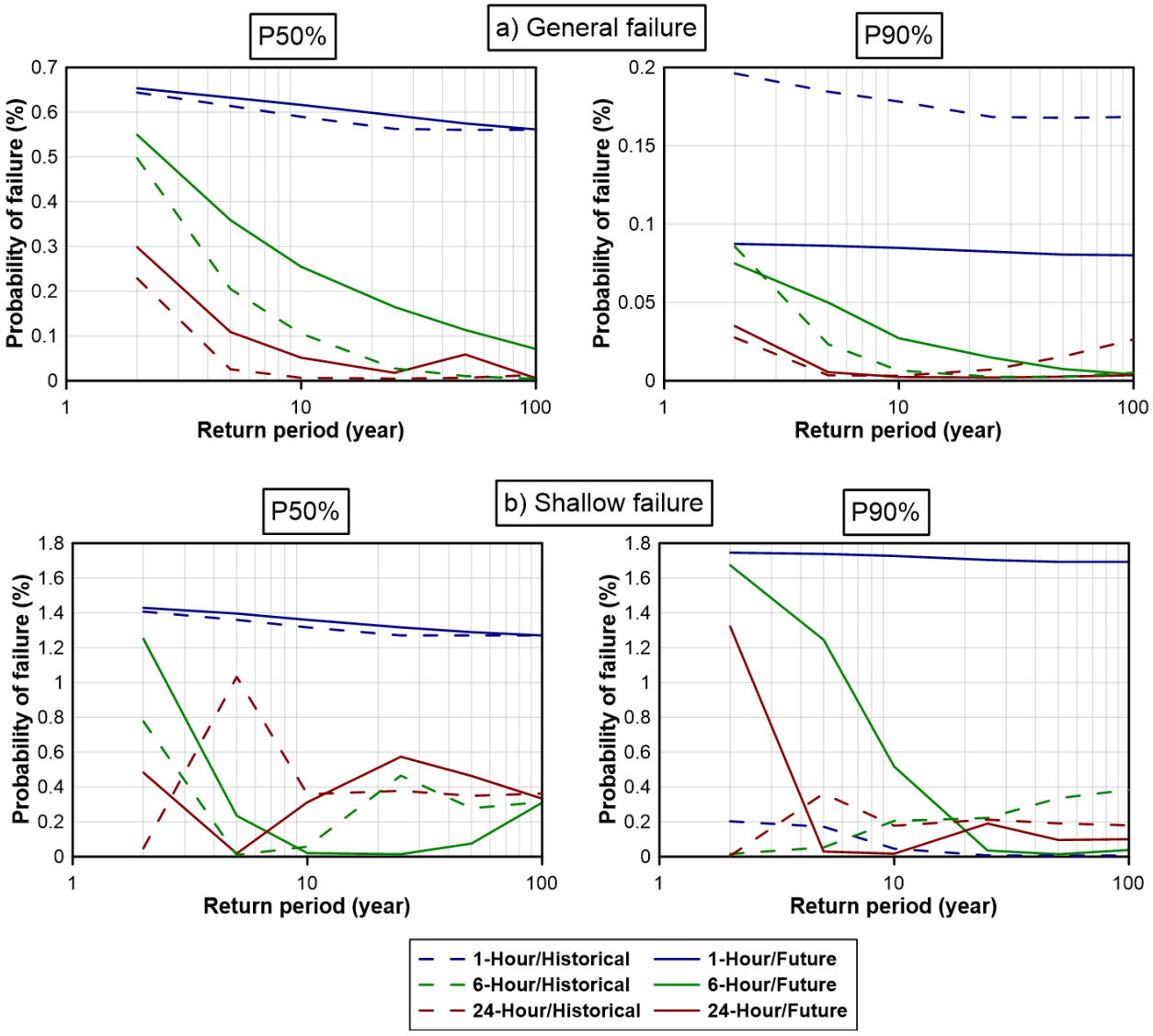

Figure D.73 Fragility curves for sand embankment in Kenora with P50% and P90% initial condition considering both types of failures

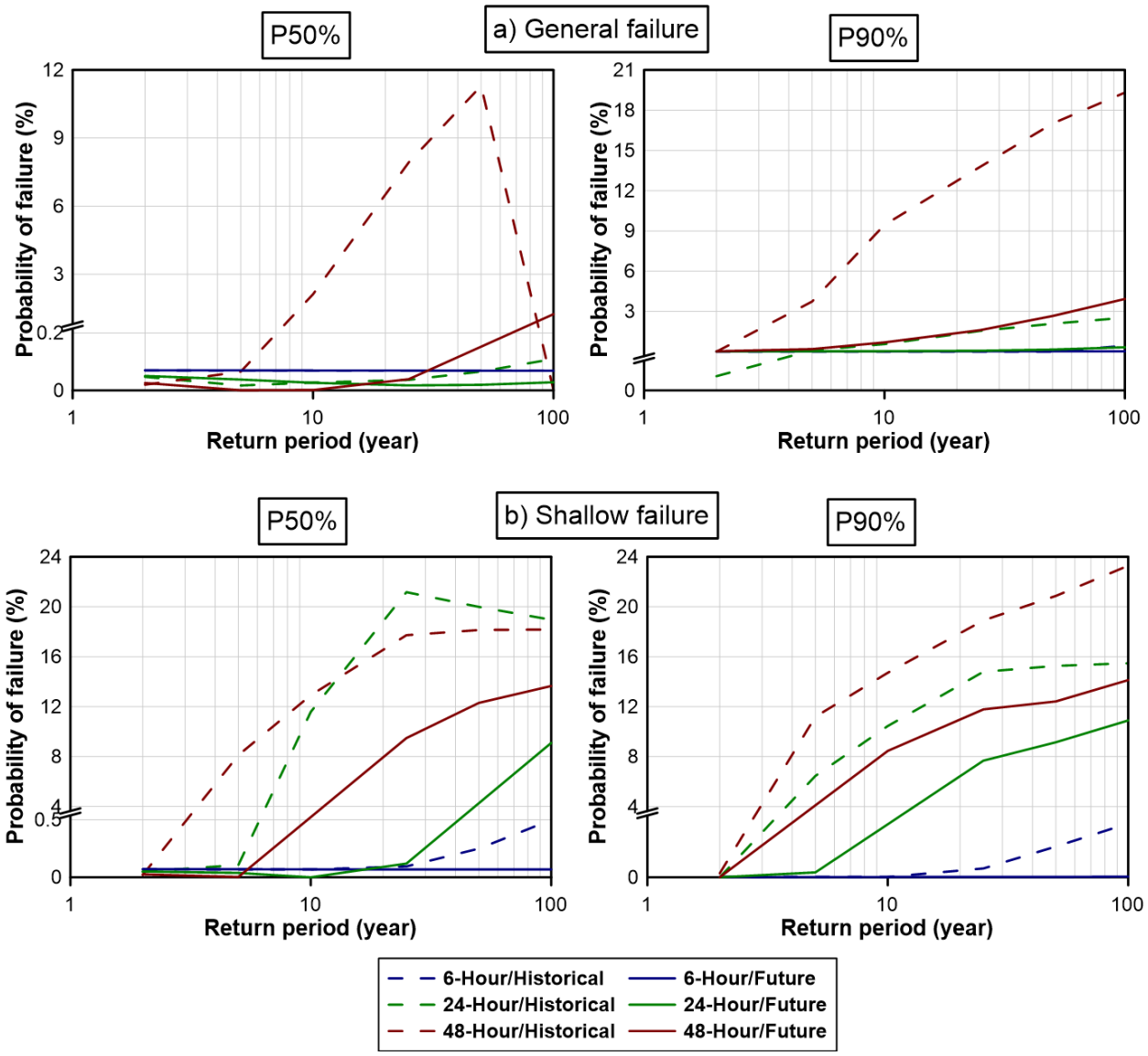

Figure D.74 Fragility curves for silt embankment in Kenora with P50% and P90% initial condition considering both types of failures